MATHEMATICAL MODELLING OF RETINAL METABOLISM

Lindsey Macdougall, MSc.

Thesis submitted to the University of Nottingham
for the degree of Doctor of Philosophy,
December 2015

Abstract

Age-related macular degeneration and diabetic retinopathy, in which the cells at the back of the eye degrade due to age and diabetes respectively, are prevalent causes of vision loss in adults. We formulate mathematical models of retinal metabolic regulation to investigate defects that may be responsible for pathology. Continuum PDE models are developed to test whether rod photoreceptors, light-detecting cells in the eye, may regulate their energy demand by adapting their length under light and dark conditions. These models assume photoreceptor length depends on the availability of nutrients, such as oxygen, which diffuse and are consumed within the photoreceptor. Our results suggest that the length is limited by oxygen and phosphocreatine shuttle-derived ATP under dark and light conditions respectively. Parameter sensitivity analysis indicates that lowered mitochondrial efficiency due to ageing may be responsible for the damage to and death of photoreceptors that are characteristic of age-related macular degeneration.

In the latter part of this thesis we shift our focus to the inner retina and examine how metabolite levels in the tissue surrounding the neurons (highly sensitive, excitable cells that transmit electrical signals) are regulated by glial cells. For instance, stimulated neurons activate their neighbours via the release of the neurotransmitter glutamate, while glial cells regulate neuronal activity via glutamate uptake. Diabetes produces large fluctuations in blood glucose levels, and eventually results in neuronal cell death, causing vision loss. We generate an ODE model for the exchange of key metabolites between neurons and surrounding cells. Using numerical and analytical techniques, we use the model to show that the fluctuations in blood glucose and metabolic changes associated with diabetes may result in abnormally high glutamate levels in the inner retina, which could lead to neuronal damage via excitotoxicity (unregulated neuronal stimulation).

ACKNOWLEDGEMENTS

I would like to express my wholehearted gratitude to everyone who has supported me during my PhD, particularly the following people without whom my thesis would not exist. Firstly, my supervisors Helen Byrne, Markus Owen, Alex Foss and Rüdiger Thul have been extremely helpful. I particularly appreciate the huge number of hours spent with Markus and Helen, and their ability to, in two sentences, convert the insurmountable complicated problem in my head into a simple obvious statement. I am also thankful to Alex for his conscientiousness and enthusiasm even after a full day's work in the operating theatre, and Rüdiger for his willingness to step up his involvement in the project at a moment's notice.

Peter deserves a huge thank you for the many hours spent advising me on maths, emergency IT support and proof reading. I also wish to thank Martin, Sunny and my parents for all of their help proof reading, and Dave Parkin for his IT support. My health may have prevented me completing my PhD without the help of Dr Nash, Emma Rowlett, Helen Cunliffe, Andrea Blackbourn and Richard Tew, all of whom are incredibly good at their jobs and genuinely caring. I would also like to thank the creators of positive distractions, including Monty Python for inventing the ancient art of fish slapping, and Sainsburys Red Label for ensuring that my teapot has never been empty (the writing of this thesis involved the consumption of an estimated 13147 cups of tea).

Finally, words cannot express my eternal gratitude to God, my friends and family who light up my world, and have remained close during the toughest of times. My parents have given me all the support I could wish for throughout my whole life: practically, financially and emotionally, and they also happen to be two of my closest friends. I am also thankful for Billy who has stood by and supported me, and Peter and Julia who have laughed and cried with me and were always there when I needed them most.

CONTENTS

I Rod Photoreceptor Metabolism 1

1 INTRODUCTION 2
1.1 Anatomy of the Eye . . . 3
1.2 Energy Provision and Demand in Inner Retinal Neurons and Photoreceptors . . . 5
1.3 Physiology of Rod Photoreceptor Metabolism . . . 7
1.4 Pathology . . . 11
1.5 Mathematical Models Relevant to Our Work on Rod Photoreceptor Metabolism . . . 16
1.5.1 Moving Boundary Problems . . . 17
1.5.2 Models of Photoreceptor Oxygen Metabolism . . . 19
1.5.3 Models of Energy Transfer via the Phosphocreatine Shuttle 20
1.6 Thesis Structure . . . 21

2 OXYGEN AS A DETERMINANT OF ROD PHOTORECEPTOR LENGTH 24
2.1 Model Development . . . 25
2.1.1 Oxygen Concentration, $U(x,t)$ . . . 26
2.1.2 Length of the Outer Segment, $L_{OS}(t)$ . . . 27
2.1.3 Nondimensionalisation . . . 29
2.2 Steady State Solutions . . . 30
2.3 Parameter Estimation . . . 34
2.3.1 Outer Segment and Inner Segment Length (L_{OS}, L_{IS}) . . . 36
2.3.2 Oxygen Concentration at the Outer Segment End ($U_{L_{OS}}$) . 37
2.3.3 Rates of Oxygen Uptake by Mitochondria (μ) . . . 39
2.3.4 Oxygen Baseline Consumption Rate (λ) . . . 40
2.3.5 Threshold Oxygen Concentration (U_{Thr}) . . . 42
2.3.6 OS Growth Parameter (k) . . . 42
2.4 Solution Techniques . . . 43
2.5 Numerical Results . . . 48
2.6 Parameter Sensitivity . . . 51

2.6.1 Physiological Interpretation of Parameter Sensitivity Diagrams . . . 51
2.6.2 Predicting Causes of Age-Related Macular Degeneration . 54
2.6.3 Sensitivity of our Model Predictions to Changes in Parameters . . . 55
2.7 Discussion . . . 57

3 THE PHOSPHOCREATINE SHUTTLE AS A DETERMINANT OF ROD PHOTORECEPTOR LENGTH 60
3.1 Model Development . . . 62
3.1.1 Creatine Phosphate, Creatine, Free Phosphate, ATP and ADP Concentrations . . . 62
3.1.2 Length of the Outer Segment . . . 65
3.1.3 Boundary and Initial Conditions . . . 67
3.1.4 Nondimensionalisation . . . 68
3.2 Parameter Estimation . . . 70
3.3 Solution Techniques . . . 76
3.4 Numerical Results . . . 78
3.5 Parameter Sensitivity . . . 83
3.6 Discussion of Phosphocreatine Shuttle Model . . . 86
3.7 Oxygen and the Phosphocreatine Shuttle as Determinants of Rod Photoreceptor Length . . . 87
3.7.1 Model Development . . . 87
3.7.2 Nondimensionalisation and Parameter Estimation . . . 87
3.7.3 Refinement of Parameter Estimates . . . 88
3.7.4 Numerical Results . . . 91
3.7.5 Parameter Sensitivity . . . 95
3.8 Discussion of Oxygen and Phosphocreatine Shuttle Models . . . 98

II Inner Retinal Metabolic Regulation 102

4 INTRODUCTION TO INNER RETINAL METABOLIC REGULATION 103
4.1 Physiology of Inner Retinal Metabolism . . . 104
4.2 Existing Mathematical Models . . . 114
4.2.1 Deterministic Spatially Averaged Compartmental Models 116
4.2.2 Aubert and Costalat's Model of Cerebral Metabolism [1] . 120
4.2.3 Other Models of Glial and Neuronal Metabolism . . . 140

4.2.4 Compartmental Models Capturing Pathology 144
4.3 Discussion 145

5 FORMULATING A MODEL OF INNER RETINAL METABOLIC REGULATION 147
5.1 Model Formulation 148
5.2 Nondimensionalisation 160
5.3 Comparison with Model of Aubert and Costalat 162
5.3.1 Development of Submodels 163
5.3.2 Asymptotic Approximation to the AC Submodel 165
5.3.3 Comparison of the IR Submodel and the Simplified AC Submodel 174
5.4 Discussion 186

6 MODEL PREDICTIONS ON DIABETIC RETINOPATHY 188
6.1 Decomposition of our Model into Glucose-Lactate and Glutamate-Glutamine Submodels 189
6.1.1 Glucose-Lactate Submodel 189
6.1.2 Glutamate-Glutamine Submodel 190
6.2 Parameter Estimation 194
6.3 Results 200
6.3.1 Simulated Dark-Light Cycle with Constant Blood Glucose 200
6.3.2 Simulated Responses to Variation in Blood Glucose 206
6.4 Parameter Sensitivity Analysis 208
6.4.1 Degeneration of Retinal Capillary Walls 211
6.4.2 Reduced Activity of Glutamine Synthetase 213
6.4.3 Decreased Glial Glutamate Uptake from the ECS 213
6.5 Discussion of our Model of Inner Retinal Metabolic Regulation 217

A REPRODUCTION OF SIMULATION RESULTS IN AUBERT AND COSTALAT'S MODEL 221

B ASYMPTOTIC ANALYSIS OF THE AC SUBMODEL 227

C CONDITIONS FOR AN OPTIMUM MATCH BETWEEN THE AC AND IR SUBMODEL RESULTS 242

D CONSTRAINTS ON PARAMETERS IN GLUTAMATE-GLUTAMINE SUBMODEL 247

E ESTIMATION OF PARAMETERS IN INNER RETINAL METABOLISM 250
E.1 Experimental Measurements of Parameters 250
E.2 Using Glucose-Lactate and Glutamate-Glutamine Submodels to Refine Parameter Estimates 253

Part I.

Rod Photoreceptor Metabolism

1

INTRODUCTION

Vision loss affects almost two million people in the UK alone, and retinal diseases are the leading cause of permanent blindness [2]. Age-related macular degeneration and diabetic retinopathy are prevalent retinal diseases, in which the back of the eye is damaged by ageing and diabetes respectively. While the prognosis for sufferers of diabetic retinopathy has improved significantly over recent years, with laser surgery now able to prevent severe vision loss in approximately 50% of patients [3], additional therapeutic strategies are urgently needed. Furthermore, age-related macular degeneration remains untreatable in over 90% of cases [4]. This highlights the importance of gaining greater insight into the underlying causes for such diseases.

While the pathological events associated with the progression of retinal diseases are well documented, the underlying mechanisms responsible for their onset are not well understood [5]. One proposed cause or contributing factor is the malfunctioning of energy metabolism in the retinal cells [5–7]. Our objectives in this thesis are to formulate mathematical models of metabolic regulation in the retina, and to use them to identify imbalances in retinal energy metabolism that may lead to pathology.

The retina is an isolated system under intense metabolic stress, thus its metabolic regulation is crucial. The energy demand of the retina is very high, blowfly photoreceptors, for example, have a higher energy consumption per gram than active mammalian muscle [8]. The rates and sites of energy demand vary markedly, e.g. under light and dark conditions. Additionally, the retina contains both neuronal cells (excitable cells that transmit electrical signals) which are highly sensitive to variations in metabolite concentrations, and blood vessels in which nutrient levels vary considerably. It is therefore vital that the environment surrounding the neurons is stringently controlled.

For these reasons, retinal metabolism possesses extremely well-adapted regulatory mechanisms. In this thesis we consider examples of retinal metabolic regulation. Firstly, in Chapters 2 and 3, we formulate PDE models to investigate how rod photoreceptor cells (light-detecting cells) may adapt their length to ensure they possess sufficient energy to function during light and dark conditions. These models are used to show that the reduced efficiency of energy production by the mitochondria in ageing retinae [9, 10] may cause photoreceptor shortening and eventually death, characteristic features of age-related macular degeneration [11, 12]. In the latter part of this thesis (Chapters 4-6) we present a compartmental ODE model constructed to examine how homeostasis (resistance to external changes) is preserved in the environment surrounding the neuronal cells in the inner retina. The model solutions suggest that, in a healthy retina, the neurons are well protected from variations in nutrient levels in the bloodstream. However, the high amplitude fluctuations in the blood glucose levels of diabetes sufferers may perturb the regulatory processes in the inner retina so that they are unable to function properly, initiating a chain of events leading to localised neuronal cell death, which may explain the blind spots that characterise diabetic retinopathy.

The remainder of this chapter is organised as follows. We review the structure of the retina in §1.1 and provide detailed information about energy metabolism in neuronal cells in §1.2, and rod photoreceptors in §1.3. In §1.4 we discuss the state of the art of research into age related macular degeneration and diabetic retinopathy, before reviewing relevant mathematical models in §1.5. Finally the structure of this thesis is outlined in §1.6.

1.1 ANATOMY OF THE EYE

Before discussing retinal diseases and modelling strategies, we introduce the composition and function of the *retina* and its components (see Figure 1.1). The retina is a layer at the back of the eye that contains many photoreceptors, neurons that convert light energy to sensory information that is transmitted to the brain [15]. *Cone* photoreceptors distinguish between different colours (i.e. different wavelengths) of light. Vision in dark conditions is facilitated by *rod* photoreceptors [16]. The central region of the retina, which is particularly densely packed with photoreceptors, is called the *macula lutea*, or *macula*.

The retina is organised in layers (see Figure 1.2). The inner retina (left-hand

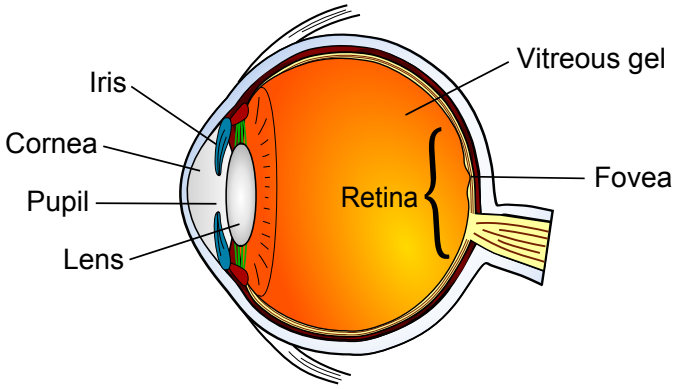


Figure 1.1.: Structure of the eye, adapted from [13, 14].

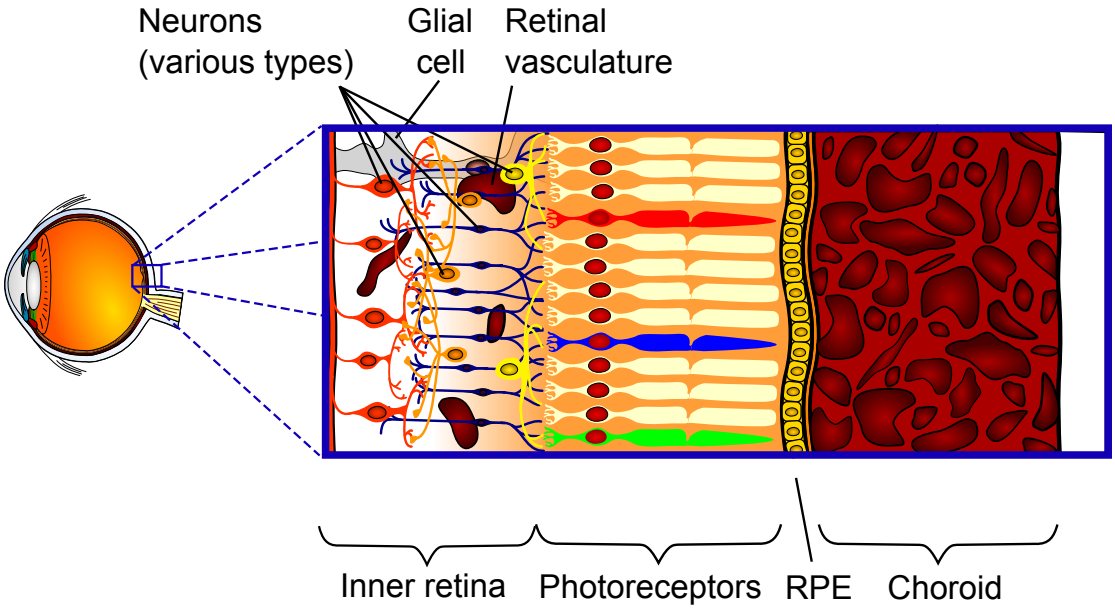


Figure 1.2.: Layers of the retina, with the innermost layers on the left hand side, adapted from [14, 17, 18].

side) contains neurons, the *retinal* blood vessels which supply the neurons with oxygen and nutrients, and *glial* cells which regulate the environment surrounding the neurons and deliver blood-borne oxygen and nutrients to them [19]. Adjacent to (to the right of) the inner retina is a layer of photoreceptors, whose outer ends are embedded in the *retinal pigment epithelium* (*RPE*), which allows regulated transport of oxygen, nutrients and waste products between photoreceptors and blood vessels in the outermost layer, the *choroid*. Between the RPE and the vasculature lies a basement membrane called *Bruch's membrane* [20]. The photoreceptors, RPE, Bruch's membrane and the choroidal vasculature constitute the *outer retina*.

The retinal and choroidal vessels are two distinct blood supplies that sustain the inner and outer retina respectively [21, 22]. The photoreceptors obtain almost all of their oxygen and nutrients from choroidal vessels, which provide approximately 90% of their oxygen under dark conditions and 100% in light [23]. In the following section we examine the energy producing and consuming processes that take place in photoreceptors and inner retinal neurons.

1.2 Energy provision and demand in inner retinal neurons and photoreceptors

The rates at which the photoreceptors and inner retinal neurons generate and expend energy are among the highest in all bodily tissues [24–26]. Thus, the mechanisms that ensure the availability of, and regulate the use of, energy in photoreceptors are paramount to their survival. Photoreceptors are a specific type of neuronal cell. As such, photoreceptors share many characteristics with inner retinal neurons, including how they produce energy, and the largest contributor to their energy consumption, the transmission of nerve impulses. Before discussing these mechanisms, we describe the form that energy takes *in vivo*.

The energy required in cellular processes is stored within the high-energy compound *adenosine triphosphate* (*ATP*). ATP can be broken down by the following biochemical reaction in the forward direction,

$$\mathrm{ATP} \rightleftharpoons \mathrm{ADP} + \mathrm{P} + \text{energy}, \tag{1.1}$$

whereby the energy it contains is released. ATP can be produced by the reverse of this reaction, but this requires energy input. Retinal neurons (including photoreceptors), like other cell types, derive ATP from blood-borne oxygen and nutrients via two metabolic pathways. The first is *oxidative metabolism* which produces ATP *aerobically* (by consuming oxygen), while the second, *glycolysis*, is *anaerobic* (does not require oxygen).

Neuronal cell membranes contain voltage-dependent *gated ion channels*: proteins that span the thickness of the cell membrane and can change their shape (*conformation*) in response to stimuli, to form pores in the membrane that are permeable to specific ions. These channels mediate regulated transport of ions through the cell membrane, enabling neurons to control their intracellular ionic concentrations relative to the extracellular environment. If a neuron is at *rest*, the gated ion channels are closed (i.e. they have a very low permeability), with different ionic concentrations and electrical charges inside and outside the cell. The concentrations of Na^+ and K^+ ions are highest in the extracellular and intracellular environments respectively. This gives rise to an electrochemical potential across the cell membrane (a *membrane potential*), which would drive the flow of electrical current through the ion channels if they were open, until the electrical potential across the cell membrane became equal to the opposing chemical potential driving diffusive flux. The electrical potential required to exactly balance the effects of diffusion of a particular ion is referred to as its *Nernst* potential, E, given by,

$$E = \frac{RT}{zF} \ln\left(\frac{[\mathrm{X}]_{\mathrm{ext}}}{[\mathrm{X}]_{\mathrm{int}}}\right), \tag{1.2}$$

where $[\mathrm{X}]_{\mathrm{ext}}$, $[\mathrm{X}]_{\mathrm{int}}$ and z refer to the extracellular and intracellular concentrations, and the electrical charge, of ion X respectively. R, T and F denote the ideal gas constant, absolute temperature and Faraday's constant (the charge of one mole of electrons) [27] respectively. The Nernst potential is approximately $57\,\mathrm{mV}$ for Na^+ and $-80\,\mathrm{mV}$ for K^+ ions [28]. We note that equation (1.2) is only applicable for a membrane that is permeable to a single type of ion whereas, in practice, the cell membrane is permeable to multiple chemical species simultaneously.

The probability that an ion channel opens is dependent upon the membrane potential. A decrease in the extracellular Na^+ concentration increases the cell membrane potential towards zero, referred to as *depolarisation*, causing some of

the gated Na^+ ion channels to open. This allows the flow of Na^+ into the cell. Consequently, the electrical charge within the cell increases, further increasing the membrane potential towards zero. If the membrane potential becomes larger than a critical value, the above events form a positive feedback loop, in which the probability of Na^+ ion channels opening is further increased, leading to a greater depolarisation of the cell membrane, and so on. This leads to a large depolarisation of the cell membrane towards the Nernst potential for Na^+. Eventually almost all Na^+ ion channels are open and the membrane potential is close to the Nernst potential for Na^+. This causes the Na^+ ion channels to close. The K^+ ion channels, which have a delayed response to cell membrane depolarisation, now begin to open. K^+ ions flow out to the extracellular environment, such that the membrane potential declines towards the Nernst potential for K^+, but never attains it since the closed Na^+ ion channels remain slightly permeable to Na^+ ions. Thus the resting potential of a neuron is approximately $-70\,\mathrm{mV}$ [28]. Finally the K^+ ion channels close. The depolarisation of neuronal cell membranes followed by their return to the resting potential as described above is referred to as an *action potential*. The original intracellular and extracellular concentrations of Na^+ and K^+ ions are restored by *Na^+/K^+ ATPase pumps*, which break down ATP using ATPase enzymes and use it to transport these ions up their concentration gradients (which requires energy).

Neurons are arranged end-to-end, separated by small gaps called *synaptic terminals*. The depolarisation of a neuronal cell membrane causes the neuron to release a chemical signal, or *neurotransmitter*, which diffuses through the synaptic terminals to adjacent neurons. On the arrival of the neurotransmitter, these neurons also depolarise. Thus an action potential propagates through the neuronal network. The majority of ATP consumption by activated neurons is by the Na^+/K^+ ATPase pumps.

Having discussed common features of all retinal neurons, in the next section we examine attributes specific to rod photoreceptors.

1.3 PHYSIOLOGY OF ROD PHOTORECEPTOR METABOLISM

Rod photoreceptors are particularly suited to light-detection in dark surroundings, as they are able to detect very weak light signals [16]. Figure 1.3 shows the structure of a rod photoreceptor, comprising an *inner segment* (*IS*), *outer segment*

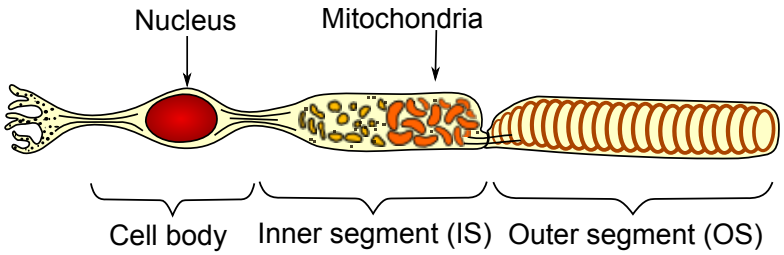


Figure 1.3.: Structure of a rod photoreceptor, adapted from [18] (innermost components on left hand side).

(*OS*) and cell body as shown. Specific organelles are localised in particular regions of the cell. Protein synthesis and oxidative metabolism take place in the IS [29], whereas the OS consists of many membrane discs, enclosed in a separate plasma membrane [30]. The discs contain the light-detecting components of the photoreceptors. The cell body, attached to the inner end of the IS, contains the nucleus [31, 32], and is connected at the opposite (left-hand) end to a *synaptic terminal*, where signals are transmitted to surrounding neurons [16, 31].

Rod photoreceptors do not divide. Instead, discs in the OS are constantly renewed [33]. The components of the discs are produced from amino acids in the IS [33], and the discs are formed as membranous growths at the IS-OS boundary. Once fully developed, the discs separate from the IS and are forced outwards by the formation of new discs [34]. Discs at the outer end of the OS are shed and phagocytosed by RPE cells [35–37]. The turnover of OS discs was first observed by Young [38], who injected a traceable radioactive isotope of one of the amino acids in OS discs into rhesus monkeys. The tracer initially accumulated in the IS, was transported into and along the OS, it then shed from the outer end of the photoreceptor and was absorbed by the RPE. Most disc shedding occurs once per day, around dawn in many vertebrates [35–37]. The entire OS is replaced approximately every 9–10 days [39].

In §1.2 we explained that photoreceptors transmit action potentials in the same way as other neurons. As such, they also possess Na^+/K^+ ATPase pumps, located in the IS [40]. The depolarisation and release of neurotransmitters from the photoreceptors occurs during dark conditions rather than light. For this reason, the overall energy consumption in the photoreceptors is greatest in dark conditions, when the Na^+/K^+ ATPase pumps are active [41]. The flow of ions through photoreceptor cell membranes is referred to as *dark current* [42]. The discovery of dark current was prompted by observations that the rate of oxygen

consumption in photoreceptors doubled under dark conditions compared to light conditions in cat and isolated toad retinae [43, 44], since more oxygen is required for energy production by the mitochondria in the IS.

When light is incident on a disc in the photoreceptor OS, it reacts with a molecule of the light-sensitive chemical *rhodopsin* [42]. This initiates a cascade of interactions within the photoreceptor which results in the breakdown of the metabolite *cGMP* [45]. The state of the gated ion channels in the cell membrane depends on the intracellular levels of cGMP, with high concentrations associated with open ion channels, and vice-versa [46]. Thus, the breakdown of cGMP decreases its concentration within the photoreceptor, causing the gated ion channels in the outer cell membrane to close [46], and the dark current ceases [42]. To balance the effect of cGMP breakdown, another pathway induces the synthesis of cGMP [42],which is highly energy consuming [47, 48]. The way in which photoreceptors respond to light signals is referred to as *phototransduction*.

The synthesis of cGMP during phototransduction is the most energy consuming process in the photoreceptors under light conditions [22]. Since this occurs in the discs of the OS, the site of highest energy consumption switches from the IS under dark conditions to the OS during light ones [22]. Under dark conditions, the ATP demand in the OS is met by glycolysis [49], which occurs throughout the photoreceptor [29, 30, 49]. Conversely, oxidative metabolism by mitochondria is localised to the IS. Under light conditions, phototransduction increases the energy requirement of the OS discs, and glycolysis provides insufficient energy. The remaining energy requirement is met by ATP produced by the mitochondria in the IS. However, the diffusion of ATP from the IS to OS is restricted by its interactions with membrane-bound proteins [50], and thus is very slow. Instead, it is thought that ATP produced by the mitochondria combines with the chemical species *creatine* (or *Cr*) which is present in high concentrations in the IS [50], to form ADP and *creatine phosphate* (*CrP*) [49]. The energy in ATP molecules is stored in high-energy bonds between the three phosphate groups. Catalysed by the enzyme *mitochondrial-type creatine kinase* [50], one of the high-energy bonds is broken and a phosphate group is transferred to creatine, with which it forms another high-energy bond, producing CrP which then contains the stored energy. Creatine phosphate molecules are small and highly mobile, and diffuse into the OS. At the sites of high energy demand, CrP donates the high-energy phosphate bond to an ADP molecule, producing ATP and Cr, catalysed by *brain-type creatine kinase* [50]. As such, ATP is supplied to

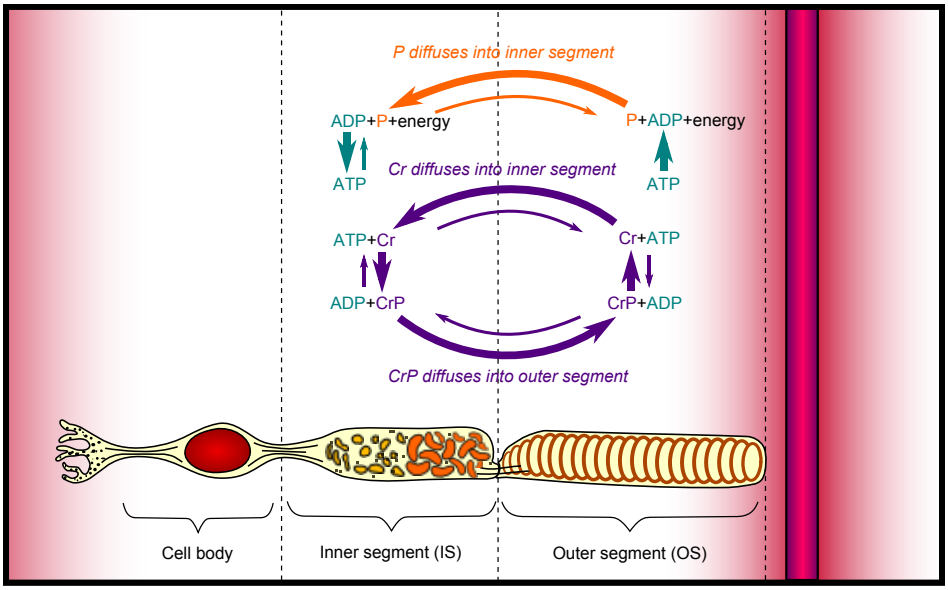


Figure 1.4.: Schematic diagram showing the key processes associated with the phosphocreatine shuttle (diagram of photoreceptor adapted from [18]).

the OS, and creatine diffuses back to the IS, to repeat the cycle. The transfer of energy from the mitochondria in the IS to the OS discs via CrP is referred to as the *phosphocreatine shuttle* (see Figure 1.4). The phosphocreatine shuttle hypothesis assumes that this is the primary mechanism by which the extra energy demand in the OS discs under light conditions is met, and is widely accepted [49–54], but not undisputed. The hypothesis provides an explanation for the difference between the energy demand of the OS under light conditions and the maximal rate of energy production there via glycolysis (e.g. see [49]), while allowing for inhibited ATP diffusion within the photoreceptors [51].

There is compelling evidence that the phosphocreatine shuttle plays a vital role in many cell types with high and oscillating energy consumption. For example, Gudbjarnason et al. [55] found that in heart muscle cells with an inhibited blood supply, the muscles were unable to contract when insufficient CrP was present, even though 80% of the ATP still remained. Many argue that, since photoreceptor cells also have extremely high metabolic demands, the phosphocreatine shuttle is equally necessary in these cell types [53, 54].

Further evidence for the phosphocreatine shuttle hypothesis includes detection of mitochondrial-type and brain-type creatine kinase in the photoreceptor IS and OS respectively, using fluorescence microscopy in chicken [56] and bovine [50] retinae, and measurements of creatine kinase activity via its effect

on the creatine phosphate concentration in bovine retinae [50]. However, Linton et al. [57] used similar techniques to [50] in mouse retinae and found brain-type creatine kinase to be absent from the photoreceptor outer segments. They argued that ATP diffusion is more rapid than previously thought.

Having familiarised ourselves with the functioning of a healthy photoreceptor, in the following section we review the state of the art regarding age-related macular degeneration and diabetic retinopathy, two retinal diseases.

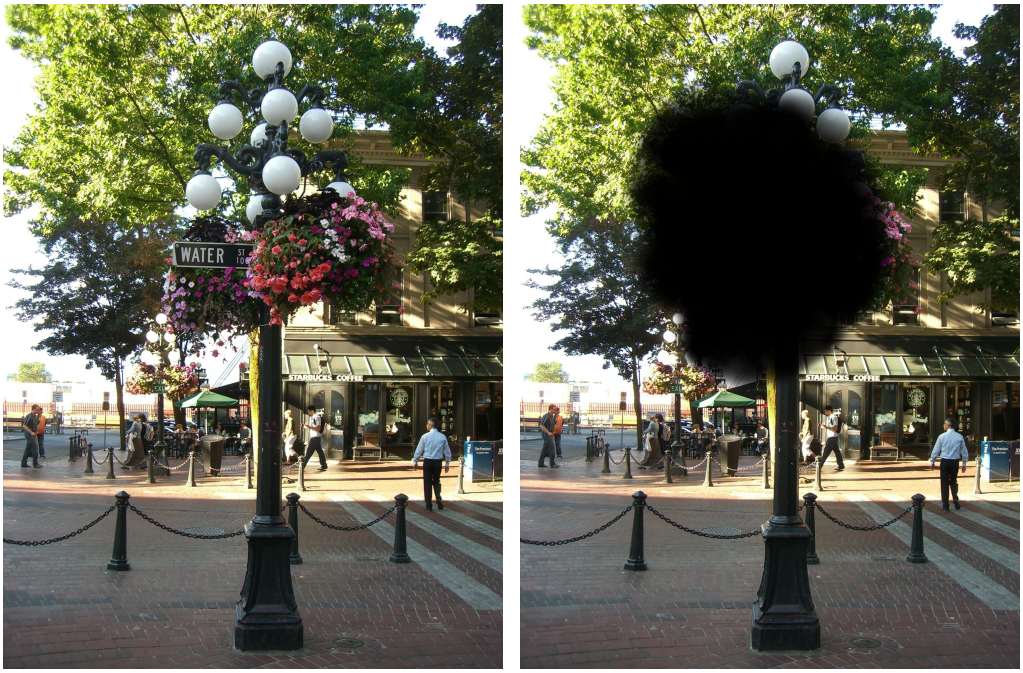
1.4 PATHOLOGY

Age-related macular degeneration (*AMD*) is characterised by a marked reduction in the number of rod photoreceptors in the macula [58, 59]. AMD presents itself in two distinct forms, the so-called *atrophic* (*dry*) and *exudative* (*wet*) types [59, 60]. The atrophic type is most common, accounting for approximately 90% of cases of AMD, and is incurable. At early stages, AMD development is the same for both types. RPE cells in the macula become damaged and eventually degrade [61–63]. Following RPE damage, the clinical signs of atrophic and exudative AMD diverge, although it is common for atrophic AMD to become exudative at some stage. The following pathogenesis is reported from studying sufferers of atrophic AMD:

- Yellow-coloured deposits called *drusen* sometimes form between the RPE and Bruch's membrane [20, 39, 64], containing waste products from photoreceptors or RPE cells;
- At the later stages of atrophic AMD, photoreceptors in the periphery of the macula become damaged and die [62, 65];
- At the most advanced stage, photoreceptors in the central macula also degrade [59];
- In severe cases, a large area of photoreceptors is lost, and a blind spot, or *scotoma*, forms [64].

Figure 1.5 illustrates the contrast between the vision field of an AMD sufferer and a non-sufferer. The development of exudative AMD has been described as follows:

- In response to the lack of nutrients and waste-disposal resulting from degradation of the RPE, the retina stimulates the growth of new blood



(a) (b)

Figure 1.5.: An example of a vision field as seen by (a) a healthy individual, and (b) a sufferer of atrophic age-related macular degeneration. The loss of large numbers of photoreceptors leads to a blind spot in the central region of the vision field.

vessels [66] by the production of *VEGF* (*vascular endothelial growth factor*), a factor that promotes angiogenesis;

- The new vessels form underneath the retina [67]. They are immature and may leak fluids [68];
- This causes swellings in the retinal surface that distort vision and, in severe cases, photoreceptor damage or death, and tissue scarring, leading to blind spots [59, 60].

Treatments for exudative AMD focus on preventing growth of new vessels by injecting anti-VEGF agents such as *ranibizumab* (*Lucentis*) and *aflibercept* (*Eylea*) [67]. This slows the progression of AMD, but does not reverse existing retinal damage. The formation of new blood vessels is thought to be the end result of a longer term defect which remains to be identified. Ciulla et al. [69] suggested that treatments targeting AMD at earlier stages (i.e. before RPE damage) may be effective against both atrophic and exudative AMD [69]. Many theories have been proposed to explain the cause of AMD. Possible candidates include decreased concentrations of vitamins [64, 70–72] or of the pigment melanin [73], accumulation of toxic chemical species due to overexposure to light [69, 74, 75], genetic factors [63, 66, 76], and immune system malfunction [24, 77, 78].

Of particular interest is a theory by Holz et al. [79] that links persistently rapid outer segment disc shedding to cell damage and degradation, explained as follows. Recalling that RPE cells phagocytose discs that are shed from photoreceptor outer segments (see §1.3), occasionally discs are not completely digested, giving rise to a product called *lipofuscin* [79]. In high concentrations, lipofuscin can be toxic to cells [80]. Holz et al. [79] proposed that, while lipofuscin concentrations in healthy retinae are typically low, rapid OS shedding over a prolonged period may lead to its accumulation and thus toxicity. In support of this theory, Holz et al. detected elevated levels of lipofuscin in regions of the macula that were later subject to RPE cell damage and death [79]. Ciulla et al. [69] suggested that this may explain the appearance of drusen, containing the remnants of incompletely digested OS discs.

While AMD mostly affects those over the age of 65 years [2], diabetic retinopathy is a leading cause of blindness within adults between 16 and 64 years of age [81]. Clinical observations in sufferers of diabetic retinopathy reveal damage to the blood vessels in the retina. In some cases, damage to the vessel walls stimulates new vessel growth, in the same way as in exudative AMD.



(a) (b)

Figure 1.6.: An example of a vision field as seen by (a) a healthy individual, and (b) a sufferer of diabetic retinopathy. The growth of vasculature underneath the retina leads to swelling of the retinal tissue, causing distorted vision, and leakages of blood vessels cause damage and death of photoreceptors resulting in blind spots in the vision field.

Fluid in such blood vessels may leak into the retina causing swelling, leading to distorted vision, and if the new vessels bleed into the retina (i.e. *vitreous haemorrhage*) this may result in severe vision loss [82–84]. Figure 1.6 illustrates the contrast between the vision field of a diabetic retinopathy sufferer and a healthy individual.

Further studies suggest that the degradation of capillary walls is preceded by damage to inner retinal neuronal cells [85, 86]. Changes in vision that characterise the early stages of diabetic retinopathy, such as impaired contrast sensitivity (ability to distinguish between light and dark) arise before any observable changes to vasculature occur.

Previous investigations on early changes in AMD and diabetic retinopathy have made use of *electroretinogram* (or *ERG*) measurements. ERG data shows the time variation in the electrical current across a patient's retina, in response to certain light stimuli [87]. An electrode is positioned on the surface of the cornea, within the vitreous fluid or in a certain retinal layer (the former technique is non-invasive while the latter two are invasive). In each case, the electrical

current flowing through retinal neurons is conducted through the extracellular matrix and to the electrode [88] (from which the potential is calculated using Ohm's Law). An additional electrode is positioned on the skin to provide a baseline with which to compare the potential in the retina. Light stimuli include individual flashes of light, regular patterns of flashes or background lighting. The colour and intensity of the background and flashing lights can be varied.

The photoreceptors are arranged in parallel and thus, since the electrical current passes from their inner segments to their outer segments, they act as components of an electrical circuit in parallel and their currents add up, yielding a larger current in the surrounding extracellular matrix. The same is true for all retinal neurons that are oriented in the same direction as the photoreceptors. In contrast, the currents through neurons that lie perpendicular to the photoreceptors cancel out due to the symmetry within the retina. Thus, homogeneous background light stimulation gives rise to radial but not azimuthal currents [88]. Two kinds of measurements can be taken: the local current through the retina and the remote current which also passes through the vitreous fluid and sclera. The latter can be measured using non-invasive methods by placing an electrode on the cornea. Via Ohm's Law, the ERG signal depends upon the change in electrical potential in the neuronal cells and also the resistance of the various tissue types within the eye, e.g. of the vitreous fluid, RPE, choroid and cornea [88]. Damage and degradation of the retinal neurons reduces the changes in electrical potential in response to stimuli, and the resistance of the other tissue types is also affected by various factors. Calculation of the voltage from the ERG signal using Ohm's Law accounts for these factors. The voltage is likely to evolve by a number of μV or nV on a timescale of ms.

Different conditions can be used to test separate components of the retina. For example, the response of the photoreceptors is dominated by rod and cone cells under dark and light surroundings respectively [89]. The rod photoreceptors also have a slower response time than cones. This means the two types of photoreceptors can also be examined separately by using the idea of *critical fusion frequency*, or *CFF*: the highest frequency of light pulses that are still perceived as separate flashes, without merging together. The CFF for rod photoreceptors is lower than that of cones, meaning that a stimulus of flickering light with a flickering frequency higher than the CFF for rod photoeceptors can be used to measure the response of the cones only [90].

At the onset of a light stimulus, the voltage of the cornea initially becomes negative, followed rapidly by a positive peak, known as the a– and b–waves respectively [91]. The a–wave measures the response of the photoreceptors to the light stimulus [92]. It is negative since it is a measure of the reduction in dark current at the onset of light. The b–wave represents the sum of the responses of the photoreceptors and inner retina to a stimulus [87]. The exact source in the inner retina is still debated, but may include certain types of glia [93] or neurons [94]. A decrease in the amplitude of both the a– and b–waves indicates that photoreceptor function is impaired, and has been detected in age-related macular degeneration sufferers [95, 96].

Under certain experimental conditions, other minor components are also observed in ERG data. For instance, if the stimulus is a bright light, wavelets of small amplitude and high frequency may be superposed on the a– and b–waves, referred to as *oscillatory potentials* or *OP*. The exact source of these wavelets is unknown, but they are particularly sensitive to minor changes in the retinal tissue, and have been used to detect early changes associated with diabetic retinopathy, before there were any detectable changes to the main a– and b–waves [97–100].

We conclude that the traditionally observed symptoms of age-related macular degeneration and diabetic retinopathy (e.g. vascular changes and cell degradation) may be the consequences of longer term problems in metabolic regulation. We introduce in the next section some relevant mathematical models that motivate our work in Chapters 2 and 3.

1.5 Mathematical models relevant to our work on rod photoreceptor metabolism

Our aim in the first part of this thesis is to develop mathematical models to investigate how the nutrient concentrations in rod photoreceptors may affect their length. Accordingly, a mathematical model is defined on a domain whose length is time-dependent and must be determined as part of the solution. In §1.5.1 we review some mathematical models that involve growing domains, and the solution methods for such models. We then, in §1.5.2, consider existing models of retinal metabolism, many of which focus on steady state concentrations of vital nutrients in the entire retina and all of which are formulated on fixed domains. Finally, in §1.5.3 we consider models of energy metabolism in

highly metabolically active tissues such as muscles. The chapter concludes in §1.6, where we outline the objectives and structure of this thesis.

1.5.1 *Moving Boundary Problems*

Mathematical models formulated on domains which change in size over time are referred to as *free-boundary problems*. For example, Crampin et al. [101] studied a system of coupled reaction-diffusion equations on a growing domain, where the timescale of domain growth is comparable with the timescale of the reaction and diffusion dynamics, and dependent on the concentrations of reactants within the domain.

In [101], Crampin et al. explain how to use the Principle of the Conservation of Mass on a general domain, Ω_t, to derive the appropriate PDEs for the reactants and rate of domain growth. For a chemical species of concentration $c(\mathbf{x}, t)$ and domain growth rate $\mathbf{u}$ in three dimensions, this gives,

$$\frac{d}{dt}\int_{\Omega_t} c(\mathbf{x}, t)\, d\mathbf{x} = \int_{\Omega_t} \left(\frac{\partial c}{\partial t} + \mathbf{u} \cdot \nabla c + c \nabla \cdot \mathbf{u} \right) d\mathbf{x}.$$

In the above equation, the advection term $\mathbf{u} \cdot \nabla c$, describing chemical movement according to local volume changes, and the dilution term, $c\nabla \cdot \mathbf{u}$, are both due to domain growth. The numerical solution to a free boundary problem such as the one outlined above can be found by mapping it onto a fixed domain. In one spatial dimension, the following transformation, which maps from (x, t) to (ρ, τ), can be defined,

$$\rho = \frac{x}{L(t)}, \qquad\qquad \tau = t,$$

where $L(t)$ is the domain length and $0 \leq \rho \leq 1$.

Jackson and Byrne [102] follow the same principle to model the growth of a spherically symmetric tumour. The tumour contains *proliferating* cells which undergo rapid division and are sensitive to an applied chemotherapy drug, and *quiescent cells* which divide more slowly and are less sensitive to the drug.

The drug concentration is modelled via a reaction-diffusion equation, incorporating decay at a constant rate (per unit concentration) and transport in and out of the tumour via linear exchange. The distributions of each type of tumour cell are governed by PDEs derived using the Principle of the Conservation of

Mass, allowing for random motility of the cells within the tumour, and two net rates of change in cell numbers, one depending solely on the number of cells and the other also dependent on the drug concentration (both rates represent the overall effect of cell proliferation and cell death).

A local velocity is defined for the tumour cells at each spatial point. The rate of tumour growth, represented by a time-dependent ODE, is defined as the radial velocity of the cells at the tumour boundary, which, in turn, depends on the number of tumour cells of each type and the concentration of the chemotherapy drug.

Some simplifying assumptions are used to eliminate one of the variables (denoting quiescent tumour cells) from the model, resulting in a coupled system of two PDEs (one governing the density of proliferating tumour cells and the other governing the drug concentration) and one ODE (determining the rate of domain growth), with associated boundary and initial conditions.

The application of no-flux boundary conditions on the cell density at the tumour boundary is demonstrated, from which we note that a no-flux boundary condition on a moving boundary is applied by ensuring the conservation of mass in the domain rather than setting the spatial derivatives to zero. For example, the total mass of a chemical X in a one-dimensional domain is given by,

$$M(t) = \int_0^{L(t)} [\mathrm{X}](x,t)\, dx,$$

where $[\mathrm{X}]$ and $L(t)$ denote the concentration and domain length respectively. Differentiating with respect to t, noting that the upper limit of the integral is time-dependent, gives,

$$\frac{dM}{dt} = \int_0^{L(t)} \frac{\partial [X]}{\partial t}\, dx + [X](L(t),t)\frac{dL}{dt}.$$

The conservation of mass implies that $dM/dt = 0$, giving,

$$\int_0^{L(t)} \frac{\partial [X]}{\partial t}\, dx = -[X](L(t),t)\frac{dL}{dt}.$$

Thus, zero flux across the boundary of a growing domain implies a non-zero derivative at the growing boundary, allowing material to flow into the newly grown part of the domain.

A different model by Greenspan [103] is developed to investigate the variation in size and shape of a tumour in response to the surrounding distribution of a vital nutrient. If the nutrient concentration falls below a certain threshold level (the concentration necessary to maintain the proliferating cells), cells die. Live cells proliferate while dead cells degrade at a constant rate. A model developed to investigate photoreceptor length adaptation in response to nutrient availability may have similar features, assuming that discs in the OS cease to be viable if nutrient concentrations fall below a critical level, leading to shortening of the OS. Production of the discs may be constant or nutrient-dependent.

To the best of our knowledge, no mathematical models of rod photoreceptor length adaptation exist. The most biologically relevant models consider the oxygen distribution in photoreceptors or throughout the retina, and energy provision via the phosphocreatine shuttle in muscles. We review these models in the following sections.

1.5.2 *Models of Photoreceptor Oxygen Metabolism*

The majority of existing models of the retinal oxygen distribution focus on the steady state concentration in the retinal layers (on a fixed domain). These models are typically defined in one spatial dimension and aim to reproduce and explain experimental measurements. They account for oxygen diffusion and assume a constant rate of oxygen consumption (independent of oxygen levels), with the oxygen concentration fixed at the outer end of the OS, due to a constant supply from the choroidal vessels. The oxygen consumption rate is assumed to differ between the retinal layers. The earliest model, produced by Dollery et al. [104], views the retina as a single layer, with uniform oxygen consumption throughout the retinal tissue. Subsequent models decompose the retina into two [105] and three [106] layers, each with distinct uniform oxygen consumption rates.

The model by Linsenmeier [105] accounts for altered oxygen consumption rates between light and dark conditions (see §1.3), while the model of Haugh et al. [106] accounts for the fact that most oxygen consumption occurs within the photoreceptor inner segments.

For the purpose of modelling rod photoreceptor length adaptation, we also require information about the time-variation in metabolite levels. In more recent work [107, 108] PDE models were used to simulate spatial and temporal

variations in the oxygen distribution in a single photoreceptor. The models by Tsacopoulos and Poitry [107] and Poitry et al. [108] include oxygen diffusion and a constant oxygen consumption term. They were used to interpret experimental data on the oxygen distribution in drone honey bee photoreceptors *in vitro* under dark conditions, with short bursts of light stimulation applied for fixed time periods. Numerical solutions were generated and parameters tuned such that the models closely matched the experimental data.

Although these models yield increasing amounts of information on the retinal oxygen concentration, all are defined on fixed domains and, as such, do not incorporate details on photoreceptor length adaptation.

1.5.3 *Models of Energy Transfer via the Phosphocreatine Shuttle*

Models of the phosphocreatine shuttle were originally developed to describe muscle cells, but it is thought to function in a similar way in photoreceptors [50, 109]. We summarise the structure of a muscle cell, to aid understanding of the models that follow. Each muscle cell contains many *myofibrils*, elongated elements that contract during muscular work [110]. These organelles have a very high energy demand [111], and thus can be viewed as the muscular analogy to OS discs undergoing phototransduction in light conditions. The myofibrils are surrounded by *sarcoplasm* (analogous to the cytoplasm in retinal cells), which, like the rod photoreceptor IS, contains the mitochondria [112].

An early mathematical model of the phosphocreatine shuttle was produced by Meyer et al. [113], who argued that its main purpose was to facilitate diffusion of ADP and ATP into/out of the myofibrils. The steady state ODE model considers two scenarios: with and without Cr and CrP. The first scenario, without Cr and CrP, incorporates the diffusion of ATP into and throughout the myofibrils, and the consumption of ATP within the myofibrils. From this, the maximum rate of ATP consumption for which the ATP concentration at the centre of the myofibrils remains positive is determined.

Cr and CrP are then added into the model such that, inside and around the myofibrils, CrP can bind reversibly with ADP to produce ATP+Cr, and this reaction is assumed to be at chemical equilibrium (with the rate of the forward and reverse reactions equal). CrP and Cr are allowed to diffuse. The maximum ATP consumption rate in the myofibrils that can be supported when Cr and CrP are present is shown to be considerably higher than when they are absent.

This suggests that a significant proportion of energy is transported into the myofibrils by the diffusion of CrP rather than ATP. Hence, we conclude that the phosphocreatine shuttle plays an important role in supplying energy to the myofibrils.

The model by Meyer et al. [113] has been criticised for assuming that ATP and ADP diffuse freely between mitochondria and myofibrils [114]. Many factors inhibit ATP and ADP diffusion, including crowding due to high concentrations of large molecules [115], and protein-protein interactions with membrane-bound proteins [116]. The rate of diffusion is particularly slow in regions that are densely packed with membranes and organelles, such as the myofibrils [117] and the mitochondrial outer membrane [118]. Recent models have defined an *apparent diffusion coefficient* of ATP which accounts for the rate of free diffusion and the effects of diffusion-restricting processes [119]. Others represent restricted ATP and ADP diffusion by decomposing cells into compartments, with limited ATP and ADP diffusion across the subcellular boundaries [51, 120].

A subsequent model of energy provision in heart muscle cells was formulated by Aliev and Saks [120]. Each cell is decomposed into compartments representing myofibrils, sarcoplasm and different compartments within the mitochondria. The concentrations of ATP, ADP, Cr, CrP and P in each compartment are considered, as are diffusion between the mitochondria and myofibrils, the conversion of ATP+Cr to ADP+CrP (and vice-versa) and ATP synthesis. The structure and function of the mitochondria is also modelled in detail. Models of energy metabolism are becoming increasingly complex, incorporating additional metabolites such as NAD^+ and NADH [121–123], enzymes and coenzymes [121, 122, 124] and changes in the mitochondrial membrane potential [123, 124]. However, our aim is to produce a simple, tractable model which can enhance our insight into retinal physiology and predict potential causes of retinal diseases.

1.6 THESIS STRUCTURE

Two distinct aspects of retinal metabolic regulation are examined in this thesis. While Chapters 2 and 3 focus on how rod photoreceptors may adapt their length to regulate their energy demand, Chapters 4–6 concentrate on mechanisms that may regulate metabolite concentrations in the inner retina in order to protect the neurons there.

In Chapter 2 we present a continuum model to investigate whether changes in the demand for oxygen may explain the observed length variation in rod photoreceptors under light and dark conditions. We consider a free-boundary problem, in which the inner and outer segments of the photoreceptor are distinguished: the inner segment is viewed as a fixed domain, while the length of the outer segment is assumed to depend on the oxygen concentration. The spatiotemporal distribution of oxygen is represented via a reaction-diffusion equation with different consumption rates in the two compartments.

We construct, in Chapter 3, a PDE model to test the alternative hypothesis that rod photoreceptor length is regulated by the availability of phosphocreatine shuttle-derived ATP to the outer segment discs. As in Chapter 2, the photoreceptor is decomposed into two compartments. The length of the outer segment is dependent upon the ATP distribution in the photoreceptor, such that the discs are generated at a constant rate, while those at the outer end cease to be viable and are shed if the local ATP concentration falls below their minimal energy requirement. The concentrations of CrP, Cr, P satisfy reaction-diffusion equations.

Solutions to the two models above, derived using a combination of numerical and analytical techniques, suggest that the outer segment length of rod photoreceptors may be regulated by oxygen levels under dark conditions but not light ones, whereas phosphocreatine shuttle-based length regulation induces disc shedding under light conditions but permits unlimited growth under dark conditions. We therefore combine these models in the second part of Chapter 3, to show that realistic diurnal variation in photoreceptor length is achieved when photoreceptor length is regulated by oxygen and the phosphocreatine shuttle. We use the combined model to predict possible causes of pathology in ageing retinae.

Our focus shifts to the inner retina in Chapter 4, where we study the way in which glial cells regulate the environment surrounding the neurons via regulated metabolite transport and neurotransmitter uptake. Chapter 4 introduces the relevant physiology and mathematical models.

We formulate a compartmental model of inner retinal metabolic regulation in Chapter 5. To derive our reaction rate expressions, we neglect many of the intermediate steps in metabolic pathways, assuming they are rapid compared to the rate-limiting steps in the same pathway. We give an example of how we justify the rapid kinetics assumptions by comparing the common components

in our model and a detailed model proposed by Aubert and Costalat [1]. Using multiple-timescale analysis, we eliminate intermediate steps in the metabolic pathways included in Aubert and Costalat's model, which yields combined reaction rates analogous to our own.

The thesis ends in Chapter 6, where we investigate the qualitative behaviour of our model from Chapter 5, using analytical and numerical techniques. We use the model to examine the diurnal variation in inner retinal metabolite levels, using the time-varying blood glucose concentrations in healthy and diabetic groups measured in [125]. This allows us to identify abnormalities in the inner retina that may be caused by diabetes. Further, the model enables us to predict mechanisms that may be responsible for, or contribute to, diabetic retinopathy.

2

OXYGEN AS A DETERMINANT OF ROD PHOTORECEPTOR LENGTH

A substantial body of empirical evidence points towards a link between disrupted rod photoreceptor length regulation and retinal diseases that lead to blindness [11, 12, 79, 80]. An understanding of mechanisms regulating rod photoreceptor length is therefore paramount in the investigation into the causes of and therapies for retinal pathology. However, the biological mechanisms controlling photoreceptor length remain a subject of debate. The structure of a rod photoreceptor cell (described in detail in §1.3) comprises an inner and outer segment (IS and OS respectively). The IS contains the mitochondria which consume oxygen and produce energy, while the OS consists of discs which convert light into sensory information. The discs in the OS are continuously produced at the IS-OS boundary, and shed from the opposite end of the OS at the onset of light conditions. We investigate the possibility that the OS length is regulated by energy metabolism. Our objective in the first part of this thesis is to identify mechanisms that can explain the observed diurnal variations in OS length, with shedding of OS discs in light conditions, and OS growth in dark conditions. To this end we test two hypotheses:

1. The time variation in OS length is regulated by oxygen levels alone;
2. Discs are shed from the end of the OS at the onset of light conditions because there is insufficient phosphocreatine shuttle-derived ATP available to maintain them.

We design a mathematical model to test hypothesis 1 in this chapter. The second hypothesis is examined in Chapter 3.

Previous models (e.g. in [108]) are designed to reproduce experimentally measured spatial oxygen profiles in the retina, as detailed in Chapter 1. The mathematical models of photoreceptor metabolism presented in this thesis

allow us to investigate the mechanisms that may regulate the outer segment length, by finding the solutions to free boundary problems.

This chapter is organised as follows. Firstly, in §2.1, we formulate a continuum PDE model of rod photoreceptor oxygen metabolism, representing the OS as a domain with an adaptive length which depends solely on the photoreceptor oxygen concentration. In §2.2 we examine the steady states of our model, which can be found analytically. After making realistic parameter estimates based on existing literature in §2.3, we describe in §2.4 how the full time-dependent solution is calculated numerically using the Method of Lines. The full spatiotemporal simulations of our model are shown in §2.5, and we discuss the meaning of these results in terms of how the photoreceptor length is regulated under light and dark conditions. Parameter sensitivity analysis in §2.6 enables us to evaluate our model, and the plausibility of OS length regulation by oxygen. Furthermore, the parameter-dependence of the model solutions is used to identify possible causes of photoreceptor malfunction. Finally, in §2.7 we discuss the implications of our model and give suggestions for future developments.

2.1 MODEL DEVELOPMENT

In this chapter we assume that the length of the rod photoreceptor OS is regulated by oxygen availability. We develop a one-dimensional model, expressed as a system of PDEs, coupling the distribution of oxygen within the photoreceptor cell to the length of the OS.

The structure of a rod photoreceptor is described in Chapter 1, with oxygen-fuelled metabolism occurring in mitochondria which are located in the IS. We define two dependent variables, $U(x,t)$ describes the oxygen distribution within the photoreceptor, and $L_{\mathrm{OS}}(t)$ denotes the length of the OS. We assume that the temporal evolution of $L_{\mathrm{OS}}(t)$ depends solely on $U(x,t)$, whilst the length of the inner segment, L_{IS}, does not change over time. In our model, the IS and OS occupy the regions $-L_{\mathrm{IS}} \leq x \leq 0$ and $0 \leq x \leq L_{\mathrm{OS}}(t)$ respectively, with x representing the spatial coordinate. We introduce below the equations that describe $U(x,t)$ and $L_{\mathrm{OS}}(t)$, and summarise some key points in schematic form in Figure 2.1.

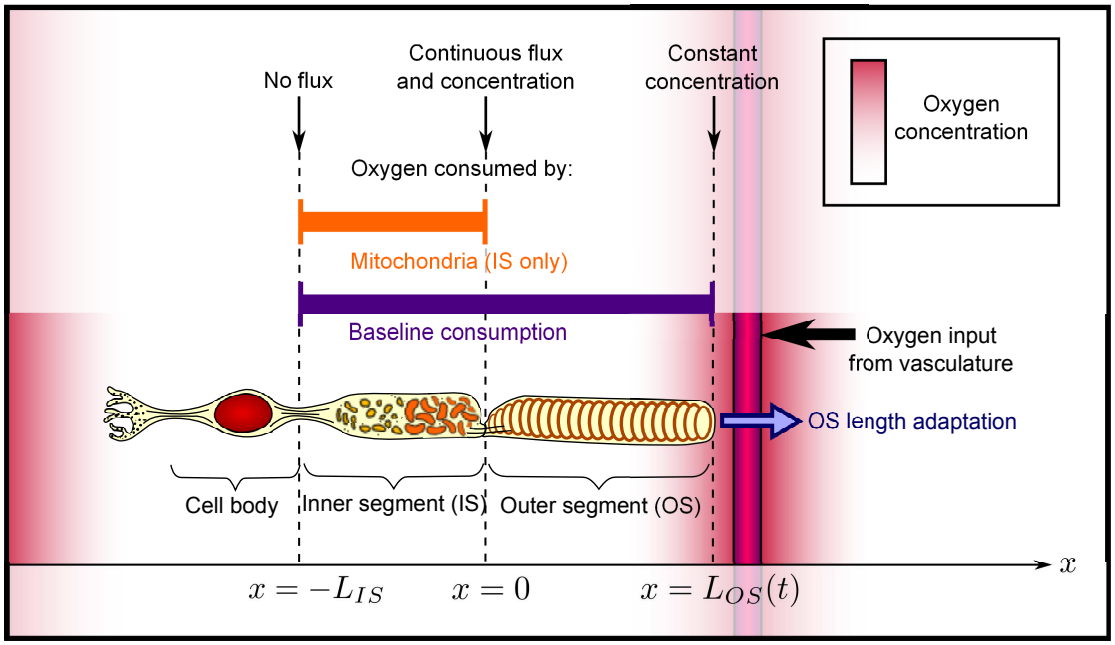


Figure 2.1.: Schematic diagram showing how our model represents the distinct regions of a rod photoreceptor (diagram of photoreceptor adapted from [18]).

2.1.1 *Oxygen Concentration, $U(x,t)$*

The dominant processes governing $U(x,t)$, the oxygen distribution within a rod photoreceptor, are taken to be diffusion with coefficient D_U, consumption by mitochondria within the IS at rate μ, and a baseline consumption throughout the photoreceptor at rate λ. Assuming that the mitochondrial and baseline consumption terms depend linearly on the oxygen concentration, we deduce that $U(x,t)$ satisfies,

$$\frac{\partial U}{\partial t} = D_U \frac{\partial^2 U}{\partial x^2} - [\lambda + \mu \mathrm{H}(-x)]\, U, \tag{2.1}$$

where $\mathrm{H}(x)$ is the Heaviside function, which ensures that mitochondrial oxygen consumption occurs only in the IS. The baseline oxygen consumption term represents other losses not explicitly included in the model, e.g. other oxygen-requiring biochemical reactions within the cell such as the breakdown of certain proteins [126] and oxidation reactions involved in detoxification [127].

2.1.2 *Length of the Outer Segment, $L_{OS}(t)$*

As discussed in Chapter 1, the choroid is the dominant supplier of oxygen to the outer retinal layers, and thus we regard it as the sole supplier. As such, oxygen enters the photoreceptor through the OS, at $x = L_{\mathrm{OS}}(t)$, and must diffuse into the IS, where the mitochondria are located, before it can be metabolised to create the energy needed by the cell to stay alive and produce new discs.

When developing our equation for the length of the OS we use the fact that the cell needs a minimum amount of energy to remain viable. We assume that, if the rate of mitochondrial energy production from oxygen in the photoreceptor exceeds a threshold level, then the excess energy is used to create new discs and increase the length of the OS. Further, we suppose that, if the rate of mitochondrial energy production is insufficient to sustain the cell (below the threshold level), discs are shed from the OS. Since the rate at which the mitochondria produce energy depends upon oxygen availability, we propose that the rate of OS growth is proportional to $(U(-L_{\mathrm{IS}}, t) - U_{\mathrm{Thr}})$. The reason for taking $U(-L_{\mathrm{IS}}, t)$ as the representative oxygen concentration is that, at any given time t, $x = -L_{\mathrm{IS}}$ is the spatial point at which the oxygen concentration is minimal. This can be seen from the fact that the oxygen concentration decreases monotonically with distance from its source, the choroid (since diffusion is the only transport mechanism while oxygen is consumed throughout the photoreceptor). If the condition $U(-L_{\mathrm{IS}}, t) > U_{\mathrm{Thr}}$ is satisfied, the oxygen levels at every other spatial point throughout the photoreceptor also exceed U_{Thr}.

We model the above effects by proposing that the time evolution of the length of the OS is governed by the following equation,

$$\frac{dL_{\mathrm{OS}}}{dt} = k\left[U(-L_{\mathrm{IS}}, t) - U_{\mathrm{Thr}}\right], \tag{2.2}$$

where k is a constant of proportionality determining the rate of disc production and degradation in the OS. This equation produces growth ($dL_{\mathrm{OS}}/dt > 0$) when the oxygen concentration at $x = -L_{\mathrm{IS}}$ exceeds the threshold level, and shedding ($dL_{\mathrm{OS}}/dt < 0$) if it is below U_{Thr}.

We close equations (2.1) and (2.2) by imposing the following boundary and initial conditions. With the choroid supplying oxygen to the outer layers of the retina as far as $x = -L_{\text{IS}}$, and a different oxygen supply for the inner retinal layers [128], we make the simplifying assumption that the photoreceptors are nourished solely by the choroidal vessels, such that there is no flux of oxygen across $x = -L_{\text{IS}}$, giving,

$$\left.\frac{\partial U}{\partial x}\right|_{x=-L_{\text{IS}}} = 0. \tag{2.3}$$

We further assume that the oxygen concentration at $x = L_{\text{OS}}(t)$ is maintained at a constant value by the choroidal vasculature, $U_{L_{\text{OS}}}$,

$$U(L_{\text{OS}}(t), t) = U_{L_{\text{OS}}}. \tag{2.4}$$

For a smooth solution, we require that the concentration of oxygen and its flux are continuous at $x = 0$, the transition point between the inner and outer segments,

$$U|_{x\to 0^-} = U|_{x\to 0^+}, \tag{2.5a}$$

$$\left.\frac{\partial U}{\partial x}\right|_{x\to 0^-} = \left.\frac{\partial U}{\partial x}\right|_{x\to 0^+}. \tag{2.5b}$$

We specify the initial oxygen distribution via $U_{\text{in}}(x)$ and the initial length of the OS by $L_{\text{OS,in}}$, so that,

$$U(x, 0) = U_{\text{in}}(x), \qquad L_{\text{OS}}(0) = L_{\text{OS,in}}, \tag{2.6}$$

where $L_{\text{OS,in}}$ is a positive constant. In summary the boundary, continuity and initial conditions in (2.3)–(2.6) close equations (2.1) and (2.2).

As discussed in Chapter 1, the energy consumptions in the photoreceptor IS and OS are at their maximum rates during dark and light conditions respectively, and the greatest total photoreceptor energy consumption occurs under dark conditions. Thus, the mitochondrial oxygen consumption rate in the photoreceptor is higher in dark conditions than in light. We account for this

by allowing μ in equation (2.1) to vary between light and dark conditions so that,

$$\mu = \begin{cases} \mu_D & \text{under dark conditions,} \\ \mu_L & \text{under light conditions,} \end{cases}$$

where $\mu_D > \mu_L > 0$. All other parameter values remain unchanged betweeen light and dark conditions. In particular, the oxygen consumption rate in the OS remains unaltered. Although the energy consumption in the OS increases under light conditions, the oxygen consumption rate there remains at the baseline level due to the lack of mitochondria: energy is obtained solely via the phosphocreatine shuttle and glycolysis.

2.1.3 *Nondimensionalisation*

Before continuing, we nondimensionalise the governing equations by scaling the oxygen concentration with its constant value at the outer end of the OS, $U_{L_{\text{OS}}}$. Lengths are scaled with L_{IS}, the assumed constant length of the IS, while and time is scaled with L_{IS}^2/D_U, the timescale for oxygen diffusion in the IS. Thus we introduce the following dimensionless variables,

$$\xi = \frac{x}{L_{\text{IS}}}, \qquad \tau = \frac{D_U}{L_{\text{IS}}^2}t, \qquad u(\xi,\tau) = \frac{U(x,t)}{U_{L_{\text{OS}}}}, \qquad \hat{L}_{\text{OS}}(\tau) = \frac{L_{\text{OS}}(t)}{L_{\text{IS}}},$$

and equations (2.1)–(2.6) transform to give,

$$\frac{\partial u}{\partial \tau} = \frac{\partial^2 u}{\partial \xi^2} - \left[\gamma_1^2 \mathrm{H}(-\xi) + \gamma_2^2 \mathrm{H}(\xi)\right] u, \tag{2.7a}$$

$$\frac{d\hat{L}_{\text{OS}}}{d\tau} = \hat{k}\left[u(-1,\tau) - u_{\text{Thr}}\right], \tag{2.7b}$$

$$\left.\frac{\partial u}{\partial \xi}\right|_{\xi=-1} = 0, \tag{2.7c}$$

$$u(\hat{L}_{\text{OS}}(\tau),\tau) = 1, \tag{2.7d}$$

$$u|_{\xi\to 0^-} = u|_{\xi\to 0^+}, \tag{2.7e}$$

$$\left.\frac{\partial u}{\partial \xi}\right|_{\xi\to 0^-} = \left.\frac{\partial u}{\partial \xi}\right|_{\xi\to 0^+}, \tag{2.7f}$$

$$u(\xi,0) = u_{\text{in}}(\xi), \tag{2.7g}$$

$$\hat{L}_{\mathrm{OS}}(0) = \hat{L}_{\mathrm{OS,in}}, \tag{2.7h}$$

where,

$$\gamma_1^2 = (\lambda + \mu)\frac{L_{\mathrm{IS}}^2}{D_U}, \qquad \gamma_2^2 = \lambda\frac{L_{\mathrm{IS}}^2}{D_U}, \qquad \hat{k} = \frac{kU_{L_{\mathrm{OS}}}L_{\mathrm{IS}}}{D_U},$$
$$u_{\mathrm{Thr}} = \frac{U_{\mathrm{Thr}}}{U_{L_{\mathrm{OS}}}}, \qquad \hat{L}_{\mathrm{OS,in}} = \frac{L_{\mathrm{OS,in}}}{L_{\mathrm{IS}}}, \qquad u_{\mathrm{in}}(\xi) = \frac{U_{\mathrm{in}}(x)}{U_{L_{\mathrm{OS}}}}. \tag{2.8}$$

2.2 STEADY STATE SOLUTIONS

In physiological conditions, photoreceptors do not grow indefinitely. This indicates that the OS length reaches a steady state under light and dark conditions. We now show analytically that our model has a unique, stable steady state. For the photoreceptor length to be bounded, the steady state solution must be real and non-negative, which gives some constraints on model parameters.

With the rates of change in equations (2.7a) and (2.7b) set to zero, we deduce that the steady state dimensionless oxygen concentration distribution, $u_{\mathrm{SS}}(\xi)$, satisfies,

$$\frac{\partial^2 u_{\mathrm{SS}}}{\partial \xi^2} = \begin{cases} \gamma_1^2 u_{\mathrm{SS}} & \text{if } -1 \leq \xi \leq 0, \\ \gamma_2^2 u_{\mathrm{SS}} & \text{if } 0 \leq \xi \leq \hat{L}_{\mathrm{OS,SS}}, \end{cases} \tag{2.9}$$

and that the steady state dimensionless OS length, $\hat{L}_{\mathrm{OS,SS}}$, is such that,

$$u_{\mathrm{SS}}(\xi = -1) = u_{\mathrm{Thr}}. \tag{2.10}$$

The solution to this system is,

$$u_{\mathrm{SS}}(\xi) = \begin{cases} A\cosh\left[\gamma_1\left(\xi + 1\right)\right] & \text{if } -1 \leq \xi \leq 0, \\ B\sinh\left[\gamma_2\left(\xi - \hat{L}_{\mathrm{OS,SS}}\right)\right] + \cosh\left[\gamma_2\left(\xi - \hat{L}_{\mathrm{OS,SS}}\right)\right] & \text{if } 0 \leq \xi \leq \hat{L}_{\mathrm{OS,SS}}, \end{cases} \tag{2.11}$$

where,

$$A = \left[\cosh(\gamma_1)\cosh(\gamma_2\hat{L}_{\mathrm{OS,SS}}) + \frac{\gamma_1}{\gamma_2}\sinh(\gamma_1)\sinh(\gamma_2\hat{L}_{\mathrm{OS,SS}})\right]^{-1}, \tag{2.12a}$$

$$B = \frac{\frac{\gamma_1}{\gamma_2}\tanh(\gamma_1) + \tanh(\gamma_2 \hat{L}_{OS,SS})}{\frac{\gamma_1}{\gamma_2}\tanh(\gamma_1)\tanh(\gamma_2 \hat{L}_{OS,SS}) + 1}. \tag{2.12b}$$

Finally, using equation (2.11), we have that $u_{SS}(\xi = -1) = A$, which is equal to u_{Thr} according to equation (2.10). Thus we find that $\hat{L}_{OS,SS}$ solves,

$$\frac{1}{u_{Thr}} = \cosh(\gamma_1)\cosh(\gamma_2 \hat{L}_{OS,SS}) + \frac{\gamma_1}{\gamma_2}\sinh(\gamma_1)\sinh(\gamma_2 \hat{L}_{OS,SS}). \tag{2.13}$$

Physiologically realistic values of parameters γ_1 and γ_2 are non-negative. Further, for the OS length to approach a steady state at long times, $\hat{L}_{OS,SS} \geq 0$. For $\hat{L}_{OS,SS} = 0$, equations (2.7a)–(2.7h) reduce to,

$$\begin{aligned}
&\frac{\partial u}{\partial \tau} = \frac{\partial^2 u}{\partial \xi^2} - \gamma_1^2 u, \\
&\left.\frac{\partial u}{\partial \xi}\right|_{\xi=-1} = 0, \\
&u(0,\tau) = 1, \\
&u(\xi,0) = u_{in}(\xi),
\end{aligned}$$

for which, setting $\partial u/\partial \tau = 0$, the steady state dimensionless oxygen concentration distribution, $u_{SS}(\xi)$, satisfies,

$$\frac{\partial^2 u_{SS}}{\partial \xi^2} = \gamma_1^2 u_{SS}.$$

The solution to this system is,

$$u_{SS}(\xi) = \frac{\cosh\left[\gamma_1\left(\xi + 1\right)\right]}{\cosh\left(\gamma_1\right)}. \tag{2.14}$$

Therefore, $u_{SS}(\xi = -1) = 1/\cosh(\gamma_1)$, which is equal to u_{Thr} according to equation (2.10). Thus we have that, for $\hat{L}_{OS,SS} = 0$,

$$\gamma_1 = \cosh^{-1}\left(\frac{1}{u_{Thr}}\right).$$

Since the oxygen source is at $\xi = \hat{L}_{OS}(\tau)$, oxygen is consumed throughout the photoreceptor, and its only transport mechanism is diffusion, the oxygen concentration distribution is a monotonic decreasing function of the OS length.

Therefore, if the OS length is greater than zero, the oxygen concentration distribution is lower than that in equation (2.14). Hence, $u_{\mathrm{Thr}} = u_{\mathrm{SS}}(\xi = -1) < 1/\cosh(\gamma_1)$. Thus, for the OS length to approach a steady state at long times,

$$0 < \gamma_1 \leq \cosh^{-1}\left(\frac{1}{u_{\mathrm{Thr}}}\right). \tag{2.15}$$

The realistic ranges for γ_1 and γ_2 are therefore given by condition (2.15) and $\gamma_2 > 0$. To find an explicit expression for the steady state OS length, we define,

$$\alpha = \cosh(\gamma_1), \qquad \beta = \frac{\gamma_1}{\gamma_2}\sinh(\gamma_1),$$

and substitute these into equation (2.13). Rearranging and making the substitution $x = \exp(\gamma_2 \hat{L}_{\mathrm{OS,SS}})$ gives the following quadratic,

$$(\alpha + \beta)\, x^2 - \frac{2}{u_{\mathrm{Thr}}} x + (\alpha - \beta) = 0.$$

For real values of $\hat{L}_{\mathrm{OS,SS}}$, $x > 0$, giving,

$$\hat{L}_{\mathrm{OS,SS}} = \frac{1}{\gamma_2} \ln\left[\frac{1}{u_{\mathrm{Thr}}(\alpha + \beta)}\left(1 + \sqrt{1 - u_{\mathrm{Thr}}^2(\alpha^2 - \beta^2)}\right)\right]. \tag{2.16}$$

We note that condition (2.15) could also be derived by setting $\hat{L}_{\mathrm{OS,SS}} \geq 0$ in equation (2.16). In summary, condition (2.15) alone guarantees that a physically reasonable (i.e. real and non-negative) steady state solution exists for $\hat{L}_{\mathrm{OS,SS}}$.

To determine the stability of the steady state OS length, we perform linear stability analysis to investigate whether a small perturbation to the steady state OS length grows or decays in time. Firstly, we assume that the OS length evolves much more slowly than the oxygen concentration in the photoreceptor. To check whether this is a sensible assumption, we compare the timescales of evolution of the corresponding variables, $U(x,t)$ and $L_{\mathrm{OS}}(t)$. Typical scalings in a photoreceptor cell are 28 μM [129] for an oxygen concentration, 32 μm for a lengthscale [130], $10^{-9}\,\mathrm{m^2\,s^{-1}}$ for a diffusion coefficient [131] and 1 $\mu\mathrm{M\,s^{-1}}$ for a rate of oxygen uptake [105, 132]. We refer to these scales as $\bar{U}$, $\bar{L}$, $\bar{D}$ and $\bar{C}$ respectively. Using these scalings and equation (2.1), we deduce that the typical timescales of changes in the intracellular oxygen concentration are of order $\bar{t}_D \sim \bar{L}^2/\bar{D} \sim 1\,\mathrm{s}$ due to diffusion and of order $\bar{t}_U \sim \bar{U}/\bar{C} \sim 28\,\mathrm{s}$ due to oxygen uptake. In contrast, experimental observations suggest that changes in the OS

length occur over a number of hours [18, 38]. We therefore conclude that, on the timescale over which changes in the OS length occur, it is reasonable to assume the spatial oxygen distribution is in a quasisteady state and is thus almost instantaneously determined by equation (2.11). We exploit this assumption to determine the stability of the steady state OS length $\hat{L}_{\mathrm{OS,SS}}$. We define a small perturbation in the OS length from the steady state,

$$\delta\hat{L}_{\mathrm{OS}}(\tau) = \hat{L}_{\mathrm{OS}}(\tau) - \hat{L}_{\mathrm{OS,SS}} \ll \hat{L}_{\mathrm{OS,SS}}.$$

Since the time evolution of $\hat{L}_{\mathrm{OS}}(\tau)$ is governed by equation (2.7b), the perturbation in the OS length satisfies,

$$\frac{d}{d\tau}\left[\delta\hat{L}_{\mathrm{OS}}(\tau)\right] = \hat{k}\left[u(-1,\tau) - u_{\mathrm{Thr}}\right]. \tag{2.17}$$

Assuming that the oxygen distribution is quasisteady compared to the OS length, we can use equation (2.11) to approximate the value of $u(-1,\tau)$, which supplies,

$$\begin{aligned} &u(-1,\tau) = \\ &\Big\{\left[\alpha\cosh\left(\gamma_2\hat{L}_{\mathrm{OS,SS}}\right) + \beta\sinh(\gamma_2\hat{L}_{\mathrm{OS,SS}})\right]\cosh\left(\gamma_2\,\delta\hat{L}_{\mathrm{OS}}\right) \\ &\qquad + \left[\alpha\sinh\left(\gamma_2\hat{L}_{\mathrm{OS,SS}}\right) + \beta\cosh\left(\gamma_2\hat{L}_{\mathrm{OS,SS}}\right)\right]\sinh\left(\gamma_2\,\delta\hat{L}_{\mathrm{OS}}\right)\Big\}^{-1}. \end{aligned}$$

We can use Taylor series expansions for $\sinh\left(\gamma_2\,\delta\hat{L}_{\mathrm{OS}}\right)$ and $\cosh\left(\gamma_2\,\delta\hat{L}_{\mathrm{OS}}\right)$ in the above expression and, for sufficiently small values of $\delta\hat{L}_{\mathrm{OS}}$, satisfying $\delta\hat{L}_{\mathrm{OS}} \ll \gamma_2^{-1}$, we neglect the terms $\mathcal{O}\left((\gamma_2\,\delta\hat{L}_{\mathrm{OS}})^2\right)$ and higher. Substituting the resulting expression into equation (2.17) yields,

$$\frac{d}{d\tau}\left(\delta\hat{L}_{\mathrm{OS}}\right) = -\hat{k}u_{\mathrm{Thr}}^2\gamma_2\left[\alpha\sinh\left(\gamma_2\hat{L}_{\mathrm{OS,SS}}\right) + \beta\cosh\left(\gamma_2\hat{L}_{\mathrm{OS,SS}}\right)\right]\delta\hat{L}_{\mathrm{OS}}.$$

Since the values of $\hat{k}$, γ_2, $\hat{L}_{\mathrm{OS,SS}}$, α and β, are non-negative, perturbations $\delta\hat{L}_{\mathrm{OS}}(\tau)$ to the OS length exponentially decay in time. Hence the steady state $\hat{L}_{\mathrm{OS,SS}}$ is stable for all physically reasonable parameter choices.

Using our quasisteady approximation for the oxygen distribution, we can now check that equation (2.2), governing the OS length, is consistent with our assumption of OS growth if the rate of mitochondrial energy production exceeds a certain threshold level, and shedding if it is below threshold. If the two are consistent then $U(-L_{\mathrm{IS}},t) > U_{\mathrm{Thr}}$ implies that the rate of mitochondrial

energy production exceeds a certain threshold level (while $U(-L_{\text{IS}}, t) < U_{\text{Thr}}$ denotes a sub-threshold energy production per unit time).

Assuming that the amount of ATP produced by the mitochondria per unit time, P_A, is proportional to the amount of oxygen consumed by mitochondria per unit time, $\mu U(x,t)$, with constant of proportionality C',

$$\int_{-L_{\text{IS}}}^{0} P_A \, dx = C' \int_{-L_{\text{IS}}}^{0} \mu U(x,t) \, dx = C \int_{-1}^{0} u(x,\tau) \, d\xi,$$

where $C = \mu U_{L_{\text{OS}}} L_{\text{IS}} C'$. The total mitochondrial ATP production per unit time exceeds a threshold level, $M^{*\prime}$, if,

$$\int_{-1}^{0} u(\xi,\tau) \, d\xi > M^*,$$

where $M^* = M^{*\prime}/C$. Substituting $u(\xi,\tau)$ with the quasisteady approximation in equation (2.11) and integrating over the IS yields,

$$\cosh(\gamma_1)\cosh(\gamma_2 \hat{L}_{\text{OS}}(t)) + \frac{\gamma_1}{\gamma_2}\sinh(\gamma_1)\sinh(\gamma_2 \hat{L}_{\text{OS}}(t)) < \frac{1}{\gamma_1 M^*}\sinh(\gamma_1). \tag{2.18}$$

Rewriting the condition $U(-L_{\text{IS}}, t) > U_{\text{Thr}}$ using equation (2.11) yields,

$$\cosh(\gamma_1)\cosh(\gamma_2 \hat{L}_{\text{OS}}(t)) + \frac{\gamma_1}{\gamma_2}\sinh(\gamma_1)\sinh(\gamma_2 \hat{L}_{\text{OS}}(t)) < \frac{1}{U_{\text{Thr}}}. \tag{2.19}$$

Inspection of equations (2.18) and (2.19) reveals they are equivalent, with,

$$U_{\text{Thr}} = \gamma_1 M^* \operatorname{csch}(\gamma_1). \tag{2.20}$$

Hence, the condition $U(-L_{\text{IS}}, t) > U_{\text{Thr}}$ is equivalent to ensuring that the ATP production by the mitochondria per unit time exceeds a threshold level, whereas the mitochondrial ATP production per unit time is below threshold if $U(-L_{\text{IS}}, t) < U_{\text{Thr}}$.

2.3 PARAMETER ESTIMATION

We can use available experimental data to obtain physically realistic estimates of the model parameters. Our findings are summarised in Table 2.1. The

Symbol	Parameter	Estimated value	Refs
D_U	Diffusion coefficient of oxygen	2.1×10^{-9} $\mathrm{m^2\,s^{-1}}$	[131]
L_{IS}	IS length	$32\,\mu\mathrm{m}$	[130]
$U_{L_{\mathrm{OS}}}$	Oxygen concentration in choroidal vasculature	$28\,\mu\mathrm{M}$	[129, 133, 134]
μ_L	Rate of oxygen uptake by mitochondria (light conditions)	$1.1\,\mathrm{s^{-1}}$	[105, 132]
μ_D	Rate of oxygen uptake by mitochondria (dark conditions)	$2.2\,\mathrm{s^{-1}}$	[26, 105, 106, 132]
λ	Baseline oxygen consumption rate	$0.57\,\mathrm{s^{-1}}$	[129, 130]
U_{Thr}	Threshold oxygen concentration below which the OS sheds discs	$8.1\,\mu\mathrm{M}$	See §2.3.5
k	OS growth parameter	$1.0\,\mu\mathrm{m\,s^{-1}\,(mM)^{-1}}$	[31]

Table 2.1.: Summary of the dimensional parameters in the oxygen model (see equations (2.1)–(2.6)), along with their estimated values.

estimated values for the corresponding dimensionless parameters are given in Table 2.2. In the following sections we detail the information used to derive our parameter estimates from empirical data. We also explain how to convert between the units of measurement specified in the literature to the standardised units used in our model.

Symbol	Dimensionless parameter	Value
$\gamma_{1\mathrm{L}}$	Oxygen consumption in IS (light conditions)	0.90
$\gamma_{1\mathrm{D}}$	Oxygen consumption in IS (dark conditions)	1.2
γ_2	Oxygen consumption in OS	0.53
$\hat{k}$	OS growth parameter	4.3×10^{-4}
u_{Thr}	Threshold oxygen concentration	0.28

Table 2.2.: Summary of the dimensionless parameter groupings in the nondimensionalised oxygen model defined by equations (2.7a)–(2.7h).

2.3.1 *Outer Segment and Inner Segment Length (L_{OS}, L_{IS})*

Duke-Elder and Wybar [130] measured photoreceptor IS and OS lengths of 32 μm and 28 μm respectively. The latter of these measurements is consistent with measurements by Young [38] in rhesus monkeys (whose photoreceptors are found to be very similar to those in humans [38]), in which OS lengths varied between 22.5 μm and 36.5 μm depending on the location in the retina. We treat the estimate of the OS length to be the mean of the steady state OS lengths under light and dark conditions (i.e. the minimum and maximum output lengths from our model).

Injection of a traceable isotope of an amino acid component of OS discs in rat and mouse retinae showed that the entire OS was replaced every 9–10 days [18]. The results in rhesus monkeys are quantitatively similar, with the entire OS being replaced every 8.8–12.8 days depending on the location in the retina. Based on these results, we assume that the human rod photoreceptor OS sheds and replaces 10% of its time averaged length (assumed to be approximately 28 μm [130]), which we estimate as approximately 2.8 μm, per day.

To find approximate values for the maximal and minimal lengths attained daily by the OS, we consider two opposite limiting cases which give bounds on them. At one limit, growth and shedding of the OS never occur at the same time, with sole growth under dark conditions and sole shedding during light ones. Assuming that a day consists of 12 hours of dark conditions followed by 12 hours of light, the OS grows by 10% of its time-averaged length within 12 hours and then sheds until it reaches its initial length during the remaining 12 hours. Here, the difference between the maximal and minimal OS lengths is 2.8 μm. At the opposite limit, the OS grows and sheds continuously at all times, in which case the OS length is time invariant and the maximal and minimal lengths are equal. The physiological situation is between these two limiting cases and we argue that it more closely resembles the former, given that there is a noticeable time variation in the OS length. We therefore estimate the steady state lengths in dark and light conditions to be 28 ± 1 μm, or 29 μm and 27 μm respectively. The values of other parameters are inferred using a steady state OS length of 29 μm under dark conditions, but nothing in our model or parameter estimates predetermines the OS length at the steady state under light conditions. We use our model to predict the value of $L_{\mathrm{OS,SS,L}}$ and

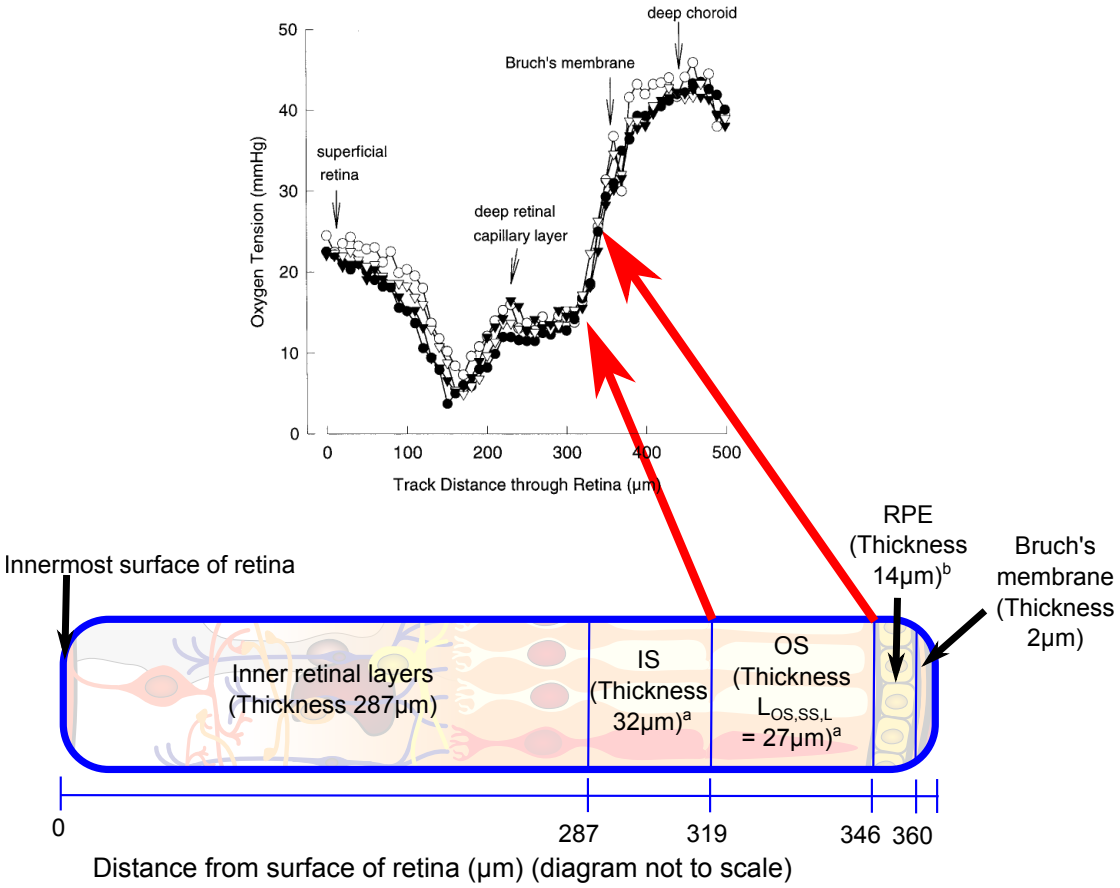


Figure 2.2.: Figure adapted from [14, 17, 18, 129], showing Yu and Cringle's measurements [129] of the oxygen concentration distribution in the rat retina. [a]taken from Duke-Elder and Wybar [130], [b]taken from Nordlund et al. [134].

compare this result with the estimated physiological value of 27 μm to test the validity of the hypothesis modelled.

2.3.2 *Oxygen Concentration at the Outer Segment End ($U_{L_{OS}}$)*

Yu and Cringle [129] measured the distribution of oxygen across the rat retina by inserting oxygen-sensitive microelectrodes under light conditions. The results of two sets of measurements are presented in Figure 2.2, together with the locations of the retinal layers. The figure shows that Bruch's membrane is located 360 μm from the innermost surface of the retina [130].

The RPE consists of a single layer of cells that have a width of 14 μm [134], so we take this value as the RPE thickness, and assume that the RPE–OS boundary is 346 μm from the innermost surface of the retina. Here the *partial pressure* of

oxygen (an empirical measure of concentration), $p_{O_2}(x = L_{OS})$, is measured to be 25 mmHg. Concentration is related to partial pressure by *Henry's Law*, which states that the concentration, C, of a gas dissolved in a solvent is proportional to the partial pressure of dry gas, p_{gas},

$$p_{gas} = k_H C, \tag{2.21}$$

where k_H is the Henry constant, which depends on the gas, the solvent and the temperature.

We estimate k_H by assuming that the Henry constant k_H in a photoreceptor cell at normal body temperature, 37°C, is the same as that in sea water at 40°C. Here the concentration of oxygen is measured to be $C_{O_2} = 0.17$ mM [135]. Further, we assume that the partial pressure of oxygen in sea water at 40°C is approximately the same as in air. The partial pressure of dry air in the atmosphere, p_{air}, can be derived from atmospheric pressure, p_{atm} by subtracting the partial pressure of water, p_{H_2O},

$$p_{air} = p_{atm} - p_{H_2O}.$$

Multiplying this by the proportion of the air which is oxygen, R_{O_2}, gives the partial pressure of oxygen in air, p_{O_2},

$$p_{O_2} = R_{O_2} p_{air}.$$

Taking atmospheric pressure as 760 mmHg, the partial pressure of water as 46 mmHg, and noting that oxygen constitutes 21% of air, we find that,

$$p_{O_2} = (760 - 46)\,\text{mmHg} \times 0.21 \approx 150\,\text{mmHg}.$$

Substituting the measured oxygen concentration and partial pressure in sea water at 40°C into equation (2.21), we estimate that the Henry constant in photoreceptors is,

$$k_H = \frac{p_{O_2}}{C_{O_2}} = 880\,\text{mmHg(mM)}^{-1}.$$

We can now estimate the concentration of oxygen at the RPE-OS boundary by substituting Yu and Cringle's [129] measurement $p_{O_2}(x = L_{OS}) = 25\,\text{mmHg}$ and the Henry constant $k_H = 880\,\text{mmHg(mM)}^{-1}$ into equation (2.21), to obtain,

$$U_{L_{OS}} = \frac{p_{O_2}(x = L_{OS})}{k_H} = 28\,\mu\text{M}.$$

Our model assumes that this value of $U_{L_{OS}}$ remains unchanged under light and dark conditions.

2.3.3 *Rates of Oxygen Uptake by Mitochondria (μ)*

The rate at which the outer retinal mitochondria consume oxygen is measured to be $150\,\text{nL}\,\text{cm}^{-2}\,\text{min}^{-1}$ ($0.025\,\text{mL}\,\text{m}^{-2}\,\text{s}^{-1}$) during light conditions [132] and approximately doubles under dark conditions [26, 105, 106, 132]. This measurement represents the volume of oxygen consumed per unit of retinal surface area per unit time. Dividing this by the thickness of the retinal layers where mitochondrial oxygen uptake takes place gives the volume of oxygen consumed per unit volume of tissue per unit time.

Over 90% of all outer retinal oxygen consumption occurs in the photoreceptors [136], so we neglect the contribution from the other outer retinal layers. Furthermore, all mitochondria in the photoreceptors are located in the inner segments. Therefore, we divide the consumption rates above by the thickness of the layer of photoreceptor inner segments, i.e. our estimated IS length, of $32\,\mu\text{m}$ [130]. Thus we estimate that the oxygen uptake rate per unit volume of tissue under light conditions is,

$$\frac{0.025\,\text{mL}\,\text{m}^{-2}\,\text{s}^{-1}}{32\,\mu\text{m}} \approx 0.78\,(\text{mL O}_2)\,(\text{L tissue})^{-1}\,\text{s}^{-1}.$$

This is equivalent to the value for $\mu_L U$ in our model, but with oxygen concentration given in units of $(\text{mL O}_2)\,(\text{L tissue})^{-1}$. We estimate the value of μ_L by dividing this quantity by a typical oxygen concentration in the photoreceptor, taking this to be $U_{L_{OS}}$, measured in units of $(\text{mL O}_2)\,(\text{L tissue})^{-1}$.

To convert our estimate of $U_{L_{OS}}$ to units of $(\text{mL O}_2)\,(\text{L tissue})^{-1}$, we treat oxygen as an ideal gas at atmospheric pressure (the pressure in the Ideal Gas

Law refers to absolute pressure rather than partial pressure) and average body temperature. Thus the volume occupied by one mole of oxygen is,

$$V = \frac{RT}{p_{\text{atm}}} = 25\,\text{L}.$$

Therefore, 28×10^{-6} moles of oxygen occupy 0.70 mL, giving $U_{L_{\text{OS}}} = 0.70\,(\text{mL } O_2)\,(\text{L retinal tissue})^{-1}$, from which we deduce that the rate of oxygen consumption in the photoreceptor inner segments is,

$$\mu_{\text{L}} = \frac{0.78\,(\text{mL } O_2)\,(\text{L tissue})^{-1}\,\text{s}^{-1}}{0.70\,(\text{mL } O_2)\,(\text{L retinal tissue})^{-1}} = 1.1\,\text{s}^{-1}$$

under light conditions, and thus $2.2\,\text{s}^{-1}$ under dark conditions.

2.3.4 *Oxygen Baseline Consumption Rate (λ)*

Here we consider light conditions and use Yu and Cringle's data [129], reproduced in Figure 2.2, to estimate λ, the baseline oxygen consumption rate, which does not change between light and dark conditions.

Yu and Cringle state that their measurements were taken after a steady state was attained under light conditions. Therefore, the oxygen concentration is given by equation (2.11), giving the steady state oxygen concentration, u_{SS}, in terms of λ (i.e. γ_2) and other parameter values which we have estimated above. We estimate the steady state oxygen concentration at a chosen spatial point, $x = 0$, under light conditions, using Yu and Cringle's data [129], and the steady state OS length $L_{\text{OS,SS}}$ is 27 μm (see earlier). We note that using this value of $L_{\text{OS,SS}}$ to estimate λ does not predetermine the OS length predicted by our model under light conditions, since there is another remaining free parameter, u_{Thr}, that also affects the steady state OS length (see equation (2.16)). Furthermore, as our chosen value of λ remains the same under dark and light conditions, it does not determine whether the OS is longest under light or dark conditions.

We can find the dimensionless steady state concentration at $\xi = 0$ under light conditions using Yu and Cringle's measurements of $p_{O_2}(x = 0)$ and $p_{O_2}(x = L_{OS})$ [129] via the following equation,

$$u_{SS}(\xi = 0) = \frac{U_{SS}(x = 0)}{U_{L_{OS}}} = \frac{p_{O_2}(x = 0)}{p_{O_2}(x = L_{OS})}. \tag{2.22}$$

The spatial point corresponding to $x = 0$ in our model (the IS-OS boundary) is 319 μm into the retina, as the RPE-OS boundary is 346 μm from the innermost surface of the retina, and the steady state OS length under light conditions, $L_{OS,SS,L}$, is 27 μm (see Figure 2.2). Here Yu and Cringle [129] measured the oxygen tension $p_{O_2}(x = 0)$ to be 15 mmHg.

Substituting the values of $p_{O_2}(x = 0)$ and $p_{O_2}(x = L_{OS})$ into equation (2.22) we obtain $u_{SS}(\xi = 0) = 0.6$. Using this value in equation (2.11) gives,

$$u_{SS}(\xi = 0) = -A \sinh\left(\gamma_2 \hat{L}_{OS,SS,L}\right) + \cosh\left(\gamma_2 \hat{L}_{OS,SS,L}\right) = 0.6,$$

where A is given by (2.12a). In terms of the dimensional parameters this gives,

$$-A \sinh\left(\sqrt{\frac{\lambda}{D_U}} L_{OS,SS,L}\right) + \cosh\left(\sqrt{\frac{\lambda}{D_U}} L_{OS,SS,L}\right) = 0.6, \tag{2.23}$$

where,

$$A = \left[\cosh\left(\sqrt{\frac{\lambda + \mu_L}{D_U}} L_{IS}\right) \cosh\left(\sqrt{\frac{\lambda}{D_U}} L_{OS,SS,L}\right) + \sqrt{\frac{\lambda + \mu_L}{\lambda}} \sinh\left(\sqrt{\frac{\lambda + \mu_L}{D_U}} L_{IS}\right) \sinh\left(\sqrt{\frac{\lambda}{D_U}} L_{OS,SS,L}\right)\right]^{-1}.$$

Substituting our estimated values for L_{IS}, D_U, μ_L and $L_{OS,SS,L}$ into equation (2.23), and finding numerical solutions using a standard root-finding algorithm [137], gives $\lambda = 0.57\,s^{-1}$, or $\gamma_2 = 0.53$. Our estimated values of L_{IS}, D_U, μ_L, μ_D and λ can be used to calculate the values of γ_{1L} and γ_{1D}, which are $\gamma_{1L} = 0.90$ and $\gamma_{1D} = 1.2$.

2.3.5 *Threshold Oxygen Concentration (U_{Thr})*

The parameter U_{Thr} represents the minimal oxygen concentration required by the mitochondria to maintain the photoreceptor. As such it is not directly measurable. Since the OS length attains a steady state when $U(x = -L_{\text{IS}}) = U_{\text{Thr}}$, we can infer its value from measurements of OS lengths and the corresponding oxygen concentration distribution predicted by our model.

We assume that, at the steady state under dark conditions, the OS length matches our estimated value of 29 μm and satisfies equation (2.13) with $\gamma_1 = \gamma_{1\text{D}}$. Rearranging this equation to give u_{Thr} in terms of $\gamma_{1\text{D}}$, γ_2 and $\hat{L}_{\text{OS,SS,D}}$, and substituting our estimated values, yields $u_{\text{Thr}} = 0.28$. This value is plausible since it is less than 1, the dimensionless oxygen concentration at the outer end of the OS, but still of the same order of magnitude. We note that our parameter estimates determine the predicted OS length under dark conditions only: during light conditions we do not place any constraint on the steady state OS length.

2.3.6 *OS Growth Parameter (k)*

In §2.3.1, we concluded from experimental data that the average rate of turnover of the OS discs is approximately 2.8 μm per day, or $3.2 \times 10^{-5}\,\mu\text{m}\,\text{s}^{-1}$. This gives us the the time-averaged value of $|dL_{\text{OS}}/dt|$, given by,

$$\int_{1\text{ day}} |k\,(U(-L_{\text{IS}}, t) - U_{\text{Thr}})|\; dt = \text{Turnover rate}$$

(see equation (2.2)). The use of the magnitude of dL_{OS}/dt is because the rate of *net* change in the OS length per day is zero since OS growth is balanced by shedding. To find the value of k, we estimate the order of magnitude of $(U(-L_{\text{IS}}, t) - U_{\text{Thr}})$ to be $U_{L_{\text{OS}}} = 28\,\mu\text{M}$. Then,

$$k = \frac{\text{Turnover rate}}{28\,\mu\text{M}} \approx 1\,\mu\text{m}\,\text{s}^{-1}\,(\text{mM})^{-1}.$$

We construct numerical solutions to the full, time-dependent system (2.7a)–(2.7h), by mapping the photoreceptor onto a fixed domain and using the Method of Lines [138–140] to convert the coupled PDEs to a system of time-dependent ODEs, which can be integrated using a standard ODE solver.

We transform our system onto a fixed domain [101] by mapping the independent variables (ξ, τ) to,

$$\rho \equiv \xi \left(\mathrm{H}(-\xi) + \frac{1}{\hat{L}_{\mathrm{OS}}(\tau)} \mathrm{H}(\xi) \right), \tag{2.24a}$$

$$s = \tau. \tag{2.24b}$$

Using the definitions (2.24a) and (2.24b), we have,

$$\frac{\partial}{\partial \xi} = \begin{cases} \dfrac{\partial}{\partial \rho} & \text{if } -1 \leq \xi < 0, \\ \dfrac{\partial \rho}{\partial \xi}\dfrac{\partial}{\partial \rho} + \dfrac{\partial s}{\partial \xi}\dfrac{\partial}{\partial s} = \dfrac{1}{\hat{L}_{\mathrm{OS}}(s)}\dfrac{\partial}{\partial \rho} & \text{if } 0 < \xi \leq \hat{L}_{\mathrm{OS}}(\tau), \end{cases}$$

and,

$$\frac{\partial}{\partial \tau} = \begin{cases} \dfrac{\partial}{\partial s} & \text{if } -1 \leq \xi < 0, \\ \dfrac{\partial \rho}{\partial \tau}\dfrac{\partial}{\partial \rho} + \dfrac{\partial s}{\partial \tau}\dfrac{\partial}{\partial s} = -\dfrac{\rho}{\hat{L}_{\mathrm{OS}}(s)}\dfrac{d\hat{L}_{\mathrm{OS}}}{ds}\dfrac{\partial}{\partial \rho} + \dfrac{\partial}{\partial s} & \text{if } 0 < \xi \leq \hat{L}_{\mathrm{OS}}(\tau). \end{cases}$$

We note that the boundary conditions of our system impose that $\partial/\partial\xi$ is continuous as $\xi \to 0$ from above and below, which means that,

$$\left.\frac{\partial}{\partial \rho}\right|_{\rho \to 0^-} = \frac{1}{\hat{L}_{\mathrm{OS}}(s)} \left.\frac{\partial}{\partial \rho}\right|_{\rho \to 0^+},$$

and $\partial/\partial\rho$ is discontinuous as $\rho \to 0$. Applying the above transformations to equations (2.7a)–(2.7h) gives,

$$\frac{\partial u}{\partial s} = \left(\mathrm{H}(-\rho) + \frac{1}{\hat{L}_{\mathrm{OS}}(s)^2} \mathrm{H}(\rho) \right) \frac{\partial^2 u}{\partial \rho^2} - \gamma_1^2 \mathrm{H}(-\rho) u + \left(\frac{\rho}{\hat{L}_{\mathrm{OS}}(s)} \frac{d\hat{L}_{\mathrm{OS}}}{ds} \frac{\partial u}{\partial \rho} - \gamma_2^2 u \right) \mathrm{H}(\rho), \tag{2.25a}$$

$$\frac{d\hat{L}_{\mathrm{OS}}}{ds} = \hat{k}\left(u(-1,s) - u_{\mathrm{Thr}}\right), \tag{2.25b}$$

$$\left.\frac{\partial u}{\partial \rho}\right|_{\rho=-1} = 0, \tag{2.25c}$$

$$u|_{\rho=1} = 1, \tag{2.25d}$$

$$u|_{\rho\to 0^-} = u|_{\rho\to 0^+}, \tag{2.25e}$$

$$\left.\frac{\partial u}{\partial \rho}\right|_{\rho\to 0^-} = \frac{1}{\hat{L}_{\mathrm{OS}}(s)}\left.\frac{\partial u}{\partial \rho}\right|_{\rho\to 0^+}, \tag{2.25f}$$

$$u(\rho,0) = u_{\mathrm{in}}(\rho), \tag{2.25g}$$

$$\hat{L}_{\mathrm{OS}}(0) = \hat{L}_{\mathrm{OS,in}}, \tag{2.25h}$$

where variables and parameters are as defined in §2.1.3.

We can now transform equations (2.25) to a system of time-dependent ODEs using the Method of Lines [138–140]. We decompose the inner and outer segments into n and m intervals of width $\Delta\rho_{\mathrm{IS}}$ and $\Delta\rho_{\mathrm{OS}}$ respectively, as shown in Figure 2.3. Then, for $i \in [0, n+m]$, ρ_i, the discretised version of the spatial variable ρ, is given by the following equations,

$$\rho_0 = -1,$$

$$\rho_{i+1} - \rho_i = \begin{cases} \Delta\rho_{\mathrm{IS}} & \text{for } i \in [0, n-1], \\ \Delta\rho_{\mathrm{OS}} & \text{for } i \in [n, n+m-1], \end{cases}$$

$$\rho_{n+m} = 1.$$

We spatially discretise equation (2.25) using finite difference methods to determine the time evolution of the discretised dependent variable,

$$u_i(s) = u(\rho_i, s).$$

The diffusion terms are discretised using a centred finite difference approximation, $F_{\mathrm{FD}}(u_i)$, defined by,

$$\frac{\partial^2 u}{\partial \rho^2} \approx F_{\mathrm{FD}}(u_i) = \begin{cases} \dfrac{u_{i+1} - 2u_i + u_{i-1}}{\left(\Delta\rho_{\mathrm{IS}}\right)^2} & \text{if } 1 \le i \le n-1, \\ \dfrac{u_{i+1} - 2u_i + u_{i-1}}{\hat{L}_{\mathrm{OS}}^2\left(\Delta\rho_{\mathrm{OS}}\right)^2} & \text{if } n+1 \le i \le n+m-1. \end{cases} \tag{2.26}$$

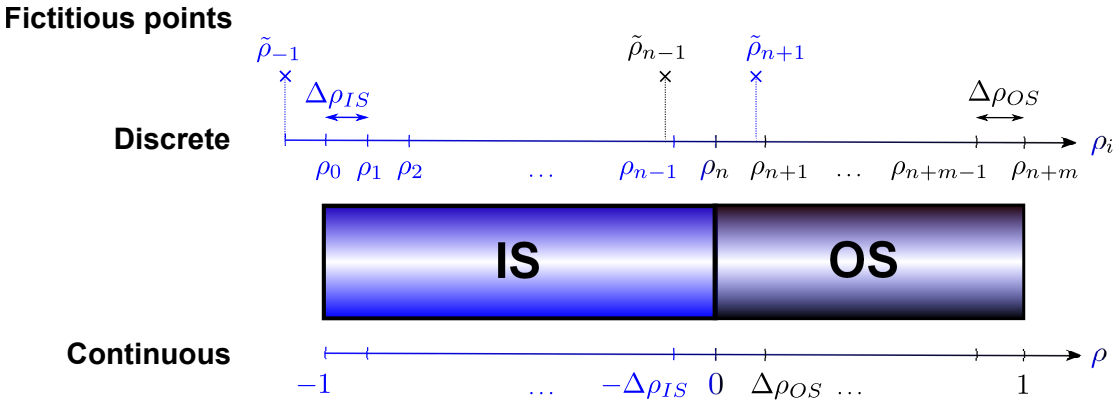


Figure 2.3.: Schematic diagram illustrating the spatial discretisation of our model. For each discrete spatial point ρ_i, the corresponding discrete concentration is $u_i = u(\rho_i, s)$. The positions of the fictitious points $\tilde{\rho}_{-1}$, $\tilde{\rho}_{n-1}$ and $\tilde{\rho}_{n+1}$ are also shown.

However, for the advection terms, the solution at any given spatial point is more heavily influenced by the oxygen concentration at the points in its direction of movement than at the points in the opposite direction. For example, if $dL_{\mathrm{OS}}/dt > 0$, then every point in the OS is moving outwards, and u_i is affected more by u_{i+1} rather than u_{i-1}. The opposite applies for $dL_{\mathrm{OS}}/dt < 0$. To account for this, the advection terms in the OS equations (for $i \in [n, n+m-1]$) are discretised using an upwind method [140], denoted by $F_{\mathrm{UW}}(u_i)$, defined by,

$$\frac{\partial u}{\partial \rho} \approx F_{\mathrm{UW}}(u_i) = \begin{cases} \dfrac{u_{i+1} - u_i}{\hat{L}_{\mathrm{OS}} \Delta\rho_{\mathrm{OS}}} & \text{for } \dfrac{dL_{\mathrm{OS}}}{dt} > 0, \\ \dfrac{u_i - u_{i-1}}{\hat{L}_{\mathrm{OS}} \Delta\rho_{\mathrm{OS}}} & \text{for } \dfrac{dL_{\mathrm{OS}}}{dt} < 0. \end{cases} \tag{2.27}$$

Here, during OS growth, $dL_{\mathrm{OS}}/dt > 0$ and the advective flux at spatial point ρ_i depends on the oxygen concentration at that spatial point and the adjacent point ρ_{i+1} in the direction of increasing ρ (i.e. the direction of domain growth). Conversely, during OS shedding, $dL_{\mathrm{OS}}/dt < 0$ and the advective flux at spatial point ρ_i is determined by the oxygen concentration there and at the spatial point ρ_{i-1} in the direction of OS retraction. We note that we choose the upwind and centred difference approximations to enhance the numerical efficiency: these approximations become exact and equivalent as $n, m \to \infty$.

Based on the above results, spatial discretisation of equation (2.25) gives,

$$\frac{du_i}{ds} = \begin{cases} F_{\mathrm{FD}}(u_i) - \gamma_1^2 u_i & \text{if } 1 \leq i \leq n-1, \\ F_{\mathrm{FD}}(u_i) + \dfrac{\rho_i}{\hat{L}_{\mathrm{OS}}} \dfrac{d\hat{L}_{\mathrm{OS}}}{ds} F_{\mathrm{UW}}(u_i) - \gamma_2^2 u_i & \text{if } n \leq i \leq n+m-1. \end{cases} \tag{2.28}$$

The boundary conditions at the inner end of the IS ($i = 0$), the outer end of the OS ($i = n + m$) and the IS-OS boundary ($i = n$) can be discretised as follows. The discrete version of boundary condition (2.7d) is,

$$u_{n+m} = 1. \tag{2.29}$$

Boundary condition (2.7e) is satisfied providing that, for $i = n$, the ODEs for the oxygen concentration in the IS and OS in (2.28) become identical, such that u_n is single-valued. The remaining two boundary conditions in equations (2.7c) and (2.7f) govern the fluxes $\partial u/\partial \rho$ at $i = 0$ and around $i = n$. It is convenient to introduce the fictitious spatial points,

$$\begin{aligned} \tilde{\rho}_{-1} &= -1 - \Delta\rho_{\mathrm{IS}}, \\ \tilde{\rho}_{n-1} &= -\Delta\rho_{\mathrm{OS}}, \\ \tilde{\rho}_{n+1} &= \Delta\rho_{\mathrm{IS}}, \end{aligned}$$

with corresponding fictitious concentrations,

$$\tilde{u}_{-1} = u(-1 - \Delta\rho_{\mathrm{IS}}, s), \tag{2.30a}$$

$$\tilde{u}_{n-1} = u(-\Delta\rho_{\mathrm{OS}}, s), \tag{2.30b}$$

$$\tilde{u}_{n+1} = u(\Delta\rho_{\mathrm{IS}}, s), \tag{2.30c}$$

as shown in Figure 2.3, and then discretise the fluxes above using a finite centred difference approximation, so that boundary conditions (2.7c) and (2.7f) become,

$$\frac{u_1 - \tilde{u}_{-1}}{2\Delta\rho_{\mathrm{IS}}} = 0 \Rightarrow u_1 = \tilde{u}_{-1}, \tag{2.31}$$

and,

$$\frac{\tilde{u}_{n+1} - u_{n-1}}{2\Delta\rho_{\mathrm{IS}}} = \frac{1}{\hat{L}_{\mathrm{OS}}} \frac{u_{n+1} - \tilde{u}_{n-1}}{2\Delta\rho_{\mathrm{OS}}}. \tag{2.32}$$

The fictitious points allow us to extend equations (2.26)–(2.28) to $i \in \{0, n\}$. With $i = 0$ in equation (2.28), and substituting from equation (2.30a) for $\tilde{u}_{-1}$ we obtain,

$$\frac{du_0}{ds} = \frac{2\left(u_1 - u_0\right)}{\left(\Delta\rho_{\mathrm{IS}}\right)^2} - \gamma_1^2 u_0. \tag{2.33}$$

Equation (2.28) supplies,

$$\frac{du_n}{ds} = \left(\frac{\tilde{u}_{n+1} - 2u_n + u_{n-1}}{\left(\Delta\rho_{\mathrm{IS}}\right)^2}\right) - \gamma_1^2 u_n, \tag{2.34}$$

for $i = n$ in the IS, and,

$$\frac{du_n}{ds} = \left(\frac{u_{n+1} - 2u_n + \tilde{u}_{n-1}}{\hat{L}_{\mathrm{OS}}^2\left(\Delta\rho_{\mathrm{OS}}\right)^2}\right) - \gamma_2^2 u_n, \tag{2.35}$$

for $i = n$ in the OS. Together equations (2.32), (2.34) and (2.35) are sufficient to eliminate the oxygen concentrations at the fictitious points, $\tilde{u}_{n+1}$ and $\tilde{u}_{n-1}$, to give the following ODE for u_n,

$$\begin{aligned}\frac{du_n}{ds} = \left(1 + \frac{1}{\hat{L}_{\mathrm{OS}}}\frac{\Delta\rho_{\mathrm{IS}}}{\Delta\rho_{\mathrm{OS}}}\right)^{-1} \Bigg\{ \frac{2}{\hat{L}_{\mathrm{OS}}^2\left(\Delta\rho_{\mathrm{OS}}\right)^2}\Bigg[u_{n+1} - 1 - \\ \frac{\hat{L}_{\mathrm{OS}}\Delta\rho_{\mathrm{OS}}}{\Delta\rho_{\mathrm{IS}}}\left(u_n + u_{n-1}\right)\Bigg] - \left(\frac{1}{\hat{L}_{\mathrm{OS}}}\frac{\Delta\rho_{\mathrm{IS}}}{\Delta\rho_{\mathrm{OS}}}\gamma_1 + \gamma_2\right)\Bigg\}.\end{aligned} \tag{2.36}$$

In summary, we now have $n + m + 1$ ODEs for u_i ($i \in [0, n + m]$), given by equation (2.33) for $i = 0$, (2.36) for $i = n$, (2.28) for $i \in [1, n-1] \cup [n+1, n+m-1]$, and (2.29) for $i = n + m$. The time evolution of the OS length is given by,

$$\frac{d\hat{L}_{\mathrm{OS}}}{ds} = \hat{k}\left(u_0 - u_{\mathrm{Thr}}\right). \tag{2.37}$$

(see equation (2.7b)) This system is subject to the initial conditions,

$$u_i(0) = u_{\mathrm{in}}(\rho_i), \qquad \hat{L}_{\mathrm{OS}}(0) = \hat{L}_{\mathrm{OS,in}}. \tag{2.38}$$

Since equations (2.28), (2.29) (2.33) and (2.36) evolve over a typical timescale of order seconds, while equation (2.37) evolves over a number of hours (see

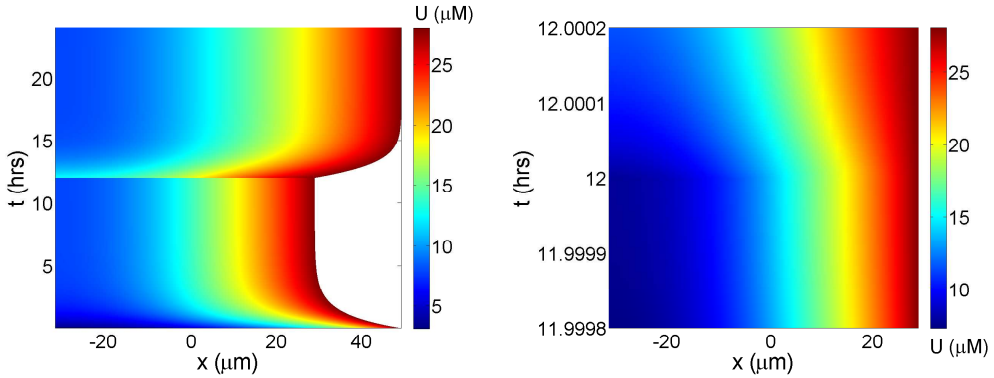
§2.1), we have a problem involving two very different timescales: a *stiff* system. This has an impact on the efficiency of our numerical solutions. When the spatial oxygen distribution is evolving rapidly, many timesteps per second are required for accurate simulations, while integration over a number of hours is necessary to capture the time-evolution of the photoreceptor length. It is therefore necessary to use a numerical ODE solver specifically designed for stiff ODEs [141]. This type of ODE solver varies the size of the timesteps used according to the predicted rate of change of the solution based on previous timesteps. This contrasts with other solvers which either do not use sufficiently small timesteps, giving inaccurate solutions due to numerical instability, or perform extremely large numbers of small integration steps, making them very computationally expensive.

Once the dimensionless equations on a fixed domain have been solved, the results can be transformed back to the dimensional system on the growing domain.

2.5 NUMERICAL RESULTS

In order to test whether our model predicts the correct time evolution for the OS length, we solve equations (2.1)–(2.6) numerically, using the techniques described in §2.4. Simulations are performed over a 24-hour period starting from the steady state under light conditions, followed by 12 hours of dark conditions and subsequently 12 hours of light. This entails setting $u_{\text{in}}(\xi)$ and $\hat{L}_{\text{OS,in}}$ to the steady state oxygen distribution and OS length under light conditions, $u_{\text{SS,L}}(\xi)$ and $\hat{L}_{\text{OS,SS,L}}$ respectively (see equations (2.11) and (2.16), with $\gamma_1 = \gamma_{1\text{L}}$), and using the parameter values specified in §2.3 (see Tables 2.1 and 2.2). In particular, we note that all model parameters are unchanged under light and dark conditions, except for the rate at which the mitochondria consume oxygen, μ.

Results from a typical simulation are presented in Figure 2.4, showing that the system approaches steady states in both dark and light conditions. Within approximately 4 hours the time evolution in both light and dark is negligible. The OS grows under light conditions and sheds during darkness, with L_{OS} reaching a steady state of approximately 29 μm under dark conditions and 49 μm under light conditions, which matches the results given by substituting the values $\gamma_{1\text{D}}$ and $\gamma_{1\text{L}}$ into equation (2.13). We note that our parameter



(a) (b)

Figure 2.4.: Spatiotemporal distribution of the oxygen concentration in a photoreceptor according to our model, defined by equations (2.1)–(2.6). Figure (a) shows simulation results over 12 hours of dark conditions followed by 12 hours of light. The oxygen concentration approaches a steady state under both light and dark conditions, the model predicts growth of the outer segment under light conditions and shortening under dark conditions. Figure (b) shows simulation results at $t = 12 \pm 0.01$ hours, illustrating the continuous but rapid time evolution of the oxygen distribution. Parameter values: see Table 2.1.

estimates are chosen such that the OS length predicted by our model closely matches measured values under dark conditions, while allowing the model to predict the length during light conditions.

Figure 2.4(b) focuses on the time evolution of the oxygen concentration profile and OS length over a short period of time close to the transition between dark and light conditions. At the transition, the value of μ changes, the oxygen concentration and OS length are now far from their new steady states and the stiffness in the system, discussed in §2.4, becomes apparent.

Figure 2.5 shows the spatial oxygen concentration distributions after 12 hours of darkness and light respectively, according to the numerical solution to the full time-dependent system (xxx), and the analytical steady state solutions under dark and light conditions according to equations (2.11) and (2.13) (—), taking the same parameter values as in Figure 2.4. As expected, the simulated oxygen distributions after 12 hours of light/dark conditions match closely with the corresponding steady state solutions.

From Figure 2.5, under dark conditions, oxygen consumption in the IS is increased, so the oxygen concentration falls more rapidly with distance from the choroid than under light conditions. As the oxygen level at $x = L_{OS}(t)$, set by boundary condition (2.4), is unchanged between light and dark conditions, the

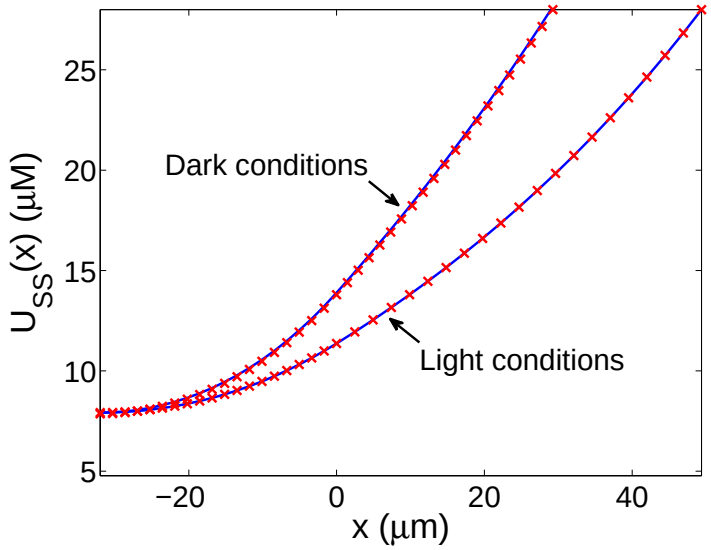


Figure 2.5.: Comparison of the numerical solution (xxx) to the oxygen model (defined by equations (2.1)–(2.6)) after 12 hours of dark/light conditions, with the corresponding analytical steady state distributions (—) using $\mu = \mu_D$ and $\mu = \mu_L$ under dark and light conditions respectively. Parameter values: see Table 2.1. After 12 hours, the numerical solutions and steady state solutions match closely, indicating that the system has reached a steady state, and the outer segment is longest under light conditions.

onset of dark conditions initially causes the oxygen concentration at $x = -L_{IS}$ to fall below its value at the steady state under light conditions, U_{Thr}. When $U(-L_{IS}, t) < U_{Thr}$, $dL_{OS}/dt < 0$ and the OS decreases in length. Consequently $U(-L_{IS}, t)$ increases until the system reaches a steady state, with $U(-L_{IS}, t) = U_{Thr}$ and $dL_{OS}/dt = 0$. Following the transition to light conditions, the oxygen consumption rate in the IS halves and $U(-L_{IS}, t)$ increases above U_{Thr}, causing OS growth and a concomitant reduction in $U(-L_{IS}, t)$, until a new steady state is reached.

Our results show that, when oxygen alone is responsible for regulation of the photoreceptor length, the OS grows to an equilibrium length $L_{OS,SS,L} \approx 49\,\mu$m under light conditions, and it sheds in dark conditions reaching a steady state length of $L_{OS,SS,D} \approx 29\mu$m.

Based on our results, we conclude that oxygen is not the sole regulator for OS length, since oxygen-based regulation yields OS growth under light conditions and shedding during darkness. In practice, OS shedding outweighs growth under light conditions. For example, Bassi and Powers [35], who measured phagosome levels in fish RPE cells under various lighting regimes, found

elevated phagosome levels following the onset of light (RPE phagosome levels correlate with the rate of phagocytosis and hence disc shedding (see Chapter 1)). LaVail [36] and White et al. [37] reported similar results in rats and rabbits. This suggests that, although oxygen availability may control the growth of the OS during dark conditions, another factor becomes rate-limiting under light conditions, which is not incorporated in this model. We examine an alternative explanation for the diurnal variation in the OS length in the next chapter.

2.6 PARAMETER SENSITIVITY

Using equation (2.16) it is possible to plot the steady state OS lengths under light and dark conditions while varying our model parameters. These parameter sensitivity plots give us insight into which physiological mechanisms are likely to be responsible for controlling the OS length. This enables us to identify possible causes of pathology. For example, we can use the model to investigate whether ageing may adversely affect the regulation of rod photoreceptor length by oxygen, leading to retinal disease. Moreover, parameter sensitivity analysis enables us to assess whether changes in parameter estimates may alter the key model predictions.

2.6.1 *Physiological Interpretation of Parameter Sensitivity Diagrams*

Figure 2.6 shows how the steady state OS length varies as some of the model parameters are varied. The dotted lines show our estimated values for each parameter, and the corresponding steady state OS lengths (with black and red denoting dark and light conditions respectively).

Figure 2.6(a) shows that a higher diffusion coefficient for oxygen increases the steady state OS length predicted by our model. More rapid diffusion of oxygen leads to a flatter spatial oxygen distribution throughout the photoreceptor. The oxygen concentration is held constant at the outer end of the OS by the choroidal blood supply (see boundary condition (2.4)), and falls with distance from $x = L_{OS}$. The decrease in oxygen concentration with distance from the choroid is less pronounced if the diffusion coefficient is increased, enabling the OS to grow longer before the oxygen concentration at the inner end of the IS falls below the threshold value and the system approaches a steady state. Also, increasing the diffusion coefficient increases the difference between the

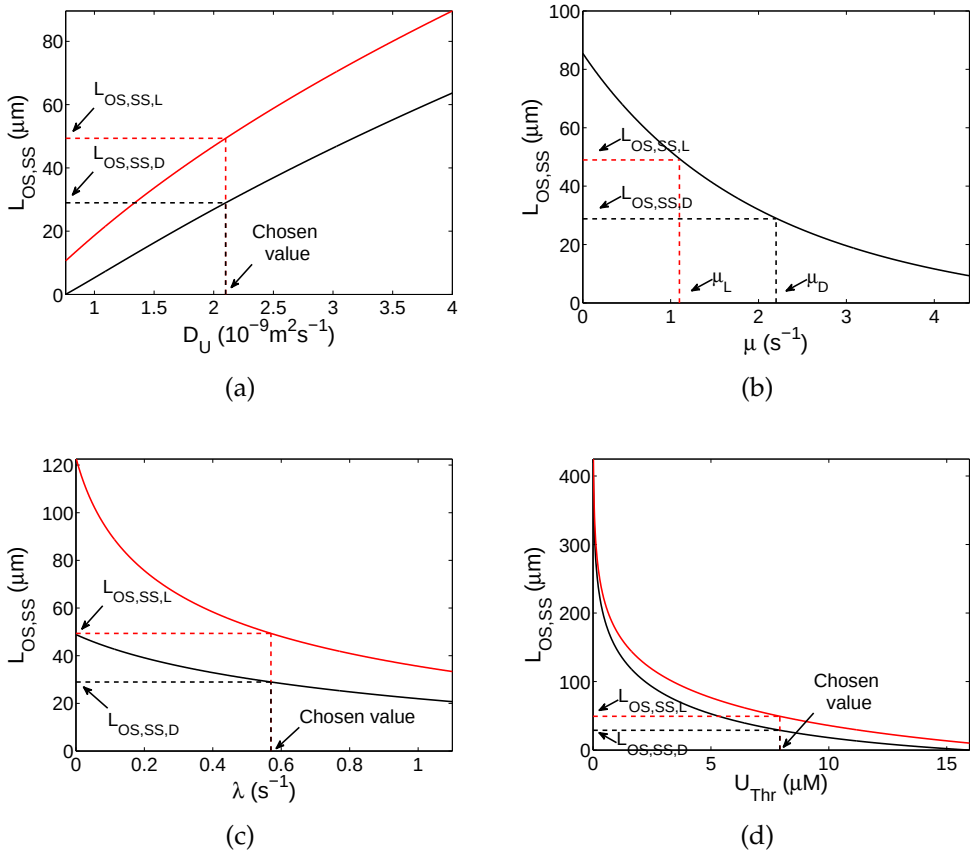


Figure 2.6.: Sensitivity diagrams showing how the steady state outer segment length in the oxygen model (defined by equations (2.1)–(2.6)) changes as we vary (a) the diffusion coefficient of oxygen in the photoreceptors, D_U; (b) the rate at which the mitochondria consume oxygen, μ; (c) the rate of baseline consumption of oxygen, λ; (d) the threshold oxygen concentration for outer segment shedding, U_{Thr}. All other parameter values are as in Table 2.1. The dotted lines represent our chosen parameter values, with the associated steady state outer segment lengths (with black and red denoting dark and light conditions respectively).

OS lengths under light and dark conditions, due to the flatter spatial oxygen profile a greater change in the photoreceptor length is needed to produce the same effect on the oxygen concentration at the inner end of the IS.

The spatial oxygen profile can also be flattened by decreasing the oxygen consumption rates λ and μ. Thus, a reduction of one of these consumption rates has the same effect as an increase in the diffusion coefficient, as indicated in Figures 2.6(b) and 2.6(c). The competing effects of diffusion and oxygen consumption are obvious from the dimensionless parameter groupings in equations (2.8), where γ_1 and γ_2 are proportional to λ and/or μ and inversely proportional to D_U. Decreasing the value of γ_1 or γ_2 flattens the spatial oxygen profile. The dotted lines in Figure 2.6(b) show the values of μ_{L} and μ_{D}. The shortening of the OS during darkness and growth under light conditions is a consequence of the increased oxygen consumption by the mitochondria in the IS under dark conditions, while the other parameters remain unchanged.

As seen in Figure 2.6(d), increasing the value of U_{Thr} decreases the steady state OS length. From §2.1, the rate of OS growth is proportional to the extent that the oxygen concentration at $x = -L_{\mathrm{IS}}$ (the inner end of the IS) exceeds the threshold value, U_{Thr}, and vice-versa for shedding. Therefore, for a given OS length, raising the value of U_{Thr} means that the oxygen concentration at $x = -L_{\mathrm{IS}}$ either exceeds U_{Thr} by a smaller amount, or it is further below the threshold level, leading to slowed OS growth or more rapid shedding. Thus the OS length that can be maintained decreases as U_{Thr} increases.

Examining the nondimensionalised system in equations (2.1)–(2.6) reveals that the parameters L_{IS} and $U_{L_{\mathrm{OS}}}$ simply scale the lengths and concentrations in our system, and thus have no effect on the qualitative behaviour. Furthermore, we note that the OS growth rate k has no effect on the steady state OS length. This is consistent with equation (2.16), in which $L_{\mathrm{OS,SS}}$ is independent of k. However, as seen in Figure 2.7, the value of this parameter determines the rate at which the OS length reaches a steady state. If the OS growth rate is small, the OS length does not reach a steady state within 12 hours under either light or dark conditions, but the length is bounded above and below by the steady state OS lengths for light and dark conditions respectively. We conclude that, according to our model, the steady state OS length depends on the diffusion coefficient of oxygen, the oxygen consumption rates and the threshold oxygen concentration for shedding, but not the rate of shedding.

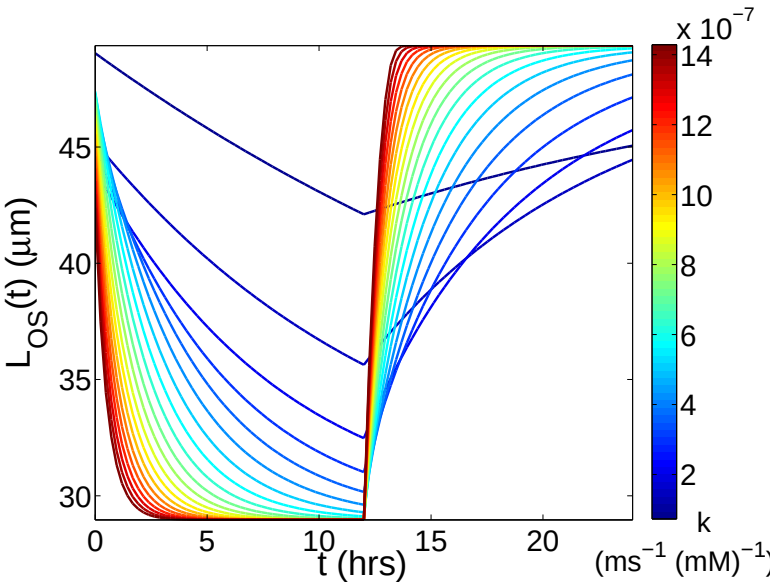


Figure 2.7.: Time evolution of the outer segment length in the oxygen model (defined by equations (2.1)–(2.6)), during 12 hours of dark conditions followed by 12 hours of light conditions, using different values of the growth rate parameter k. All other parameter values are as in Table 2.1. The outer segment length reaches a steady state within 12 hours if $k > 6 \times 10^{-7}\,\mathrm{m\,s^{-1}(mM)^{-1}}$ but not for smaller values of k.

2.6.2 *Predicting Causes of Age-Related Macular Degeneration*

Certain conditions may cause changes in the regulation of the OS length. For example, a known effect of ageing is a reduction in the efficiency of the mitochondria [9]. This may have two effects on parameters in our model. Firstly, in order to produce sufficient energy for the photoreceptors, the mitochondria in the inner segments may consume oxygen at an abnormally rapid rate, increasing μ under both light and dark conditions. Secondly, a higher threshold oxygen concentration may be needed to ensure the mitochondria supply enough energy to maintain the photoreceptor, increasing the value of U_{Thr}. According to Figures 2.6(b) and 2.6(d), an increase in μ or U_{Thr} causes a decrease in OS length (see §2.6.1). Age-related shortening of photoreceptor outer segments has been observed clinically [11]. It also explains loss in visual acuity with age, since the shortening of the OS implies a reduction in the number of OS discs in which phototransduction can occur, resulting in impaired light-sensitivity. In practice, if the OS becomes too short then the photoreceptor cell may die. Thus, our model results suggest that a decrease in mitochondrial efficiency, as occurs

in ageing, may lead to the loss of rod photoreceptors, a characteristic feature of age-related macular degeneration [11, 12].

2.6.3 *Sensitivity of our Model Predictions to Changes in Parameters*

Since the parameters in our model have not been directly measured *in vivo* in human photoreceptors, their values are not known to a high level of accuracy. Our estimated values in §2.3 are derived using measurements on other mammalian species and simplifying assumptions regarding the intracellular environment in human photoreceptors. No direct measurements exist for the baseline oxygen consumption parameter λ and the OS growth rate k, so we infer their values from the resulting effects on the oxygen concentration and photoreceptor length.

However, in the regions of parameter space we have examined, the qualitative behaviour of our model is impressively robust to changes in parameters. The parameter value known with the least certainty is growth rate k, and the steady state OS length is independent of this parameter.

According to Figure 2.6, the OS length varies monotonically with each parameter, meaning that our predictions in §2.6.2 are unchanged by using a different estimated value for one of the parameters. Furthermore, regardless of the estimated values of μ_{L} and μ_{D}, provided that $\mu_{\mathrm{L}} < \mu_{\mathrm{D}}$, the steady state OS length predicted by our model is always longer under light conditions compared to darkness. Since it is widely agreed that the oxygen consumption in the IS increases during dark conditions [42–44], and also that the OS shortens during light conditions [35–37], our model predictions of the diurnal variation in outer segment length contradict empirical findings. Based on this we conclude that oxygen cannot be the only factor regulating OS length. However, the fact that the OS length in our model reaches a steady state under both light and dark conditions highlights the possibility that oxygen-based OS length regulation may prevent unlimited OS growth under dark conditions.

We check our prediction that oxygen is not the sole regulator for photoreceptor length by examining the behaviour of the system over a wide range of parameter choices, as illustrated in Figure 2.8. Using the results in this figure, we consider changes to parameters γ_1 and γ_2 in combination. This enables us to cover a greater amount of parameter space. The figure shows how the difference $\Delta L_{\mathrm{OS,SS}} = L_{\mathrm{OS,SS,D}} - L_{\mathrm{OS,SS,L}}$ between the OS length under dark and

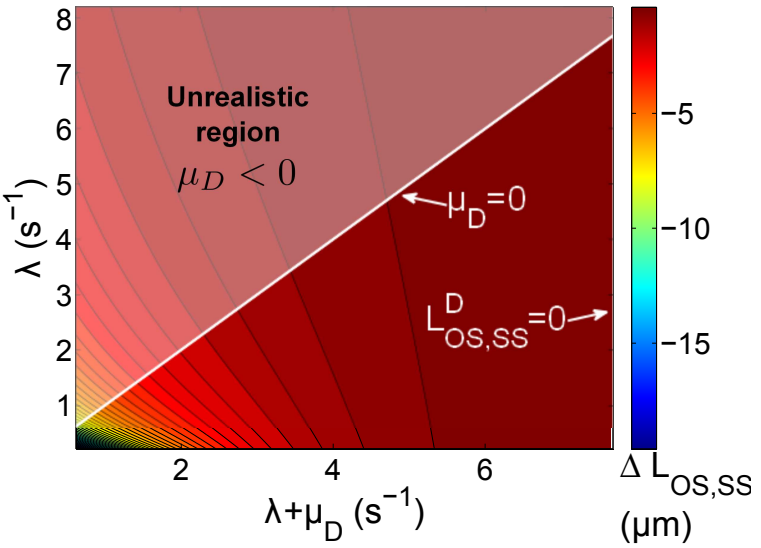


Figure 2.8.: Sensitivity diagram showing how the difference between the steady state outer segment length in the oxygen model (defined by equations (2.1)–(2.6)) under dark and light conditions, $\Delta L_{OS,SS} = L_{OS,SS,D} - L_{OS,SS,L}$, changes as we vary the rate of oxygen consumption in the inner and outer segments, $\lambda + \mu_D$ and λ respectively. For each value of μ_D, μ_L is set such that $\mu_L = \mu_D/2$. In the realistic region of λ-μ_D parameter space, decreasing λ or μ_D or both increases the difference between the outer segment lengths under light and dark conditions, and the photoreceptor is always longest during light conditions. All other parameter values are as in Table 2.1.

light conditions varies with the values of λ and $\lambda + \mu$ (corresponding to the dimensionless parameter groupings γ_1 and γ_2). We vary the values of λ_L and μ_L, and from these values derive the corresponding parameter values $\lambda_D = \lambda_L$ and $\mu_D = 2\mu_L$ (we assume that the oxygen consumption by mitochondria doubles during dark conditions according to experimental findings, see §2.3). The region of parameter space shown in this figure is within the bounds $\lambda \geq 0$, $\mu \geq 0$ and $\lambda + \mu \leq 7.7\,s^{-1}$. Physically realistic rates of oxygen consumption are non-negative, giving the first two conditions. The latter condition is supplied by substituting our realistic parameter estimates (see Table 2.1) into equation (2.15), which ensures that the OS length predicted by our model is real and non-negative. From this figure we see that decreasing either or both of the oxygen consumption rates λ and μ increases the difference $\Delta L_{OS,SS}$ between the steady state OS lengths under dark and light conditions. Decreasing either of the oxygen consumption rates leads to a flatter spatial oxygen profile through the photoreceptor. While the oxygen concentration at $x = L_{OS}$ is held constant

by the choroid, it falls more slowly with distance from $x = L_{OS}$, meaning that it does not fall to the threshold level U_{Thr} at $x = -L_{IS}$ until the photoreceptor is longer. Consequently, decreasing λ and/or μ increases the steady state OS lengths under light and dark conditions. Since there is also more photoreceptor growth during light conditions, the difference between the steady state length approached, $L_{OS,SS,L}$ and the length at the onset of light ($L_{OS,SS,D}$) is also greater, implying an increase in $\Delta L_{OS,SS}$. From equation (2.16) we see that in the extreme case where $\lambda \to 0$ (or equivalently $\gamma_2 \to 0$), $\hat{L}_{OS,SS} \to \infty$. For this reason, Figure 2.8 does not include very small values of λ or μ.

Figure 2.8 shows that, for all physiologically reasonable estimates of the oxygen consumption rates in the IS and OS, $\Delta L_{OS,SS} < 0$. This implies that, throughout the realistic region of λ–μ parameter space, the model yields the same predictions regarding the diurnal changes in the OS length.

2.7 DISCUSSION

We have devised a model to simulate the distribution of oxygen within a rod photoreceptor, and how it regulates OS length if it is the growth-rate-limiting nutrient. We used the model to show that oxygen may regulate OS length under dark conditions (where it prevents indefinite growth), but not under light conditions (where it permits OS growth, rather than stimulating disc shedding). In the next chapter, we propose an alternative model to explain disc shedding under light conditions. The new model accounts for the phosphocreatine shuttle and assumes that the length of the OS is regulated by the distribution of ATP in the OS.

The model presented in this chapter is designed to determine the time variation, and possible intracellular oxygen dependence of photoreceptor OS length, progressing beyond existing models of retinal nutrient levels [104, 105, 107, 108] (see Chapter 1). As demonstrated in §2.6, these aspects of photoreceptor metabolism may play an important role in the onset or progression of retinal diseases. For instance, we used our model to show that if the efficiency of the mitochondria in the IS diminishes, this can lead to a shortening in the OS length. Excess shortening of the photoreceptor may lead to impaired light sensitivity or cell death.

Our parameter sensitivity analysis demonstrated that the qualitative results of the model and conclusions remain unchanged with variations in the threshold

oxygen concentration for OS shedding and the rates of oxygen consumption in both the IS and OS: despite variations in each parameter value, the OS length under light conditions was always predicted to be greater than under dark conditions.

While the model captures key processes in photoreceptor oxygen metabolism and how it may affect the OS length, there are a variety of ways it can be extended in future work, to include additional metabolites and regulatory processes, or combine it with other models of metabolism. For instance, the chemical *neuroglobin* is present in high concentrations in the photoreceptors, particularly in the IS where oxygen consumption is very rapid [142]. The necessity of neuroglobin for the survival of photoreceptors under hypoxic conditions is undisputed, but its exact function remains a subject of debate [142]. Two popular theories are that:

1. it may enhance the rate of oxygen uptake by the cells [142];
2. it may facilitate oxygen diffusion [143].

An adaptation of our model incorporating neuroglobin may provide valuable information to add to the debate. Neuroglobin is diffusible and binds reversibly with oxygen to form a diffusible complex [144], i.e.,

$$\mathrm{Ngb} + \mathrm{O}_2 \underset{k_\mathrm{B}}{\overset{k_\mathrm{F}}{\rightleftharpoons}} \mathrm{NgbO}_2.$$

Therefore we suggest that the neuroglobin distribution can be included in the oxygen model by making the following changes. We denote the neuroglobin concentration and the neuroglobin-oxygen complex as the dependent variables $N(x,t)$ and $W(x,t)$, governed by,

$$\begin{aligned}\frac{\partial N}{\partial t} &= D_N \frac{\partial^2 N}{\partial x^2} - k_\mathrm{F} N U + k_\mathrm{B} W,\\ \frac{\partial W}{\partial t} &= D_W \frac{\partial^2 W}{\partial x^2} + k_\mathrm{F} N U - k_\mathrm{B} W,\end{aligned}$$

where neuroglobin and the neuroglobin-oxygen complex do not pass through the photoreceptor cell membranes, so no-flux boundary conditions apply,

$$\left.\frac{\partial N}{\partial x}\right|_{x=-L_\mathrm{IS}} = 0 = \left.\frac{\partial W}{\partial x}\right|_{x=-L_\mathrm{IS}},$$

$$D_N \left.\frac{\partial N}{\partial x}\right|_{x=L_{\mathrm{OS}}(t)} = -N(L_{\mathrm{OS}}(t),t)\frac{dL_{\mathrm{OS}}}{dt},$$
$$D_W \left.\frac{\partial W}{\partial x}\right|_{x=L_{\mathrm{OS}}(t)} = -W(L_{\mathrm{OS}}(t),t)\frac{dL_{\mathrm{OS}}}{dt},$$

and the concentration and flux are continuous across the IS-OS boundary,

$$[N]_{x=-L_{\mathrm{IS}}}^{x=L_{\mathrm{OS}}(t)} = 0 = [W]_{x=-L_{\mathrm{IS}}}^{x=L_{\mathrm{OS}}(t)},$$
$$\left[\frac{\partial N}{\partial x}\right]_{x=-L_{\mathrm{IS}}}^{x=L_{\mathrm{OS}}(t)} = 0 = \left[\frac{\partial W}{\partial x}\right]_{x=-L_{\mathrm{IS}}}^{x=L_{\mathrm{OS}}(t)}.$$

Therefore, the total amount of bound and unbound neuroglobin throughout the photoreceptor remains constant in time, i.e.,

$$\int_{-L_{\mathrm{IS}}}^{L_{\mathrm{OS}}(t)} \left(N(x,t)+W(x,t)\right)\,dx = \int_{-L_{\mathrm{IS}}}^{L_{\mathrm{OS}}(t)} \left(N(x,0)+W(x,0)\right)\,dx \equiv M_N,$$

and we assume that, initially, all neuroglobin is unbound, and distributed uniformly, giving,

$$N(x,0) = \frac{M_N}{L_{\mathrm{IS}}+L_{\mathrm{OS}}(0)},$$
$$W(x,0) = 0.$$

Equation (2.1) is adapted by adding two extra terms to account for the interactions between oxygen and neuroglobin, and taking the rate of oxygen uptake by the mitochondria to be an increasing function of the neuroglobin concentration, $\mu = \mu(N(x,t))$, giving,

$$\frac{\partial U}{\partial t} = D_U\frac{\partial^2 U}{\partial x^2} - \left[\lambda + \mu(N)\mathrm{H}(-x)\right]U - k_{\mathrm{F}}NU + k_{\mathrm{B}}W.$$

Equation (2.2) governing the OS length, and the boundary and initial conditions (2.3)–(2.6) are unchanged.

Theories 1 and 2 are both incorporated in the equations above, but they can also be tested separately by setting k_{F} and k_{B} to zero and setting $\mu(N(x,t))$ constant, respectively. The validity of each hypothesis can be tested by investigating the effects on the diurnal variation of the OS length.

3

THE PHOSPHOCREATINE SHUTTLE AS A DETERMINANT OF ROD PHOTORECEPTOR LENGTH

Based on the predicted links between rod outer segment (OS) length regulation and retinal pathology discussed in Chapters 1 and 2, in this chapter we develop a model to examine the role of the transport mechanism for ATP (adenosine triphosphate, from which cells derive their energy) in OS length regulation. In Chapter 2 we tested the hypothesis that the OS length is regulated solely by oxygen levels. We concluded that oxygen may be involved in controlling the OS length, but it is not the sole regulator: our model of oxygen-based regulation does not exhibit OS shedding during light conditions. In the first part of this chapter, we formulate a continuum PDE model to assess a second hypothesis: that discs are shed from the OS if there is insufficient ATP available to them. In this model, the rate of change of the OS length is solely dependent on the ATP distribution. In the latter part of this chapter we combine these two hypotheses and develop a model which assumes that the OS length is regulated both by oxygen and ATP availability.

As discussed in §1.3, there are two mechanisms by which rod photoreceptors produce ATP: glycolysis and oxidative metabolism. Glycolysis takes place throughout the photoreceptor whereas oxidative metabolism occurs within mitochondria located within the inner segment (IS). The energy demand of OS discs increases during light conditions, since energy is required to convert light to a sensory response (via phototransduction). While the baseline energy demand of the OS discs during darkness can be met by glycolysis [49], the increased ATP requirement under light conditions cannot. The additional ATP required in light conditions is provided via oxidative metabolism in the IS. Energy is transported from the IS to the sites of high energy demand via the phosphocreatine shuttle, described in §1.3. The availability of ATP in the OS is thus dependent on the rate at which the phosphocreatine shuttle operates.

Thus, in this chapter, we focus on the role of the phosphocreatine shuttle and test whether regulation by phosphocreatine-derived ATP alone can explain the observed diurnal variation in OS length.

In §3.1 we present our model of the phosphocreatine shuttle in an individual photoreceptor cell, including the creatine phosphate, creatine, free phosphate, ATP and ADP levels, along with the OS length. The length variation of the photoreceptor depends on the levels of ATP made available in the OS via the phosphocreatine shuttle. We nondimensionalise the model and estimate physiologically realistic parameter values in §3.2. Simulations of our model in §3.4 and parameter sensitivity analysis in §3.5 using realistic parameter estimates enable us to assess whether the model predicts the observed patterns of OS length changes. The OS length predicted by our model approaches a realistic steady state under light conditions, but there is no mechanism to prevent indefinite OS growth during darkness, so physically unrealistic behaviour is exhibited under prolonged dark conditions. We evaluate and draw conclusions from our model of the phosphocreatine shuttle in §3.6.

The oxygen model (Chapter 2) is able to predict the correct OS length regulation under dark conditions only, whereas the phosphocreatine shuttle model can correctly predict the OS length only under light conditions. In the second part of this chapter, we explore whether the correct diurnal behaviour, and bounded OS growth, is observed when the two models are combined. Our combined model, developed in §3.7, is based on the hypothesis that rod photoreceptor length depends on the availability of oxygen in the IS and phosphocreatine-derived ATP in the OS. Results from simulations of this model demonstrate the experimentally observed time variation of the photoreceptor length. The OS length is regulated by oxygen under dark conditions and the phosphocreatine shuttle under light conditions. Parameter sensitivity analysis of the combined model enables us to predict possible causes of retinal disease. Finally, in §3.8 of this chapter we conclude with a discussion of all three models of photoreceptor length regulation (the oxygen model in Chapter 2, the phosphocreatine shuttle model in §3.1–3.6 of this chapter and the combined model in §3.7) and give ideas for future developments.

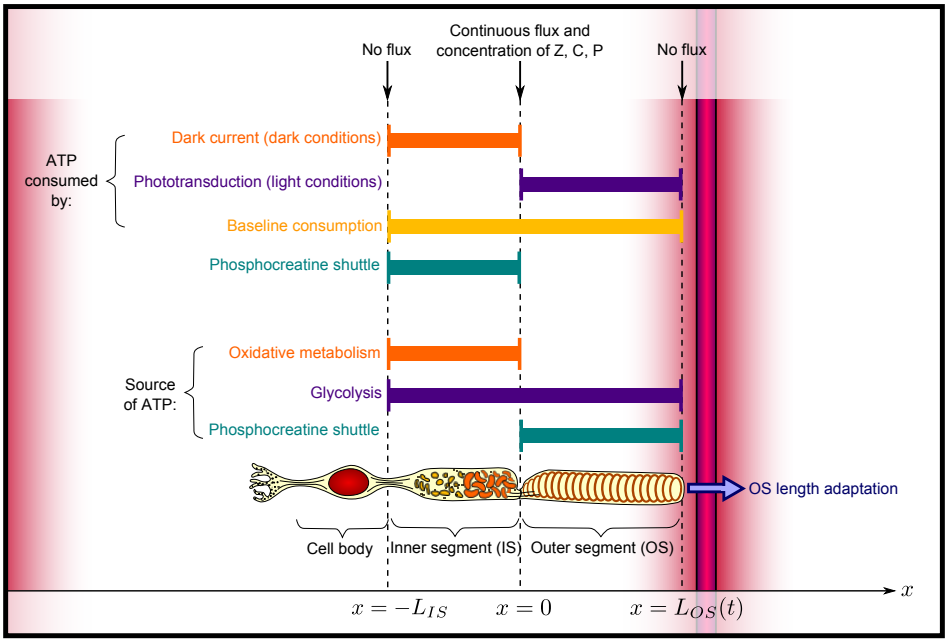


Figure 3.1.: Schematic diagram showing the location of processes that produce or consume ATP within a rod photoreceptor (diagram of photoreceptor adapted from [18]).

3.1 MODEL DEVELOPMENT

Assuming that the rod photoreceptor OS length depends on the distribution of ATP in the OS, as regulated by the phosphocreatine shuttle, we formulate a model that couples the spatiotemporal distributions of creatine phosphate ($Z(x,t)$), creatine ($C(x,t)$), free phosphate ($P(x,t)$), ATP ($A(x,t)$) and ADP ($B(x,t)$) in a rod photoreceptor to the time-varying OS length, $L_{\text{OS}}(t)$. As in §2.1, we treat the photoreceptor as a growing domain with the IS and OS occupying the regions $-L_{\text{IS}} \leq x \leq 0$ and $0 \leq x \leq L_{\text{OS}}(t)$ respectively. Figure 3.1 summarises the locations of ATP production and consumption by the mechanisms described in the introduction to this chapter.

3.1.1 *Creatine Phosphate, Creatine, Free Phosphate, ATP and ADP Concentrations*

Our model focuses on whether limited ATP availability in the OS can explain the observed disc shedding. Since the OS has a plentiful glycolytic supply of ATP under dark conditions [49], we examine the additional energy requirement that is provided by the phosphocreatine shuttle under light conditions, which

is more likely to be limiting. We denote by $k_{-1,OS}$ the rate of the breakdown of phosphocreatine shuttle-derived ATP in the OS (which increases with the energy demand of the OS discs). This ATP is originally produced in the IS (where the mitochondria are located), from ADP and free phosphate (P) with rate constant $k_{1,\mathrm{IS}}$. The biochemical reaction,

$$\mathrm{ADP} + \mathrm{P} \underset{k_{-1,\alpha}}{\overset{k_{1,\alpha}}{\rightleftharpoons}} \mathrm{ATP} \tag{3.1}$$

represents ATP production and breakdown ($\alpha \in \{\mathrm{IS}, \mathrm{OS}\}$). We note that, since our focus is solely on IS-derived (i.e. phosphocreatine shuttle-derived) ATP (rather than that produced locally in the OS by glycolysis) we assume,

$$k_{1,\mathrm{OS}} = 0. \tag{3.2}$$

Moreover, using the assumptions described above yields,

$$k_{-1,\mathrm{OS}} = \begin{cases} k_{-1,\mathrm{L}} & \text{light conditions,} \\ 0 & \text{dark conditions,} \end{cases} \tag{3.3}$$

where $k_{-1,\mathrm{L}}$ is a positive constant. Diffusion of ATP through the photoreceptor is very slow (due to interactions between ATP and membrane-bound proteins [50]) and thus provides insufficient ATP to sustain phototransduction. Instead, energy is transferred to the OS via the phosphocreatine shuttle. This process is described in detail in §1.3 and summarised in Figure 3.2. ATP generated in the IS combines reversibly with the highly diffusible chemical creatine (Cr) via the following reaction,

$$\mathrm{Cr} + \mathrm{ATP} \underset{k_{2,\alpha}}{\overset{k_{-2,\alpha}}{\rightleftharpoons}} \mathrm{CrP} + \mathrm{ADP}, \tag{3.4}$$

($\alpha \in \{\mathrm{IS}, \mathrm{OS}\}$), catalysed by the creatine kinase enzyme, producing creatine phosphate (CrP) and ADP with rate constant $k_{-2,\alpha}$. CrP diffuses throughout the photoreceptor. In regions with high energy demands (and hence low ATP concentrations), CrP combines reversibly with ADP to produce ATP and creatine, via the reaction (3.4) in the reverse direction, with rate constant $k_{2,\alpha}$. Since, under typical physiological conditions, reaction (3.4) favours the forward and reverse directions in the IS and OS respectively, the CrP concentration decreases

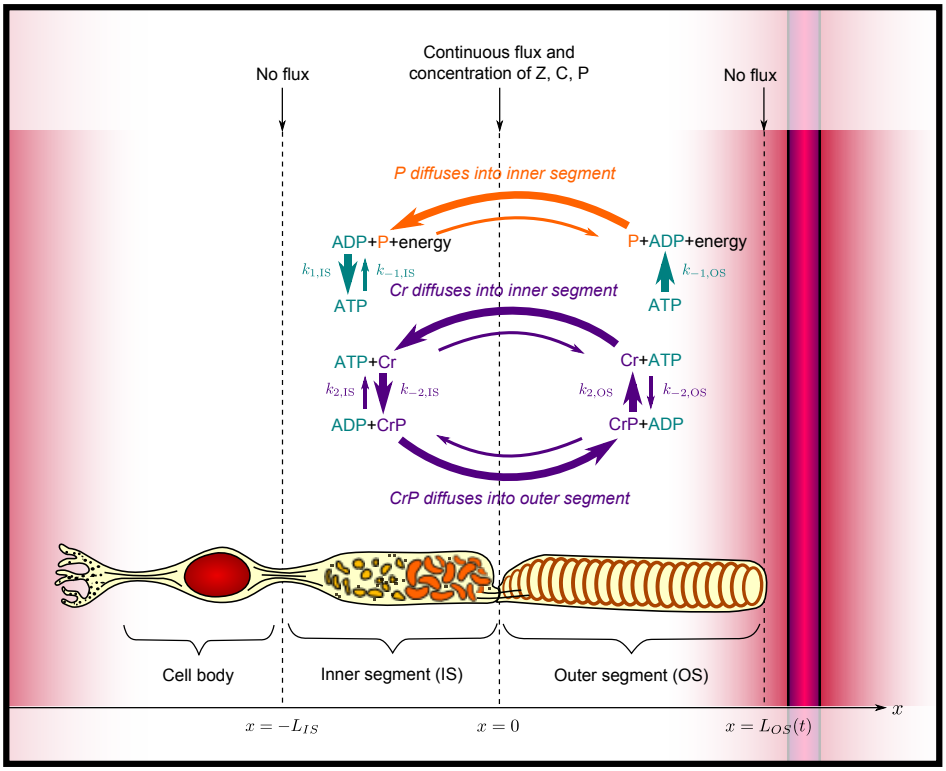


Figure 3.2.: Schematic diagram showing energy transfer within a rod photoreceptor via the phosphocreatine shuttle (diagram of photoreceptor adapted from [18]).

monotonically with x, and conversely for the Cr concentration. Therefore, CrP diffuses down its concentration gradient from the IS to the OS, where it combines with ADP to produce ATP and creatine. ATP is broken down to release energy where it is needed while the creatine diffuses back to the IS, and the process repeats.

For simplicity we restrict our attention to reactions (3.1) and (3.4) and the diffusion of CrP, Cr, P in our model, all other processes are neglected, and necessary substrates and enzymes are treated as abundant. In particular, we neglect ATP diffusion (which is slow), other substrates and intermediates of oxidative metabolism and any up or down regulation of creatine kinase. Reaction terms are derived by applying the Law of Mass Action. The following equations can therefore be used to model the photoreceptor nutrient concentrations,

$$\frac{\partial Z}{\partial t} = D_Z \frac{\partial^2 Z}{\partial x^2} + \nu_C, \tag{3.5a}$$

$$\frac{\partial C}{\partial t} = D_C \frac{\partial^2 C}{\partial x^2} - \nu_C, \tag{3.5b}$$

$$\frac{\partial P}{\partial t} = D_P \frac{\partial^2 P}{\partial x^2} - \nu_P, \tag{3.5c}$$

$$\frac{\partial A}{\partial t} = \nu_P - \nu_C, \tag{3.5d}$$

$$\frac{\partial B}{\partial t} = \nu_C - \nu_P, \tag{3.5e}$$

where D_Z, D_C and D_P are the diffusion coefficients for CrP, Cr and P respectively, and,

$$\nu_C = k_{-2,\alpha} CA - k_{2,\alpha} ZB, \qquad \nu_P = k_{1,\alpha} BP - k_{-1,\alpha} A. \tag{3.6}$$

We note that equations (3.5d) and (3.5e) imply that the total adenine nucleotide pool is conserved at each spatial point,

$$A + B = A_r, \tag{3.7}$$

where A_r is the total concentration of ATP and ADP, which is constant [145]. From equations (3.5a) and (3.5b) we have conservation of the total creatine pool,

$$\int_{-L_{\mathrm{IS}}}^{L_{\mathrm{OS}}(t)} (Z + C)\, dx = \mathrm{Cr}_{\mathrm{Tot}}, \tag{3.8}$$

and, from equations (3.5), (3.5d) and (3.5c), conservation of the total phosphate pool,

$$\int_{-L_{\mathrm{IS}}}^{L_{\mathrm{OS}}(t)} (Z + A + P)\, dx = \mathrm{Phos}_{\mathrm{Tot}}, \tag{3.9}$$

within the photoreceptor, where $\mathrm{Cr}_{\mathrm{Tot}}$ and $\mathrm{Phos}_{\mathrm{Tot}}$ are positive constants.

3.1.2 *Length of the Outer Segment*

We assume that OS discs are produced at a constant rate, K_{grow}, passing outwards through the OS from the IS-OS boundary, and that they are viable only if the ATP concentration, $A(x,t)$, exceeds a threshold level, A^*. Otherwise the discs at the outer end of the OS are shed. We define the spatial point

$x = L^*_{\mathrm{OS}}(t)$ as the point at which the ATP concentration passes through the threshold level A^*,

$$A(x,t) = A^* \text{ for } x = L^*_{\mathrm{OS}}(t). \tag{3.10}$$

As discussed earlier in this section, the spatial x-dependence of the CrP and Cr concentration is monotonic decreasing and increasing respectively. This, and the fact that $k_{1,\mathrm{OS}} = 0$, imply that the ATP concentration is a monotonic decreasing function of x. Therefore, condition (3.10) implies that $A(x,t) > A^*$ for $x < L^*_{\mathrm{OS}}(t)$ and $A(x,t) < A^*$ for $x > L^*_{\mathrm{OS}}(t)$. We assume that the rate of tip shedding is proportional to the distance over which $A(x,t) < A^*$ in the OS. Accordingly, the equation governing the time evolution of the OS length is,

$$\frac{dL_{\mathrm{OS}}}{dt} = K_{\mathrm{grow}} - \sigma \left(L_{\mathrm{OS}}(t) - L^*_{\mathrm{OS}}(t)\right) \mathrm{H}\left(L_{\mathrm{OS}}(t) - L^*_{\mathrm{OS}}(t)\right), \tag{3.11}$$

where $\mathrm{H}(x)$ denotes the Heaviside function. Shedding occurs at all spatial points in the OS between $x = L^*_{\mathrm{OS}}(t)$ and $x = L_{\mathrm{OS}}(t)$.

We note that an alternative way to define dL_{OS}/dt rather than that in equation (3.11) would be to use an analogous expression to that in the oxygen model (see equation (2.2)), in which the rate of shedding of the OS is proportional to the difference between the ATP concentration at the outer end of the OS and a certain threshold concentration for shedding, A_{Thr}. For example, the shedding term $\sigma \left(L_{\mathrm{OS}}(t) - L^*_{\mathrm{OS}}(t)\right) \mathrm{H}\left(L_{\mathrm{OS}}(t) - L^*_{\mathrm{OS}}(t)\right)$ in equation (3.11) could be replaced by the term $\chi \left[A_{\mathrm{Thr}} - A(L_{\mathrm{OS}}(t), t)\right] \mathrm{H}\left(A_{\mathrm{Thr}} - A(L_{\mathrm{OS}}(t), t)\right)$. For the case where the ATP concentration in the OS is a linear function of x (i.e. $A(x,t) = A(0,t) - \lambda x$ where λ is a constant), the altered shedding term reduces to the original term in equation (3.11), with $\sigma = \lambda\chi$ and $L^*_{\mathrm{OS}}(t) = (A(0,t) - A_{\mathrm{Thr}})\lambda^{-1}$. We note that, compared to the alternative representation, equation (3.11) best represents the physiology of disc shedding, since it allows for the fact that the rate of change in the OS length is proportional to the amount of discs being shed. The altered shedding rate could become very rapid in the limit where $A(x,t) > A_{\mathrm{Thr}}$ for $x < L_{\mathrm{OS}}(t)$ and $A(x,t) = 0$ for $x = L_{\mathrm{OS}}(t)$, which is unlikely to be the case in typical physiological conditions.

However we demonstrated that, in the oxygen model, equation (2.2) was a suitable way to represent our assumption that OS length is regulated by the energy production per unit time by mitochondria. Thus, the different forms

of equations (2.2) and (3.11) reflect the different physiology of the proposed mechanisms regulating OS length in each model.

3.1.3 *Boundary and Initial Conditions*

We prescribe boundary and initial conditions to close equations (3.5) and (3.11) (except for the dependent variables A and B, which we will show can be eliminated later in this section). We assume no flux of CrP, Cr or P through the photoreceptor cell membranes, giving no flux boundary conditions on Z, C and P at $x = -L_{\mathrm{IS}}$, and a boundary condition ensuring no flux through the moving cell membrane at $x = L_{\mathrm{OS}}(t)$. For $Y \in \{Z, C, P\}$,

$$\left.\frac{\partial Y}{\partial x}\right|_{x=-L_{\mathrm{IS}}} = 0, \tag{3.12a}$$

$$D_Y \left.\frac{\partial Y}{\partial x}\right|_{x=L_{\mathrm{OS}}(t)} = -Y\frac{dL_{\mathrm{OS}}}{dt}. \tag{3.12b}$$

For physically realistic solutions, we also impose continuity of the concentrations and fluxes of CrP, Cr and P across the IS-OS boundary at $x = 0$, giving,

$$Y|_{x\to 0^-} = Y|_{x\to 0^+}, \tag{3.13a}$$

$$\left.\frac{\partial Y}{\partial x}\right|_{x\to 0^-} = \left.\frac{\partial Y}{\partial x}\right|_{x\to 0^+}, \tag{3.13b}$$

and assume the following initial distributions,

$$Y(x,0) = Y_{\mathrm{in}}(x), \qquad L_{\mathrm{OS}}(0) = L_{\mathrm{OS,in}} \tag{3.14}$$

($Y \in \{Z, C, P\}$). The term on the right hand side of equation (3.12b) accounts for the time-dependence of the domain length by allowing material to flow into the newly grown part of the domain, or in the opposite direction if the domain contracts (as discussed in §1.5.1).

3.1.4 *Nondimensionalisation*

To nondimensionalise, we define the following dimensionless parameter groupings,

$$\hat{K}_{\text{grow}} = \frac{K_{\text{grow}}}{k_{2,\text{IS}} A_r L_{\text{IS}}}, \qquad \hat{\sigma} = \frac{\sigma}{k_{2,\text{IS}} A_r}, \qquad a^* = \frac{A^*}{A_r},$$

$$\hat{D}_Z = \frac{D_Z}{k_{2,\text{IS}} A_r L_{\text{IS}}^2}, \qquad \hat{D}_C = \frac{D_C}{k_{2,\text{IS}} A_r L_{\text{IS}}^2}, \qquad \hat{D}_P = \frac{D_P}{k_{2,\text{IS}} A_r L_{\text{IS}}^2},$$

$$\hat{k}_{1,\text{IS}} = \frac{k_{1,\text{IS}}}{k_{2,\text{IS}}}, \qquad \hat{k}_{1,\text{OS}} = 0, \qquad \hat{k}_{-1,\text{IS}} = \frac{k_{-1,\text{IS}}}{k_{2,\text{IS}} Z_r},$$

$$\hat{k}_{2,\text{IS}} = 1, \qquad \hat{k}_{2,\text{OS}} = \frac{k_{2,\text{OS}}}{k_{2,\text{IS}}}, \qquad \hat{k}_{-2,\text{IS}} = \frac{k_{-2,\text{IS}}}{k_{2,\text{IS}}},$$

$$\hat{k}_{-2,\text{OS}} = \frac{k_{-2,\text{OS}}}{k_{2,\text{IS}}} \qquad a_{\text{Tot}} = \frac{A_{\text{Tot}}}{A_r}, \qquad z_{\text{in}} = \frac{Z_{\text{in}}}{Z_r},$$

$$c_{\text{in}} = \frac{C_{\text{in}}}{Z_r}, \qquad p_{\text{in}} = \frac{P_{\text{in}}}{Z_r},$$

$$\hat{k}_{-1,\text{OS}} = \begin{cases} \frac{k_{-1,\text{L}}}{k_{2,\text{IS}} Z_r} & \text{light conditions,} \\ 0 & \text{dark conditions,} \end{cases}$$

and the following scalings. We rescale Z, C and P by a typical CrP concentration, Z_r, while A and B are scaled by A_r, a typical ATP concentration. Lengths are rescaled with the IS length, and we rescale times with the timescale of reaction 3.4 in the forward direction in the IS, $(k_{2,\text{IS}} A_r)^{-1}$. The resulting dimensionless variables are, for $(Y, y) \in \{(Z, z), (C, c), (P, p)\}$ and $(V, v) \in \{(A, a), (B, b)\}$,

$$(z, c, p) = \frac{1}{Z_r}(Z, C, P), \qquad (a, b) = \frac{1}{A_r}(A, B),$$

$$\xi = \frac{x}{L_{\text{IS}}}, \qquad \hat{L}_{\text{OS}}(T) = \frac{L_{\text{OS}}(t)}{L_{\text{IS}}},$$

$$T = k_{2,\text{IS}} A_r t.$$

Guided by typical ATP and CrP concentrations, $A_r = 1\,\text{mM}$ [50, 146–148] and $Z_r = 14\,\text{mM}$ [149] respectively, we infer that $A_r \ll Z_r$, and define,

$$0 < \epsilon = \frac{A_r}{Z_r} \ll 1. \tag{3.15}$$

This then gives the following dimensionless equations for the nutrient concentrations,

$$\frac{\partial z}{\partial T} = \hat{D}_Z \frac{\partial^2 z}{\partial \xi^2} + \hat{v}_C, \qquad \frac{\partial c}{\partial T} = \hat{D}_C \frac{\partial^2 c}{\partial \xi^2} - \hat{v}_C, \quad \frac{\partial p}{\partial T} = \hat{D}_P \frac{\partial^2 p}{\partial \xi^2} - \hat{v}_P, \tag{3.16a}$$

$$\epsilon \frac{\partial a}{\partial T} = \hat{v}_P - \hat{v}_C, \qquad \epsilon \frac{\partial b}{\partial T} = \hat{v}_C - \hat{v}_P, \tag{3.16b}$$

where,

$$\hat{v}_C = \hat{k}_{-2,\alpha} ca - \hat{k}_{2,\alpha} zb, \qquad \hat{v}_P = \hat{k}_{1,\alpha} bp - \hat{k}_{-1,\alpha} a. \tag{3.17}$$

As indicated by (3.16), ATP and ADP have fast reaction kinetics compared to CrP, Cr and P. Since we are considering the timescale $T \geq \mathcal{O}(1)$, on which CrP, Cr and P evolve (since their dynamics limit the rate at which ATP is made available to the OS), we are justified in assuming that the ATP and ADP concentrations are quasisteady. As such, the leading order approximation to equations (3.16) is,

$$\hat{v}_C = \hat{v}_P. \tag{3.18}$$

Combining (3.18) with the fact that $a + b = a_{\text{Tot}}$ (see equation (3.7)) enables us to reduce the PDEs to the following simplified dimensionless system,

$$\frac{\partial z}{\partial T} = \hat{D}_Z \frac{\partial^2 z}{\partial \xi^2} + \hat{v}, \qquad \frac{\partial c}{\partial T} = \hat{D}_C \frac{\partial^2 c}{\partial \xi^2} - \hat{v}, \qquad \frac{\partial p}{\partial T} = \hat{D}_P \frac{\partial^2 p}{\partial \xi^2} - \hat{v}, \tag{3.19a}$$

where, for $\alpha \in \{\text{IS, OS}\}$, $\hat{v}$ is given by,

$$\hat{v} = \frac{\left(\dfrac{\hat{k}_{1,\alpha} \hat{k}_{-2,\alpha}}{\hat{k}_{-1,\alpha}} cp - \hat{k}_{2,\alpha} z \right) a_{\text{Tot}}}{1 + \dfrac{\hat{k}_{1,\alpha}}{\hat{k}_{-1,\alpha}} p + \dfrac{\hat{k}_{2,\alpha}}{\hat{k}_{-1,\alpha}} z + \dfrac{\hat{k}_{-2,\alpha}}{\hat{k}_{-1,\alpha}} c}, \tag{3.19b}$$

and the ATP and ADP concentrations are defined by the algebraic equations,

$$a = \frac{\left(\frac{\hat{k}_{1,\alpha}}{\hat{k}_{-1,\alpha}}p + \frac{\hat{k}_{2,\alpha}}{\hat{k}_{-1,\alpha}}z\right)a_{\text{Tot}}}{1 + \frac{\hat{k}_{1,\alpha}}{\hat{k}_{-1,\alpha}}p + \frac{\hat{k}_{2,\alpha}}{\hat{k}_{-1,\alpha}}z + \frac{\hat{k}_{-2,\alpha}}{\hat{k}_{-1,\alpha}}c}, \qquad b = a_{\text{Tot}} - a. \tag{3.19c}$$

The dimensionless OS length is governed by,

$$\frac{d\hat{L}_{\text{OS}}}{dT} = \hat{K}_{\text{grow}} - \hat{\sigma}\left(\hat{L}_{\text{OS}}(T) - \hat{L}^*_{\text{OS}}(T)\right)\text{H}\left(\hat{L}_{\text{OS}}(T) - \hat{L}^*_{\text{OS}}(T)\right), \tag{3.19d}$$

and $\hat{L}^*_{\text{OS}}(T)$ is defined such that $a(\xi, T) = a^*$ for $\xi = \hat{L}^*_{\text{OS}}(T)$. The boundary and initial conditions become, for $y \in \{z,\, c,\, p\}$,

$$\left.\frac{\partial y}{\partial \xi}\right|_{\xi=-1} = 0, \tag{3.19e}$$

$$\hat{D}_Y \left.\frac{\partial y}{\partial \xi}\right|_{\xi=\hat{L}_{\text{OS}}(T)} = -y(\hat{L}_{\text{OS}}(T), T)\frac{d\hat{L}_{\text{OS}}}{dT}, \tag{3.19f}$$

$$y|_{\xi\to 0^-} = y|_{\xi\to 0^+}, \tag{3.19g}$$

$$\left.\frac{\partial y}{\partial \xi}\right|_{\xi\to 0^-} = \left.\frac{\partial y}{\partial \xi}\right|_{\xi\to 0^+}, \tag{3.19h}$$

$$y(\xi, 0) = y_{\text{in}}(\xi), \tag{3.19i}$$

$$\hat{L}_{\text{OS}}(0) = \hat{L}_{\text{OS,in}}. \tag{3.19j}$$

3.2 PARAMETER ESTIMATION

In Table 3.1 we present our parameter estimates, and the corresponding dimensionless parameter values are given in Table 3.2. In the following sections we give details of how each parameter estimate was obtained.

Experimental measurements of concentration are often given in units of mol (g wet weight)$^{-1}$. Since wet weight refers to tissue mass, we can convert from these units to mM by dividing by the density of human tissue. Human tissue has approximately the same density as water, at 1 g (mL)$^{-1}$ [151], since the majority of a human cell consists of water. Therefore, 1 mol (g wet weight)$^{-1}$ = 1×10^6 mM.

Symbol	Parameter	Value	Ref(s)
D_Z, D_C	Diffusion coefficient of CrP, Cr	$2.6 \times 10^{-10}\,\mathrm{m^2\,s^{-1}}$	[124, 150]
D_P	Diffusion coefficient of P	$3.3 \times 10^{-10}\,\mathrm{m^2\,s^{-1}}$	[150]
C_{Tot}	Total concentration of CrP+Cr at each spatial point during darkness	21.4 mM	[149, 151]
P_{Tot}	Total concentration of CrP+P at each spatial point during darkness	21.6 mM	[149, 151, 152]
A_{Tot}	Total concentration of ATP+ADP at each spatial point	3.6 mM	[50, 146–148]
Z_r	Typical CrP concentration	14 mM	[149]
A_r	Typical concentration ATP	1 mM	[50, 146–148]
$k_{1,\mathrm{IS}}$	Rate constant of ATP production by reaction (3.1) in IS	$18\,(\mathrm{mM\,s})^{-1}$	[50, 146, 147]
$k_{1,\mathrm{OS}}$	Rate constant of ATP production by reaction (3.1) in OS	0	[18]
$k_{-1,\mathrm{IS}}$	Rate of ATP breakdown in (3.1) in IS	$210\,\mathrm{s^{-1}}$	[149]
$k_{-1,\mathrm{L}}$	Rate of ATP breakdown in (3.1) in OS under light conditions ($k_{-1,\mathrm{OS}} = 0$ under dark conditions)	$210\,\mathrm{s^{-1}}$	[149]
$k_{2,\mathrm{IS}}$	Rate constant of conversion of ADP+CrP to ATP+Cr by reaction (3.4) in IS	$15\,(\mathrm{mM\,s})^{-1}$	Estimate
$k_{2,\mathrm{OS}}$	Rate constant of conversion of ADP+CrP to ATP+Cr by reaction (3.4) in OS	$15\,(\mathrm{mM\,s})^{-1}$	Estimate
$k_{-2,\mathrm{IS}}$	Rate constant of conversion of ATP+Cr to ADP+CrP by reaction (3.4) in IS	$150\,(\mathrm{mM\,s})^{-1}$	[50, 146, 147]
$k_{-2,\mathrm{OS}}$	Rate constant of conversion of ATP+Cr to ADP+CrP by reaction (3.4) in OS	$150\,(\mathrm{mM\,s})^{-1}$	[50, 146, 147]
K_{grow}	OS growth parameter	$3.2 \times 10^{-5}\,\mu\mathrm{m\,s^{-1}}$	[31]
σ	OS shedding rate (see equation (3.11))	$7.0 \times 10^{-5}\,\mathrm{s^{-1}}$	[36]
A^*	Threshold ATP concentration for shedding	$4.6\,\mu\mathrm{M}$	[130]
L_I	IS length	$32\,\mu\mathrm{m}$	[130]

Table 3.1.: Summary of the dimensional parameters in the phosphocreatine shuttle model (see equations (3.5)–(3.14)), along with their estimated values.

Symbol	Dimensionless parameter	Value
$\hat{D}_Z$, $\hat{D}_C$	Diffusion coefficient of CrP, Cr	0.017
$\hat{D}_P$	Diffusion coefficient of P	0.022
c_{Tot}	Total concentration of CrP+Cr at each spatial point during darkness	1.5
p_{Tot}	Total concentration of CrP+P at each spatial point during darkness	1.5
a_{Tot}	Total concentration of ATP+ADP at each spatial point	3.6
$\hat{k}_{1,\text{IS}}$	Rate constant of ATP production by reaction (3.1) in IS	1.2
$\hat{k}_{1,\text{OS}}$	Rate constant of ATP production by reaction (3.1) in OS	0
$\hat{k}_{-1,\text{IS}}$	Rate of ATP breakdown by reaction (3.1) in IS	1
$\hat{k}_{-1,\text{L}}$	Rate of ATP breakdown by reaction (3.1) in OS under light conditions	1
$\hat{k}_{2,\text{IS}}$	Rate constant of conversion of ADP+CrP to ATP+Cr by reaction (3.4) in IS	1
$\hat{k}_{2,\text{OS}}$	Rate constant of conversion of ADP+CrP to ATP+Cr by reaction (3.4) in OS	1
$\hat{k}_{-2,\text{IS}}$	Rate constant of conversion of ATP+Cr to ADP+CrP by reaction (3.4) in IS	10
$\hat{k}_{-2,\text{OS}}$	Rate constant of conversion of ATP+Cr to ADP+CrP by reaction (3.4) in OS	10
$\hat{K}_{\text{grow}}$	OS growth parameter	6.7×10^{-8}
$\hat{\sigma}$	OS shedding rate (see equation (3.19d))	4.7×10^{-6}
a^*	Threshold ATP concentration for shedding	4.6×10^{-3}

Table 3.2.: Summary of dimensionless parameter values in the phosphocreatine shuttle model defined by equations (3.19c)–(3.19i).

Diffusion Coefficients of Creatine Phosphate, Creatine and Free Phosphate (D_Z, D_C, D_P)

Estimates of the diffusion coefficients and typical concentrations of CrP, Cr and P are available from experimental measurements in muscle cells [153]. We assume the diffusion coefficients and typical concentrations are similar to those in photoreceptors, since both cell types contain many obstacles to diffusion (e.g. protein-protein interactions), and have a high energy demand so that Cr and CrP play an important role in the cellular ATP supply.

Our estimates of D_Z, D_C and D_P are taken from the work of Vendelin et al. [124], in which the diffusion coefficients are found to be D_Z, $D_C \approx 2.6 \times 10^{-10}\,\mathrm{m^2\,s^{-1}}$ and $D_P \approx 3.3 \times 10^{-10}\,\mathrm{m^2\,s^{-1}}$.

Typical Concentrations of Creatine Phosphate and ATP (Z_r, A_r)

Green et al. [149] and Smith et al. [152] made *in vivo* measurements of the resting CrP, Cr and P concentrations in human skeletal muscle cells. We assume that the parameters of the phosphocreatine shuttle under resting conditions in human skeletal muscle and dark conditions in photoreceptors are similar. Phototransduction does not occur in the OS under dark conditions, meaning a reduced energy requirement that can be met by glycolysis alone. Thus, there is no need for CrP breakdown to produce ATP, leading to a higher CrP (and lower Cr) concentration under dark conditions than during light conditions. In resting muscle cells, activity is also minimal, so there is little need to derive ATP from CrP [149, 152].

Based on this argument, we estimate that the concentrations of CrP, Cr and P in the photoreceptor under dark conditions are the same as those measured in resting skeletal muscle, $Z_{\mathrm{rest}} \approx 17 \times 10^{-3}\,\mathrm{mol\,(kg\ wet\ weight)^{-1}}$, $C_{\mathrm{rest}} \approx 4.4 \times 10^{-3}\,\mathrm{mol\,(kg\ wet\ weight)^{-1}}$ [149] and $P_{\mathrm{rest}} \approx 4.6 \times 10^{-3}\,\mathrm{mol\,(kg\ wet\ weight)^{-1}}$ [152], or $Z_{\mathrm{rest}} \approx 17\,\mathrm{mM}$, $C_{\mathrm{rest}} \approx 4.4\,\mathrm{mM}$ and $P_{\mathrm{rest}} \approx 4.6\,\mathrm{mM}$. We therefore find that the total concentrations of CrP+Cr and of CrP+P at each spatial point during darkness are given by $\mathrm{C_{Tot}} = \mathrm{CrP} + \mathrm{Cr} \approx 21.4\,\mathrm{mM}$ and $\mathrm{P_{Tot}} = \mathrm{CrP} + \mathrm{P} \approx 21.6\,\mathrm{mM}$ respectively.

The energy demand of the photoreceptor OS is greater under light conditions than dark, and thus so is the activity of the phosphocreatine shuttle. Assuming that the distributions of CrP, Cr and P in photoreceptors under light conditions are approximately the same as in skeletal muscle cells at maximum activity during exercise, we estimate that a typical CrP concentration under light

conditions is $Z_{\max} \approx 9.5\,\text{mM}$ [149]. To represent a typical CrP concentration in a photoreceptor cell, we take the mean of the typical CrP concentrations under dark and light conditions, giving $Z_r = 14\,\text{mM}$.

The ATP concentration in photoreceptors is approximately 1.0 mM [50, 146, 147]. According to Notari et al. [154], the ratio of the ADP to ATP concentration in photoreceptor outer segments is approximately 2.3 and 2.8 under light and dark conditions respectively. Accordingly, we assume that the time averaged ratio of the ADP to ATP concentration in photoreceptors is approximately 2.6, giving a typical ADP concentration of 2.6 mM and a typical A_{Tot} of 3.6 mM.

Reaction Rates and Rate Constants within the Inner and Outer Segments ($k_{1,\alpha}$, $k_{-1,\alpha}$, $k_{2,\alpha}$, $k_{-2,\alpha}$)

Here we estimate the rate constant for ATP production by the mitochondria ($k_{1,\alpha}$), the rate of its breakdown to produce energy ($k_{-1,\alpha}$) via reaction (3.1), and the rate constants for conversion of ADP+CrP into ATP+Cr ($k_{2,\alpha}$), and vice versa ($k_{-2,\alpha}$) by reaction (3.4). We established in §3.1 that $k_{1,\text{OS}} = 0$, and under dark conditions $k_{-1,\text{OS}} = 0$ (see equations (3.2) and (3.3)). To test our hypothesis that the sole regulator for OS length is phosphocreatine-derived ATP, we make the assumption that, apart from the distinct values in the inner and outer segments of $k_{1,\alpha}$, and of $k_{-1,\alpha}$ under dark conditions, the other rate constants do not differ between the IS and OS, i.e.,

$$k_{-1,\text{OS}} = \begin{cases} k_{-1,\text{IS}} = k_{-1,\text{L}} & \text{light conditions,} \\ 0 & \text{dark conditions,} \end{cases},$$

$$k_{2,\text{OS}} = k_{2,\text{IS}}, \qquad k_{-2,\text{OS}} = k_{-2,\text{IS}}.$$

In particular, we neglect the dark current in this model. As discussed in Chapter 2, in practice the dark current consumes energy during dark conditions, which would increase $k_{-1,\text{IS}}$ during darkness. However, our objective is to test whether OS length may be regulated by the ability of the phosphocreatine shuttle to transfer energy, rather than whether the energy level is itself limiting.

We take $k_{1,\text{IS}}$ to be the rate constant of ATP production via oxidative metabolism in the IS, assuming that all mitochondrial-derived ATP under light conditions is available to combine with creatine phosphate, and constitutes the majority of

such available ATP. From §2.3, the rate of oxygen consumption by mitochondria in the photoreceptor IS under light conditions is approximately $1.1\,\mathrm{s}^{-1}$. Multiplying this by a typical oxygen concentration, $28\,\mu\mathrm{M}$ (see §2.3) gives the concentration of oxygen consumed by oxidative metabolism per unit time, i.e. approximately $30\,\mu\mathrm{M\,s}^{-1}$. The corresponding ATP concentration produced per unit time is five times larger than this (since oxidative metabolism yields approximately 5 molecules of ATP per oxygen molecule), and is equivalent to the value of $k_{1,\mathrm{IS}}BP$ in our model. Taking typical concentrations of free phosphate and ADP to be P_{rest} and $A_{\mathrm{Tot}}/2$ respectively we obtain $k_{1,\mathrm{IS}} = 18\,(\mathrm{mM})^{-1}\mathrm{s}^{-1}$.

For $k_{2,\alpha}$ we use Bittl and Ingwall's measurement of $1\,\mathrm{s}^{-1}$ which is equivalent to $k_{2,\alpha}/Z_r$ in our model. Multiplying this by $Z_r = 14\,\mathrm{mM}$, we obtain $k_{2,\alpha} = 14\,\mathrm{mM\,s}^{-1}$. We infer the values of parameters $k_{-2,\mathrm{OS}}$ and $k_{-1,\mathrm{IS}}$ from their effects on the steady state ATP concentration. Given that $k_{1,\mathrm{OS}} = k_{-1,\mathrm{OS}} = 0$ under dark conditions, the expression in (3.19c), for the dimensionless ATP concentration, a, becomes,

$$a = \begin{cases} \dfrac{\left(\frac{\hat{k}_{1,\mathrm{IS}}}{\hat{k}_{-1,\mathrm{IS}}}p + \frac{1}{\hat{k}_{-1,\mathrm{IS}}}z\right)a_{\mathrm{Tot}}}{1 + \frac{\hat{k}_{1,\mathrm{IS}}}{\hat{k}_{-1,\mathrm{IS}}}p + \frac{1}{\hat{k}_{-1,\mathrm{IS}}}z + \frac{\hat{k}_{-2,\mathrm{IS}}}{\hat{k}_{-1,\mathrm{IS}}}c}, & \text{if } -1 \le \xi \le 0, \\ \dfrac{z a_{\mathrm{Tot}}}{z + \hat{k}_{-2,\mathrm{OS}}c}, & \text{if } 0 < \xi \le \hat{L}_{\mathrm{OS}}(T). \end{cases} \tag{3.20}$$

We substitute our estimated values for Z_{rest}/Z_r, C_{rest}/Z_r and P_{rest}/Z_r (corresponding to dark conditions) for z, c and p, and choose the value of dimensionless parameter $\hat{k}_{-2,\mathrm{OS}}$ such that $a = 1$ (and therefore $A = A_r$) in the OS, which gives,

$$\hat{k}_{-2,\mathrm{OS}} = \frac{z}{c}\left(a_{\mathrm{Tot}} - 1\right) \approx 10. \tag{3.21}$$

We then set $a = 1$ in the IS and substitute $\hat{k}_{1,\mathrm{IS}} = k_{1,\mathrm{IS}}/k_{2,\mathrm{IS}}$, $\hat{k}_{-2,\mathrm{IS}} = \hat{k}_{-2,\mathrm{OS}}$, and our estimates for z, c and p, to obtain the value of the dimensionless parameter $\hat{k}_{-1,\mathrm{IS}}$,

$$\hat{k}_{-1,\mathrm{IS}} = \left(\hat{k}_{1,\mathrm{IS}}p + z\right)a_{\mathrm{Tot}} - \hat{k}_{1,\mathrm{IS}}p - z - \hat{k}_{-2,\mathrm{IS}}c \approx 1. \tag{3.22}$$

This choice of parameters guarantees that values of CrP, Cr and P concentrations under dark conditions match our estimated values.

Rates of Growth and Shedding of the Outer Segment, and Threshold ATP Concentration for Shedding (K_{grow}, σ, A^*)

We established in §2.1 that the OS sheds and replaces approximately 2.8 μm of its length per day. Therefore, the average OS growth rate in dark conditions, K_{grow}, is approximately $3.2 \times 10^{-5}\,\mu\text{m}\,\text{s}^{-1}$.

The shedding rate of the OS is represented by σ, and A^* denotes the ATP concentration below which the OS discs cease to be viable. Neither of these quantities is directly measurable. We therefore infer their values using the following information. Firstly, we take the measured OS length in [130] (28 μm) to be the time-averaged OS length. Secondly, LaVail [36] found that the number of phagosomes in the rat RPE was elevated after the onset of light conditions, with a peak approximately 2 hours after light onset. These phagosomes are indicative of RPE cell phagocytosis of the OS discs that have been shed.

Since we have estimates for the values of all other parameters in our model, the values of σ and A^* can be inferred from these two pieces of information, by adjusting the values of these parameters in our simulations until the time-averaged OS length predicted by our model is approximately 28 μm and that the period in which OS disc shedding occurs lasts approximately 2 hours, giving estimated values of $\sigma = 10^{-4}\,\text{s}^{-1}$ and $A^* = 4.6 \times 10^{-3}\,\text{mM}$ respectively.

3.3 SOLUTION TECHNIQUES

Using the same technique as in §2.4, we construct numerical solutions by mapping the governing equations given in (3.5)–(3.14) onto a fixed domain and discretising using the Method of Lines, to produce a system of time-dependent ODEs, which can be integrated using a standard ODE solver. This treatment yields the following discretised system,

$$\frac{dy_i}{ds} = \hat{D}_Y F_{\text{FD}}(y_i) + \frac{\rho_i}{\hat{L}_{\text{OS}}} \text{H}\left(\rho_i\right) \frac{d\hat{L}_{\text{OS}}}{ds} F_{\text{UW}}(y_i) + \hat{v}_{Y,i}, \tag{3.23a}$$

where we use the centred finite difference ($F_{\text{FD}}(y_i)$) and upwind ($F_{\text{UW}}(y_i)$) discretisation schemes for the same reasons as in §2.4,

$$\frac{d\hat{L}_{\text{OS}}}{ds} = \hat{K}_{\text{grow}} - \hat{\sigma}\left(1 - \frac{\hat{L}^*_{\text{OS}}(s)}{\hat{L}_{\text{OS}}(s)}\right) \text{H}\left(1 - \frac{\hat{L}^*_{\text{OS}}(s)}{\hat{L}_{\text{OS}}(s)}\right), \tag{3.23b}$$

$$y_1 = \tilde{y}_{-1}, \tag{3.23c}$$

$$\frac{\tilde{y}_{n+m+1} - y_{n+m-1}}{2\hat{L}_{\mathrm{OS}}\Delta\rho_{\mathrm{OS}}} = 0, \tag{3.23d}$$

$$\frac{\tilde{y}_{n+1} - y_{n-1}}{2\Delta\rho_{\mathrm{IS}}} = \frac{y_{n+1} - \tilde{y}_{n-1}}{2\hat{L_{\mathrm{OS}}}\Delta\rho_{\mathrm{OS}}}, \tag{3.23e}$$

$$y_i(0) = y_{i,\mathrm{in}}, \tag{3.23f}$$

$$\hat{L}_{\mathrm{OS}}(0) = \hat{L}_{\mathrm{OS,in}}, \tag{3.23g}$$

where variables and parameters are defined in §3.1.4,

$$\hat{v}_i = \frac{\left(\frac{\hat{k}_{1,\alpha}\hat{k}_{-2,\alpha}}{\hat{k}_{-1,\alpha}} c_i p_i - \hat{k}_{2,\alpha} z_i\right) a_{\mathrm{Tot}}}{1 + \frac{\hat{k}_{1,\alpha}}{\hat{k}_{-1,\alpha}} p_i + \frac{\hat{k}_{2,\alpha}}{\hat{k}_{-1,\alpha}} z_i + \frac{\hat{k}_{-2,\alpha}}{\hat{k}_{-1,\alpha}} c_i}, \tag{3.23h}$$

the ATP concentration is given by,

$$a_i(s) = \frac{\left(\frac{\hat{k}_{1,\alpha}}{\hat{k}_{-1,\alpha}} p_i + \frac{\hat{k}_{2,\alpha}}{\hat{k}_{-1,\alpha}} z_i\right) a_{\mathrm{Tot}}}{1 + \frac{\hat{k}_{1,\alpha}}{\hat{k}_{-1,\alpha}} p_i + \frac{\hat{k}_{2,\alpha}}{\hat{k}_{-1,\alpha}} z_i + \frac{\hat{k}_{-2,\alpha}}{\hat{k}_{-1,\alpha}} c_i}, \tag{3.23i}$$

and $\hat{L}^*_{\mathrm{OS}}(s)$ fulfils the following condition,

$$a_i(s) = a^*, \text{ for } \rho_i = \frac{\hat{L}^*_{\mathrm{OS}}(s)}{\hat{L}_{\mathrm{OS}}(s)},$$

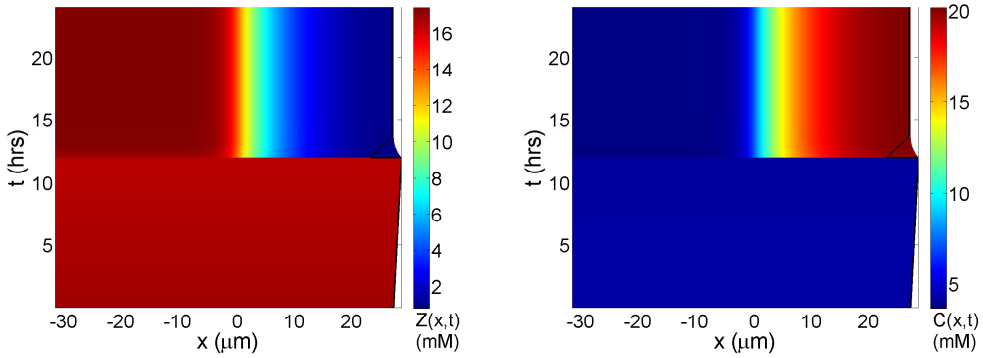
noting that boundary condition (3.19g) is met automatically since z_n, c_n and p_n are single-valued. Applying the boundary conditions gives,

$$\frac{dy_i}{ds} = \begin{cases} 2\hat{D}_Y \dfrac{y_1 - y_0}{(\Delta\rho_{\mathrm{IS}})^2} + \hat{v}_{Y,0}, & \text{for } i = 0, \\ \hat{D}_Y F_{\mathrm{FD}}(y_i) + \hat{v}_{Y,i}, & \text{for } 1 \leq i < n, \\ \left(1 + \dfrac{1}{\hat{L}_{\mathrm{OS}}} \dfrac{\Delta\rho_{\mathrm{IS}}}{\Delta\rho_{\mathrm{OS}}}\right)^{-1} \left\{ \dfrac{2\hat{D}_Y}{\hat{L}_{\mathrm{OS}}^2 (\Delta\rho_{\mathrm{OS}})^2} \left[y_{n+1} \right.\right. & \\ \quad \left.\left. + \dfrac{\hat{L}_{\mathrm{OS}} \Delta\rho_{\mathrm{OS}}}{\Delta\rho_{\mathrm{IS}}} (y_{n-1} - y_n) \right] + \hat{v}_Y \right\} & \text{for } i = n, \\ \hat{D}_Y F_{\mathrm{FD}}(y_i) + \dfrac{\rho_i}{\hat{L}_{\mathrm{OS}}} \dfrac{d\hat{L}_{\mathrm{OS}}}{ds} F_{\mathrm{UW}}(y_i) + \hat{v}_{Y,i} & \text{for } n+1 \leq i \\ & \qquad \leq n + m - 1, \\ 2 \dfrac{\hat{D}_Y}{\hat{L}_{\mathrm{OS}}^2 (\Delta\rho_{\mathrm{OS}})^2} \left(y_{n+m-1} - y_{n+m} \right) + \hat{v}_{Y,n+m} & \\ \quad + \dfrac{1}{\hat{L}_{\mathrm{OS}} \Delta\rho_{\mathrm{OS}}} \dfrac{d\hat{L}_{\mathrm{OS}}}{ds} (y_{n+m-1} - y_{n+m}) \operatorname{sign}\left(\dfrac{d\hat{L}_{\mathrm{OS}}}{ds} \right) & \text{for } i = n + m, \end{cases} \tag{3.24}$$

with the OS length given by equation (3.23b) and initial conditions given by equations (3.23f) and (3.23g). Since our discretised system yields $n + m + 1$ ODEs for each concentration, CrP, Cr and P, and a separate equation governs the time evolution of the OS length, $\hat{L}_{\mathrm{OS}}$, the above system comprises $3n + 3m + 4$ coupled equations. This system, like the oxygen model, involves multiple very different timescales, and is therefore stiff (see §2.4), so we use a numerical solver for stiff ODEs [141].

3.4 NUMERICAL RESULTS

We consider a 24-hour period comprising 12 hours of dark conditions followed by 12 hours of light, using the same protocol as in §2.5, with initial conditions set to the long time solution in light conditions (determined by running simulations under light conditions until the time evolution of each dependent variable is below a chosen tolerance). In Figure 3.3 we present results from a typical simulation, showing that the OS length settles to a steady state approximately two hours after the onset of light conditions, but grows linearly under dark conditions.



(a) $Z(x,t)$ (b) $C(x,t)$

(c) $P(x,t)$ (d) $A(x,t)$

Figure 3.3.: Spatiotemporal distribution of the (a) creatine phosphate (b) creatine, (c) free phosphate, and (d) ATP concentrations in a photoreceptor over 12 hours of dark conditions followed by 12 hours of light, according to the phosphocreatine shuttle model, defined by equations (3.5)–(3.14). The solid black line in each panel represents $L^*_{\mathrm{OS}}(t)$. The model predicts that the outer segment shortens until a steady state length is reached under light conditions, and grows linearly throughout the 12 hour period of dark conditions. For parameter values see Table 3.1.

During light stimulation, the OS requires energy for phototransduction. This activates the breakdown of ATP into ADP and free phosphate in the OS via the reverse reaction in (3.1). Hence, the ATP concentration decreases from the inner to the outer end of the photoreceptor, and $A < A^*$ at the end of the OS. As a result, the shedding term in equation (3.11) switches on, $dL_{\mathrm{OS}}/dt < 0$, and the OS shortens until a steady state is reached when the growth and shedding terms balance. The lowered ATP concentration in the OS under light conditions means that ATP production from CrP and ADP via the reverse reaction in (3.4) increases, reducing the concentration of CrP and increasing the Cr levels in the OS. Furthermore, the concentration of free phosphate is increased in the OS due to the increased rate of ATP breakdown there. This explains the direction of the concentration gradients of CrP, Cr and P under light conditions, shown in Figures 3.3(a)–(d). At the IS-OS boundary, the ATP concentration predicted by our simulations is discontinuous (see Figure 3.3(d)). This is permissible since we assume no ATP diffusion. Moreover, we note that at the onset of light conditions all concentrations evolve rapidly but continuously.

Under dark conditions, the reverse reaction in (3.1) switches off, the concentration of ATP in the OS increases and, for our estimated parameter values, $A > A^*$ throughout the OS. The shedding term in equation (3.11) switches off and $L_{\mathrm{OS}}(t)$ grows linearly until the onset of light conditions, with an OS length at dimensionless time T_{D} after the onset of dark conditions given by,

$$\hat{L}_{\mathrm{OS}}(T_{\mathrm{D}}) = \hat{L}_{\mathrm{OS}}(0) + \hat{K}_{\mathrm{grow}} T_{\mathrm{D}}. \tag{3.25}$$

It is possible to obtain an implicit expression for the steady state OS length under light conditions, $\hat{L}_{\mathrm{OS,SS}}$. Setting $d\hat{L}_{\mathrm{OS}}/dT$ to zero in equation (3.19d) yields,

$$\hat{L}_{\mathrm{OS,SS}} = \hat{L}^*_{\mathrm{OS,SS}} + \frac{\hat{K}_{\mathrm{grow}}}{\hat{\sigma}}, \tag{3.26}$$

where $\hat{L}^*_{\mathrm{OS,SS}}$ depends on the concentrations z_{SS}, c_{SS} and p_{SS}, which, in turn, depend on $\hat{L}_{\mathrm{OS,SS}}$. Substituting realistic parameter estimates into (3.26), we obtain $\hat{L}^*_{\mathrm{OS,SS}} \approx 0.829$ as found numerically. Since $\hat{K}_{\mathrm{grow}}/\hat{\sigma} \approx 0.0144 \ll \hat{L}^*_{\mathrm{OS,SS}}$,

$$\hat{L}_{\mathrm{OS,SS}} \approx \hat{L}^*_{\mathrm{OS,SS}}, \tag{3.27}$$

and at the steady state $a \approx a^*$ at the outer end of the OS.

For long periods of continuous darkness, our model simulations predict that the photoreceptor grows indefinitely. Continuous photoreceptor growth is unrealistic, allowing the photoreceptor to become infinitely long. Thus the model loses validity during prolonged periods of darkness. Figures 3.3(a)–(c) suggest that during prolonged darkness, the spatial distributions of CrP, Cr and P become approximately uniform. Therefore, to analyse the behaviour in this regime, we consider the system while the OS is growing linearly at rate $\hat{K}_{\text{grow}}$ (i.e. there is no shedding) a period of time after the onset of dark conditions (under dark conditions, $k_{1,\text{OS}} = k_{-1,\text{OS}} = 0$ and $\hat{v} = 0$ in the OS (see equation (3.19b))). Using the dimensionless model mapped onto a fixed domain during dark conditions, since $k_{1,\text{OS}} = k_{-1,\text{OS}} = 0$ and $\hat{v} = 0$ in the OS (see equation (3.19b)) the system becomes, for $y \in \{z,\, c,\, p\}$,

$$\frac{\partial y}{\partial s} = \hat{D}_Y \left(\mathrm{H}(-\rho) + \frac{1}{\hat{L}_{\text{OS}}^2} \mathrm{H}(\rho) \right) \frac{\partial^2 y}{\partial \rho^2} + \frac{\rho}{\hat{L}_{\text{OS}}} \hat{K}_{\text{grow}} \frac{\partial y}{\partial \rho} \mathrm{H}(\rho) + \hat{v}_Y \mathrm{H}(-\rho), \tag{3.28a}$$

$$\hat{L}_{\text{OS}}(s) = \hat{L}_{\text{OS,in}} + \hat{K}_{\text{grow}} s, \tag{3.28b}$$

$$\left. \frac{\partial y}{\partial \rho} \right|_{\rho=-1} = 0, \tag{3.28c}$$

$$\left. \frac{\partial y}{\partial \rho} \right|_{\rho=1} = 0, \tag{3.28d}$$

$$y|_{\rho \to 0^-} = y|_{\rho \to 0^+}, \tag{3.28e}$$

$$\left. \frac{\partial y}{\partial \rho} \right|_{\rho \to 0^-} = \frac{1}{\hat{L}_{\text{OS}}} \left. \frac{\partial y}{\partial \rho} \right|_{\rho \to 0^+}, \tag{3.28f}$$

$$y(\rho, 0) = y_{\text{in}}(\rho). \tag{3.28g}$$

Based on Figures 3.3(a)–(c), we suppose that, following a period of prolonged darkness, the spatial distributions of CrP, Cr and P are approximated by $y(\rho, s) \approx y_0(s)$ for $y \in \{z,\, c,\, p\}$. Substituting this ansatz into (3.28) implies that the concentrations approach a quasisteady state for which $\hat{v}_Y = 0$ in the IS (in the OS, $\hat{v}_Y = 0$ under dark conditions by definition), i.e. using equation (3.19b),

$$\frac{z_0(s)}{c_0(s) p_0(s)} \approx \frac{\hat{k}_{1,\text{IS}} \hat{k}_{-2,\text{IS}}}{\hat{k}_{-1,\text{IS}} \hat{k}_{2,\text{IS}}}. \tag{3.29}$$

The corresponding ATP concentration is given by equation (3.20). In particular, the ATP concentration at $\rho = 1$ (i.e. $x = L_{\mathrm{OS}}(t)$) is,

$$a|_{\rho=1} = \frac{a_{\mathrm{Tot}}\, z_0}{z_0 + \hat{k}_{-2,\alpha} c}. \tag{3.30}$$

Once the concentrations in the IS satisfy equation (3.29), the following argument applies. There is no flux of CrP, Cr or P through into/out of the photoreceptor, and almost no conversion between CrP, Cr or P. Thus the mass of CrP, Cr and P, given by,

$$m_y = \int_{-1}^{0} y_{\mathrm{in}}(\rho)\, d\rho + \int_{0}^{1} y_{\mathrm{in}}(\rho) \hat{L}_{\mathrm{OS,in}}\, d\rho$$

($y \in \{z, c, p\}$), is approximately conserved, such that,

$$y_0(s) \approx \frac{m_y}{1 + \hat{L}_{\mathrm{OS}}(s)}.$$

Combining this with equation (3.30) gives, for the ATP concentration at $\rho = 1$,

$$a|_{\rho=1} = \frac{a_{\mathrm{Tot}} m_z}{m_z + \hat{k}_{-2,\alpha} m_c},$$

for which the time variation is negligible. Hence, if the ATP concentration at the outer end of the OS exceeds a^* at any time during dark conditions, then it does so indefinitely, hence the shedding term in equation (3.19d) remains at zero and the OS grows linearly at rate $\hat{K}_{\mathrm{grow}}$. Since our model exhibits linear OS growth during the first 12 hours of dark conditions, this indicates that the rate of OS growth remains linear indefinitely if dark conditions persist. In our simulations, taking two representative times $s_1 = 6\,\mathrm{hrs}/T_0$ and $s_2 = 11.9\,\mathrm{hrs}/T_0$, at $s = s_1$, the CrP, Cr and P concentrations predicted by our model are spatially uniform at 16.65 mM, 4.26 mM and 4.53 mM respectively, while at $s = s_2$, they are spatially uniform at 16.44 mM, 4.23 mM and 4.50 mM respectively (see Figures 3.3(a)–(b)). Therefore, both at $s = s_1$ and at $s = s_2$, $z/cp = Z_r Z/CP = 12.0$. From our parameter values in Table 3.2, the value of $\hat{k}_{1,\mathrm{IS}}\hat{k}_{-2,\mathrm{IS}}/(\hat{k}_{-1,\mathrm{IS}}\hat{k}_{2,\mathrm{IS}})$ is 12.0. Thus, the CrP, Cr and P concentrations predicted by our simulations fulfil equation (3.29). Further, substituting these concentrations into equation (3.30) gives, at both $s = s_1$ and $s = s_2$, $a|_{\rho=1} = 0.28 > a^*$. From our simulations the ATP concentration at the outer end of the OS remains constant in time at

1.00 mM (see Figure 3.3(d)) which, divided by A_{Tot}, is 0.28, consistent with the value found analytically.

In summary, our model exhibits OS growth under dark conditions and shedding during light ones, consistent with experimental findings. However, the predicted indefinite growth during prolonged dark conditions is physically unrealistic. We conclude based on our results that the phosphocreatine shuttle may regulate OS length in light conditions but not under dark conditions. As we will show later in this chapter, by combining the model of the phosphocreatine shuttle with our model of oxygen-based regulation of OS length (see Chapter 2), it is possible to achieve appropriate regulation of OS length in both light and dark conditions.

3.5 PARAMETER SENSITIVITY

To gain further insight into how the phosphocreatine shuttle may regulate the photoreceptor OS length and possible causes of retinal disease, we study the sensitivity of our model to changes in parameter values.

We concluded in §3.4 that, for our estimates of realistic parameter values, the phosphocreatine shuttle model predicts the observed diurnal variation in photoreceptor OS length, with growth under dark conditions and shedding in light ones. However if the ATP concentration at the outer end of the OS exceeds A^* at any time during dark conditions, provided that $K_{\text{grow}} > 0$, the OS grows indefinitely thereafter, for as long as dark conditions persist. Conversely, if the ATP concentration is lower than A^* at all times during dark conditions, then no growth occurs during darkness. In either case, the OS length does not exhibit the observed variation during prolonged darkness, indicating that different parameter choices would not enable it to do so. These facts indicate that the phosphocreatine shuttle may be the regulator for the OS length during light conditions, but another regulatory mechanism must play a significant role in dark conditions, preventing indefinite growth. A potential candidate for the OS length regulation under dark conditions is the oxygen concentration, as demonstrated in Chapter 2.

At the steady state in light conditions, the spatial point, $L^*_{\text{OS,SS}}$, at which the ATP concentration passes below the threshold A^*, is very close to the outer end of the OS. Hence in equation (3.26) $L_{\text{OS,SS}} \approx L^*_{\text{OS,SS}}$ and the OS length is very insensitive to changes in the parameters K_{grow} and σ. The parameters that

affect $L^*_{\mathrm{OS,SS}}$ are the most important ones in OS length regulation. The value of $L^*_{\mathrm{OS,SS}}$ depends on the ATP concentration in the OS, which, via equation (3.19a), depends on the concentrations of CrP, Cr, P and parameters $k_{1,\alpha}$, $k_{-1,\alpha}$ and $k_{-2,\alpha}$. The CrP, Cr and P concentrations depend on the diffusion coefficients D_Z, D_C and D_P (and the OS length) as well as $k_{1,\alpha}$, $k_{-1,\alpha}$ and $k_{-2,\alpha}$. Although the following discussion refers to the steady state OS length under light conditions, using equation (3.25), the OS length after 12 hours of dark conditions has the same qualitative variation with each parameter, except for K_{grow}, with which it linearly increases.

Figure 3.4(a) shows that increasing $k_{1,\mathrm{IS}}$ or decreasing A^* leads to a longer OS. Since $k_{1,\mathrm{IS}}$ denotes the rate of ATP production in the IS, increasing this parameter increases the overall amount of ATP in the photoreceptor. Consequently, the ATP concentration at the outer end of the OS is larger relative to the threshold level A^*, reducing the distance over which $A < A^*$, leading to a lower shedding rate and hence a longer OS once a steady state is reached. The same effect is achieved by decreasing the value of A^*.

Figure 3.4(b) illustrates the variation of $L_{\mathrm{OS,SS,L}}$ with the parameters $k_{-2,\mathrm{IS}}$ and $k_{-2,\mathrm{OS}}$. These are the rate constants of the conversion of Cr and ATP to CrP and ADP via the forward reaction in (3.4), in the IS and OS respectively. Increasing the value of $k_{-2,\mathrm{IS}}$ and $k_{-2,\mathrm{OS}}$ leads to higher CrP concentrations and lower Cr and P concentrations in the IS and OS respectively (see equations (3.19a)). The effects of increasing $k_{-2,\mathrm{IS}}$ in the IS are transferred to the OS as CrP, Cr and P diffuse. Hence a larger value of either $k_{-2,\mathrm{IS}}$ or $k_{-2,\mathrm{OS}}$ means that CrP concentrations rise and Cr and P concentrations fall in the OS. According to the first equation in (3.19c), the elevated CrP and lowered Cr levels in the OS increase the ATP concentration there (the decreased P levels in the OS have no effect on the ATP concentration since $k_{1,\mathrm{OS}} = 0$). The increased ATP concentration in the OS is more likely to exceed the threshold value A^*, and thus the OS lengthens when $k_{-2,\mathrm{IS}}$ and/or $k_{-2,\mathrm{OS}}$ is increased.

The effects of varying the diffusion coefficients of CrP and Cr are illustrated in Figure 3.4(c). Increasing D_Z enables CrP to travel more quickly from the IS to the OS, raising the CrP concentration in the OS, which then increases the Cr concentration there. The increased CrP concentration leads to an increase in ATP production in the OS while the increased Cr concentration lowers the ATP production. These two effects compete but overall the ATP production

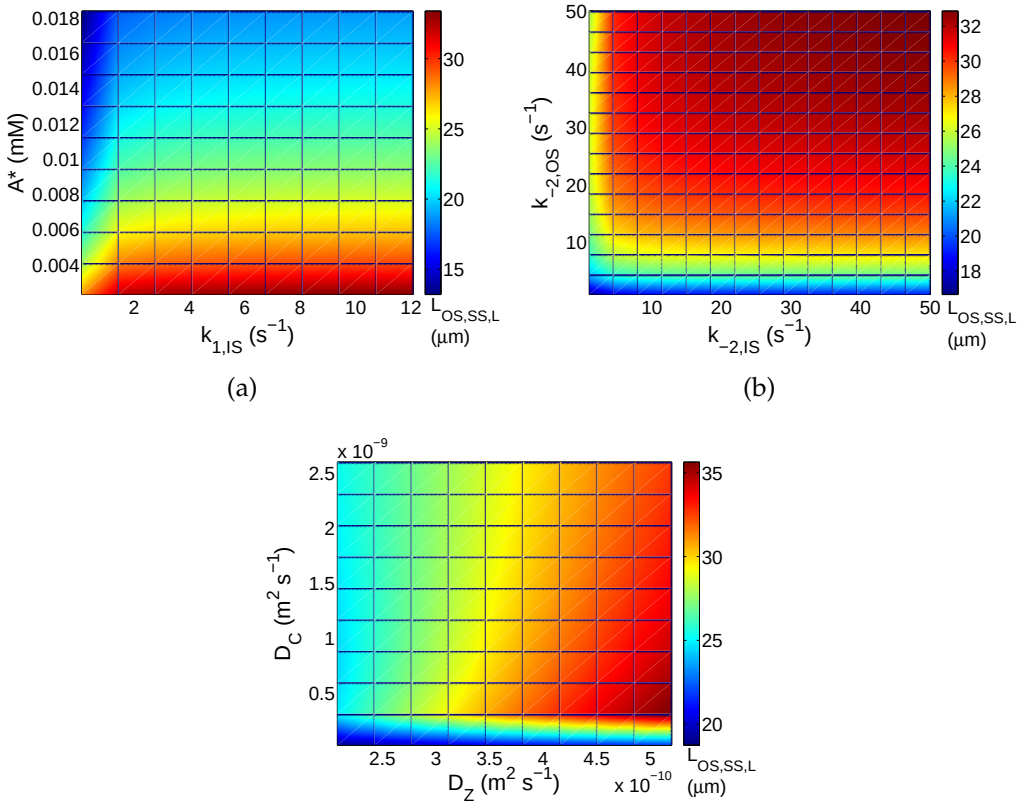


Figure 3.4.: Parameter sensitivity of the steady state outer segment length under light conditions predicted by the phosphocreatine shuttle model, defined by equations (3.5)–(3.14), to (a) the rate constant of ATP production from ADP+P in the mitochondria within the inner segment, $k_{1,\mathrm{IS}}$, and the threshold ATP concentration for shedding, A^*, (b) the rate constants of the conversion of Cr+ATP to CrP+ADP in the inner and outer segments, $k_{-2,\mathrm{IS}}$ and $k_{-2,\mathrm{OS}}$ respectively, and (c) the diffusion coefficients of creatine phosphate and creatine, D_Z and D_C respectively. All other parameter values are taken from Table 3.1.

rate increases for the range of D_Z shown in Figure 3.4(c), meaning greater ATP levels in the OS and hence a longer steady state OS length.

A larger value of D_C flattens the spatial Cr profile through the photoreceptor, raising the Cr concentration in the IS and lowering it in the OS. This also lowers the CrP concentration in the OS. Since the ATP levels in the OS increase with local CrP levels and decrease with local Cr levels, the reduction in the CrP and Cr concentrations have competing effects on the ATP concentration. For small values of D_C, the effects of the lowered Cr concentration outweigh those of the lowered CrP concentration, meaning that an increase in D_C raises the ATP levels in the OS and hence the OS length. For higher values of D_C, the effect of the lowered CrP concentration dominates, meaning that increasing D_C shortens the OS.

3.6 DISCUSSION OF PHOSPHOCREATINE SHUTTLE MODEL

To investigate whether OS length is regulated by the ATP available to OS discs, we have developed a mathematical model of the concentration distributions of CrP, Cr and P in the rod photoreceptor. We have used this model to examine how these concentrations affect the OS length.

As far as possible, we ensured that physiologically realistic parameter values were used in our model. However, there are some parameters that are not directly measurable in experiments, for instance, the threshold ATP concentration for shedding, A^* and the rate constant for disc shedding, σ. The values of these parameters were inferred from the measured OS length and the time at which phagosomes (indicators of disc shedding) were produced. Their values were set in our simulations such that our model yielded the observed OS length and timescale for shedding. However, the majority of parameter values in the model are taken from direct measurements.

According to our model results, the system reaches a steady state in light but not dark conditions, indicating that the phosphocreatine shuttle may regulate the length of the OS in light conditions but not dark. However, in the previous chapter, we found that oxygen may regulate OS growth in dark conditions, so we expect that combining both models will produce a model that can control OS length in both light and dark conditions.

3.7 OXYGEN AND THE PHOSPHOCREATINE SHUTTLE AS DETERMINANTS OF ROD PHOTORECEPTOR LENGTH

Our conclusion based on Chapter 2 and §3.1–§3.6 of this chapter is that photoreceptor length may be regulated by oxygen levels under dark conditions and the availability of phosphocreatine shuttle-derived ATP during light conditions. In this section we test these predictions by combining the models from §2.1 and §3.1, and investigate the diurnal variation of the OS length assuming that it is regulated by both oxygen and phosphocreatine shuttle-derived ATP.

3.7.1 *Model Development*

We combine the PDEs of the oxygen model in §2.1 with those of the phosphocreatine shuttle model in §3.1. The oxygen concentration, $U(x,t)$, is determined by equations (2.7a) and (2.7c)–(2.7h), while the CrP, Cr, P and ATP concentrations, $Z(x,t)$, $C(x,t)$, $P(x,t)$ and $A(x,t)$ respectively, evolve according to equations (3.19a) and (3.19e)–(3.19i). The ODE for the time evolution of the OS length depends upon both oxygen levels, $U(x,t)$, and available ATP levels, $A(x,t)$,

$$\frac{dL_{\mathrm{OS}}}{dt} = k\left(U(-L_{\mathrm{IS}},t) - U_{\mathrm{Thr}}\right) - \sigma\left(L_{\mathrm{OS}}(t) - L^{*}_{\mathrm{OS}}(t)\right)\mathrm{H}\left(L_{\mathrm{OS}}(t) - L^{*}_{\mathrm{OS}}(t)\right). \tag{3.31}$$

In equation (3.31) the meaning of the parameters k, U_{Thr} and σ, and of $L^{*}_{\mathrm{OS}}(t)$, is the same as in §2.1 and §3.1. Growth is oxygen-dependent, as in §2.1, while shedding occurs where insufficient ATP is present, as in §3.1. The following initial condition is used to close equation (3.31),

$$L_{\mathrm{OS}}(0) = L_{\mathrm{OS,in}}. \tag{3.32}$$

3.7.2 *Nondimensionalisation and Parameter Estimation*

The oxygen model and phosphocreatine model are nondimensionalised differently; in particular distinct timescales are used. We nondimensionalise the combined model by using the same lengthscales and concentration scalings as the previous models, and the timescale from the oxygen model, L_{IS}^2/D_U. The dimensionless equations governing the concentrations are unchanged from the

earlier models, as are the dimensionless parameter groupings from the oxygen model. The dimensionless parameter groupings from the phosphocreatine shuttle model are redefined in the combined model as follows,

$$\hat{K}_{\text{grow}} = \frac{K_{\text{grow}} L_{\text{IS}}}{D_U}, \qquad \hat{\sigma} = \frac{\sigma L_{\text{IS}}^2}{D_U}, \qquad a^* = \frac{A^*}{A_r},$$
$$\hat{D}_Z = \frac{D_Z}{D_U}, \qquad \hat{D}_C = \frac{D_C}{D_U}, \qquad \hat{D}_P = \frac{D_P}{D_U},$$
$$\hat{k}_{1,\text{IS}} = \frac{k_{1,\text{IS}} A_r L_{\text{IS}}^2}{D_U}, \qquad \hat{k}_{1,\text{OS}} = 0, \qquad \hat{k}_{-1,\text{IS}} = \frac{k_{-1,\text{IS}} A_r L_{\text{IS}}^2}{D_U Z_r},$$

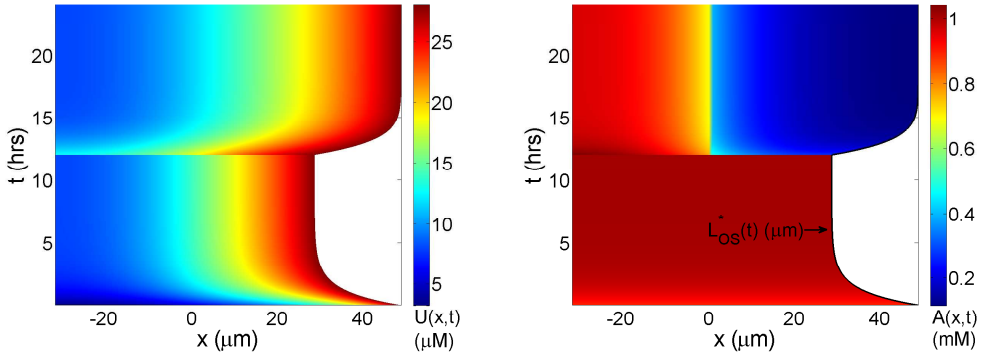
$$\hat{k}_{-1,\text{OS}} = \begin{cases} \dfrac{k_{-1,\text{L}} A_r L_{\text{IS}}^2}{D_U Z_r} & \text{light conditions,} \\ 0 & \text{dark conditions,} \end{cases} \qquad \hat{k}_{2,\text{IS}} = \frac{k_{2,\text{IS}} A_r L_{\text{IS}}^2}{D_U Z_r},$$

$$\hat{k}_{2,\text{OS}} = \frac{k_{2,\text{OS}} A_r L_{\text{IS}}^2}{D_U Z_r}, \qquad \hat{k}_{-2,\alpha} = \frac{k_{-2,\alpha} A_r L_{\text{IS}}^2}{D_U Z_r}, \qquad a_{\text{Tot}} = \frac{A_{\text{Tot}}}{A_r}$$
$$z_{\text{in}} = \frac{Z_{\text{in}}}{Z_r}, \qquad c_{\text{in}} = \frac{C_{\text{in}}}{Z_r}, \qquad p_{\text{in}} = \frac{P_{\text{in}}}{Z_r}.$$

The only change from the phosphocreatine shuttle model is the incorporation of the alternative timescale.

3.7.3 *Refinement of Parameter Estimates*

In this section we explain our parameter estimates in the combined model. For most parameter values we use our realistic estimates from the oxygen model (see Table 2.1) and the phosphocreatine shuttle model (see Table 3.1). However, the rate of OS growth, k, and threshold oxygen concentration, U_{Thr}, from the oxygen model and the rate, σ, and threshold ATP concentration, A^*, of disc shedding in the phosphocreatine shuttle model are not directly measurable. We inferred the values of these parameters by tuning their values in our simulations until other measurable outputs matched experimental results. Therefore, the estimated values of these parameters were influenced by the models. The combined model gives us further insight into the role of each of these parameters.

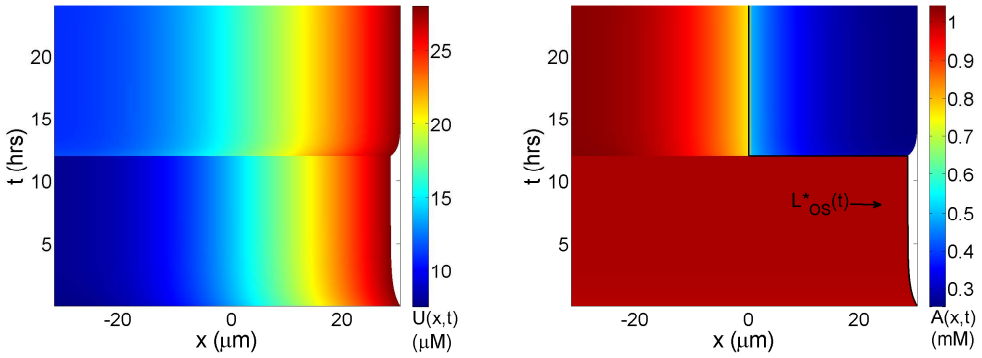


(a) $U(x,t)$ (b) $A(x,t)$

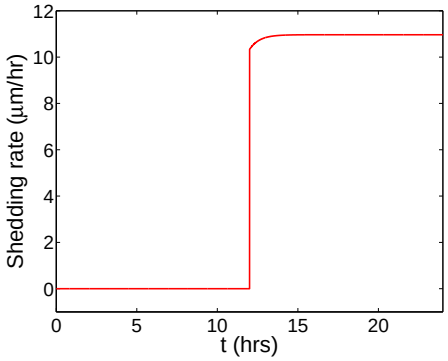
Figure 3.5.: Spatiotemporal distribution of the (a) oxygen and (b) phosphocreatine shuttle-derived ATP concentrations in a photoreceptor during 12 hours of dark conditions followed by 12 hours of light, calculated by using the parameter values in Tables 2.1 and 3.1 in the combined model (given by equations (2.1), (2.3)–(2.6), (3.5), (3.12a)–(3.14) and (3.31)). The solid black line in panel (b) represents $L^*_{\text{OS}}(t)$. There is no outer segment shedding during dark or light conditions since $A(x,t) > A^*$ throughout the photoreceptor, and thus the outer segment exhibits the same time evolution as in the oxygen model in Chapter 2.

To derive new estimates for k, U_{Thr}, σ and A^*, we begin by showing the outcome of using the previous estimates from Tables 2.1 and 3.1. The results, shown in Figure 3.5, indicate that the OS shedding term in equation (3.31) is outweighed by the growth term from the oxygen model. As such, the phosphocreatine shuttle plays a negligible role in governing the OS length and equation (3.31) is approximated by equation (2.2) from the oxygen model. Thus the OS exhibits the same time evolution as in Chapter 2.

Increasing the threshold ATP concentration for shedding to $A^* = 0.15\,\text{mM}$ gives the results shown in Figure 3.6. Figure 3.6(c) shows that, following the onset of light conditions, the ATP concentration throughout the OS rapidly drops lower than A^*, meaning that $L^*_{\text{OS}} = 0$ and the rate of disc shedding is maximal. However, the rate of growth still outbalances shedding initially, leading to a net increase in the OS length, until it reaches a steady state, as seen in Figure 3.6(b). At the steady state, the rates of OS growth and shedding are equal and of order $10\,\mu\text{m}\,\text{hr}^{-1}$ (see Figure 3.6(c)). This is unrealistically rapid compared to our estimated typical rate of outer segment disc turnover, $K_{\text{grow}} = 3.7\,\mu\text{m}\,\text{day}^{-1}$. We conclude from these results that the OS growth rate predicted by the oxygen model in Chapter 2 is too high to be physically realistic. Reducing the value of k by two orders of magnitude in our simulations yields



(a) $U(x,t)$ (b) $A(x,t)$



(c)

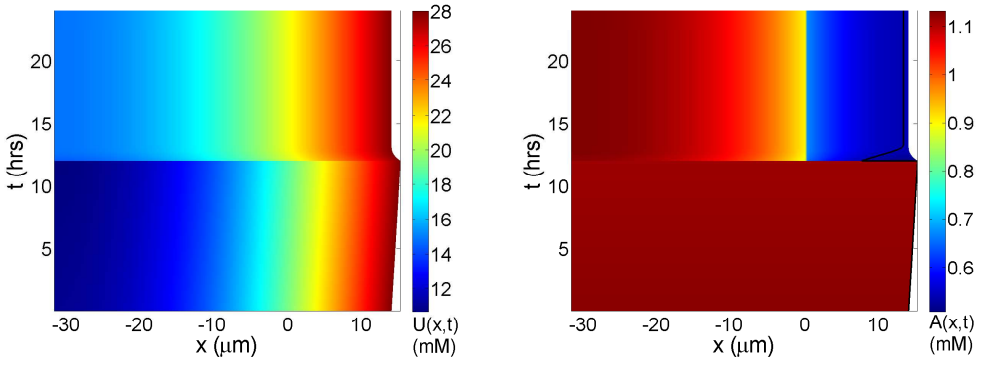
Figure 3.6.: Spatiotemporal distribution of the (a) oxygen and (b) phosphocreatine shuttle-derived ATP concentrations in a photoreceptor during 12 hours of dark conditions followed by 12 hours of light, and (c) the time variation of the outer segment shedding rate, calculated by using the parameter values in Tables 2.1 and 3.1, except that $A^* = 0.15\,\text{mM}$, in the combined model (given by equations (2.1), (2.3)–(2.6), (3.5), (3.12a)–(3.14) and (3.31)). The solid black line in panel (b) represents $L^*_{\text{OS}}(t)$. Under light conditions, the rate of outer segment shedding is large and positive, but still outbalanced by the growth rate. This indicates that the growth parameter k is too large.

qualitatively realistic behaviour, with growth and shedding under dark and light conditions respectively, as shown in Figure 3.7. However, the OS length now grows very slowly under dark conditions, and the predicted OS length is shorter than our estimated values during both light and dark conditions. We note that, during the first 12 hours of dark conditions, the rate of OS growth is approximately constant, and a steady state is not reached within this time period. Therefore, to increase the OS growth rate under dark conditions, it is necessary to increase the predicted steady state length by lowering our estimated value of U_{Thr}. However, a lower value of U_{Thr} not only increases the growth term in equation (3.31) under dark conditions, but also under light conditions. We therefore estimate the values of k and U_{Thr} as those which yield the observed diurnal patterns in the OS length during both dark and light conditions, which are $k = 2 \times 10^{-8}\,\text{m}\,\text{s}^{-1}\,(\text{mM})^{-1}$ and $U_{\text{Thr}} = 5.6\,\mu\text{M}$. These parameter estimates, along with the other parameter estimates in Table 2.1, set the value of $k\,(U(-L_{\text{IS}}, t) - U_{\text{Thr}})$ in equation (3.31). The values of A^* and σ can then be inferred from our estimates for the steady OS length under light conditions and the timescale over which the majority of shedding takes place, in the same way as in the phosphocreatine shuttle model, discussed in §3.2. This yields $A^* = 0.3\,\text{mM}$ and $\sigma = 10^{-4}\,\text{s}^{-1}$.

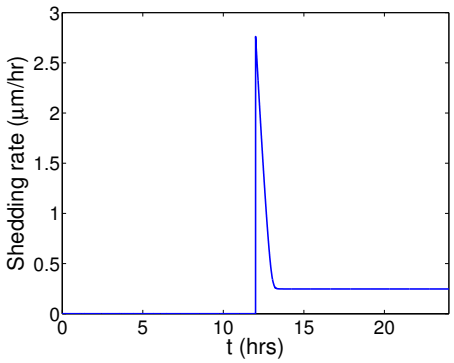
In summary, our parameter estimates for the combined model are the same as those given in Tables 2.1 and 3.1, except for the values of k, U_{Thr}, σ and A^*. The inferred values of these parameters in the combined model are $k = 2 \times 10^{-8}\,\text{m}\,\text{s}^{-1}\,(\text{mM})^{-1}$, $U_{\text{Thr}} = 5.6\,\mu\text{M}$, $\sigma = 10^{-4}\,\text{s}^{-1}$ and $A^* = 0.3\,\text{mM}$.

3.7.4 *Numerical Results*

Results from a typical simulation are presented in Figure 3.8, in which the combined model is evolved over a 24-hour period, comprising 12 hours of darkness followed by 12 hours of light conditions. The OS grows in dark conditions and sheds in light conditions, as observed *in vivo*. Moreover, the OS length is regulated, attaining a steady state both during light and dark conditions (see Figures 3.8 and 3.9 respectively). The CrP, Cr and P concentrations (see Figures 3.8(c)–(e)) are approximately spatially uniform during dark conditions and satisfy equation (3.29), in the same way as in the phosphocreatine shuttle model (see §3.4), since the equations governing these concentrations are the same in the combined model and the phosphocreatine shuttle model. As such

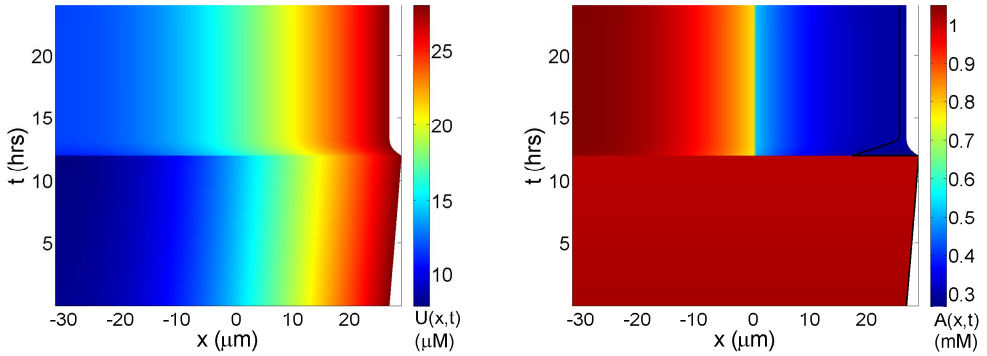


(a) $U(x,t)$ (b) $A(x,t)$



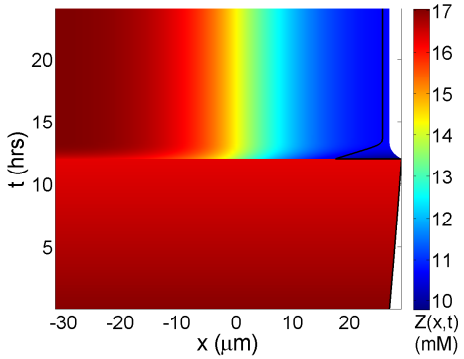
(c)

Figure 3.7.: Spatiotemporal distribution of the (a) oxygen and (b) phosphocreatine shuttle-derived ATP concentrations in a photoreceptor during 12 hours of dark conditions followed by 12 hours of light, and (c) the time variation of the outer segment shedding rate, calculated by using the parameter values in Tables 2.1 and 3.1, except that $A^* = 0.15\,\text{mM}$ and $k = 2 \times 10^{-8}\,\text{m}\,\text{s}^{-1}\,(\text{mM})^{-1}$, in the combined model (given by equations (2.1), (2.3)–(2.6), (3.5), (3.12a)–(3.14) and (3.31)). The solid black line in panel (b) represents $L^*_{\text{OS}}(t)$. The photoreceptor now grows under dark conditions and sheds in light, as observed in experiments, but the predicted OS lengths under light and dark conditions are too short, and the OS growth during dark conditions is slow.

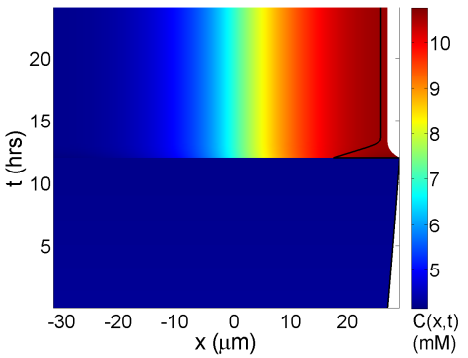


(a) $U(x,t)$

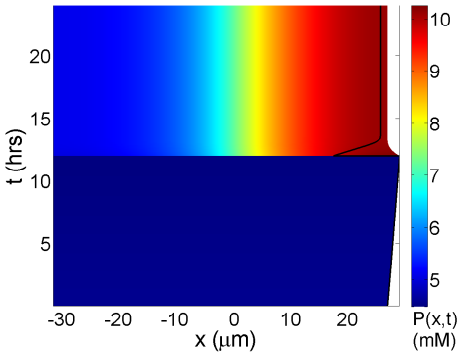
(b) $A(x,t)$



(c) $Z(x,t)$



(d) $C(x,t)$



(e) $P(x,t)$

Figure 3.8.: Spatiotemporal (a) oxygen, (b) ATP, (c) CrP, (d) Cr, and (e) P concentration distributions during 12 hours of dark conditions followed by 12 hours of light, for the combined model (given by equations (2.1), (2.3)–(2.6), (3.5), (3.12a)–(3.14) and (3.31)), showing growth of the outer segment under dark conditions and shortening under light conditions. Further, the outer segment attains a steady state length under both dark and light conditions. The solid black line in panels (b)–(e) represents $L_{\mathrm{OS}}^{*}(t)$. For parameter values see Tables 2.1 and 3.1, but with $A^{*} = 0.3\,\mathrm{mM}$, $\sigma = 10^{-4}\,\mathrm{s}^{-1}$, $k = 2 \times 10^{-8}\,\mathrm{m\,s}^{-1}\,(\mathrm{mM})^{-1}$ and $U_{\mathrm{Thr}} = 5.6\,\mu\mathrm{M}$.

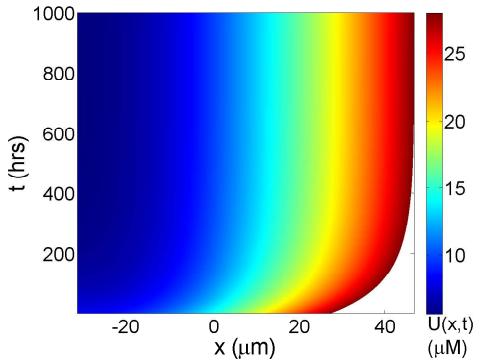


Figure 3.9.: Spatiotemporal evolution of the oxygen concentration according to the combined model (given by equations (2.1), (2.3)–(2.6), (3.5), (3.12a)–(3.14) and (3.31)) during a prolonged period of continuous dark conditions, showing growth of the outer segment until a steady state length is reached. For parameter values see Tables 2.1 and 3.1, but with $A^* = 0.3\,\mathrm{mM}$, $\sigma = 10^{-4}\,\mathrm{s}^{-1}$, $k = 2 \times 10^{-8}\,\mathrm{m\,s}^{-1}\,(\mathrm{mM})^{-1}$ and $U_{\mathrm{Thr}} = 5.6\,\mu\mathrm{M}$.

the ATP concentration at $x = L_{\mathrm{OS}}(t)$ is given by equation (3.30). Likewise, since the oxygen concentration satisfies the same equations in the oxygen model and the combined model, the argument in §2.5 applies in Figure 3.8(a), with the quasisteady oxygen concentration given by equation (2.11).

As shown in Figure 3.8(b), under dark conditions, the ATP concentration increases and exceeds the threshold level A^*, so, in equation (3.31), the shedding term turns off, and it reduces to equation (2.7b), which depends only on the oxygen concentration. Therefore, the combined model predicts that the OS length eventually reaches a steady state which satisfies equation (2.16) under dark conditions.

Figure 3.9 shows the effect of prolonged dark conditions on the oxygen distribution and OS length. The OS continues to grow linearly for a number of days before the oxygen-based regulation becomes significant. A steady state length is reached after approximately 1000 hours, or 42 days. Like the phosphocreatine shuttle model results, this is consistent with experimental findings of Bassi and Powers [35], in which the photoreceptor outer segments in goldfish grew at an approximately constant rate for the duration of the experiment, 7 days, under continual dark conditions. However, the fact that a steady state length is eventually reached is more realistic than the indefinite OS growth exhibited by the phosphocreatine shuttle model during continual darkness (see §3.4).

During light conditions, the fall in the ATP concentration below the threshold level A^* in the OS induces disc shedding, since $L^*_{\mathrm{OS}} < L_{\mathrm{OS}}$ in equation (3.31). At the onset of light conditions, the rate of oxygen consumption by mitochondria in the IS halves, leading to an increase in $U(-L_{\mathrm{IS}}, t)$. Therefore, the oxygen-based growth term in equation (3.31) also increases. Initially at the onset of light, the rate of disc shedding exceeds the rate of OS growth, so the OS shortens. In the same way as in the phosphocreatine shuttle model, the reduction in the OS length allows ATP levels to increase and a concomitant fall in the disc shedding rate, until the growth and shedding rates balance and a steady state is reached, for which equation (3.31) gives,

$$L_{\mathrm{OS,SS}} = L^*_{\mathrm{OS,SS}} + \frac{k}{\sigma}\left(U_{\mathrm{SS}}(-L_{\mathrm{IS}}) - U_{\mathrm{Thr}}\right). \tag{3.33}$$

We note from Figures 3.8(b)–(e) that, at the steady state in light conditions, the combined model predicts that $L_{\mathrm{OS,SS}} = 27\,\mu$m and $L^*_{\mathrm{OS,SS}} = 25.8\,\mu$m. As such, the ATP concentration is below the threshold level A^*, and shedding takes place, over 4% of the OS length. Although this is a small proportion, we argue that it is not unreasonable, since we expect that, in a healthy photoreceptor, sufficient ATP is available to maintain the OS discs throughout most of the OS.

In summary, the combined model, with realistic parameter estimates, reproduces the documented diurnal variation in the OS length, with growth of the outer segment under dark conditions and disc shedding at the onset of light. Moreover, the outer segment length is regulated at all times, with unlimited growth prevented by oxygen-based regulation under dark conditions.

3.7.5 *Parameter Sensitivity*

Given that the OS length governed by the combined model exhibits realistic qualitative behaviour, in this section we test whether the model predictions are robust to variations in parameter values, and also examine ways that the model can inform us about causes and potential treatment targets for retinal diseases.

In order to predict disruptions to OS length regulation that may lead to age related macular degeneration, we investigate, in our model, the effects of a reduced mitochondrial efficiency, a known consequence of ageing [9].

In §2.6, we implemented this by increasing the value of μ and reducing the value of U_{Thr} in the oxygen model. However, the OS lengths predicted by the

combined model following 12 hours of continuous light or dark conditions change by very little when these these parameter values are varied. Under dark conditions, the steady state OS length varies with μ and U_{Thr} in qualitatively the same way as in Figures 2.6(b) and (d). However, the steady state OS length is not reached within 12 hours of dark conditions in the combined model, and these changes are insufficient to produce a significant change in the rate of OS growth within this time period. Under light conditions, equation (3.33) applies, and, as discussed in §3.7.4, at the steady state, $L^*_{\text{OS,SS}}$ is close to $L_{\text{OS,SS,L}}$. The oxygen-based growth term in equation (3.33) is comparatively small (approximately 4% of $L_{\text{OS,SS,L}}$) and so the parameters that affect the oxygen concentration play a negligible role in the diurnal variation of the OS length. However, the role of the oxygen component of the combined model plays a significant role under prolonged dark conditions.

In terms of the phosphocreatine shuttle parameters, we argue that a reduction in the mitochondrial efficiency decreases the rate at which ATP is produced from ADP and free phosphate by mitochondria in the IS, with rate constant $k_{1,\text{IS}}$. Figure 3.10 shows how the OS length at the steady state under light conditions varies with $k_{1,\text{IS}}$, and also with the threshold ATP concentration for shedding, A^*. Under dark conditions, since the OS length is regulated by oxygen, the steady state OS length is unchanged by variations in $k_{1,\text{IS}}$ or A^*. During light conditions, the OS length is regulated by the phosphocreatine shuttle, so it increases with $k_{1,\text{IS}}$ and decreases with A^*, as in the phosphocreatine shuttle model (see Figure 3.4(a)), explained as follows.

According to our explanation earlier, decreasing the rate of ATP production by the mitochondria, $k_{1,\text{IS}}$, means that less energy is available to the OS discs, causing more rapid shedding and a shortened outer segment. As seen in §2.6, shortening of photoreceptors is a clinically acknowledged characteristic of age related macular degeneration [11], and the resulting loss of OS discs and concomitant decrease in phototransduction provides an explanation for the loss of light sensitivity in regions of the retina with age. Furthermore, photoreceptors whose outer segments have become too short may die, a typical problem causing vision loss in age related macular degeneration [11, 12].

The results in Figure 3.10 also suggest that the OS shortens if the threshold level of ATP for disc shedding, A^*, is elevated. In practice, this identifies another possible explanation for the photoreceptor damage in an ageing retina. If OS discs make less efficient use of energy with age, more ATP is required

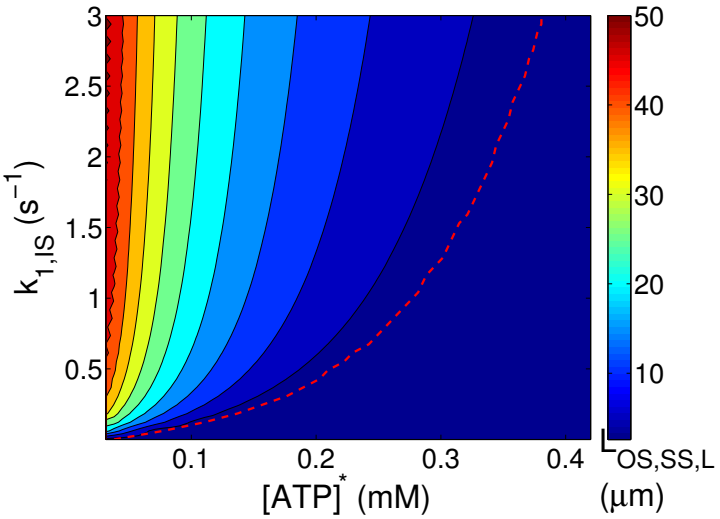


Figure 3.10.: Parameter sensitivity of the steady state outer segment length under light conditions predicted by the combined model (given by equations (2.1), (2.3)–(2.6), (3.5), (3.12a)–(3.14) and (3.31)) to the rate constant of ATP production from ADP+P in the mitochondria within the inner segment, $k_{1,\mathrm{IS}}$, and the threshold ATP concentration for shedding, A^*. For parameter values see Tables 2.1 and 3.1, but with $A^* = 0.3\,\mathrm{mM}$, $\sigma = 10^{-4}\,\mathrm{s}^{-1}$, $k = 2 \times 10^{-8}\,\mathrm{m\,s}^{-1}\,(\mathrm{mM})^{-1}$ and $U_{\mathrm{Thr}} = 5.6\,\mu\mathrm{M}$. The red dotted line represents the points in parameter space for which $L^*_{\mathrm{OS}} = 0$ at the steady state (i.e. the whole OS is shedding).

to maintain them, denoted by an increase in A^*. According to our model, this results in shortening of the outer segments which may lead to photoreceptor damage and death, and ultimately vision loss.

3.8 DISCUSSION OF OXYGEN AND PHOSPHOCREATINE SHUTTLE MODELS

In the first part of this thesis we have presented three PDE models respresenting key aspects of rod photoreceptor metabolism, which we use to examine whether oxygen levels, phosphocreatine shuttle-derived ATP or both may be regulators for photoreceptor outer segment length. We present in Chapter 2 a model that regards oxygen as the sole regulator for OS length, in which the OS grows if the oxygen concentration at the inner end of the IS exceeds a threshold level, and shortens if it is below threshold. Simulations of this model suggest that this oxygen dependence can prevent unlimited OS growth during both light and dark conditions, but cannot induce shedding under light conditions. This suggests that oxygen is not the only regulator for OS length variation, but may regulate the growth of the OS under dark conditions.

The second model, discussed in §3.1–§3.6 of this chapter, is developed to test a second proposed mechanism that may regulate the OS length variation: the ATP provision by the phosphocreatine shuttle. The model couples the time dependence of the outer segment length with the spatiotemporal concentration distribution of ATP in the photoreceptor, which depends on the local creatine phosphate, creatine and free phosphate concentrations. According to the model, the outer segment discs are produced at a constant rate, while discs are shed from the outer end of the OS if there is insufficient ATP there to maintain them. Our model predicts that the OS grows at a constant rate during dark conditions and sheds during light ones, which is physiologically realistic. However, under continual dark conditions, the OS grows indefinitely. The results of the phosphocreatine shuttle model indicate that the phosphocreatine shuttle may regulate the OS length by inducing shedding in light conditions, but permits unregulated OS growth in darkness.

Our combined model, imparted in §3.7.1–§3.7.5 of this chapter, combines the two previous models by assuming that the outer segment growth is regulated by the oxygen distribution and shedding is brought about due to the lack of phosphocreatine shuttle-derived ATP. The concentration of oxygen is modelled as in Chapter 2, while the CrP, Cr, P and ATP concentrations are governed

by the equations in §3.1–§3.6 of this chapter. This model improves upon the oxygen model and the phosphocreatine shuttle model. Whereas the oxygen model predicts OS growth under light conditions and retraction in darkness, the combined model exhibits the observed diurnal variation in photoreceptor length, with growth during darkness and disc shedding at the onset of light conditions. We are able to reproduce the findings of Bassi and Powers [35], that under 7 days of continual darkness, the OS grows at an approximately constant rate. Moreover, unlimited growth of the OS during dark conditions is prohibited in the combined model, meaning that it is applicable under prolonged darkness as well as for typical daily light-dark cycles.

Our combined model gives us predictions on which metabolic processes may be responsible for regulating photoreceptor length. The oxygen and phosphocreatine shuttle models highlight the failure of each hypothesis alone to fully describe the regulation of the OS length. The combined model shows that the correct timing of net production and shedding of the OS discs and also regulation of OS growth are exhibited when both hypotheses are incorporated. It treats the oxygen distribution and the phosphocreatine shuttle as independent mechanisms that are both regulators of OS length. There are a number of alternative ways the oxygen and phosphocreatine shuttle models could be amalgamated. For instance, the time evolution of the concentrations in the oxygen and phosphocreatine shuttle models could be coupled, while assuming that the OS length is solely dependent upon the ATP concentration. This involves accounting for the oxygen-dependence of the rate of ATP production via oxidative metabolism (i.e. the forward reaction in (3.1)). Thus the reaction rate $k_{1,\alpha}BP$ in the phosphocreatine shuttle model becomes oxygen-dependent, e.g. using the Law of Mass Action, reaction rate ν_P becomes,

$$\nu_P = \bar{k}_{1,\alpha} UBP - k_{-1,\alpha} A,$$

where $\bar{k}_{1,\alpha} = k_{1,\alpha}/U_{L_{\mathrm{OS}}}$. The doubled energy demand in the IS under dark conditions can be accounted for by assuming that the rate, $k_{-1,\mathrm{IS}}$, of ATP breakdown in the IS doubles under dark conditions. Equation (2.1) becomes,

$$\frac{\partial U}{\partial t} = D_U \frac{\partial^2 U}{\partial x^2} - \left[\lambda + k_{1,\alpha} BP\right] U, \tag{3.34}$$

while the PDEs for the CrP, Cr, P, ATP and ATP concentrations, and the ODE for the OS length in the phosphocreatine shuttle model are unchanged, except

for the new definitions of ν_P and $k_{-1,\mathrm{IS}}$. Then, under dark conditions, the increased value of $k_{-1,\mathrm{IS}}$ leads to a rise in the ADP levels (and fall in the ATP concentration) in the IS. This leads to an increased oxygen consumption in equation (3.34), analogous to the doubled oxygen consumption rate μ in equation (2.1) of the oxygen model.

Although the OS length is not explicitly oxygen-dependent, the rate of ATP production via oxidative metabolism is limited by oxygen availability, hence limiting the ATP concentration in the OS, on which the OS length depends. The oxygen concentration becomes limiting under dark conditions, as in the combined model, since the overall energy consumption (and hence oxygen consumption) in the photoreceptor is highest during darkness. The above arguments indicate that the time evolution of the OS length according to the combined model and the alternative model outlined here are qualitatively the same. The advantage of the combined model is that it can be easily broken down into the oxygen and phosphocreatine shuttle components, enabling us to apply the knowledge already gained from the two earlier models.

While previous models of retinal metabolism are able to predict spatial distributions of oxygen concentrations measured *in vivo* within the retina at a steady state [104, 105, 107, 108], they do not give information on the role of metabolism in the regulation of photoreceptor growth and disc shedding, whereas our combined model provides all of the above. It also enables us to identify potential causes of or contributors to retinal diseases. For example, ageing may decrease the efficiency of mitochondrial ATP production [9]. This means that either more oxygen is required to supply sufficient ATP to maintain the photoreceptor, or that the ATP production rate is reduced (or both). According to the combined model, an increase in oxygen consumption by the mitochondria or a decreased ATP production (or both) may lead to a shortened outer segment, which is reported in clinical observations in sufferers of age related macular degeneration [11]. If the OS becomes too short this may result in, at best, impaired retinal light sensitivity, and, at worst, photoreceptor death and vision loss [12].

As discussed in §1.4, Holz et al. [79] measured elevated concentrations of *lipofuscin*, a potentially toxic byproduct occasionally generated by phagocytosis of OS discs, in regions of the retina that afterwards became subject to RPE degradation. This led to the theory that if rapid OS shedding occurs and persists over a long time, this could lead to cell damage and death [79, 80]. Our

findings that the reduced mitochondrial efficiency arising due to age may result in OS shortening (and thus rapid shedding) are consistent with this theory.

Due to the lack of mathematical models on retinal metabolism and of *in vivo* experimental data on human retinae, the models in this chapter and the last are kept simple and tractable. Additional processes can be included in the combined model such as the role of neuroglobin, outlined in §2.7 and other aspects of mitochondrial metabolism as discussed in §3.6. The role of the retinal layers in between the photoreceptors and the choroidal blood vessels could also be included. For example, there is a layer of retinal pigment epithelial cells which interact with the photoreceptors via intercellular signalling molecules and also phagocytose the OS discs shed from the outer segments. These signalling processes may also be involved in the regulation of photoreceptor length.

Another possible extension is the incorporation of surrounding photoreceptors, possibly using an agent-based model. For instance, retinal diseases such as age related macular degeneration and retinitis pigmentosa begin with the death of a small number of photoreceptors, but this develops into regions of photoreceptor loss. A further development on our model may be able to provide an explanation for this as follows. Healthy photoreceptors are known to release factors to promote the survival of their neighbours. It is possible to extend our combined model to include a group of photoreceptors whose lengths are regulated by oxygen, the phosphocreatine shuttle and also the concentration of a survival factor. By incorporating the release of factors by healthy photoreceptors which ceases if the OS lengths become too short, it may be possible to predict certain conditions in which photoreceptor damage propagates throughout entire regions of the retina, and to identify prevention or treatment strategies.

Part II.

Inner Retinal Metabolic Regulation

4

INTRODUCTION TO INNER RETINAL METABOLIC REGULATION

Diabetic retinopathy is the most common cause of visual impairment and preventable blindness in adults of working age [156], with more than 60% of type 2 diabetes patients affected at some point in their lives [157]. This underlines the importance of understanding the mechanisms responsible for the development of this disease.

Inner retinal neuronal cells are highly sensitive to variations in metabolite concentrations, while there is considerable variation of these concentrations in the blood vessels. Blood glucose levels fluctuate throughout the day, being highest immediately after, and lowest immediately before meals. It is therefore vital that metabolite transport to the neurons is stringently controlled. *Glial cells* regulate metabolite levels in the inner retinal tissue, controlling transport rates and also absorbing/removing potentially toxic chemical species. Retinal diseases in which these regulatory mechanisms are disrupted may lead to increases in the levels of certain metabolites until they reach cytotoxic levels. For example, the large fluctuations in blood glucose experienced by diabetes sufferers may lead to neuronal cell damage or death, and vision loss, characteristic features of diabetic retinopathy.

In the second part of this thesis we shift our focus away from individual photoreceptor cells, to investigate how metabolite levels are regulated within the inner retina, and consider changes that may lead to retinal disease. Before we present and analyse our own model of inner retinal metabolic regulation (see Chapters 5 and 6) we pause to introduce in §4.1 the key components of inner retinal metabolism, and, in §4.2, previous mathematical modelling strategies. The chapter concludes in §4.3, where we summarise those features of existing models which are to be incorporated in our own work.

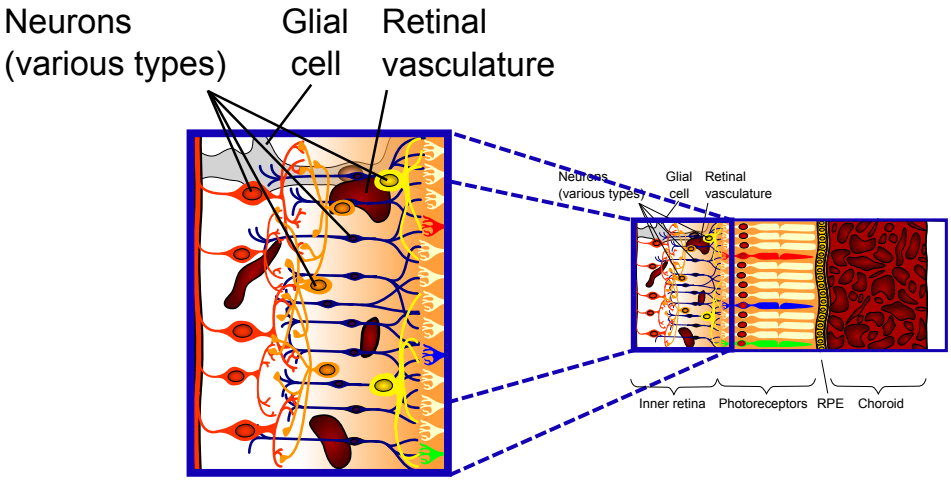


Figure 4.1.: Schematic diagram of inner retinal tissue, adapted from [14, 17, 18].

4.1 PHYSIOLOGY OF INNER RETINAL METABOLISM

The inner retina consists of neurons, *glial* cells, extracellular space (ECS) and capillaries (see Figure 4.1). As stated in Chapter 1, incoming light signals activate the inner retinal neurons, which causes depolarisation of their cell membranes (an increase in the cell membrane potential) [158], and the release of a neurotransmitter into the synaptic terminals at their ends. The neurotransmitter diffuses through the synaptic terminals until it reaches the adjacent neurons, which then become depolarised. This process repeats, with consecutive neurons in a network becoming depolarised and releasing a neurotransmitter signal to neighbouring neurons, thus an action potential propagates through the network, and eventually to the brain. The major neurotransmitter responsible for the transmission of sensory information from the retina to the brain is glutamate [159–161]. Neurons that release glutamate are termed *glutamatergic* neurons [162].

Metabolite levels in the bloodstream vary significantly, whilst the neuronal cells are extremely sensitive and need to be protected from changes in their environment. Glial cells play a significant role in homoeostasis within the inner retinal tissue, regulating the delivery of blood-borne nutrients and clearing away potentially toxic chemicals. The structure of glial cells facilitates these functions: their surface area is large, due to their long processes and large end-feet which almost completely envelop the capillaries [163–165] (see Figure

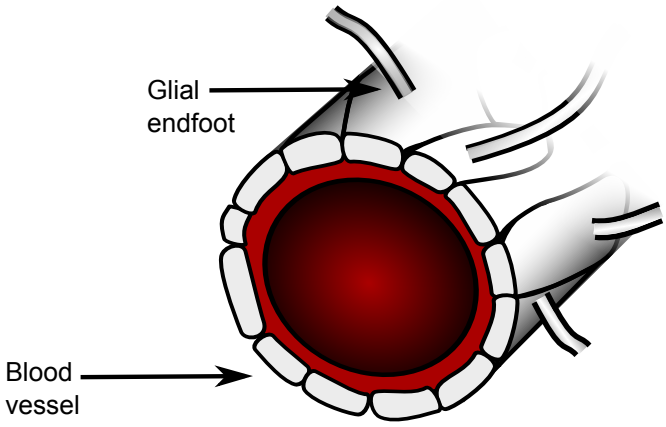


Figure 4.2.: Schematic diagram of glial endfeet surrounding the blood vessels, adapted from [166].

4.2). Therefore, to reach the neuronal cells from the bloodstream, nutrients must first travel through transporter molecules in the capillary walls, and likely the glial cells, before passing into the ECS and being taken up by the neurons. Whether nutrients must always pass through glial cells when moving from the capillaries to the ECS remains debated, with some experiments finding small gaps between glial cells through which metabolites may be transported. However, Iadecola and Nedergaard [167] point out that these studies are based on detection of a chemical that was once thought to be expressed by all glial cells, but later found to be expressed only in some. We follow Iadecola and Nedergaard [167], assuming that capillary walls are completely ensheathed by glial end-feet.

The capillary walls comprise two layers: an inner layer of *endothelial cells* and an outer *basement membrane*, or *basal lamina* (see Figure 4.2). This arrangement of vessel walls, glial cells and the ECS between the capillaries and neurons constitutes the *blood-brain barrier*.

Glial and neuronal cells derive their energy from blood-borne nutrients via glycolysis and oxidative metabolism, see §1.3). The general consensus among researchers is that the majority of energy production in glial cells is via glycolysis, both in the brain and inner retina, whilst the neuronal cells derive a large amount of their energy via oxidative metabolism [168–173]. However, this view is still subject to debate and is disputed by Gjedde and Marrett [174].

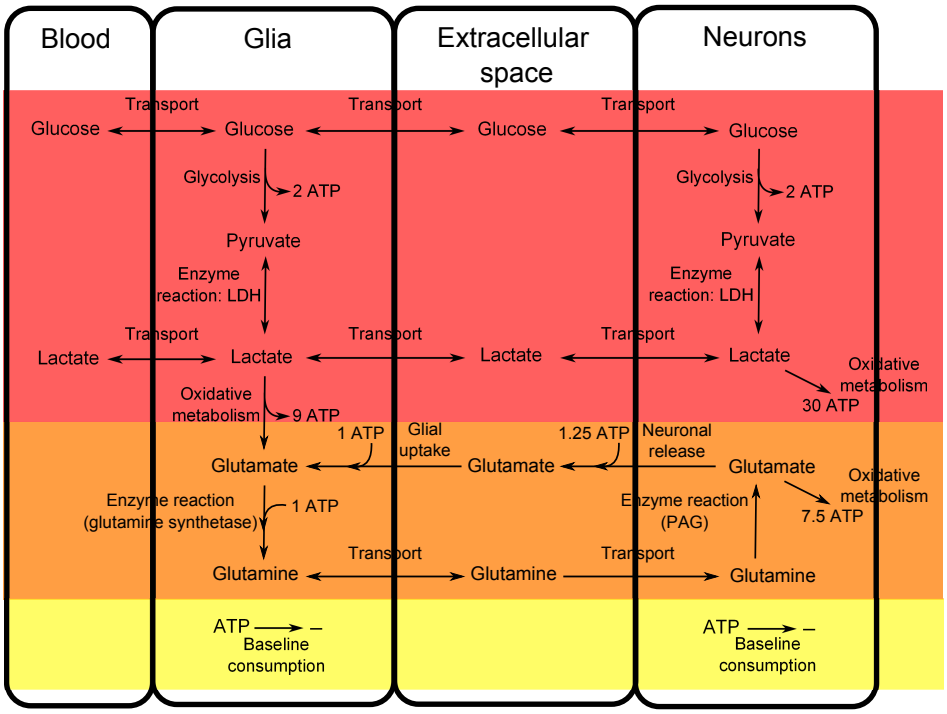


Figure 4.3.: Schematic diagram of glial and neuronal metabolism, metabolite exchange and the glutamate-glutamine cycle

In response to light stimulation, glutamatergic inner retinal neuronal cells release glutamate to stimulate surrounding neurons [110, 175]. (We remark that this contrasts with the outer retinal photoreceptors, which are active during dark conditions.) Neuronal activation ceases when glutamate is consumed by the glial cells [176–179]. Following its uptake by glial cells, glutamate can be either metabolised to produce ATP, or converted to *glutamine* by an enzyme called *glutamine synthetase* [180, 181]. Glutamine is not *neuroactive* (it does not stimulate surrounding neurons) so it can be transported through the ECS without causing further neuronal activation [177, 182]. It is transported to the neurons and converted to glutamate [176, 181], which either enters the TCA cycle to produce ATP, or is released into the ECS following the next sensory stimulus [183]. This process is called the *glutamate-glutamine* cycle, and the reactions involved are shaded in orange in Figure 4.3.

Glial cells are crucial to the glutamate-glutamine cycle for several reasons. Glutamate uptake by glia is essential, as excess glutamate in the ECS is toxic to the neurons [19, 176, 178]. Also, the only input into the glutamate-glutamine cycle is the glial production of glutamate. Neurons cannot convert lactate into glutamate because a necessary enzyme (pyruvate carboxylase) is absent

[184, 185]. Glial cells also contain the glutamine-producing enzyme glutamine synthetase which is not present in neurons [162, 176, 186]. The net effects of the processes described above are summarised in Figure 4.3, with the glycolytic and oxidative pathways shaded in red. We now consider each process in more detail.

Glycolysis

The glycolytic pathway comprises 10 steps, and its net effect is the consumption of 1 glucose, 2 ADP, 2 free phosphate and 2 NAD^+ molecules and the production of 2 pyruvate, 2 ATP, 2 NADH, 2 H^+ and 2 H_2O molecules. We can therefore summarise glycolysis via the following reaction,

$$\begin{aligned}\mathrm{Glucose} + 2\,\mathrm{ADP} + 2\,\mathrm{P} + 2\,\mathrm{NAD}^+ \rightarrow 2\,\mathrm{Pyruvate} + 2\,\mathrm{ATP} + 2\,\mathrm{NADH} \\ + 2\,\mathrm{H}^+ + 2\,\mathrm{H_2O}, \quad (4.1)\end{aligned}$$

where P represents free phosphate. It is important that we treat reaction (4.1) with caution as it conceals some important information. While the rate of a single-step irreversible reaction is commonly assumed to be a monotonic increasing function of its substrate concentrations (e.g. using the Law of Mass Action or Michaelis-Menten kinetics), this may not be an accurate representation of a multi-step reaction pathway such as glycolysis. For instance, assuming the rate of reaction in (4.1) is a monotonic increasing function of the concentrations of glucose, ADP, free phosphate and NAD^+ implies that it does not require ATP to take place. However, the first and third steps of glycolysis each convert 1 molecule of ATP to ADP, glycolysis cannot occur if ATP is absent.

Oxidative metabolism

The net effect of oxidative metabolism is captured by the net reaction,

$$2\,\mathrm{Pyruvate} + 30\,\mathrm{ADP} + 30\,\mathrm{P} + 6\,\mathrm{O_2} \rightarrow 6\,\mathrm{CO_2} + 30\,\mathrm{ATP} + 6\,\mathrm{H_2O}. \quad (4.2)$$

Many steps are involved, which are summarised in Figure 4.4.

Two pyruvate molecules, derived from glycolysis, are used to produce two molecules of acetyl CoA, which pass once through the TCA cycle (from point A to D in Figure 4.4). The products of the TCA cycle include a number of NADH and $FADH_2$ molecules from which ATP is produced via *oxidative*

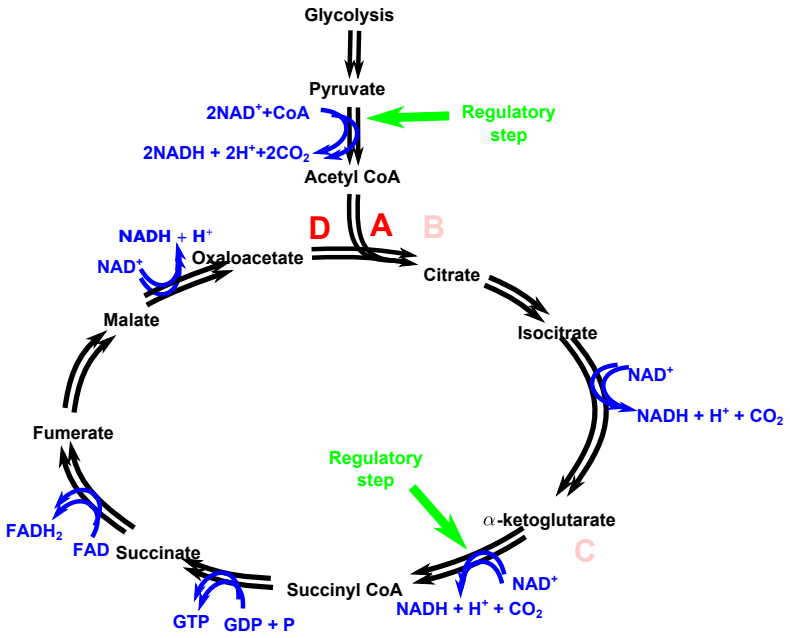


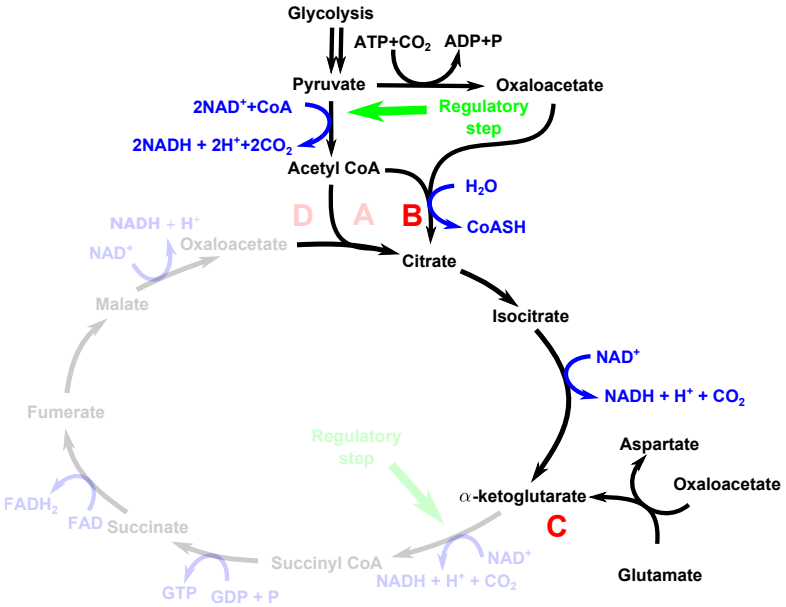
Figure 4.4.: Two pyruvate molecules passing through the TCA cycle, adapted from [110].

phosphorylation [187]. We remark that the estimated yield of 30 ATP molecules is only approximate, since there are currently no universally agreed quantities, and the ATP yields may not always be fixed values [187].

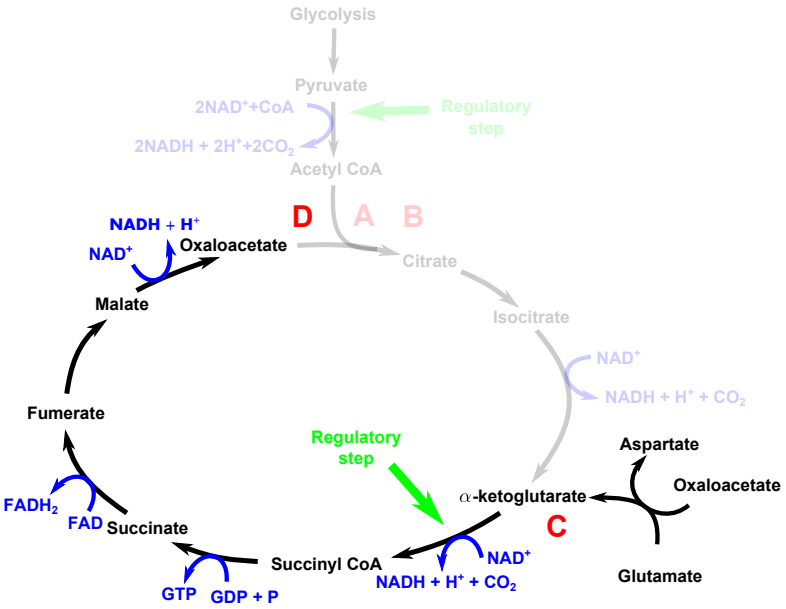
Glial cells can produce glutamate by partial oxidative glutamate metabolism [181, 188–192], as shown in Figure 4.5(a). In complete oxidative metabolism, both pyruvate molecules produced by glycolysis (see equation (4.1)) are converted to acetyl CoA and pass through the TCA cycle. However, in glutamate synthesis, one pyruvate molecule is converted to acetyl CoA while the other is converted to oxaloacetate. Then, acetyl CoA and oxaloacetate combine to form citrate which passes partially through the TCA cycle (from point B to C in Figure 4.5(a)) and out to produce glutamate. Glutamate production uses 2 pyruvate molecules to produce 1 glutamate and 9 ATP molecules.

Glutamate can be oxidised in neurons by passing from point C to D in Figure 4.5(b), producing 7.5 ATP molecules per glutamate molecule. Glutamate can also be catabolised in glial cells, but very slowly, so this contributes little to their ATP production compared to glycolysis.

As shown in Figures 4.4 and 4.5, the two major regulatory steps are the formation of acetyl CoA and the conversion of α-ketoglutarate to succinyl CoA in the TCA cycle. The latter of these is the slowest [187]. The regu-



(a) Glutamate synthesis: two pyruvate molecules are converted to one molecule of citrate, which passes partially through the TCA cycle.



(b) Glutamate catabolism: glutamate is converted to α-ketoglutarate which passes partially through the TCA cycle.

Figure 4.5.: Schematic diagram of glutamate synthesis and catabolism whose substrates partially pass through the TCA cycle, adapted from [110].

latory step in glutamate synthesis is the formation of Acetyl CoA, whereas glutamate catabolism involves the other rate-limiting step: the conversion of α-ketoglutarate to succinyl CoA. Full oxidative metabolism passes through both regulatory steps, meaning that its rate is limited by the slowest of the two steps, i.e. the conversion of α-ketoglutarate to succinyl CoA.

Conversion between Pyruvate and Lactate

The conversion between pyruvate and lactate is a single step enzyme reaction, catalysed by the enzyme *lactate dehydrogenase* (or *LDH*),

$$\text{Pyruvate} + \text{NADH} + \text{H}^+ \underset{k_-}{\overset{k_+}{\rightleftharpoons}} \text{Lactate} + \text{NAD}^+. \tag{4.3}$$

This reaction is fast compared to the timescale over which substrates pass through the glycolytic and oxidative pathways, meaning that the forward and backward reaction rates quickly equilibrate, i.e. using the Law of Mass Action we have that,

$$k_+[\text{Pyruvate}][\text{NADH}] = k_-[\text{Lactate}][\text{NAD}^+]. \tag{4.4}$$

The LDH reaction regulates the pyruvate concentrations within the glial and neuronal cells: if pyruvate levels become depleted by rapid oxidative metabolism, this promotes the reverse direction of reaction (4.3), resulting in net pyruvate production from lactate (assuming the intracellular NADH and NAD^+ concentrations are unchanged). Lactate levels are easily replenished since lactate can be transported through the cell membranes. This mechanism ensures that pyruvate is available for energy production at times of high energy demand. In contrast, if pyruvate accumulates, the LDH reaction operates in the forward direction, converting pyruvate to lactate which can be transported out of the cells.

Glucose and Lactate transport

Glucose and lactate are transported into/out of glial and neuronal cells via diffusion through transporter molecules. Transport is passive (requiring no energy input), reversible and occurs at a rate that increases and saturates with the concentrations of each substrate [193, 194]. Glucose transport is via GLUT1–3 molecules, mostly via the GLUT1-type in the glia [195] and the GLUT3-type

in the neurons [193, 196, 197] and these have different kinetic parameters. The lactate transporter molecules are called *monocarboxylate transporters*, or *MCTs*. The primary glial and neuronal transporters of lactate are thought to be MCT-1 and MCT-2 respectively [181, 194, 198–200].

Magistretti (1999) [165] introduced the concept of *lactate shuttling* between the glial and neuronal cells. As discussed above, during high energy demand, oxidative metabolism of pyruvate by neuronal cells is rapid. If insufficient pyruvate is provided by neuronal glycolysis, pyruvate levels fall, biasing reaction (4.3) in favour of a net conversion of lactate to pyruvate, and thus depleting the neuronal lactate concentration. This creates a negative lactate gradient, and hence a flux, from glial cells to neurons. The concomitant decrease in the glial lactate concentration biases reaction (4.3) in the direction of net lactate production from pyruvate in the glia. According to the *glia-neuron lactate shuttle hypothesis*, or *GNLSH*, this is the source of some or all of the neuronal pyruvate required for oxidative metabolism (in contrast with purely glycolytic pyruvate production). The extra pyruvate sink in the glial cells also provides an explanation of why glycolysis is rapid in glial cells compared to other cell types. This hypothesis is now widely accepted [168–171], although not universally (e.g. [172]).

Glutamate-Glutamine Cycle

Neuronal glutamate is synthesised in the mitochondria, transported to the cytosol by *glutamate translocator* molecules, and packed at high concentrations into synaptic vesicles [201, 202]. The energy required to move glutamate into vesicles, against its concentration gradient, is provided by a Mg^{2+}-ATPase proton pump [203–206]. The pump uses energy from ATP breakdown to transport protons into the vesicles, creating an excess positive charge inside. Glutamate, which is negatively charged, then enters the vesicles [205, 207]. One molecule of ATP is consumed for each glutamate molecule transported [208]. Glutamate is then stored in the vesicles until neuronal activation. In response to a sensory stimulus, the vesicles in the neurons migrate to the cell membrane and release their stores, with 1 ATP being consumed for every four molecules of glutamate released [202, 209].

The uptake of glutamate from the ECS by the glial cells is primarily through *excitatory amino acid transporters* 1–2 (*EAAT*1–2). For each glutamate molecule transported through the EAAT, 3 Na^+ ions and one H^+ ion enter, and one K^+

ion exits the glia [158, 176, 210, 211]. The transport of Na^+ and K^+ ions down their concentration gradients is an energy-producing process, which fuels the movement of glutamate up its concentration gradient [176, 186] (which would otherwise require ATP). For this transport mechanism to function, intracellular and extracellular ion concentrations must be returned to their original levels following glutamate uptake. To balance the changes caused by glutamate transport, an Na^+/K^+-ATPase pump transports Na^+ ions out of, and K^+ ions into the cell [183, 200]. For each glutamate molecule transported, the Na^+/K^+-ATPase pump uses 1 ATP molecule [212]. The direction of glutamate transport through the EAAT depends on the relative intracellular and extracellular ionic concentrations; these are maintained at a constant level by the Na^+/K^+-ATPase pumps. Normal physiological ionic concentrations bias the direction of glutamate transport in favour of glial glutamate uptake from the ECS, regardless of the relative glutamate levels either side of the glial cell membranes [176].

In the glial cells glutamate is converted to glutamine via the following reaction [178, 211],

$$\text{Glutamate} + \text{ATP} + \text{NH}_4 \rightleftharpoons \text{glutamine} + \text{ADP} + \text{P} + \text{H}_2\text{O}, \tag{4.5}$$

which is catalysed by the enzyme *glutamine synthetase* [19, 211, 212]. Production of each glutamine molecule consumes one molecule of ATP [165, 192, 212] (see Figure 4.3). While the reverse reaction can occur, and the glutamate produced can enter the TCA cycle, this is negligible compared to glutamine synthesis [178].

Glutamine is transported passively and reversibly between the glial cells and ECS via *system N* (*SN*1) transporter molecules in the cell membranes [213, 214]. Since the glutamine concentration tends to be greater in the glia than in the ECS, the flux of glutamine down its concentration gradient tends to be outwards from the glial cells, into the ECS [213].

Glutamine transport into neurons from the ECS is primarily via *system A* (*SAT* and *ATA*) transporter molecules [213, 214]. Active transport is required to carry glutamine up its concentration gradient (glutamine levels are low in the ECS and high in neurons) [213]. For each glutamine molecule transferred, one Na^+ ion is transferred in the same direction [214], *down* its own concentration gradient. The energy released facilitates active transport of glutamine, so no extra ATP input is necessary. In physiological conditions the majority of

glutamine transported is from the ECS to the neurons, with a negligible flux in the opposite direction.

The final step in the glutamate-glutamine cycle is the following enzymatic reaction [178, 211, 215],

$$\text{Glutamine} + H_2O \underset{k_B}{\overset{k_F}{\rightleftharpoons}} \text{Glutamate} + NH_4, \tag{4.6}$$

which occurs in the mitochondria and converts glutamine to glutamate. Both the forward and reverse reactions are catalysed by *phosphate-activated glutaminase* (*PAG*) [211, 215, 216], and are inhibited by their product glutamate/glutamine via competitive inhibition [217]. For example, the forward reaction is slowed when glutamate molecules bind to PAG in place of glutamine molecules. Glutamate is four times more likely to bind with PAG than glutamine [217]. However, the rate at which PAG converts bound glutamate to glutamine is very slow compared to the rate of glutamate production from glutamine. Overall, glutamine is almost always converted to glutamate and not vice versa [217], but the presence of glutamate slows this reaction.

Links between Metabolism and Pathology in the Inner Retina

The later stages of diabetic retinopathy are well documented (see §1.4), with degradation of the retinal capillary walls leading to an increased permeability, e.g. to glucose [218, 219]. However, the events that initiate the early stages of the disease and damage the retinal neurons remain elusive [85, 86]. Many studies have shown accelerated neuronal cell death in diabetics [218]. In particular, [220] detected elevated extracellular glutamate levels as well as accelerated neuronal cell death. High concentrations of glutamate in the ECS are toxic to neuronal cells, referred to as *excitotoxicity*. This suggests a link between diabetes and excitotoxic damage to the neuronal cells [220]. Our objective is to test whether disruptions to inner retinal metabolism associated with diabetes may explain these findings.

As discussed above, glial cells play a key role in preventing neuronal damage in the inner retina. In healthy individuals, such regulation is very effective. For example, the glial cells regulate glucose delivery to the neurons from the bloodstream, such that glucose arrives in the neuronal cells at approximately the same rate during periods of high blood glucose levels after meals, and low levels just before meals, particularly in the morning. Therefore the fluctuations in the

glucose concentration in the inner retinal tissue surrounding the neurons have an extremely small amplitude compared to the variations in the bloodstream. This regulatory mechanism is tested to the extreme in diabetes patients, who suffer from abnormally high and/or low blood glucose levels at different times of the day.

As well as glucose delivery to the neurons, experimental measurements suggest that diabetes may compromise the glial cells' ability to regulate metabolite levels in the inner retinal tissue in the following ways. Lieth et al. [221] recorded a reduced expression of glutamine synthetase in the glial cells, and also slowed oxidative glutamate metabolism following the onset of diabetes. The former was attributed to a lack of insulin rather than hyperglycemia [221]. Others noted a slowed expression of glutamate transporter proteins, inhibiting glial glutamate uptake from the ECS [220, 222] and speculated this was caused by diabetes-induced damage to glial cells.

Our objective is to test whether the disruptions to inner retinal metabolism outlined above may cause certain chemical species to accumulate until they reach cytotoxic levels in the tissue. Glucose, lactate and glutamate may damage or kill cells if present in high concentrations. As well as glutamate-induced excitotoxicity, if intracellular glucose or lactate concentrations rise too high, osmotic effects draw water into the cell which causes the cells to swell and burst. Furthermore, lactate is acidic, and a build-up changes the intracellular pH, denaturing the enzymes that catalyse vital reactions. Such accumulations of metabolites may lead to neuronal cell damage or death, characteristic features of retinal diseases such as diabetic retinopathy.

4.2 EXISTING MATHEMATICAL MODELS

The objectives outlined in §4.1 suggest that a suitable model of inner retinal metabolism should contain three necessary features. Firstly, it should capture the key aspects of intracellular energy metabolism, the glutamate-glutamine cycle, intercellular transport, and the interactions between these processes in the inner retina. Secondly, it should account for the retinal glial cells' ability to maintain homoeostasis in the inner retinal tissue during normal fluctuations in nutrient levels in the bloodstream. Finally, it should track the glial, neuronal and extracellular concentrations of glucose, lactate and glutamate, so we can investigate the causes of, or contributors to, the accumulation of these toxic

metabolites. We evaluate the modelling approaches discussed below against these criteria.

To our knowledge, no existing mathematical models consider the energy metabolism or the glutamate-glutamine cycle in the inner retina. The most closely related models of retinal metabolism are those describing retinal nutrient concentrations, discussed in Chapter 1, and models considering other aspects of metabolic regulation by the retinal glial cells, such as Ca^{2+} signalling (for example, see [223]), glial regulation of K^+ currents between photoreceptors [224] and glial clearance of NH_4^+ to regulate pH [225].

In order to detect the steps in energy metabolism or the glutamate-glutamine cycle in which chemical species accumulate, and the implications for the neuronal cells, an appropriate model distinguishes between the glial cells, neuronal cells and ECS. Such detail can be included in a variety of different types of mathematical model, including discrete agent-based models, PDE models and compartmental ODE models.

Agent-based models define distinct components of a system, *agents*, and a number of possible states for each agent, with associated probabilities. The state of each agent is allocated initially and updated at every timestep. The probability of a transition to a new state (or remaining in the same state) depends on the agent's current state, its neighbours, and the environment (e.g. the spatial distribution of nutrients). Simulations show the interactions between agents and their response to the environment. Some multi-cell models treat each cell as a separate agent [226], while more detailed models define subcellular agents such as the cytosol, mitochondrial matrix, mitochondrial membrane and the extracellular environment [227], or the elements of a cell membrane [228]. Agent-based models can account for stochasticity, and also spatial heterogeneity in the distribution of nutrients and cells in the tissue.

An alternative way to account for spatial variations within each cell or in the environment is via a PDE model. Kleinle et al. formulated a system of spatiotemporal PDEs to model glutamate release and diffusion through a synaptic terminal [229]. A PDE model by Höfer et al. [223] is designed to examine the transmission of Ca^{2+} waves between retinal glial cells in two dimensions. These waves act as a signalling mechanism, diffusing throughout the ECS and through gap junctions between cells. In a similar vein, using a complex system of PDEs, Tuckwell and Miura [230] model the spread of membrane potential waves in the cortex, including the concentrations of Na^+,

Cl^-, K^+, and Ca^{2+} ions inside and outside the neurons, and the conductance of the cell membranes.

The simplest models that include this level of detail are *compartmental models*, which distinguish between different components or compartments. All elements in a particular compartment are assumed to possess the same important characteristic. We discuss models of this type in detail below, since in Chapter 5 we construct a compartmental model of inner retinal metabolism.

4.2.1 *Deterministic Spatially Averaged Compartmental Models*

A common way to distinguish between different cell types is by using deterministic *spatially averaged* (or so-called "spatially lumped") compartmental models, in which all cells of a particular type are assumed to behave as one homogeneous bulk of tissue within which each constituent cell has the same properties. That is, the behaviour is averaged over all cells within the same compartment. This assumes that each compartment is *well mixed* so that all nutrients are present at sufficiently close proximity to each other to interact, and that there are no time-delays due to diffusion or translocation within each compartment [231]. Time-dependent ODEs describe the processes within the cells in each compartment. Compartmental models have the advantage of simplicity, making analysis of the results possible. Incorporating spatial heterogeneities in a model can significantly increase its complexity, making analysis intractable.

Spatially averaged compartmental models of cellular metabolism use the *Principle of Mass Balance*. This is based on the concept that the rate of change in mass of a nutrient in a given compartment is equal to the sum of the rates at which the nutrient enters or leaves that compartment. Reaction rates are typically given in terms of the rate of change in concentration (in units of $\mathrm{mM\,s^{-1}}$). Multiplying a reaction rate by the volume of the compartment where it occurs gives the resulting rate of change in mass. Sources of a nutrient in a particular compartment include its production from other nutrients and its inward transport from adjacent compartments (and conversely for sinks).

We explain this concept using the simple two compartment system shown in Figure 4.6 in which compartments A and B are assumed to have constant fractional volumes V_A and V_B respectively. There are $M_{C,A}$ and $M_{C,B}$ moles of the chemical species C in compartments A and B respectively, giving concentrations of C_A and C_B respectively ($M_{C,A} = V_A C_A$ and $M_{C,B} = V_B C_B$).

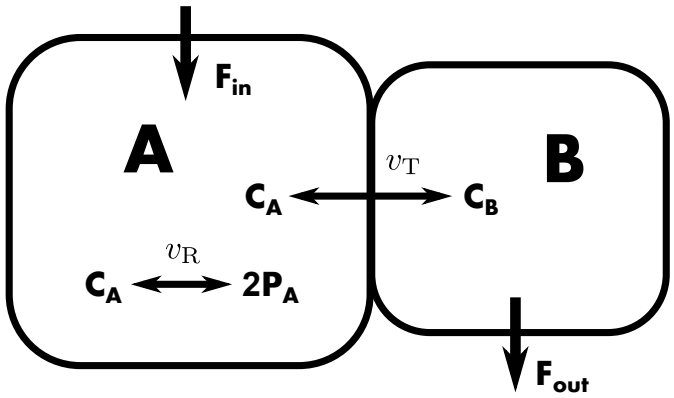


Figure 4.6.: Schematic diagram showing a simple two-compartment problem in which chemical species C is transported reversibly between compartments A and B at rate v_{T}, and reversibly converted to product P at rate v_{R}. Both rates are in units of $\mathrm{mM\,s^{-1}}$. The two-compartment system also interacts with its environment, with fluxes of chemical C into/out of the system via fluxes F_{in} and F_{out}.

Compartment A also contains $M_{P,A}$ moles of chemical species P, at concentration P_A ($M_{P,A} = V_A P_A$). C is transported reversibly from compartment A to B at rate $v_{\mathrm{T}} = v_0(C_A - C_B)$ (i.e. at a rate of $v_0\,\mathrm{s^{-1}}$ in each direction). In compartment A, a reaction reversibly converts each mole of C to 2 moles of the product P at rate $v_{\mathrm{R}} = v_0(C_A - 2P_A)$ (again at a rate of $v_0\,\mathrm{s^{-1}}$ in each direction). There is also an influx of chemical C into compartment A from an external source at rate F_{in}, and an efflux from compartment B at rate F_{out}, where F_{in} and F_{out} are specified in units of $\mathrm{mmol\,s^{-1}}$.

Using the Principle of Mass Balance the following ODE represents the rate of change in the number of moles of C in compartment A,

$$\frac{dM_{C,A}}{dt} = \frac{d}{dt}\left(V_A C_A\right) = F_{\mathrm{in}} - \underbrace{V_A v_0\left(C_A - C_B\right)}_{\text{Transport (compartment A}\rightarrow\text{B)}} - \underbrace{V_A v_0\left(C_A - 2P_A\right)}_{\text{Conversion of C to P}}. \tag{4.7a}$$

Since V_A is constant we have,

$$\frac{dC_A}{dt} = \frac{F_{\mathrm{in}}}{V_A} - 2v_0 C_A + v_0 C_B + 2v_0 P_A. \tag{4.7b}$$

Transport of C from compartment A to B depletes the number of moles in compartment A at the same rate that it increases the number of moles in

compartment B. Thus the rate of change in the number of moles of C in compartment B is,

$$\frac{d}{dt}\left(V_B C_B\right) = \underbrace{V_A v_0 \left(C_A - C_B\right)}_{\text{Transport (compartment A}\rightarrow\text{B)}} - F_{\text{out}}. \tag{4.7c}$$

Since the reaction in compartment A produces 2 moles of P per mole of C consumed, the rate of change in the number of moles of P in compartment A is,

$$\frac{d}{dt}\left(V_A P_A\right) = \underbrace{V_A v_0 \left(C_A - 2P_A\right)}_{\text{Conversion of C to P}}. \tag{4.7d}$$

We note that the total rate of change of the number of moles in the system $(M_{C,A} + M_{C,B} + M_{P,A})$ is,

$$\frac{d}{dt}\left(M_{C,A} + M_{C,B} + M_{P,A}\right) = \underbrace{F_{\text{in}}}_{\text{Influx into system}} - \underbrace{F_{\text{out}}}_{\text{Efflux out of system}}.$$

We now make a more general statement of the Principle of Mass Balance for a system involving N compartments, each denoted by index i, having a constant fractional volume of V_i and containing n_i chemical species, k_i reactions and q_i transport rates. For each chemical species, there is a corresponding total influx/efflux from/to the external environment. In the system there are a total of $n_{\text{Tot}} = \sum_{i=0}^{N} n_i$ concentrations, $k_{\text{Tot}} = \sum_{i=0}^{N} k_i$ chemical reactions and $q_{\text{Tot}} = \sum_{i=0}^{N} q_i$ transport rates. We denote the fractional compartmental volumes by $V_1, V_2, \cdots V_N$, concentrations by $C_1, C_2, \cdots C_{n_{\text{Tot}}}$, reaction rates by $v_{\text{R},1}, v_{\text{R},2}, \cdots v_{\text{R},k_{\text{Tot}}}$, transport rates by $v_{\text{T},1}, v_{\text{T},2}, \cdots v_{\text{T},q_{\text{Tot}}}$, and influxes/effluxes to the system by $F_1, F_2, \cdots F_{n_{\text{Tot}}}$, and incorporate these quantities in the following vectors,

$$\begin{aligned}
\mathbf{C} &= \left(C_1, C_2, \cdots C_{n_{\text{Tot}}}\right)^T, \\
\mathbf{v} &= \left(v_{\text{R},1}, v_{\text{R},2}, \cdots v_{\text{R},k_{\text{Tot}}}, v_{\text{T},1}, v_{\text{T},2}, \cdots v_{\text{T},q_{\text{Tot}}}\right)^T, \\
\mathbf{F} &= \left(F_1, F_2, \cdots F_{n_{\text{Tot}}}\right)^T.
\end{aligned}$$

We note that, in general, the elements of $\mathbf{v}$ and $\mathbf{F}$ depend on the concentrations and time, reflecting the appropriate reaction kinetics involved. Then the Principle of Mass Balance gives the following equation,

$$\frac{d\mathbf{C}}{dt} = \boldsymbol{\theta}\mathbf{S}\mathbf{v}(\mathbf{C}, t) - \mathbf{F}(\mathbf{C}, t), \tag{4.8}$$

where $\boldsymbol{\theta}$ and $\mathbf{S}$ denote the (constant) *relative volume* matrix and the *stoichiometry* matrix respectively. The stoichiometry matrix is an $n_{\text{Tot}} \times (k_{\text{Tot}} + q_{\text{Tot}})$ matrix whose ith column represents the number of molecules of each chemical produced/consumed when the ith transport or reaction takes place ($i = 1, 2, \cdots (k_{\text{Tot}} + q_{\text{Tot}})$). We note that each transport rate affects the concentrations in two compartments, whereas its value quantifies the rate of change of concentration in just one of the compartments, which we refer to as the *reference compartment* (see, for example, the effect of the rate v_{T} on the concentrations C_A and C_B in equations (4.7a) and (4.7c)). This is the reason for defining the relative volume matrix $\boldsymbol{\theta}$, a $(k_{\text{Tot}} + q_{\text{Tot}}) \times n_{\text{Tot}}$ matrix, whose components $\theta_{i,j}$ are the relative volumes of the reference compartment for the ith transport or reaction rate, and the compartment containing the jth affected concentration. All elements of $\boldsymbol{\theta}$ that multiply the reaction rates in $\mathbf{v}$ rather than transport rates (i.e. those in rows 1 to k_{Tot}) are equal to 1.

The earliest compartmental models of cerebral metabolism are simple, focusing on reaction rates at the steady state [232], where, from equation (4.8), $\boldsymbol{\theta}\mathbf{S}\mathbf{v} = \mathbf{F}$. The outputs from the whole system (i.e. the elements of $\mathbf{F}$) are referred to as *cerebral metabolic rates* (*CMR*). The CMR can be measured using brain imaging techniques such as MRI and PET, in which patients are injected with radioactive isotopes of molecules involved in cellular metabolism (*tracer molecules*). These isotopes are incorporated into the cerebral metabolic pathways and scans reveal the concentrations of the tracer molecules at each step of the relevant pathways. Steady state compartmental models use nonlinear tracer kinetics to incorporate this clinical data, and estimate the reaction fluxes at specific steps of the TCA and glutamate-glutamine cycles [233–237]. These models facilitate the interpretation of clinical data, and enable researchers to estimate parameters in humans. However, since these models assume steady state metabolite levels and reaction rates, model solutions from one dataset cannot be used to make predictions about future brain scans, since nutrient levels (e.g. glucose and lactate concentrations) vary in time and also between patients.

More realistic models incorporate substrate levels and are dynamic. The mathematical models that give the greatest insight into glial and neuronal metabolic regulation of glucose, lactate and glutamate levels are those designed to test the viability of the glia-neuron lactate shuttle hypothesis (GNLSH, see §4.1), particularly four models of cerebral metabolism, by Aubert and Costalat [1], Cloutier et al. [238], Simpson et al. [239] and Calvetti and Somersalo [240]. In the following sections we summarise these models and the results they generate. The first model, constructed by Aubert and Costalat [1], incorporates all of the processes we consider important in energy metabolism and nutrient transport. The latter three models are similar to the first, with a small number of alterations. The addition of the glutamate-glutamine cycle in [238] and [240] is also important, but these models do not incorporate its links with energy metabolism, meaning they cannot be used to fulfil our objective: to predict accumulations in the glutamate-glutamine cycle that result from fluctuating blood glucose levels. We begin by describing Aubert and Costalat's model [1], and then explain how the other models differ from it.

4.2.2 *Aubert and Costalat's Model of Cerebral Metabolism [1]*

We now discuss Aubert and Costalat's model [1], summarised in Figure 4.7. To facilitate comparison with the model we will develop in Chapter 5, we modify the notation from that originally proposed in [1]. The dependent variables are glucose (G), lactate (L), glyceraldehyde-3-phosphate (GAP), phosphoenolpyruvate (PEP), pyruvate (PYR), nicotinamide adenine dinucleotide (NADH), ATP (A), ADP (B), AMP (AMP), creatine phosphate (Z), Na^+ (Na^+), oxygen (U), venous volume (V_v) and deoxyhemoglobin (dHb). The capillary, glial, ECS and neuronal compartments are denoted by subscripts b, g, s, n respectively, with the fractional capillary, glial, ECS and neuronal volumes given by V_b, V_g, V_s and V_n respectively. Concentrations are measured in units of mM or μM, whereas the fractional volumes represent a proportion of the tissue volume and, as such, are dimensionless.

Intracellular reaction rates are denoted by $v_{E,c}$, where E denotes the intracellular reaction, (usually the enzyme catalysing it), and c indicates the compartment in which it occurs ($c \in \{b, g, s, n\}$). Transport rates are denoted by $v_{I,jk}$, where I

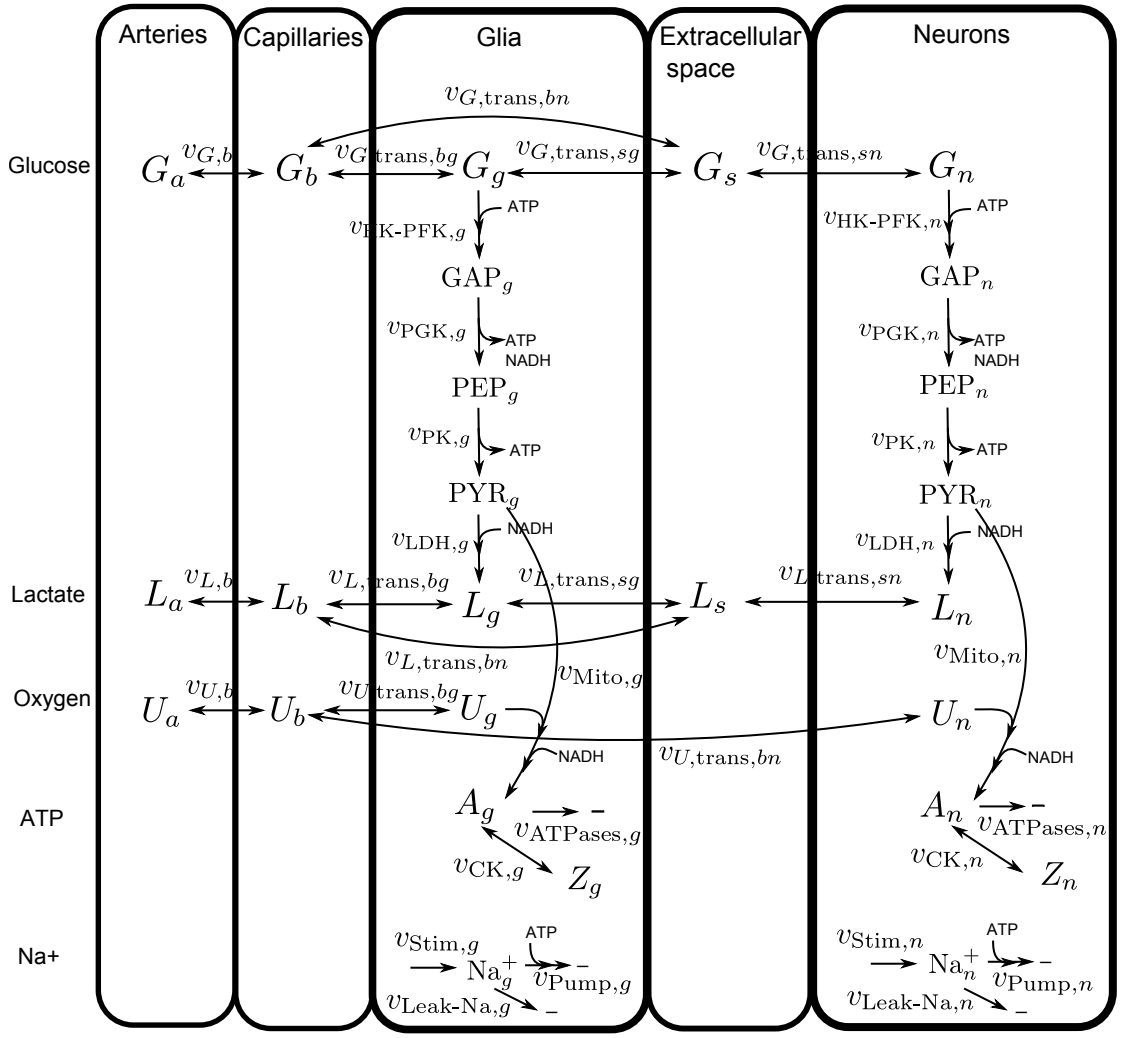


Figure 4.7.: Schematic diagram of Aubert and Costalat's model [1] of cerebral metabolism (see equations (4.10)–(4.19)).

represents the chemical being transported from compartment j to compartment k. We indicate Michaelis-Menten kinetics in the following way,

$$\mathrm{M}\left(S; V_{\max}, K_m\right) = V_{\max}\frac{S}{S+K_m}, \tag{4.9}$$

where $V_{\max}$ and K_m are positive constants. The reaction rate increases monotonically with the substrate concentration S, but saturates at the value $V_{\max}$ for large substrate concentrations. We note that when the substrate concentration S is equal to K_m, $\mathrm{M}\left(S; V_{\max}, K_m\right) = V_{\max}/2$ and the rate is half maximal. Using the above notation the metabolite dynamics are governed by the following system of time-dependent ODEs. In the glial and neuronal cells (i.e. for $x \in \{g, n\}$),

$$\frac{dG_x}{dt} = v_{G,\text{trans},x} - v_{\text{HK-PFK},x}, \tag{4.10a}$$

$$\frac{d\text{GAP}_x}{dt} = 2v_{\text{HK-PFK},x} - v_{\text{PGK},x}, \tag{4.10b}$$

$$\frac{d\text{PEP}_x}{dt} = v_{\text{PGK},x} - v_{\text{PK},x}, \tag{4.10c}$$

$$\frac{d\text{PYR}_x}{dt} = v_{\text{PK},x} - v_{\text{LDH},x} - v_{\text{Mito},x}, \tag{4.10d}$$

$$\frac{d\text{NADH}_x}{dt} = v_{\text{PGK},x} - v_{\text{LDH},x} - v_{\text{Mito},x}, \tag{4.10e}$$

$$\frac{dL_x}{dt} = v_{L,\text{trans},x} - v_{\text{LDH},x}, \tag{4.10f}$$

$$\frac{dA_x}{dt} = \left(1-\phi(A_x)\right)^{-1}\left[-2v_{\text{HK-PFK},x} + v_{\text{PGK},x} + v_{\text{PK},x} - v_{\text{ATPases},x} - v_{\text{Pump},x} + n_{\text{OP}}v_{\text{Mito},x} + v_{\text{CK},x}\right], \tag{4.10g}$$

$$\frac{dZ_x}{dt} = -v_{\text{CK},x}, \tag{4.10h}$$

$$\frac{d\text{Na}_x^+}{dt} = v_{\text{Leak-Na},x} - 3v_{\text{Pump},x} + v_{\text{Stim},x}(t), \tag{4.10i}$$

$$\frac{dU_x}{dt} = v_{U,bx} - n_{\text{Aero}}v_{\text{Mito},x}; \tag{4.10j}$$

in the blood vessels,

$$\frac{dG_b}{dt} = v_{G,b} - \theta_{sb}v_{G,\text{trans},bs} - \theta_{gb}v_{G,\text{trans},bg}, \tag{4.11a}$$

$$\frac{dL_b}{dt} = v_{L,b} - \theta_{sb}v_{L,\text{trans},bs} - \theta_{gb}v_{L,\text{trans},bg}, \tag{4.11b}$$

$$\frac{dU_b}{dt} = v_{U,b} - \theta_{nb} v_{U,bn} - \theta_{gb} v_{U,bg}; \tag{4.11c}$$

in the ECS,

$$\frac{dG_s}{dt} = v_{G,\text{trans},bs} - \theta_{gs} v_{G,\text{trans},sg} - \theta_{ns} v_{G,\text{trans},sn}, \tag{4.12a}$$

$$\frac{dL_s}{dt} = v_{L,\text{trans},bs} - \theta_{gs} v_{L,\text{trans},sg} - \theta_{ns} v_{L,\text{trans},sn}; \tag{4.12b}$$

where,

$$\theta_{sb} = \frac{V_s}{V_b}, \qquad \theta_{gb} = \frac{V_g}{V_b}, \qquad \theta_{xs} = \frac{V_x}{V_s}, \tag{4.13}$$

$$v_{G,\text{trans},x} = \begin{cases} v_{G,\text{trans},bg} + v_{G,\text{trans},sg} & \text{if } x = g, \\ v_{G,\text{trans},sn} & \text{if } x = n, \end{cases} \tag{4.14}$$

$$v_{L,\text{trans},x} = \begin{cases} v_{L,\text{trans},bg} + v_{L,\text{trans},sg} & \text{if } x = g, \\ v_{L,\text{trans},sn} & \text{if } x = n, \end{cases} \tag{4.15}$$

and the quantity $\phi(A_x)$ in equation (4.10g) is given by,

$$\phi(A_x) = -1 + \frac{1}{2} q_{\text{AK}} - \frac{1}{2} \sqrt{q_{\text{AK}}^2 + 4 q_{\text{AK}} \left(\frac{A_{\text{Tot}}}{A_x} - 1 \right)} + \frac{q_{\text{AK}} A_{\text{Tot}}}{A_x \sqrt{q_{\text{AK}}^2 + 4 q_{\text{AK}} \left(\frac{A_{\text{Tot}}}{A_x} - 1 \right)}}. \tag{4.16}$$

Details on the reaction rates in equations (4.10)-(4.14) are given below. The model has several conserved quantities: $(\text{ATP} + \text{ADP} + \text{AMP})$, $(\text{NADH} + \text{NAD}^+)$ and $(\text{CrP} + \text{Cr})$. We can exploit these identities to eliminate the following dependent variables,

$$B_x = \frac{A_x}{2} \left(-q_{\text{AK}} + \sqrt{q_{\text{AK}}^2 + 4 q_{\text{AK}} \left(\frac{A_{\text{Tot}}}{A_x} - 1 \right)} \right), \tag{4.17a}$$

$$\text{AMP}_x = A_{\text{Tot}} - A_x - B_x, \tag{4.17b}$$

$$\text{NAD}_x^+ = N_{\text{Tot}} - \text{NADH}_x, \tag{4.17c}$$

$$C_x = C - Z_x. \tag{4.17d}$$

To close the system, the following initial conditions are prescribed,

$$W_x(t=0) = W_{x,0}, \tag{4.18}$$

where $W \in \{G, \mathrm{GAP}, \mathrm{PEP}, \mathrm{PYR}, \mathrm{NADH}, L, A, Z, \mathrm{Na}^+, U\}$ and where $W_{x,0}$ represents the resting steady state value of the corresponding variable. Resting steady state values are as follows,

$$\begin{aligned}
G_{b,0} &= 4.56\,\mathrm{mM}, & G_{x,0} &= 1.2\,\mathrm{mM}, & G_{s,0} &= 1.2\,\mathrm{mM},\\
\mathrm{GAP}_{x,0} &= 5.6\,\mu\mathrm{M}, & \mathrm{PEP}_{x,0} &= 20\,\mu\mathrm{M}, & \mathrm{PYR}_{x,0} &= 0.16\,\mathrm{mM},\\
L_{b,0} &= 0.35\,\mathrm{mM}, & L_{g,0} &= 1.09\,\mathrm{mM}, & L_{s,0} &= 1\,\mathrm{mM},\\
L_{n,0} &= 1\,\mathrm{mM}, & A_{x,0} &= 2.2\,\mathrm{mM}, & U_{b,0} &= 7\,\mathrm{mM},\\
U_{x,0} &= 26\,\mu\mathrm{M}, & \mathrm{NADH}_{g,0} &= 28\,\mu\mathrm{M}, & \mathrm{NADH}_{n,0} &= 26\,\mu\mathrm{M},\\
Z_{x,0} &= 5\,\mathrm{mM}, & \mathrm{Na}^+_{x,0} &= 15\,\mathrm{mM}, &&
\end{aligned} \tag{4.19}$$

for $x \in \{g, n\}$. Aubert and Costalat also included ODEs for two additional dependent variables, V_v and dHb, on which the signal detected in MRI scans depends. This enabled them to use their model to predict MRI signals and compare their predictions with experimental results. We note that these two variables decouple from the others and are thus not shown in equations (4.10)-(4.14).

Nutrient Transport

Experimental observations suggest that the rates of glucose and lactate transport between the capillaries, glial cells, ECS and neurons follow Michaelis-Menten kinetics [193, 194]. In Aubert and Costalat's model the rate of glucose and lactate transport from compartment A to B is given by,

$$\begin{aligned}
v_{G,\mathrm{trans},AB} = {} & \mathrm{M}\left(G_A; v^{\max}_{G,\mathrm{trans},AB}, K_{G,\mathrm{trans},AB}\right)\\
& -\mathrm{M}\left(G_B; v^{\max}_{G,\mathrm{trans},AB}, K_{G,\mathrm{trans},AB}\right),
\end{aligned} \tag{4.20a}$$

$$\begin{aligned}
v_{L,\mathrm{trans},AB} = {} & \mathrm{M}\left(L_A; v^{\max}_{L,\mathrm{trans},AB}, K_{L,\mathrm{trans},AB}\right)\\
& -\mathrm{M}\left(L_B; v^{\max}_{L,\mathrm{trans},AB}, K_{L,\mathrm{trans},AB}\right),
\end{aligned} \tag{4.20b}$$

respectively, where G_A and G_B are the concentrations of glucose in compartments A and B respectively and similarly for lactate transport. This reaction rate is also used to model glucose and lactate transport in [1, 238, 240–243]. Implicit in this expression is the assumption that the binding kinetics for glucose/lactate molecules and their transporter molecules are the same on either side of the cell membrane (*symmetric*), and that the action of the transporter molecules is not inhibited by binding with molecules on the opposite side of the membrane. From the definitions of $v_{L,\text{trans},sg}$ and $v_{L,\text{trans},sn}$, glia-neuron lactate shuttling occurs if $v_{L,\text{trans},sg} < 0$ and $v_{L,\text{trans},sn} > 0$.

Linear exchange of glucose and lactate between the arteries and capillaries, and of oxygen between the bloodstream and the glial/neuronal cells are modelled via the following reactions,

$$v_{G,b} = \frac{2F_{\text{in}}(t)}{V_b}\left(G_a - G_b\right), \tag{4.21a}$$

$$v_{L,b} = \frac{2F_{\text{in}}(t)}{V_b}\left(L_a - L_b\right), \tag{4.21b}$$

$$v_{U,b} = \frac{2F_{\text{in}}(t)}{V_b}\left(U_a - U_b\right), \tag{4.21c}$$

$$v_{U,bx} = \frac{PS_{\text{cap}}}{V_x}\left(k_{U,bx}\left(\frac{\text{HbOP}}{U_b} - 1\right)^{-1/\text{nh}} - U_x\right), \tag{4.21d}$$

with,

$$F_{\text{in}}(t)\begin{cases}\left(1 + \dfrac{\alpha_F t}{t_1}\right)F_0 & \text{if } t < t_1,\\ \left(1 + \alpha_F\right)F_0 & \text{if } t_1 \leq t < t_{\text{end}},\\ \left(1 - \alpha_F\dfrac{t - (t_{\text{end}} + t_1)}{t_1}\right)F_0 & \text{if } t_{\text{end}} \leq t < t_{\text{end}} + t_1,\\ F_0 & \text{if } t > t_{\text{end}} + t_1.\end{cases} \tag{4.22}$$

In equation (4.21d), P, S_{cap} and V_x denote the permeability of the blood-brain barrier to oxygen, the surface area of the capillaries and the fractional glial/neuronal intracellular volume respectively. The term $k_{U,bx}\left((\text{HbOP}/U_b) - 1\right)^{-1/\text{nh}}$ represents the average concentration of oxygen in the blood plasma. The expression for $F_{\text{in}}(t)$ in equation (4.22) is taken from [244] where it was found to fit well with the capillary blood flow measured in human participants during a finger-tapping task and the subsequent resting period. The parameters F_0

and α_F denote the resting capillary blood flow rate and its increase fraction respectively. Further details on glucose, lactate and oxygen dynamics in the bloodstream are given in [241, 245, 246].

Energy Metabolism

The glycolytic pathway is modelled via three combined reaction rates. Steps 1–3 of the glycolytic pathway (i.e. conversion of glucose to GAP, with the first and third steps catalysed by HK and PFK enzyme respectively) are represented by the following reaction rate,

$$v_{\text{HK-PFK},x} = \mathrm{M}\left(G_x; v^{max}_{\text{HK-PFK},x}, K_{\text{HK-PFK},G,x}\right) \frac{A_x}{A_x^4 + K_{\text{HK-PFK},A,x}}; \tag{4.23}$$

steps 4–9 (conversion of GAP to PEP, with step 9 catalysed by PGK) are represented by,

$$v_{\text{PGK},x} = k_{\text{PGK},x}\text{GAP}_x B_x \frac{\text{NAD}^+_x}{\text{NADH}_x}; \tag{4.24}$$

and step 10 (conversion of PEP to pyruvate, catalysed by PK) is represented by,

$$v_{\text{PK},x} = k_{\text{PK},x}\text{PEP}_x B_x. \tag{4.25}$$

The ATP-dependence of $v_{\text{HK-PFK},x}$, taken from [247], is chosen so that $v_{\text{HK-PFK},x}$ tends to zero as $A_x \to 0$ while at typical intracellular ATP levels $v_{\text{HK-PFK},x}$ is a decreasing function of A_x. Aubert and Costalat multiply the ATP-dependent expression in [247] by an increasing, saturating function of the other key substrate (glucose) to give equation (4.23). The rates of irreversible reactions $v_{\text{PGK},x}$, $v_{\text{PK},x}$ are assumed not to saturate and thus modelled using the Law of Mass Action. The reaction rate $v_{\text{PGK},x}$ is a linear function of $\text{NAD}^+_x/\text{NADH}_x$ (which represents the *redox state*, see [1] for more details).

Pyruvate produced by glycolysis is the substrate for oxidative metabolism. All processes involved in oxidative metabolism are combined into a single reaction in which pyruvate, ADP, free phosphate and oxygen combine to produce ATP, carbon dioxide and water (see net reaction (4.2)), at rate,

$$v_{\text{Mito},x} = \mathrm{M}\left(\text{PYR}_x; v^{\max}_{\text{Mito},x}, K_{\text{Mito,PYR},x}\right) \mathrm{M}\left(U_x; 1, K_{\text{Mito},U,x}\right) \mathrm{M}\left(B_x; 1, K_{\text{Mito},B,x}\right). \tag{4.26}$$

Energy metabolism and lactate transport are linked by the reversible conversion of pyruvate to lactate by LDH enzyme at rate,

$$v_{\mathrm{LDH},x} = k^{+}_{\mathrm{LDH},x}\mathrm{PYR}_x\mathrm{NADH}_x - k^{-}_{\mathrm{LDH},x}L_x\mathrm{NAD}^{+}_x. \tag{4.27}$$

This reaction is modelled using the Law of Mass Action, so that it does not saturate with increasing substrate concentrations in either direction.

Effects of Neuronal Activation

Aubert and Costalat suppose that the neurons are activated from time $t = 0$ until $t = t_{\mathrm{end}}$ followed by a period of inactivity. The rate at which Na^+ ions flow into the neurons is assumed to be,

$$v_{\mathrm{Stim},n}(t) = \begin{cases} v_{1,n} + v_{2,n}\dfrac{t}{\tau_{\mathrm{Stim},n}}\exp\left(-\dfrac{t}{\tau_{\mathrm{Stim},n}}\right) & \text{if } 0 \leq t \leq t_{\mathrm{end}}, \\ 0 & \text{otherwise.} \end{cases} \tag{4.28}$$

According to equation (4.28), there is an influx of Na^+ ions into the neurons during neuronal activation, due to action potentials and postsynaptic potentials. The exponential decay of the term $v_{2,n}(t/\tau_{\mathrm{Stim},n})\exp(-t/\tau_{\mathrm{Stim},n})$ at long times accounts for neuronal habituation (i.e. a decreased neuronal response to a stimulus if its presence is prolonged). $v_{\mathrm{Stim},n}(t) = 0$ when the neurons are inactive, but there is still a small current of Na^+ through the cell membrane, referred to as the *leak current* (see §1.2 for more details), represented by the term v_{Leak} in [1]. v_{Leak} is equal to the current, I, of Na^+ ions through the closed channels (which is the charge passing through the membrane per unit time) multiplied by the Na^+ concentration per unit charge. One molecule of Na^+ has a charge of 1e, where e is the elementary charge. Therefore, the charge of one mole of Na^+ is $F = N_A\mathrm{e}$, which is Faraday's constant (where N_A is Avagadro's number). Then the rate of change in the number of moles of Na^+ inside the neuronal cells is,

$$v_{\mathrm{Leak}}V_x = I \times (\mathrm{Na}^+ \text{ concentration per unit charge}) = \frac{I}{F}. \tag{4.29}$$

According to Ohm's Law, the current passing through the cell membrane is equal to the potential difference across the membrane multiplied by its

conductivity, σ. In [1], $g^x_{\text{Na}} S_m / V_x$ denotes the conductivity of the cell membrane per unit cell volume. Hence,

$$I = \sigma \times \text{Potential difference} = \left(g^x_{\text{Na}} \frac{S_m}{V_x} \right) V_x \times \text{Potential difference}.$$

The potential difference across the cell membrane is equal to the difference between the Nernst potential, E, for Na^+ (see equation (1.2) with $z = 1$) and the membrane potential, V_m, so that,

$$I = \left(g^x_{\text{Na}} \frac{S_m}{V_x} \right) V_x (E - V_m). \tag{4.30}$$

Then, combining equations (4.29) and (4.30), and substituting for E using equation (1.2), we obtain,

$$v_{\text{Leak-Na},x} = \frac{S_m}{V_x} \frac{g_{\text{Na},x}}{F} \left(\frac{RT}{F} \ln \left(\frac{\text{Na}^+_e}{\text{Na}^+_x} \right) - V_m \right). \tag{4.31}$$

Aubert and Costalat [1] assumed V_m to be constant since they found in [241] that including the dependence on $v_{\text{Stim}}(t)$ made little difference to the results.

The Na^+/K^+ ATPase pumps rebalance ionic concentrations across the cell membrane via active transport which consumes ATP at rate $v_{\text{Pump},n}$ (see §4.1 for more details), and causes an outflow of Na^+ ions at rate $3v_{\text{Pump},n}$ (i.e. 1 molecule of ATP is consumed for the transport of 3 Na^+ ions out of the neuronal cells). Reaction rate $v_{\text{Pump},n}$ is modelled as,

$$v_{\text{Pump},n} = \text{Na}^+_n \text{M} \left(A_n; v^{\max}_{\text{Pump},n} \frac{S_m}{V_n}, K_{\text{Pump},n} \right). \tag{4.32}$$

This expression is taken from [248], who found this functional form to be the best fit for experimental measurements of the dose-dependence on ATP.

There is an influx of Na^+ to the glial cells at rate $v_{\text{Stim},g}(t)$ during neuronal stimulation, representing the cotransport of Na^+ ions with glutamate into the glia. The rate of glial glutamate (and hence Na^+) uptake is proportional to the rate of glutamate release from the neurons. This, in turn, is proportional to $v_{\text{Stim},n}(t)$. Therefore, the expression for $v_{\text{Stim},g}(t)$ has the same functional form as its neuronal counterpart. The glial cells also possess Na^+/K^+ ATPase pumps, performing active transport at rate $v_{\text{Pump},g}$, and are assumed to have a baseline rate of Na^+ (and glutamate) uptake, $v_{\text{Leak},g}$, analogous to the leak

current in the neurons. Both $v_{\text{Pump},g}$ and $v_{\text{Leak},g}$ are assumed to have the same functional forms as their neuronal counterparts since the physical mechanisms are the same.

Neuronal activation (i.e. an increase in $v_{\text{Stim},g}$ and $v_{\text{Stim},n}$) leads to an influx of Na^+ ions into the glia and neurons (see equations (4.10i) and (4.28)). Na^+ becomes more highly concentrated inside glial and neuronal cells, increasing the rate at which it is actively transported out via Na^+/K^+ ATPase pumps (see equation (4.32)), with a concomitant rise in the ATP demand (see equation (4.10g)). Therefore, ATP is more rapidly broken down into ADP, leading to a higher ADP concentration, increasing the rate of ATP production via glycolysis, oxidative metabolism and/or from creatine phosphate. Thus, the change in $v_{\text{Stim},g}$ and $v_{\text{Stim},n}$ between resting and active conditions perturbs other concentrations as described above, causing the time-evolution of the system at the onset of neuronal stimulation and the return to resting conditions.

Other Rates of ATP Production and Consumption

As discussed in Chapter 1, ATP can combine reversibly with creatine, catalysed by creatine kinase (CK), to produce ADP and creatine phosphate, storing energy in a form which can be quickly converted to ATP as required. The forward and reverse reactions associated with the CK reaction are modelled using the Law of Mass Action, giving,

$$v_{\text{CK},x} = k^+_{\text{CK},x} Z_x B_x - k^-_{\text{CK},x} C_x A_x. \tag{4.33}$$

The rate,

$$v_{\text{ATPases},x} = \bar{v}_{\text{ATPases},x}, \tag{4.34}$$

represents the assumed constant baseline rate of ATP consumption. As a result ATP consumption occurs even when the ATP levels are very low and physically unrealistic negative concentrations can arise. Our model, presented in Chapter 5 overcomes this difficulty.

Parameter Estimates and Reproduction of Simulation Results

Where possible parameter values and typical concentrations were estimated from the literature (see [241] for details). The remaining parameters were

determined by fitting simulation results to empirical data on the time courses of lactate concentrations. The parameter values stated in [1] are given in Tables 4.1–4.2.

In Chapter 5 we will compare parts of Aubert and Costalat's model [1] with components of our own model. For this comparison we require information about concentrations and reaction rates not recorded in [1]. We therefore integrate equations (4.10)–(4.19) using *ode15s*, a solver for stiff ODEs (since the concentrations evolve over very different timescales, this is a stiff system; see Chapter 2 for more details on solving stiff ODEs).

Using the parameter values in Tables 4.1–4.2 and the resting steady state concentrations in equations (4.18) as initial conditions, we can replicate the results in Figures 2–4 of [1], as shown in Figures 4.8–4.13. In order to reproduce the resting steady states and simulations results in Figures 2–4 of [1], we found it necessary to modify the values of $v_{\text{Mito},x}$ and $v_{\text{ATPases},x}$ from the values in the left hand column of Table 4.1 to those in the right hand column (for details, see Appendix A).

Interpretation of Results and Conclusions

Figures 4.8–4.13 show the time evolution of certain model variables and the following quantities:

- The ratio of the NADH to the NAD^+ concentration in the neuronal cells is shown in Figures 4.8(a), 4.10(a) and 4.12(e). This ratio in the glial cells is plotted in Figures 4.8(b), 4.10(b) and 4.12(f), and the averaged ratio over the whole tissue (including all cell types), i.e.,

$$\text{rNAD}_T = \frac{V_g\text{NADH}_g + V_n\text{NADH}_n}{V_g\text{NAD}_g^+ + V_n\text{NAD}_n^+},$$

  is plotted in Figures 4.9(b), 4.11(b) and 4.13(f).

- The average lactate concentration in the whole tissue,

$$L_T = V_bL_b + V_gL_g + V_sL_s + V_nL_n,$$

  is plotted in Figures 4.9(a), 4.11(a) and 4.13(e).

- The increase in pyruvate production from the resting level in each cell type x, $v_{\text{PK},x} - v_{\text{PK},x,0}$, is shown in Figures 4.9(c), 4.11(c) and 4.13(a).

Parameter	Value used in [1]	Modified value (if any)
n_{OP}	15	
n_{Aero}	3	
$k_{\mathrm{HK\text{-}PFK},n}$	$0.12\,\mathrm{s}^{-1}$	
$k_{\mathrm{HK\text{-}PFK},g}$	$0.047\,\mathrm{s}^{-1}$	
$K_{\mathrm{HK\text{-}PFK},G,x}$	0.05 mM	
$K_{\mathrm{HK\text{-}PFK},A,x}$	1 mM	
$k_{\mathrm{PGK},n}$	$42.6\,\mathrm{mM\,s}^{-1}$	
$k_{\mathrm{PGK},g}$	$18.2\,\mathrm{mM\,s}^{-1}$	
N	0.212 mM	
$k_{\mathrm{PK},n}$	$86.7\,\mathrm{mM\,s}^{-1}$	
$k_{\mathrm{PK},g}$	$34\,\mathrm{mM\,s}^{-1}$	
$k^{+}_{\mathrm{LDH},n}$	$2000\,(\mathrm{mM})^{-1}\,\mathrm{s}^{-1}$	
$k^{+}_{\mathrm{LDH},g}$	$780\,(\mathrm{mM})^{-1}\,\mathrm{s}^{-1}$	
$k^{-}_{\mathrm{LDH},n}$	$44.8\,(\mathrm{mM})^{-1}\,\mathrm{s}^{-1}$	
$k^{-}_{\mathrm{LDH},g}$	$17.6\,(\mathrm{mM})^{-1}\,\mathrm{s}^{-1}$	
$v^{\max}_{\mathrm{Mito},n}$	$0.021\,\mathrm{mM\,s}^{-1}$	$0.0403\,\mathrm{mM\,s}^{-1}$
$v^{\max}_{\mathrm{Mito},g}$	$5 \times 10^{-3}\,\mathrm{mM\,s}^{-1}$	$9.7 \times 10^{-3}\,\mathrm{mM\,s}^{-1}$
$K_{\mathrm{Mito,PYR},x}$	0.05 mM	
$K_{\mathrm{Mito},U,x}$	1×10^{-3} mM	
$K_{\mathrm{Mito},B,x}$	5×10^{-3} mM	
$v_{\mathrm{ATPases},n}$	$0.17\,\mathrm{mM\,s}^{-1}$	$0.1716\,\mathrm{mM\,s}^{-1}$
$v_{\mathrm{ATPases},g}$	$0.02\,\mathrm{mM\,s}^{-1}$	$0.0212\,\mathrm{mM\,s}^{-1}$
$k^{+}_{\mathrm{CK},n}$	$0.36\,(\mathrm{mM})^{-1}\,\mathrm{s}^{-1}$	
$k^{+}_{\mathrm{CK},g}$	$0.14\,(\mathrm{mM})^{-1}\,\mathrm{s}^{-1}$	
$k^{-}_{\mathrm{CK},n}$	$2 \times 10^{-3}\,(\mathrm{mM})^{-1}\,\mathrm{s}^{-1}$	
$k^{-}_{\mathrm{CK},g}$	$7.8 \times 10^{-4}\,(\mathrm{mM})^{-1}\,\mathrm{s}^{-1}$	
C	10 mM	

Table 4.1.: Values of energy metabolism parameters stated in [1], and the changes that were made in our simulations to reproduce Aubert and Costalat's results in [1].

Parameter	Value given in [1]
V_s	0.2
V_b	5.5×10^{-3}
V_g	0.25
V_n	0.45
$v^{\max}_{G,\text{trans},sn}$	$5230\,\text{mM}\,\text{s}^{-1}$
$v^{\max}_{G,\text{trans},sg}$	$1020\,\text{mM}\,\text{s}^{-1}$
$K_{G,\text{trans},sn}$	9 mM
$K_{G,\text{trans},sg}$	9 mM
$v^{\max}_{G,\text{trans},bg}$	$9.3 \times 10^{-3}\,\text{mM}\,\text{s}^{-1}$
$K_{G,\text{trans},bg}$	9 mM
$v^{\max}_{G,\text{trans},bs}$	$0.118\,\text{mM}\,\text{s}^{-1}$
$K_{G,\text{trans},bs}$	9 mM
$v^{\max}_{L,\text{trans},sn}$	$0.29\,\text{mM}\,\text{s}^{-1}$
$v^{\max}_{L,\text{trans},sg}$	$0.076\,\text{mM}\,\text{s}^{-1}$
$K_{L,\text{trans},sn}$	0.5 mM
$K_{L,\text{trans},sg}$	0.5 mM
$v^{\max}_{L,\text{trans},bg}$	$5.8 \times 10^{-3}\,\text{mM}\,\text{s}^{-1}$
$K_{L,\text{trans},bg}$	0.5 mM
$v^{\max}_{L,\text{trans},bs}$	$7.83 \times 10^{-3}\,\text{mM}\,\text{s}^{-1}$
$K_{L,\text{trans},bs}$	0.5 mM
PS_{cap}/V_n	$1.73\,\text{s}^{-1}$
PS_{cap}/V_g	$0.414\,\text{s}^{-1}$
$k_{U,bx}$	0.0361 mM
HbOP	8.6 mM
nh	2.73
U_a	8.34 mM
G_a	4.8 mM
L_a	0.313 mM

Parameter	Value given in [1]
S_m/V_n	$9 \times 10^6\,\text{m}^{-1}$
S_m/V_g	$3.5 \times 10^6\,\text{m}^{-1}$
g^n_{Na}	$0.039\,\text{S}\,\text{m}^{-2}$
g^g_{Na}	$0.039\,\text{S}\,\text{m}^{-2}$
F	$9.65 \times 10^4\,\text{C}\,\text{mol}^{-1}$
RT/F	0.02673 V
Na^+_e	150 mM
V_m	-0.07 V
$v^{\max}_{\text{Pump},x}$	$2.9 \times 10^{-9}\,\text{m}\,(\text{mM})^{-1}\,\text{s}^{-1}$
$K_{m,\text{Pump}}$	0.5 mM
$v_{1,n}$	$0.41\,\text{mM}\,\text{s}^{-1}$
$v_{1,g}$	$0.16\,\text{mM}\,\text{s}^{-1}$
$v_{2,n}$	$14.44\,\text{mM}\,\text{s}^{-1}$
$v_{2,g}$	$15.7\,\text{mM}\,\text{s}^{-1}$
$\tau_{\text{Stim},n}$	2 s
$\tau_{\text{Stim},g}$	2 s
α_F	0.7
F_0	$0.012\,\text{s}^{-1}$
t_1	5 s
t_{end}	360 s
α	0.5
τ_v	35 s

Table 4.2.: Values of blood flow and neuronal stimulation parameters stated in [1].

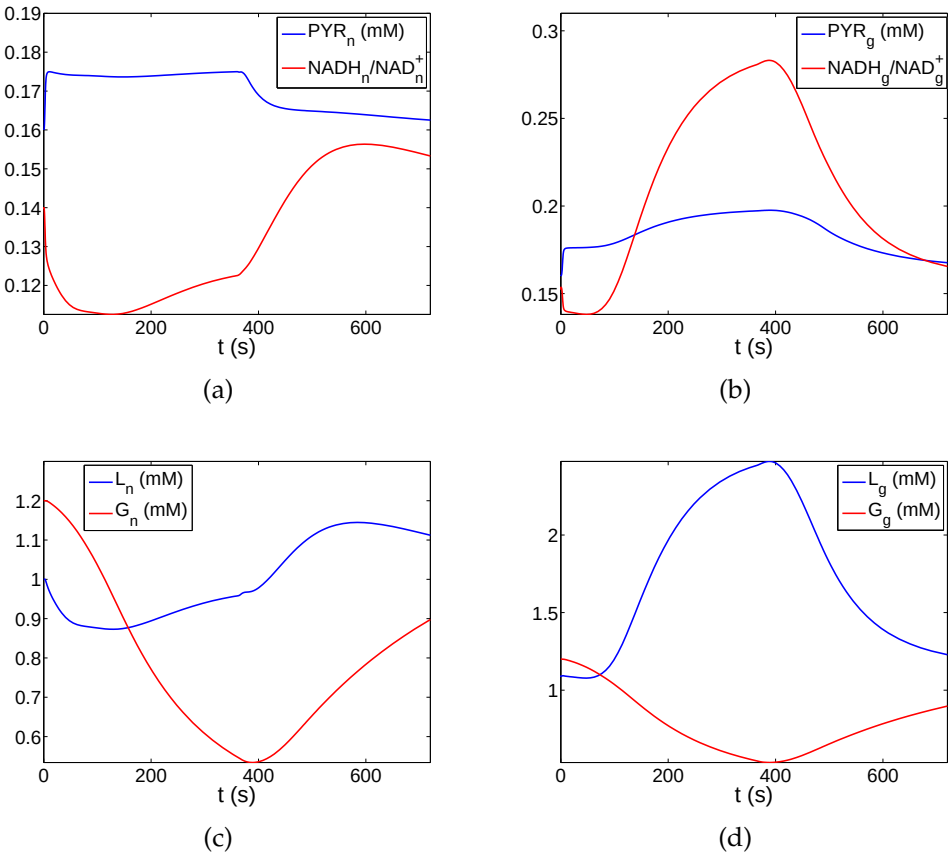


Figure 4.8.: Our reproduction of the first part of Figure 2 from Aubert and Costalat's paper [1], with $v_{1,n} = 0.41\,\mathrm{mM\,s^{-1}}$, $v_{2,n} = 14.4\,\mathrm{mM\,s^{-1}}$, $v_{1,g} = 0.16\,\mathrm{mM\,s^{-1}}$, $v_{2,g} = 15.7\,\mathrm{mM\,s^{-1}}$ and all other parameters as specified in Tables 4.1 and 4.2.

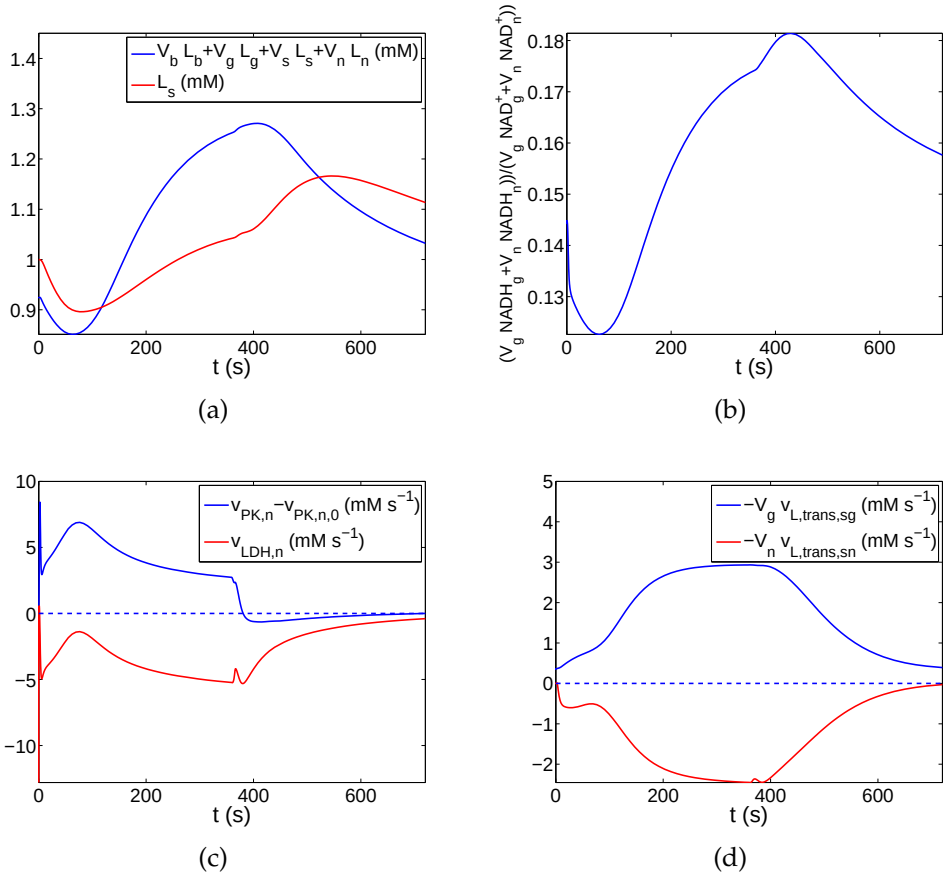


Figure 4.9.: Our reproduction of the second part of Figure 2 from Aubert and Costalat's paper [1], with $v_{1,n} = 0.41\,\mathrm{mM\,s^{-1}}$, $v_{2,n} = 14.4\,\mathrm{mM\,s^{-1}}$, $v_{1,g} = 0.16\,\mathrm{mM\,s^{-1}}$, $v_{2,g} = 15.7\,\mathrm{mM\,s^{-1}}$ and all other parameters as specified in Tables 4.1 and 4.2.

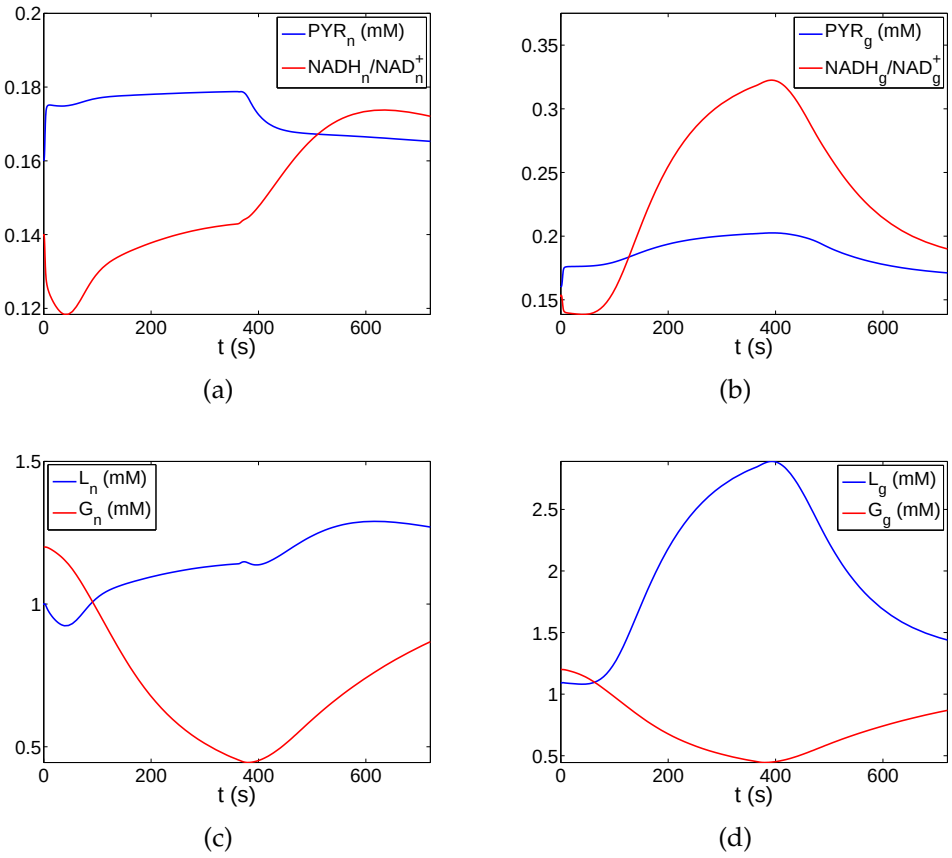


Figure 4.10.: Our reproduction of the first part of Figure 3 from Aubert and Costalat's paper [1], with $v_{1,n} = 0.43\,\mathrm{mM\,s^{-1}}$, $v_{2,n} = 15.2\,\mathrm{mM\,s^{-1}}$, $v_{1,g} = 0.16\,\mathrm{mM\,s^{-1}}$, $v_{2,g} = 15.7\,\mathrm{mM\,s^{-1}}$ and all other parameters as specified in Tables 4.1 and 4.2.

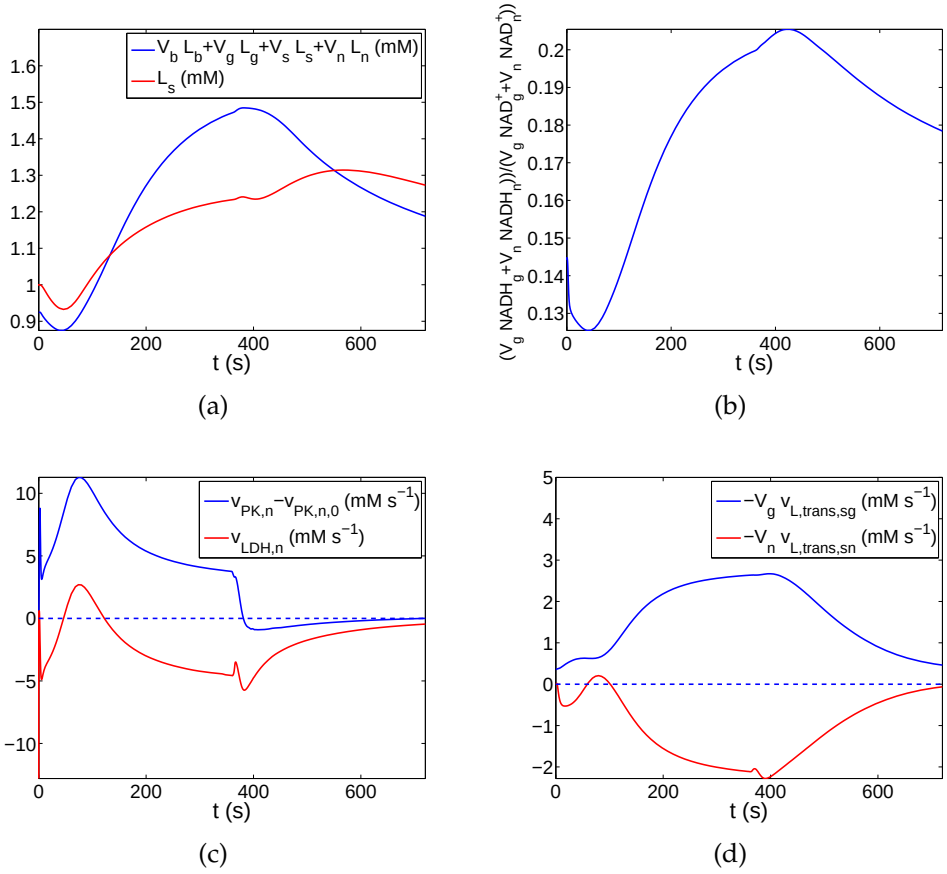


Figure 4.11.: Our reproduction of the second part of Figure 3 from Aubert and Costalat's paper [1], with $v_{1,n} = 0.43\,\mathrm{mM\,s^{-1}}$, $v_{2,n} = 15.2\,\mathrm{mM\,s^{-1}}$, $v_{1,g} = 0.16\,\mathrm{mM\,s^{-1}}$, $v_{2,g} = 15.7\,\mathrm{mM\,s^{-1}}$ and all other parameters as specified in Tables 4.1 and 4.2.

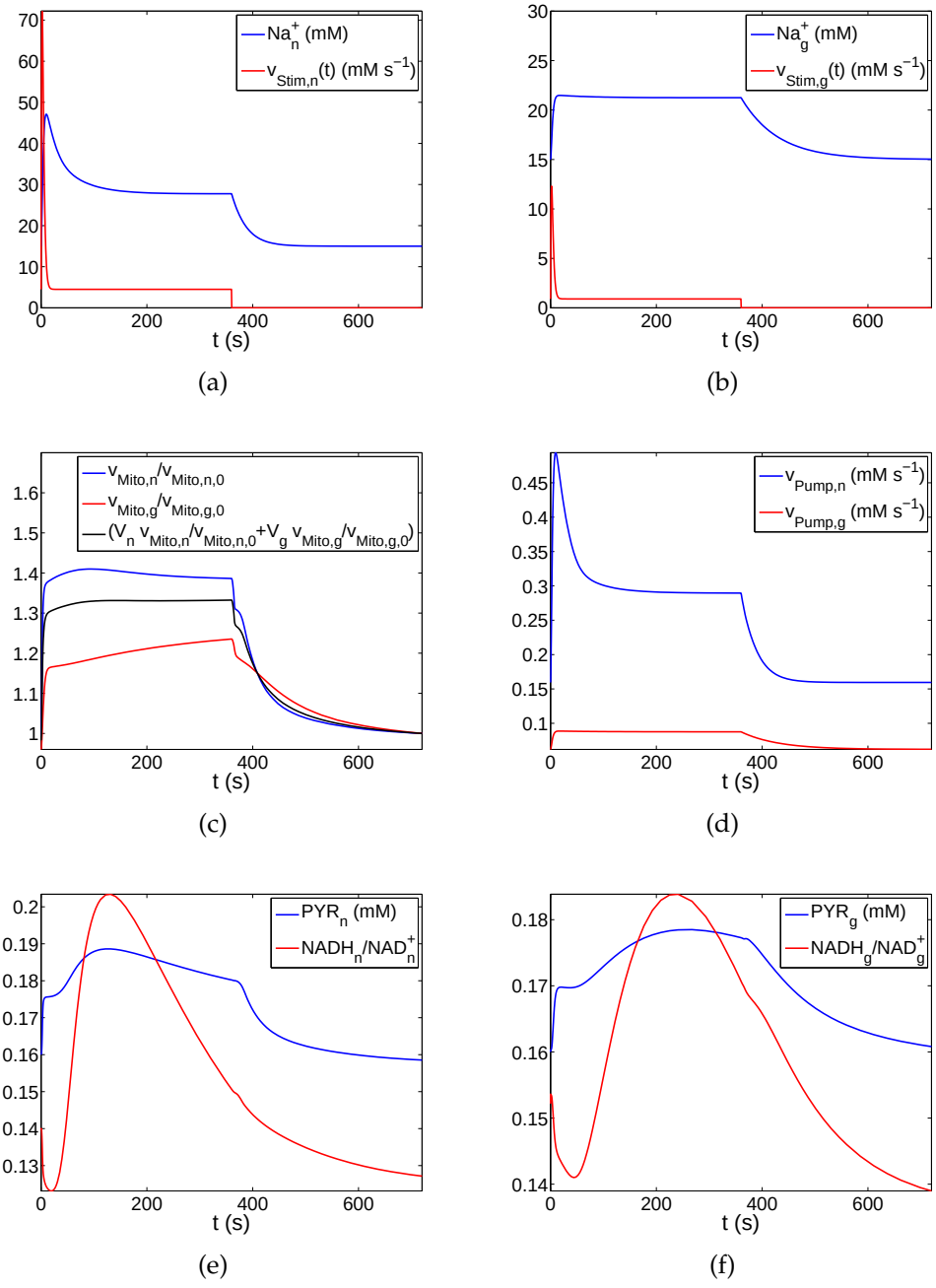


Figure 4.12.: Our reproduction of the first part of Figure 4 from Aubert and Costalat's paper [1], with $v_{1,n} = 0.45\,\mathrm{mM\,s^{-1}}$, $v_{2,n} = 18.4\,\mathrm{mM\,s^{-1}}$, $v_{1,g} = 0.09\,\mathrm{mM\,s^{-1}}$, $v_{2,g} = 3.1\,\mathrm{mM\,s^{-1}}$ and all other parameters as specified in Tables 4.1 and 4.2.

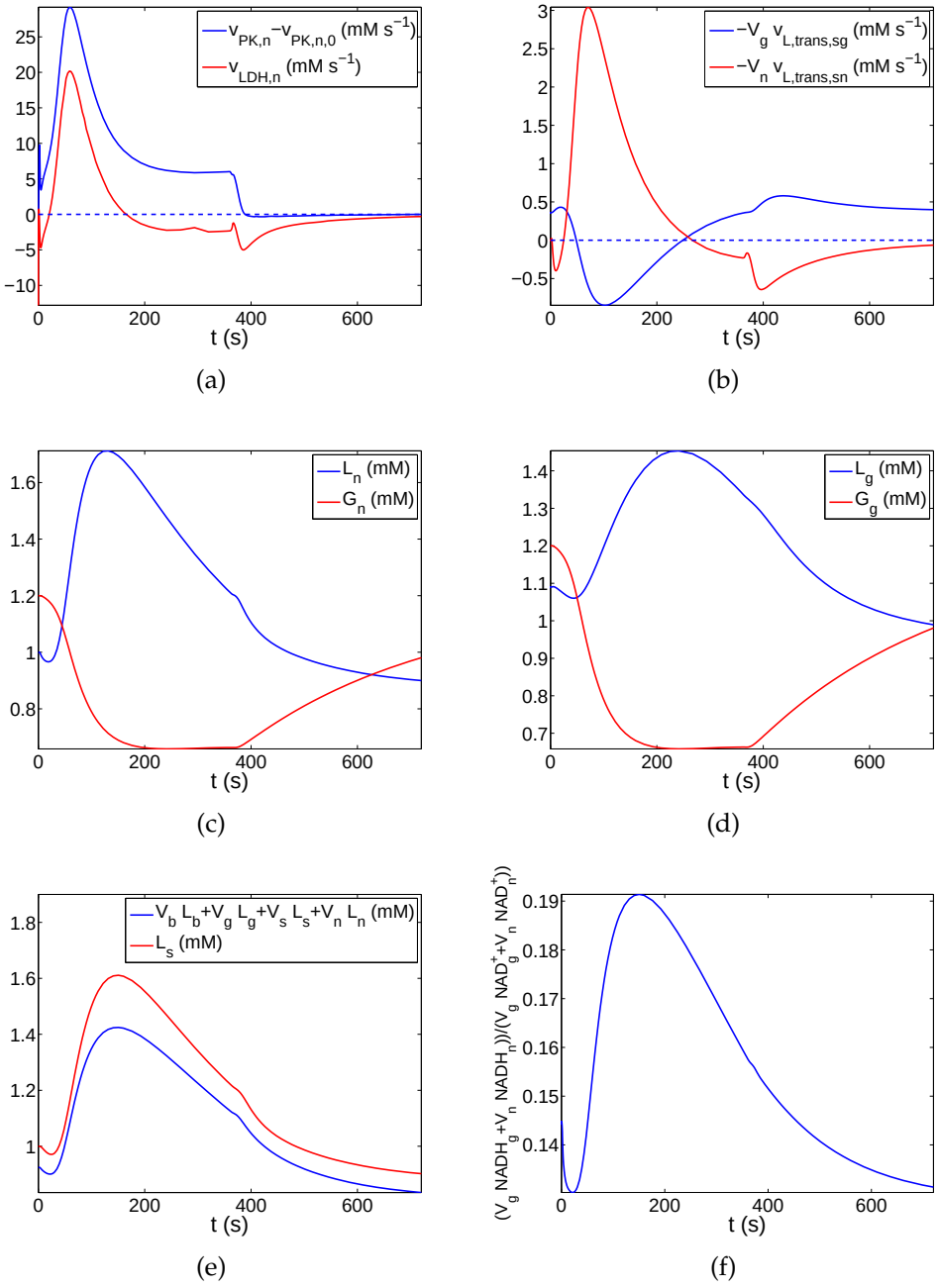


Figure 4.13.: Our reproduction of the second part of Figure 4 from Aubert and Costalat's paper [1], with $v_{1,n} = 0.45\,\mathrm{mM\,s^{-1}}$, $v_{2,n} = 18.4\,\mathrm{mM\,s^{-1}}$, $v_{1,g} = 0.09\,\mathrm{mM\,s^{-1}}$, $v_{2,g} = 3.1\,\mathrm{mM\,s^{-1}}$ and all other parameters as specified in Tables 4.1 and 4.2.

- Quantities $-V_g v_{L,\text{trans},sg}$ and $-V_n v_{L,\text{trans},sn}$ plotted in Figures 4.9(d), 4.11(d) and 4.13(b), represent the number of moles of lactate transported *out of* cell type x into the ECS per second.

- Figure 4.12(c) shows the fractional increase in oxygen consumption by oxidative metabolism in each cell type x from its resting level, $v_{\text{Mito},x}/v_{\text{Mito},x,0}$, and that for the whole tissue, rCMRO_{2T}, given by,

$$\text{rCMRO}_{2T} = \left(\frac{V_g}{V_g + V_n}\right)\frac{v_{\text{Mito},g}}{v_{\text{Mito},g,0}} + \left(\frac{V_n}{V_g + V_n}\right)\frac{v_{\text{Mito},n}}{v_{\text{Mito},n,0}}.$$

For low level neuronal stimulation, as shown in Figures 4.8 and 4.9, the number of moles of lactate transported *out of* the glial and neuronal cells into the ECS per second are $-V_g v_{L,\text{trans},sg} > 0$ and $-V_n v_{L,\text{trans},sn} < 0$ respectively, for all time. This denotes a flux of lactate from the glia into the ECS, and from the ECS to the neurons, i.e. glia-neuron lactate shuttling. Additionally, after a very short time, $v_{\text{LDH},n}$ becomes negative and remains so throughout the simulation, indicating a net conversion from lactate to pyruvate in the neurons. Examining the value of $(v_{\text{PK},n} - v_{\text{PK},n,0})$ we find that, in response to neuronal stimulation, the additional pyruvate requirement due to the increased rate of oxidative metabolism is met via both an increase in pyruvate production by neuronal glycolysis and also a net pyruvate production from glia-borne lactate. Figures 4.10–4.13 show the results when the neuronal stimulation is increased. Glia-neuron lactate shuttling is still exhibited during neuronal stimulation but it ceases for a short period and then restarts.

In addition to assessing the feasibility of the GNLSH, simulations were also compared with an earlier model by Aubert and Costalat [241] where the brain was treated as homogeneous rather than using separate compartments for glial and neuronal cells, and the ECS. This model provided better agreement with experimental results than the earlier model, correctly predicting a dip in lactate levels at the onset of neuronal stimulation. From this result, Aubert and Costalat concluded that this feature in the lactate dynamics is likely to be due to the presence of distinct cell types in the brain.

Aubert and Costalat's model pioneered investigations into the validity of the GNLSH, and revealed new information regarding key mechanisms determining cerebral metabolite dynamics. Furthermore, simulation results of the model are in good agreement with the time evolution of the extracellular lactate concentration observed using MRI imaging in the human brain during and

following, visual stimulation, and in rat brains during and following neuronal stimulation via tail pinching.

4.2.3 *Other Models of Glial and Neuronal Metabolism*

We review other compartmental models of glial and neuronal metabolism by focusing on how they differ from Aubert and Costalat's model. In general, the simplest kinetic models of cerebral metabolism view the brain as a homogeneous mass of cells comprising two compartments: the vasculature and the cerebral tissue [243, 249]. A more detailed model [241] separates the brain into intracellular and extracellular compartments. This model is extended in [1] (see §4.2.2) and in [238–240, 250, 251] to distinguish between glial and neuronal cells, allowing for their different roles in energy metabolism.

Subcellular effects, such as the shuttling of metabolites in and out of the mitochondria, have also been considered [252, 253] by including the cytosolic and mitochondrial compartments separately within each cell type, allowing more accurate reproduction of measured metabolite dynamics.

Calvetti and Somersalo [240] introduced a compartment for the synaptic terminals (see §4.1), assuming that neurotransmitters remain in these regions of the ECS. Denoting compartmental volumes by V, glutamate concentrations by GLT and the number of moles of glutamate by M_{GLT}, with subscripts Syn and ECS denoting the synaptic and extracellular compartments respectively, it is true that $V_{\text{Syn}} < V_{\text{ECS}}$. Thus, a change in the number of moles of glutamate, ΔM_{GLT}, flowing into/out of the synaptic terminals changes the glutamate concentration by $\Delta\text{GLT}_{\text{Syn}} = M_{\text{GLT}}/V_{\text{Syn}}$. The same change modelled using an extracellular compartment alters the glutamate concentration by $\Delta\text{GLT}_{\text{ECS}} = M_{\text{GLT}}/V_{\text{ECS}} < M_{\text{GLT}}/V_{\text{Syn}}$. However, qualitative effects are unchanged.

Glucose and Lactate Transport

One of the objectives of a model by Simpson et al. [239] is to test whether capillary-ECS transport plays an important role in nutrient transport through the blood-brain barrier. Hence, their model incorporates both capillary-ECS transport and a detailed representation of capillary-glial transport. Layers in the capillaries are included as additional compartments, since Simpson et al. argued that they play an important role in restricting nutrient diffusion between the bloodstream and glial cells. A good match between experimental

data and simulations was achieved when capillary-ECS diffusion was allowed. In this case the final destination of the majority of glucose was the neurons and consequently most lactate production took place in this compartment. Excess lactate was exported into the ECS, and consumed and oxidised by the glial cells in which glucose and lactate levels were low. i.e. the model exhibits *neuron-glial* lactate shuttling (opposing the model predictions in [1, 238, 242, 252, 254]). When capillary-ECS diffusion was neglected, glucose delivery to the neurons was slowed, depleting the rate of neuronal lactate production. The glial cells consumed lactate from the ECS at the same rate as above while the ECS-neuron lactate flux was lowered, meaning the extracellular lactate concentration fell unrealistically low. Based on these findings, a model by Calvetti and Somersalo [240] assumes that all blood-brain nutrient transport is between the capillaries and ECS (with no blood-glial transport). Despite Simpson et al.'s findings [239], since empirical observations show that glial end-feet envelop the capillaries [163–165], capillary-ECS transport is thought to be rare. Based on this we argue that the models of Aubert and Costalat [1] Aubert and Costalat [1, 241] and Cloutier et al. [238] can be simplified by neglecting the rates of capillary-ECS glucose and lactate transport.

Although subsequent work has been produced by Simpson et al.'s group [250, 251, 255–257], supporting their original findings in [239], they have been criticised for using parameters from a small portion of brain tissue, and for using *in vitro* data [258]. In [239], the value of $V_{\max}$ for blood-glial glucose transport is approximately an order of magnitude lower than that for ECS-glial glucose transport which is, in turn, an order of magnitude lower than that for ECS-neuronal glucose transport. This restricts the rate of glucose transport between the capillaries and ECS through the glial cells. The need for direct capillary-ECS glucose transport to reproduce realistic results is a consequence of the parameter values used. If physiological parameter values are consistent with the assumptions above, then Simpson et al.'s predictions (and Calvetti and Somersalo's assumptions) are justified. However, these assumptions are not supported by other researchers such as [1, 238, 242, 252, 254].

Energy Metabolism

Rizzi et al. [253] proposed a mathematical model of glycolysis in yeast cells, accounting for the mitochondrial and cytoplasmic compartments, extracellular conditions, nutrient transport and all ten steps of the glycolytic pathway. The

model uses detailed kinetics for each reaction and includes 21 metabolites and over 80 parameters. It is intended to be valid only on short timescales, on which it can successfully reproduce the time-evolution of some of the metabolite concentrations, but not all. The difficulty is that many mechanisms in the cell are not known accurately enough. Since then, several simpler models have been produced.

Some researchers, e.g. [239, 243], use a single reaction rate expression to model the glycolytic pathway, given by irreversible Michaelis-Menten kinetics, so that the rate increases and saturates with substrate concentrations. Although they are simpler than [1], such models are still able to qualitatively reproduce measured metabolite dynamics, with the exception of some key metabolites that are not included, e.g. ATP and ADP. In contrast, Cloutier et al.'s model [238] incorporates more detail than [1], including two additional intermediate steps in the glycolytic pathway, allowing them to model its links with a mechanism for storing glucose (by converting it to *glycogen*). This mechanism may become important if blood glucose levels fall very low.

The model in [252], which does not explicitly incorporate Na^+, GAP, PEP or glucose, is found to reproduce experimentally measured metabolite dynamics and generate predictions which are consistent with other models [1, 242], suggesting that Na^+, GAP, PEP and glucose may have little effect on the model behaviour. The models in [238–240] each use a single phenomenological reaction rate for oxidative metbaolism, which is also the case in [1]. Based on [252], we propose that it may be equally accurate to use an analogous single phenomenological rate to represent glycolysis.

Neuronal Stimulation and the Glutamate-Glutamine Cycle

Since Simpson et al.'s model [239] does not include ATP levels, it represents the increased energy demand during neuronal stimulation indirectly. It is assumed that neuronal stimulation induces a transient increase in the rate of glial and neuronal oxidative metabolism, followed by a longer transient increase in the rate of neuronal glycolysis (denoted via a transient stepwise increase in the $V_{\max}$ values for the relevant reaction rates). Increasing the glycolytic rate in the neurons but not the glia during neuronal stimulation means that the neuronal lactate levels are more likely to exceed those in the glia, promoting lactate shuttling from neurons to glia. This provides another explanation why the model predictions differ from those in [1, 238, 242, 252], in which the glycolytic

and oxidative rates evolve due to the altered ATP demands during neuronal activity (i.e. via the effects of changes in $v_{\text{Stim},x}(t)$ and $v_{\text{Pump},x}$ on dA_x/dt (see §4.2.2)). We conclude from this that it is important to incorporate ATP and ADP as dependent variables.

In order to track the glutamate concentration in the ECS and hence detect excitotoxicity, it is important to include the glutamate concentration as dependent variable, and the effects of the glutamate-glutamine cycle. This is a feature of Cloutier et al.'s model [238] (but not [1, 239, 241]). The model includes the glutamate concentration in the glia, neurons and ECS, glutamate release by the neurons when they are active and the clearance of glutamate from the ECS by the glial cells. Instead of accounting for glutamine concentrations, for the sake of simplicity, one reaction rate is used to model several steps in the glutamate-glutamine cycle: conversion of glutamate to glutamine in the glia, glia-ECS and ECS-neuron glutamine transport and conversion of glutamine to glutamate in the neurons. To predict potential toxicity, it is important to distinguish whether accumulations are in the glutamate or glutamine concentration (or both), since glutamate is toxic in high concentrations while a build-up of its non-neuroactive counterpart, glutamine, is less harmful.

Calvetti and Somersalo's model [240] includes the glutamate-glutamine cycle in a greater level of detail, incorporating the following features:

- Dependent variables for glutamate, glutamine, ATP and ADP concentrations;
- Neuronal glutamate release during activity;
- Glutamate clearance from the synaptic cleft and conversion to glutamine by the glial cells (modelled as one combined reaction);
- Glutamine transport between glia, synaptic terminals and neurons;
- Neuronal conversion of glutamine to glutamate;
- Baseline ATP consumption;
- ATP consumption by neuronal glutamate release, glial glutamate clearance and glial conversion of glutamate to glutamine.

The rate of glutamate release by the neurons into the synaptic cleft is assumed to depend on the (time-dependent) level of neuronal activity, $v_{\text{Stim}}(t)$ (see [240]

for more details of the time-dependence), and also the neuronal glutamate concentration as follows,

$$v_{\mathrm{GLT},ns} = v^{\max}_{\mathrm{GLT},ns}(t)\frac{\mathrm{GLT}}{\mathrm{GLT} + K_{\mathrm{GLT},ns}(t)},$$

where,

$$v^{\max}_{\mathrm{GLT},ns}(t) = v^{\max,0}_{\mathrm{GLT},ns}\left(1 + 2v_{\mathrm{Stim}}(t)\right)$$

and,

$$K_{\mathrm{GLT},ns}(t) = K^{0}_{\mathrm{GLT},ns}\left(1 - \frac{1}{2}v_{\mathrm{Stim}}(t)\right).$$

Calvetti and Somersalo's reason for choosing this functional form was that it has the desired qualitative behaviour: an increase in $v_{\mathrm{Stim}}(t)$ leads to an increase in $v^{\max}_{\mathrm{GLT},ns}(t)$ and a decrease in $K_{\mathrm{GLT},ns}(t)$, both of which increase $v_{\mathrm{GLT},ns}$. Consequently, neuronal stimulation increases glutamate release by the neurons. Other steps in the glutamate-glutamine cycle are modelled by assuming Michaelis-Menten type dependence on their substrates, in a similar way to the other reaction rates discussed above.

While [240] includes both the glutamate and glutamine concentrations in each compartment, and many of the steps in the glutamate-glutamine cycle, it does not incorporate its links with energy metabolism. Production of glutamate from TCA cycle intermediates in glial cells and glutamate breakdown into ATP in the neurons are the input and output for the glutamate-glutamine cycle respectively. In particular, our objective to test the effects of fluctuating blood glucose levels on the glutamate-glutamine cycle cannot be achieved without including these links.

4.2.4 *Compartmental Models Capturing Pathology*

Many variants of the models discussed above have been used to investigate the mechanisms involved in cerebral disease. We discuss a few of these here.

A model in [259–261], based on [1], is developed to investigate lactate metabolism in cancerous glial cells, also including compartments for the ECS and capillaries. The resulting system has a single steady state. Applying conditions to ensure that the steady state concentrations are non-negative leads to

constraints on the lactate transport parameters that allow the cancer cells to be viable. This reveals potential targets for treatment, in particular reducing the lactate transport rates, blood lactate levels and intracellular pH within the cancer cells.

Orlowski et al. [262], in an adaptation of the model in [238], account for pH variations in brain cells following the decreased blood flow experienced during a stroke. An extension to this model [263] incorporates the effects of gradients between regions of restricted blood flow in the brain and the surrounding normal regions. These gradients can alter the dynamics of nutrients in the ECS and inside the cells, and also result in the accumulation of fluid in the ECS, thought to cause or contribute to pathology. A different revision of [238] adds information on key cellular processes involved in the development of Parkinson's disease [264].

Other models have studied the effects of nutrient-deprived situations. For example, Genc et al.'s [265] model compared hypoxic and normal conditions to investigate whether glia to neuron lactate shuttling could be advantageous to cells in terms of their capacity to meet their energy demands during hypoxia. Empirical measurements of enzyme and transporter molecule regulation in response to hypoxia were used to estimate parameters in the model. It was found that the GNLSH increases the ATP available to the neurons during hypoxia, at the expense of the glia which are more resilient to variations in their nutrient levels. Despite these and other models relevant to pathology in the brain, to our knowledge there are no models that investigate possible causes of retinal pathology.

4.3 DISCUSSION

Our review of cerebral and retinal metabolism and the blood-brain barrier reveals the key role of glial cells in provision of nutrients to the neurons, clearance of glutamate from the ECS following neuronal stimulation and generation of its non-neuroactive counterpart, glutamine, which can then be taken up by the neurons.

Some aspects of retinal metabolism continue to be debated. These include the validity of the glia-neuron lactate shuttle hypothesis, the extent to which glial cells regulate nutrient transport between the blood and inner retinal tissue,

and how the glycolytic and oxidative rates compare between glial and neuronal cells.

Of the many possible approaches to mathematical modelling of inner retinal metabolism, we conclude that deterministic spatially averaged compartmental ODE models are well suited for investigating retinal pathology due to metabolite accumulation: they distinguish between different cell types and represent their interactions, while being relatively simple compared to alternative approaches. This makes both analytical and numerical progress feasible.

The models in [1, 238–240] provide detailed representations of nutrient transport through the blood-brain barrier. While the representation of energy metabolism in [239] neglects the effects of ATP and ADP (see §4.2), the other three models give detailed descriptions of how metabolite levels in the tissue are affected by glycolysis and oxidative metabolism. [238] and [240] also incorporate the glutamate-glutamine cycle but not its links with energy metabolism (and hence blood glucose levels). Thus, although the above models provide useful insights, no existing models incorporate all of the necessary components to investigate whether fluctuations in blood glucose levels may lead to excitotoxic damage to the neurons. A suitable model must consider energy metabolism, nutrient transport, the glutamate-glutamine cycle and the links between them.

The above information highlights the need for a new model to investigate whether inner retinal pathology may arise from metabolite accumulation. Both the biology and mathematical models in the literature provide valuable insights into the most important aspects of metabolic regulation, and those that are most prone to disruption. This enables us to formulate our own model of inner retinal metabolic regulation and investigate possible causes of retinal disease in the following two chapters.

5

FORMULATING A MODEL OF INNER RETINAL METABOLIC REGULATION

Motivated by the information reviewed in Chapter 4, in this chapter we construct a spatially-averaged ODE model of inner retinal metabolites. Our model is designed to capture the key aspects of inner retinal metabolic regulation, while remaining simple enough to be tractable. Although there are other aspects of inner retinal metabolism that could be considered, some of which were discussed in §4.2, we focus on nutrient transport through the blood-brain barrier, glycolysis, oxidative metabolism and the glutamate-glutamine cycle. In Chapter 6 we present and analyse the solutions of this model, together with the insights they provide into how inner retinal metabolite levels are regulated by glial cells, and the ways in which abnormal metabolism may lead to diabetic retinopathy.

Before analysing our model, we justify our modelling choices. A simple phenomenological approach is used to represent some of the complex metabolic pathways involved in cellular energy metabolism. The rates of some pathways are assumed to depend on the concentrations of substrates for one step, neglecting all other intermediate steps. This is a sensible approach if the neglected steps are rapid compared to the overall reaction rates. We test whether this approach is likely to give accurate results by comparing the outputs of key metabolic processes included in our system with those from the model proposed by Aubert and Costalat [1]. From each model, we derive a subsystem comprising metabolic pathways common to both models.

Asymptotic analysis on the subsystem derived from Aubert and Costalat's model [1] reveals that some of the metabolic intermediates that appear in [1] can be neglected. This suggests that our rapid kinetics assumptions are justified, at least for the components included in both our model and [1], placing our model on a stronger biological foundation.

Finally, we investigate the physiological conditions under which the two subsystems exhibit the same behaviour. Treating the relevant energy metabolism pathways as "black boxes", we concern ourselves only with the dependence of the metabolic outputs (the products and reaction rates) on the inputs (substrates), analysing the results via substrate dose response curves. Where our model is valid, the dose response curves in both subsystems match closely. We conclude that, although our model is simpler than Aubert and Costalat's [1], it captures the key behaviours in which we are interested, predicting qualitatively the same glucose dose response of the concentrations, production and consumption rates of lactate and ATP over timescales of minutes, hours and days. Our model also allows us to assess the impact of fluctuating blood glucose levels on inner retinal metabolism and potential causes for retinal disease. This has not been possible using previous models, due to the missing links between the blood glucose, cellular energy metabolism and the glutamate-glutamine cycle in the inner retinal cells.

The remainder of this chapter is organised as follows. In §5.1 we derive our mathematical model of inner retinal metabolism, which we nondimensionalise in §5.2. Focusing on the pathways involved in cellular energy metabolism, in §5.3 we compare our model with the work of Aubert and Costalat [1]. Firstly, we define the submodels (see §5.3.1). Secondly, using asymptotic analysis, we derive an approximation to the submodel derived from Aubert and Costalat's work in §5.3.2. Then, in §5.3.3 we compare simulations of the two submodels. The chapter concludes in §5.4 with a discussion of our model and its relationship to existing work on cerebral metabolism.

5.1 MODEL FORMULATION

We present a simple time-dependent ODE model that incorporates processes associated with energy production by glial and neuronal cells, intercellular metabolite transport and neurotransmission. The tissue is decomposed into four distinct compartments, which represent blood vessels (b), glial cells (g), ECS (s) and neurons (n). We focus on levels of glucose (G), lactate (L), glutamate (W), glutamine (N), ATP (A) and ADP (B), where each concentration is measured in units of mM. The concentration of each nutrient is affected by its production or consumption by intracellular reactions within a compartment, and also its transport between compartments. The levels of all other metabolites and ions

not included here are assumed to be abundant or clamped and, as such, not rate limiting. We also neglect spatial effects due to substrate diffusion inside cells and the ECS, which are incorporated in some previous models of metabolism (see [223, 226–230] for example). We argue that, since our intention is to detect pathological accumulation of metabolites in certain compartments of the inner retina, information about average nutrient levels in each compartment is sufficient. Furthermore, we are interested in the effects in the whole inner retinal tissue which consists of millions of glial/neuronal cells, so heterogeneities on a cellular lengthscale do not significantly affect the system dynamics. However, using a compartmental model also enables us to exploit the available data on intracellular processes. As discussed in §4.2, spatially averaged compartmental models are simple, making model analysis possible.

A schematic diagram of our model is presented in Figure 5.1. Transport rates are in the form $v_{U,jk}$, where U represents the chemical being transported from compartment j to compartment k, ($U \in \{G, L, W, N\}$ and $j, k \in \{b, g, s, n\}$). Intracellular reaction rates are denoted by $v_{SP,x}$, where S and P represent a key substrate and product of each reaction/pathway, and x indicates the compartment in which it occurs (S, $P \in \{G, L, W, N, A, B\}$ and $x \in \{g, n\}$).

The model accounts for reversible glucose and lactate transport between the bloodstream and glial cells, between glial cells and ECS, and ECS and neurons. Reaction rates $v_{GL,g}$ and $v_{GL,n}$ represent glycolysis, which, in our model, consumes glucose to produce lactate and ATP. Lactate or glutamate is consumed by oxidative metabolism, denoted by reactions $v_{LW,g}$, $v_{LA,n}$ and $v_{WA,n}$, which produces ATP, and also glutamate in the glial cells (all three of these reaction pathways involve different mechanisms, see §4.1 for more details). Glycolysis and oxidative metabolism are assumed to be unidirectional metabolic pathways.

Under neuronal activation, the neurotransmitter glutamate is released from the neurons into the ECS at rate $v_{W,ns}$. From the ECS it is taken up by the glial cells at rate $v_{W,sg}$, and then converted to its non-neuroactive counterpart, glutamine, at rate $v_{WN,g}$. These reactions are assumed to be irreversible, and to consume ATP. Glutamine is passively and reversibly transported between the glial cells and ECS, at rate $v_{N,sg}$. From the ECS, glutamine can also be transported into the neurons at rate $v_{N,sn}$, and then converted to glutamate at rate $v_{NW,n}$. These latter two reactions are treated as unidirectional (see §4.1 for

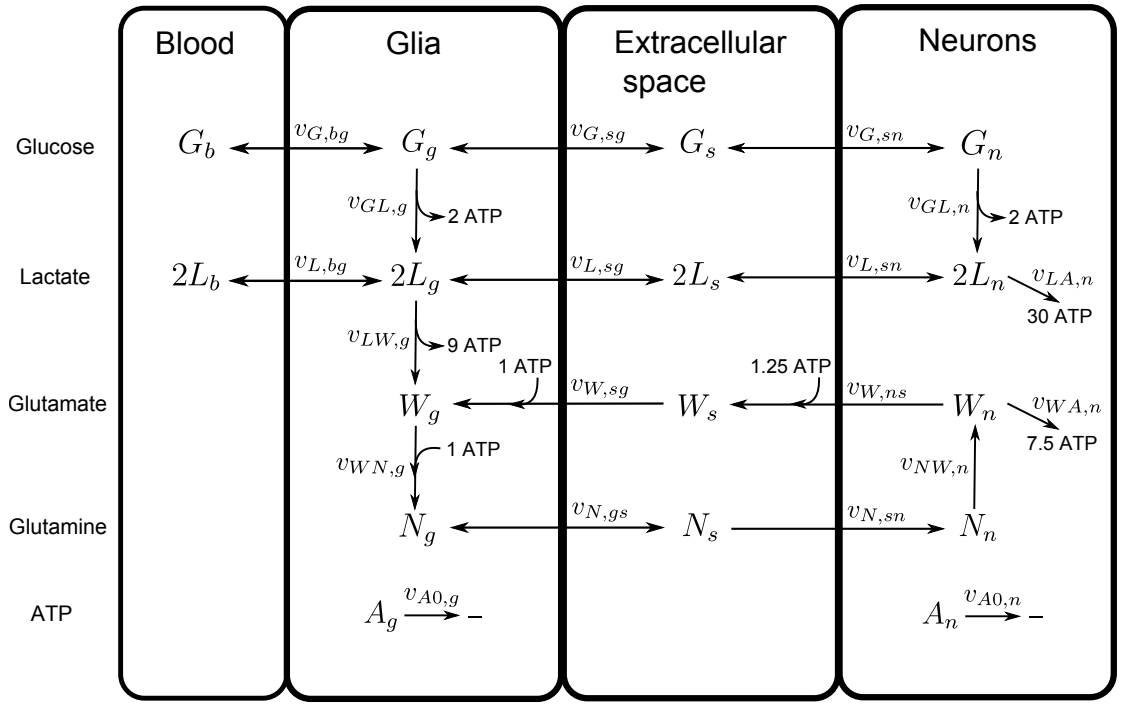


Figure 5.1.: Schematic diagram of our model of inner retinal metabolism given by equations (5.2)–(5.6)

more details and justification). The glial and neuronal cells are also assumed to have background ATP consumption rates of $v_{A0,g}$ and $v_{A0,n}$ respectively.

We note that the letter x denotes both intracellular compartments (g and n) collectively, i.e. it is implied that $x \in \{g, n\}$. For the rates of nutrient transport, we use the convention that a positive rate indicates transport into a glial or neuronal cell, and conversely for a negative one.

The ODEs governing the temporal evolution of the metabolite concentrations are constructed by applying the Principle of Mass Balance to each compartment. The concepts involved are explained in detail in §4.2.1, but we summarise them here via example. The mass of glucose in glial cells changes due to its inward transport from the blood vessels and ECS, and also its consumption by glycolysis (see Figure 5.1). The resulting rate of change in the mass of glial glucose is,

$$\frac{d}{dt}\left(V_g G_g\right) = V_g v_{G,bg} + V_g v_{G,sg} - V_g v_{GL,g}, \tag{5.1}$$

which is the sum of the following components. There is an influx at rates $V_g v_{G,bg}$ and $V_g v_{G,sg}$ due to blood-glial and ECS-glial transport, where V_g denotes the

assumed constant glial volume and $v_{G,bg}$ and $v_{G,sg}$ denote the transport rates in units of $\mathrm{mM\,s^{-1}}$. Additionally, glial glucose is consumed at rate $V_g v_{GL,g}$ by glycolysis. Dividing equation (5.1) by the glial volume gives equation (5.2a). Using a similar method yields the following equation for the rate of change in the mass of glucose in the ECS,

$$\frac{d}{dt}\left(V_s G_s\right) = -V_g v_{G,sg} - V_n v_{G,sn},$$

and dividing by the assumed constant volume of the ECS, V_s, gives equation (5.3a).

Figure 5.1 shows that the glycolytic reactions, $v_{GL,g}$ and $v_{GL,n}$, produce two lactate and two ATP molecules for each glucose molecule consumed, while the reactions involved in oxidative metabolism, $v_{LW,g}$, $v_{LA,n}$ and $v_{WA,n}$, produce an average of 9, 30 and 15 ATP molecules respectively per pair of lactate or glutamate molecules consumed (1 glutamate molecule is also produced per pair of lactate molecules consumed by the reaction $v_{LW,g}$). Other ATP consuming reactions are $v_{WN,g}$ and $v_{W,sg}$ which consume 1 ATP molecule per glutamate molecule consumed/transported, $v_{W,ns}$ which consumes an average of 1.25 ATP molecules per glutamate molecule transported, and background ATP consumption rates $v_{A0,g}$ and $v_{A0,n}$. Using the Principle of Mass Balance ensures these reaction stoichiometries are included. For example, the reaction stoichiometry in the glycolytic pathway is accounted for as follows. Given that glycolysis consumes glial glucose at rate $V_g v_{GL,g}$ and produces 2 lactate molecules and 2 ATP molecules per glucose molecule consumed, we add $2V_g v_{GL,g}$ to $d\left(V_g L_g\right)/dt$ and to $d\left(V_g A_g\right)/dt$.

The techniques outlined above can be used to derive the following system. In the glial cells,

$$\frac{dG_g}{dt} = v_{G,bg} + v_{G,sg} - v_{GL,g}, \tag{5.2a}$$

$$\frac{dL_g}{dt} = 2\left(v_{L,bg} + v_{L,sg} + v_{GL,g} - v_{LW,g}\right), \tag{5.2b}$$

$$\frac{dW_g}{dt} = v_{LW,g} + v_{W,sg} - v_{WN,g}, \tag{5.2c}$$

$$\frac{dN_g}{dt} = -v_{N,gs} + v_{WN,g}, \tag{5.2d}$$

$$\frac{dA_g}{dt} = 2v_{GL,g} + 9v_{LW,g} - v_{W,sg} - v_{WN,g} - v_{A0,g}, \tag{5.2e}$$

and in the ECS,

$$\frac{dG_s}{dt} = -\theta_{gs} v_{G,sg} - \theta_{ns} v_{G,sn}, \tag{5.3a}$$
$$\frac{dL_s}{dt} = 2\left(-\theta_{gs} v_{L,sg} - \theta_{ns} v_{L,sn}\right), \tag{5.3b}$$
$$\frac{dW_s}{dt} = -\theta_{gs} v_{W,sg} + \theta_{ns} v_{W,ns}, \tag{5.3c}$$
$$\frac{dN_s}{dt} = \theta_{gs} v_{N,gs} - \theta_{ns} v_{N,sn}, \tag{5.3d}$$

where, for $x \in \{g, n\}$,

$$\theta_{xs} = \frac{V_x}{V_s}, \tag{5.4}$$

are relative compartment volumes, with V_x denoting the volume of compartment x, and V_s denoting the volume of the ECS. Finally, in the neurons,

$$\frac{dG_n}{dt} = v_{G,sn} - v_{GL,n}, \tag{5.5a}$$
$$\frac{dL_n}{dt} = 2\left(v_{L,sn} + v_{GL,n} - v_{LA,n}\right), \tag{5.5b}$$
$$\frac{dW_n}{dt} = -v_{W,ns} + v_{NW,n} - v_{WA,n}, \tag{5.5c}$$
$$\frac{dN_n}{dt} = v_{N,sn} - v_{NW,n}, \tag{5.5d}$$
$$\frac{dA_n}{dt} = 2v_{GL,n} + 30v_{LA,n} - 1.25v_{W,ns} + 7.5v_{WA,n} - v_{A0,n}. \tag{5.5e}$$

The reaction rates and stoichiometries are described below. To close the system, we use the initial conditions,

$$U_c\left(t = 0\right) = U_{c,0}, \qquad A_x\left(t = 0\right) = A_{x,0}, \tag{5.6}$$

where $U_{c,0}$ and $A_{x,0}$ are positive constants ($U \in \{G, L, W, N\}$ and $c \in \{g, s, n\}$).

We treat G_b and L_b as input parameters to our system, although in some models they are included as dependent variables, e.g. in [1]. We also assume that within each cell (and hence in each compartment) the total adenine nucleotide pool is conserved [145], giving,

$$A_x + B_x \equiv A_{\mathrm{Tot},x} = \text{constant}. \tag{5.7}$$

Equation (5.7) is used to eliminate B_g and B_n from the model. Furthermore, since ATP is not exchanged between cells [165], we neglect intercellular ATP transport.

Under dark conditions, neurons do not fire and thus do not release glutamate neurotransmitter into the ECS. In our model this corresponds to setting $v_{W,ns} = 0$. Under light conditions, the neurons become activated and $v_{W,ns} > 0$. To summarise this,

$$v_{W,ns}^{\max} = \begin{cases} 0 & \text{dark conditions,} \\ v_{W,ns}^{\max}\Big|_{\text{Light}} & \text{light conditions.} \end{cases} \tag{5.8}$$

Neuronal cells consume more energy when they are active (see Chapter 4), i.e. $v_{A0,n}$ increases under light conditions, and hence we set,

$$v_{A0,n}^{\max} = \begin{cases} v_{A0,n}^{\max}\Big|_{\text{Dark}} & \text{dark conditions,} \\ v_{A0,n}^{\max}\Big|_{\text{Light}} & \text{light conditions,} \end{cases} \tag{5.9}$$

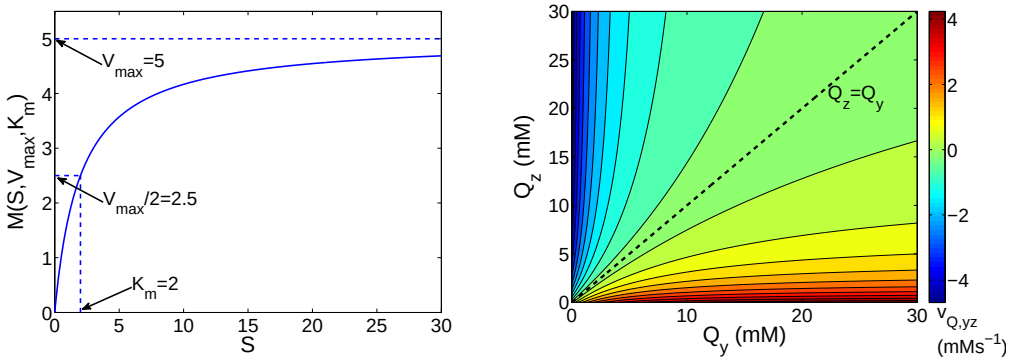
where $v_{W,ns}|_{\text{Light}} > 0$ and $v_{A0,n}^{\max}\Big|_{\text{Light}} > v_{A0,n}^{\max}\Big|_{\text{Dark}}$.

We aim to minimise the number of processes and pathways incorporated in our model, reducing the level of uncertainty introduced by estimating reaction rates and parameters for which there is limited availability of empirical data. This approach also allows for more in-depth analysis and physiological interpretation.

In the following sections, we justify the functional forms used for the reaction rates that appear in our model and, where appropriate, compare them to expressions used in existing similar models.

Glucose and Lactate Transport Rates, ($v_{G,bg}$, $v_{G,sg}$, $v_{G,sn}$, $v_{L,bg}$, $v_{L,sg}$, $v_{L,sn}$)

As the endfeet of glial cells almost completely envelop the capillaries, we assume that nutrient transport between the capillaries and ECS is negligible: transport is mostly via glial cells. This view is widely supported [165, 212], but not unanimously: e.g. when Simpson et al. [239] neglected direct transfer of nutrients between the blood vessels and ECS their mathematical model yielded unphysically high extracellular lactate levels.



(a) (b)

Figure 5.2.: Plots showing examples of Michaelis-Menten reaction kinetics. (a) Irreversible Michaelis-Menten kinetics, $\mathrm{M}(S; V_{\max}, K_m)$, where the maximal rate ($V_{\max}$) and the value of S when the rate is half-maximal (K_m) are set to 5 and 2 units respectively. (b) A typical rate of intercellular transport in our model, exhibiting reversible Michaelis-Menten kinetics, symmetric in the forward and reverse directions, given by equation (5.10). Here $v^{\max}_{Q,yz} = 5\mathrm{mMs}^{-1}$, and $K_m = 2\mathrm{mM}$.

Following [1, 242], glucose and lactate transport through cell membranes can be modelled using Michaelis-Menten kinetics (see equation (4.9)). Since intercellular glucose and lactate transport are independent of ATP (assuming a uniform pH, see §4.1), we use the following general form,

$$v_{Q,yz} = \mathrm{M}\left(Q_y; v^{\max}_{Q,yz}, K_{Q,yz}\right) - \mathrm{M}\left(Q_z; v^{\max}_{Q,yz}, K_{Q,yz}\right), \tag{5.10}$$

with $Q \in \{G, L\}$ and $yz \in \{bg, sg, sn\}$. The variation of a typical intercellular transport rate $v_{Q,yz}$ with the concentrations of chemical species Q in compartments y and z (Q_y and Q_z) is plotted in Figure 5.2(b). We note that using the same K_m in the forward and reverse transport rates corresponds to assuming that glucose and lactate transport are symmetric, evident from the symmetry of Figure 5.2(b) about the line $Q_z = Q_y$, and from the fact that along this line, $v_{Q,yz} = 0$. We could relax the assumed symmetry in equation (5.10) following [239, 249], at the cost of increasing the complexity of the model.

Glycolytic Pathway ($v_{GL,g}$, $v_{GL,n}$)

Pyruvate is produced by glycolysis and then becomes the substrate for ATP production via oxidative metabolism. However, we use simplifying assumptions to eliminate pyruvate from our model, yielding the lactate-dependent reaction

rate expressions $v_{GL,x}$, $v_{LW,x}$ and $v_{LA,n}$. We begin by examining the pyruvate dependence of the glycolytic and oxidative rates and then explain how it is eliminated.

Instead of modelling all ten reactions in the glycolytic pathway separately (e.g. [253]), or using a multi-step representation (e.g. [1, 238]), we use a single phenomenological reaction rate that exhibits the observed dependence on its substrates. Thus our model accounts for the net effect of glycolysis, which is summarised via reaction (4.1). The rate of pyruvate production by glycolysis, $v_{G\,\mathrm{PYR},x}$, is assumed to be an increasing, saturating function of the glucose concentration, which we model using Michaelis-Menten kinetics (see equation (4.9)). As explained in §4.1, the rate of glycolysis increases with the energy demand. The energy-producing reaction is summarised via (1.1). Hence, the rate of glycolytic pyruvate production increases with ADP levels and, as no evidence has been found to suggest saturation, we assume it is linear in B_x. Thus we use the following expression to model the rate of pyruvate production by glycolysis,

$$v_{G\,\mathrm{PYR},x} = \mathrm{M}\left(G_x; v^{\max}_{G\,\mathrm{PYR},x}, K_{G\,\mathrm{PYR},x}\right) B_x, \tag{5.11}$$

with $x \in \{g, n\}$ in the glial and neuronal cells respectively, and PYR denoting the pyruvate concentration.

Oxidative Pathway ($v_{LA,n}$, $v_{LW,g}$, $v_{WA,n}$)

In both glial and neuronal cells, ATP is produced when pyruvate molecules pass through the TCA cycle and also when glutamate is metabolised (see §4.1 for more details). In the glial cells, the rate of ATP production via full oxidative metabolism of pyruvate is small compared to that via glycolysis [170, 171, 173, 254] so we neglect it. In contrast, it is important to include partial oxidative metabolism of pyruvate molecules in the glia (this will be incorporated into reaction rate $v_{LW,g}$) since it is a major source of ATP, and also glutamate.

In the neurons, we account for ATP production via full oxidative metabolism of pyruvate (which will be incorporated in reaction rate $v_{LA,n}$) and glutamate (to be incorporated in reaction rate $v_{WA,n}$). Partial oxidative metabolism of pyruvate in the neurons is neglected since it is slow.

We assume that the rates of full and partial oxidative pyruvate metabolism depend on pyruvate levels via Michaelis-Menten kinetics. Using a similar argument to that for the glycolytic rate, we assume a linear dependence on ADP levels. These assumptions lead to a reaction rate expression for oxidative pyruvate metabolism of the same general functional form as the expression in equation (5.11), but with a Michaelis-Menten dependence on pyruvate rather than glucose levels. Therefore, we define the more general reaction rate expression,

$$v_{YZ,m} = \mathrm{M}\left(Y_m; v^{\max}_{YZ,m}, K_{YZ,m}\right) B_m, \tag{5.12}$$

to represent both the glycolytic and oxidative rates. We model oxidative pyruvate metabolism using this expression with $(YZ, m) \in \{(\mathrm{PYR}\, A, n), (\mathrm{PYR}\, W, g)\}$ (whereas $(YZ, m) \in \{(G\,\mathrm{PYR}, g), (G\,\mathrm{PYR}, n)\}$ for glycolysis). The reaction rate $v_{WA,n}$ is modelled in a similar way, assuming Michaelis-Menten dependence on the key substrate glutamate and linear dependence on ADP, giving an equation of the form of (5.12) with $(YZ, m) = (WA, n)$.

Relationship between Pyruvate and Lactate Concentrations (PYR_x, L_x)

As discussed in the previous two sections, pyruvate is produced by glycolysis and consumed by oxidative metabolism. It is also reversibly converted to lactate, catalysed by lactate dehydrogenase or LDH (see equation (4.3)). Since this reaction is rapid compared to glycolysis and oxidative metabolism [245], we assume that pyruvate and lactate are in chemical equilibrium, meaning that $\mathrm{PYR}_x = \alpha L_x$, where α is a constant (see equation (4.4)). This enables us to eliminate the pyruvate concentration from our model while still including glycolysis and oxidative metabolism via their effect on the lactate concentration.

Since pyruvate is produced via glycolysis at rate $v_{G\,\mathrm{PYR},x}$, the resulting lactate production occurs at rate $v_{GL,x} = v_{G\,\mathrm{PYR},x}/\alpha$, where $v_{GL,x}$ has the same glucose and ADP dependence as $v_{G\,\mathrm{PYR},x}$ but its $V_{\max}$ value is rescaled such that $v^{\max}_{GL,x} = v^{\max}_{G\,\mathrm{PYR},x}/\alpha$. For the rates of oxidative pyruvate metabolism, $v_{YZ,m}$ with $(YZ, m) \in \{(\mathrm{PYR}\, A, n), (\mathrm{PYR}\, W, g)\}$, substituting $\mathrm{PYR}_x = \alpha L_x$ into equation (5.12) gives the same general reaction rate expression but with $K_{LZ,m} = K_{\mathrm{PYR}\,Z,m}/\alpha$ and $v^{\max}_{LZ,m} = v^{\max}_{\mathrm{PYR}\,Z,m}/\alpha$. Thus the glycolytic and oxidative rates in our model have the general functional form given in equation (5.12), but with $(YZ, m) \in \{(GL, g), (GL, n)\}$ for glycolysis and $(YZ, m) \in$

$\{(LA, n), (LW, g), (WA, n)\}$ for oxidative metabolism, and where the $V_{\max}$ and K_m values are rescaled.

Neuronal Release and Glial Uptake of Glutamate ($v_{W,ns}$, $v_{W,sg}$)

We assume that glutamate release from the neurons into the ECS at rate $v_{W,ns}$ has a Michaelis-Menten dependence on the neuronal glutamate and ATP concentrations, yielding,

$$v_{W,ns} = \mathrm{M}\left(W_n; v_{W,ns}^{\max}, K_{W,ns,W}\right) \mathrm{M}\left(A_n; 1, K_{W,ns,A}\right). \tag{5.13}$$

The dependence on neuronal glutamate, W_n, means that $v_{W,ns} \to 0$ as $W_n \to 0$, and hence (since $v_{WA,n}$ also tends to 0 as $W_n \to 0$), the neuronal glutamate concentration cannot become negative. Our assumption that the value of $v_{W,ns}^{\max}$ is positive when the neurons are active and zero otherwise (see earlier) means that our reaction rate expression has the same qualitative behaviour as in [240], except that our expression also incorporates the ATP-dependence.

We assume the rate at which glial cells clear glutamate from the ECS is an increasing, saturating function of extracellular glutamate levels [158, 210, 211] and of ATP [186, 212], and that uptake is unidirectional [176]. Thus we write,

$$v_{W,sg} = \mathrm{M}\left(W_s; v_{W,sg}^{\max}, K_{W,sg,W}\right) \mathrm{M}\left(A_g; 1, K_{W,sg,A}\right). \tag{5.14}$$

By contrast, Cloutier et al. [238] do not account for the dependence on glial ATP levels. Since we will use our model to investigate the results of metabolic stress, we argue that such ATP dependence is important because, if glial cells become ATP-deprived, glutamate clearance from the ECS may be hindered, allowing glutamate to accumulate in the ECS, leading to excitotoxicity.

Glutamine Transport ($v_{N,gs}$ and $v_{N,sn}$)

We assume that glutamine transport out of glial cells, $v_{N,gs}$, is reversible and using the same argument as for glucose and lactate transport, we obtain,

$$v_{N,gs} = \mathrm{M}\left(N_g; v_{N,gs}^{\max}, K_{N,gs}\right) - \mathrm{M}\left(N_s; v_{N,gs}^{\max}, K_{N,gs}\right). \tag{5.15}$$

Although glutamine transport into the neurons, at rate $v_{N,sn}$, is also reversible, the influx to the neurons dominates the outflux under physiological conditions,

so we approximate it using a unidirectional uptake term, dependent only on the extracellular glutamine concentration, giving,

$$v_{N,sn} = \mathrm{M}\left(N_s; v^{\max}_{N,sn}, K_{N,sn}\right). \tag{5.16}$$

Synthesis of Glial Glutamine Neuronal Glutamate ($v_{WN,g}$ and $v_{NW,n}$)

In the glial cells, glutamine synthesis is a single enzyme reaction with substrate glutamate, requiring one molecule of ATP per glutamate molecule converted. We model the reaction via Michaelis-Menten functions of ATP and glutamate, giving,

$$v_{WN,g} = \mathrm{M}\left(W_g; v^{\max}_{WN,g}, K_{WN,g,W}\right)\mathrm{M}\left(A_g; 1, K_{WN,g,A}\right). \tag{5.17}$$

This reaction is combined with glial glutamate uptake in [240]. The resulting combined rate determines the conversion of extracellular glutamate (W_s) to glial glutamine (N_g), and thus eliminates the dependent variable W_g representing glial glutamate. However, we argue that glial cells may become damaged if the intracellular glutamate levels become extremely high, so our model incorporates W_g to allow for this.

As for glial glutamine synthesis, neuronal synthesis of glutamate from glutamine is via a single enzyme reaction at rate $v_{NW,n}$. We note that the enzyme catalysing neuronal glutamate production, PAG, is inhibited by glutamate, with which it is four times more likely to bind than with glutamine [217]. This is a reversible reaction, but the forward reaction rate is much larger than the reverse one [217]. We therefore use a unidirectional rate that incorporates the competitive inhibition in the standard way [217], giving,

$$v_{NW,n} = v^{\max}_{NW,n}\left(\frac{N_n}{N_n + 4Wn + K_{NW,n}}\right). \tag{5.18}$$

The appearance of the extra term $4Wn$ in the denominator ensures that the presence of large glutamate concentrations, W_n, slows the rate of glutamate production. To our knowledge, no kinetic models of the glutamate-glutamine cycle include this competitive inhibition, but we consider it important as it may affect the model predictions on whether certain parameter changes lead to excitotoxicity.

Baseline ATP Consumption ($v_{A0,g}$, $v_{A0,n}$)

We introduce additional baseline ATP consumption terms in glia and neurons to account for energy usage by mechanisms not included in our model. For example, energy is required to keep the glial and neuronal cells alive, and active neurons require a large amount of energy to restore ionic gradients to original levels after depolarisation. We assume a Michaelis-Menten dependence on the ATP levels, with a K_m value much smaller than typical physiological ATP concentrations, A_r, so that ATP consumption is approximately constant when $A_x \sim A_r$ and tends to zero if $A_x \to 0$, preventing physically unrealistic negative concentrations. Accordingly, the glial and neuronal ATP consumption terms are given by,

$$v_{A0,x} = \mathrm{M}\left(A_x; v_{A0,x}^{\max}, K_{A0,x}\right), \qquad K_{A0,x} \ll A_r, \tag{5.19}$$

with $x \in \{g, n\}$. In [266] the effects of neuronal firing on cellular energy metabolism are studied in detail but here, for simplicity, we consider neuronal energy consumption in response to a constant demand, which is increased under light conditions (see earlier).

Summary

Our model comprises a system of 14 ODEs (having eliminated the equations for B_g and B_n using equation (5.7)), given in equations (5.2)–(5.5), describing the time evolution of the glucose, lactate, glutamate and glutamine concentrations in the glia, ECS and neurons, and the glial and neuronal ATP concentrations.

Under light conditions the neurons release glutamate into the ECS ($v_{W,ns} > 0$) and the baseline energy consumption of the neurons, $v_{A0,n}$, increases (in darkness $v_{W,ns} = 0$).

The reaction rates in the model are given in equations (5.10)–(5.19). Our model includes glucose, lactate, glutamate and glutamine transport between inner retinal compartments, glucose and lactate transport between blood vessels and the inner retinal tissue, ATP production via glycolysis and oxidative metabolism, glutamate production by oxidative lactate metabolism in the glial cells and the steps within the glutamate-glutamine cycle.

We rescale all concentrations by their typical values/orders of magnitude,

$$G_r = 1\text{mM}, \qquad L_r = 1\text{mM}, \qquad W_r = 10\text{mM}, \qquad N_r = 10\text{mM},$$
$$A_r = 2\text{mM}, \qquad B_r = 0.1\text{mM}, \tag{5.20}$$

and time by the timescale of blood-glial lactate transport, i.e. $T_0 = L_r / v^{\max}_{L,bg}$, which is of order minutes, representing a typical timescale over which intracellular reactions and intercellular transport occur in our model. Then dimensionless concentrations are defined as,

$$U_c = U_r u_c, \qquad A_x = A_r a_x, \qquad B_x = B_r b_x,$$

where $(U,u) \in \{(G,g),(L,l),(W,w),(N,n)\}$, $c \in \{g,s,n\}$, and dimensionless time as,

$$t = T_0 \tau.$$

As discussed in §5.1, the total ATP plus ADP levels are conserved (see equation (5.7)). We rescale ATP and ADP differently because ADP concentrations are typically lower than ATP levels (see (5.20)), and can become very low in some cases (e.g. during resting conditions in [1]). Thus, the dimensionless version of equation (5.7) is,

$$a_x + \frac{B_r}{A_r} b_x = a_{\text{Tot},x}, \tag{5.21}$$

where $x \in \{g,n\}$ and $a_{\text{Tot},x}$ is a positive constant.

Nondimensionalisation leads naturally to the introduction of the following dimensionless parameter groupings,

$$\hat{v}^{\max}_{Q,yz} = \frac{T_0}{Q_r} v^{\max}_{Q,yz}, \qquad \hat{K}_{Q,yz} = \frac{K_{Q,yz}}{Q_r}, \qquad \hat{v}^{\max}_{YZ,m} = \frac{T_0 B_r}{A_r} v^{\max}_{YZ,m},$$
$$\hat{K}_{YZ,m} = \frac{K_{YZ,m}}{Y_r}, \qquad \hat{v}^{\max}_{WN,g} = \frac{T_0}{A_r} v^{\max}_{WN,g}, \qquad \hat{K}_{WN,g,W} = \frac{K_{WN,g,W}}{W_r},$$
$$\hat{K}_{WN,g,A} = \frac{K_{WN,g,A}}{A_r}, \qquad \hat{v}^{\max}_{N,jk} = \frac{T_0}{N_r} v^{\max}_{N,jk}, \qquad \hat{K}_{N,jk} = \frac{K_{N,jk}}{N_r},$$
$$\hat{v}^{\max}_{NW,n} = \frac{T_0}{N_r} v^{\max}_{NW,n}, \qquad \hat{K}_{NW,n} = \frac{K_{NW,n}}{N_r}, \qquad \hat{k}_{NW,n,W} = \frac{4}{N_r},$$

$$\hat{v}^{\max}_{W,kj} = \frac{T_0}{A_r} v^{\max}_{W,kj}, \qquad \hat{K}_{W,kj,W} = \frac{K_{W,kj,W}}{W_r}, \qquad \hat{K}_{W,kj,A} = \frac{K_{W,kj,A}}{A_r},$$
$$\hat{v}^{\max}_{A0,x} = \frac{T_0}{A_r} v^{\max}_{A0,x}, \qquad \hat{K}_{A0,x} = \frac{K_{A0,x}}{A_r}, \qquad a_{\mathrm{Tot},x} = \frac{A_{\mathrm{Tot},x}}{A_r}, \tag{5.22}$$

where $jk \in \{gs, sn\}$ (and hence $kj \in \{sg, ns\}$) and $(YZ, m) \in \{(GL, x), (LW, g), (LA, n), (WA, n)\}$. Under the above rescalings equations (5.2)–(5.5) transform to give,

$$\text{Glia:} \begin{cases} \dfrac{dg_g}{d\tau} = \hat{v}_{G,bg} + \hat{v}_{G,sg} - \dfrac{A_r}{G_r}\hat{v}_{GL,g}, & \text{(5.23a)} \\ \dfrac{dl_g}{d\tau} = 2\left(\hat{v}_{L,bg} + \hat{v}_{L,sg} + \dfrac{A_r}{L_r}\hat{v}_{GL,g} - \hat{v}_{LW,g}\right), & \text{(5.23b)} \\ \dfrac{dw_g}{d\tau} = \dfrac{W_r}{L_r}\hat{v}_{LW,g} + \dfrac{A_r}{W_r}\hat{v}_{W,sg} - \dfrac{A_r}{W_r}\hat{v}_{WN,g}, & \text{(5.23c)} \\ \dfrac{dn_g}{d\tau} = -\hat{v}_{N,gs} + \dfrac{A_r}{N_r}\hat{v}_{WN,g}, & \text{(5.23d)} \\ \dfrac{da_g}{d\tau} = 2\hat{v}_{GL,g} + 9\dfrac{L_r}{A_r}\hat{v}_{LW,g} + \hat{v}_{W,sg} - \hat{v}_{WN,g} - \hat{v}_{A0,g}, & \text{(5.23e)} \end{cases}$$

$$\text{ECS:} \begin{cases} \dfrac{dg_s}{d\tau} = -\left(\theta_{gs}\hat{v}_{G,sg} + \theta_{ns}\hat{v}_{G,sn}\right), & \text{(5.24a)} \\ \dfrac{dl_s}{d\tau} = -2\left(\theta_{gs}\hat{v}_{L,sg} + \theta_{ns}\hat{v}_{L,sn}\right), & \text{(5.24b)} \\ \dfrac{dw_s}{d\tau} = -\theta_{gs}\dfrac{A_r}{W_r}\hat{v}_{W,sg} + \theta_{ns}\dfrac{A_r}{W_r}\hat{v}_{W,ns}, & \text{(5.24c)} \\ \dfrac{dn_s}{d\tau} = \theta_{gs}\hat{v}_{N,gs} - \theta_{ns}\hat{v}_{N,sn}, & \text{(5.24d)} \end{cases}$$

$$\text{Neurons:} \begin{cases} \dfrac{dg_n}{d\tau} = \hat{v}_{G,sn} - \dfrac{A_r}{G_r}\hat{v}_{GL,n}, & \text{(5.25a)} \\ \dfrac{dl_n}{d\tau} = 2\left(\hat{v}_{L,sn} + \dfrac{A_r}{L_r}\hat{v}_{GL,n} - \dfrac{A_r}{L_r}\hat{v}_{LA,n}\right), & \text{(5.25b)} \\ \dfrac{dw_n}{d\tau} = -\dfrac{A_r}{W_r}\hat{v}_{W,ns} + \dfrac{N_r}{W_r}\hat{v}_{NW,n} - \dfrac{A_r}{W_r}\hat{v}_{WA,n}, & \text{(5.25c)} \\ \dfrac{dn_n}{d\tau} = \hat{v}_{N,sn} - \hat{v}_{NW,n}, & \text{(5.25d)} \\ \dfrac{da_n}{d\tau} = 2\hat{v}_{GL,n} + 30\hat{v}_{LA,n} - 1.25\hat{v}_{W,ns} \\ \qquad\qquad +7.5\hat{v}_{WA,n} - \hat{v}_{A0,n}. & \text{(5.25e)} \end{cases}$$

We solve equations (5.23)–(5.25) subject to the following initial conditions,

$$u_c\,(t=0) = u_{c,0}, \qquad\qquad a_x\,(t=0) = a_{x,0}, \tag{5.26}$$

where $u_{c,0}$ and $a_{x,0}$ are positive constants ($u \in \{g,l,w,n\}$ and $c \in \{g,s,n\}$). The six rates of intercellular glucose and lactate transport are given by,

$$\hat{v}_{Q,yz} = \mathrm{M}\left(q_y; \hat{v}^{\max}_{Q,yz}, \hat{K}_{Q,yz}\right) - \mathrm{M}\left(q_z; \hat{v}^{\max}_{Q,yz}, \hat{K}_{Q,yz}\right), \tag{5.27}$$

where $Q \in \{G,L\}$, $yz \in \{bg,sg,sn\}$ and $\mathrm{M}(S; \hat{v}^{\max}_{Q,yz}, K_m)$ is the Michaelis-Menten expression (see (4.9)) and the rates of intercellular glutamate and glutamine transport satisfy,

$$\hat{v}_{N,gs} = \mathrm{M}\left(n_g; \hat{v}^{\max}_{N,gs}, \hat{K}_{N,gs}\right) - \mathrm{M}\left(n_s; \hat{v}^{\max}_{N,gs}, \hat{K}_{N,gs}\right), \tag{5.28a}$$

$$\hat{v}_{N,sn} = \mathrm{M}\left(n_s; \hat{v}^{\max}_{N,sn}, \hat{K}_{N,sn}\right), \tag{5.28b}$$

$$\hat{v}_{W,ns} = \mathrm{M}\left(w_n; \hat{v}^{\max}_{W,ns}, \hat{K}_{W,ns,W}\right) \mathrm{M}\left(a_n; 1, \hat{K}_{W,ns,A}\right), \tag{5.28c}$$

$$\hat{v}_{W,sg} = \mathrm{M}\left(w_s; \hat{v}^{\max}_{W,sg}, \hat{K}_{W,sg,W}\right) \mathrm{M}\left(a_g; 1, \hat{K}_{W,sg,A}\right). \tag{5.28d}$$

The eight intracellular reaction rates are given by,

$$\begin{aligned} \hat{v}_{YZ,m} &= \frac{A_r}{B_r}\mathrm{M}\left(y_m; \hat{v}^{\max}_{YZ,m}, \hat{K}_{YZ,m}\right)\left(a_{\mathrm{Tot},m} - a_m\right), \\ &\qquad (YZ,m) \in \{(GL,g),(GL,n),(LW,g),(LA,n),(WA,n)\}, \end{aligned} \tag{5.29a}$$

$$\hat{v}_{WN,g} = \mathrm{M}\left(w_g; \hat{v}^{\max}_{WN,g}, \hat{K}_{WN,g,W}\right) \mathrm{M}\left(a_g; 1, \hat{K}_{WN,g,A}\right), \tag{5.29b}$$

$$\hat{v}_{NW,n} = \hat{v}^{\max}_{NW,n}\left(\frac{n_n}{n_n + \hat{k}_{NW,n,W} w_n + \hat{K}_{NW,n}}\right), \tag{5.29c}$$

$$\hat{v}_{A0,x} = \mathrm{M}\left(a_x; \hat{v}^{\max}_{A0,x}, \hat{K}_{A0,x}\right), \tag{5.29d}$$

where $x \in \{g,n\}$ and $\hat{K}_{A0,x} \ll 1$.

5.3 COMPARISON WITH MODEL OF AUBERT AND COSTALAT

Compared to previous models, our model has a detailed representation of the glutamate-glutamine cycle, and a more phenomenological description of energy metabolism. By incorporating the links between energy metabolism and the glutamate-glutamine cycle we can investigate the effects of blood glucose levels

on inner retinal glutamate levels. In order to compensate for this complexity, we have used a simple representation of energy metabolism so that the model remains amenable to mathematical analysis and physiological interpretation.

In §5.1 we introduced rates of substrate consumption and product formation for entire metabolic pathways. By using such combined rates we assume that only one of the intermediate steps is rate-limiting while the others are rapid. In the following section we give an example of how the intermediates in metabolic pathways can be eliminated by the use of rapid kinetics assumptions. We use asymptotic analysis to show how Aubert and Costalat's multi-step representations of glycolysis, oxidative metabolism and pyruvate-lactate conversion (via the LDH reaction) in [1] can be condensed into two single reaction rates such as ours on the timescale used in our model, subject to certain conditions on parameter values. These conditions are fulfilled by the parameter values in [1], suggesting that our phenomenological reaction rate expressions for glycolysis and oxidative metabolism will exhibit the same behaviour as the more complex multi-step representation in [1].

Aubert and Costalat's model [1] and ours cannot be directly compared as some mechanisms and metabolites are not common to both models (e.g. Na^+ and oxygen are included in [1] while the glutamate-glutamine cycle is included in our model). Therefore, in the following section, we consider submodels derived from [1] (the *AC* submodel) and from our own model (the *IR* submodel) that are directly comparable. In §5.3.2 we describe how rapid kinetics approximations can be made to simplify the AC submodel to combine the multiple steps in reaction pathways into single rates like those in the IR submodel.

5.3.1 *Development of Submodels*

In our model of inner retinal energy metabolism, glycolysis, oxidative pyruvate metabolism and pyruvate-lactate conversion (via the LDH reaction discussed in §5.1) are incorporated using three metabolites (glucose, lactate and ATP) and two reaction rate expressions in each cell type ($v_{GL,g}$ and $v_{LW,g}$ in the glia, $v_{GL,n}$ and $v_{LA,n}$ in the neurons). The same processes have been modelled using multiple steps (with $v_{\text{HK-PFK},x}$, $v_{\text{PGK},x}$ and $v_{\text{PK},x}$ representing glycolysis, and $v_{\text{Mito},x}$ and $v_{\text{LDH},x}$ representing the rate of oxidative metabolism and pyruvate-lactate conversion respectively where $x \in \{g, n\}$) and more metabolites (glucose, GAP,

PEP, pyruvate, lactate and ATP) in [1]. These rates in the two systems are the subjects of our comparison. Our primary interest is in how the rates of these pathways and the concentrations of their products depend on the substrate levels. Therefore, we can treat both pathways as black boxes, and consider only the input (substrate levels) and output (reaction rates and product levels). The rates of glycolysis and oxidative metabolism both depend on glucose levels: glucose is the substrate for glycolysis, which produces pyruvate/lactate, the substrate for oxidative metabolism. The levels of glucose determine the rate of pyruvate/lactate production, which affects the rate of oxidative metabolism. We therefore focus on how the rates of glycolysis and oxidative metabolism, and the concentrations of their products (pyruvate/lactate and ATP) depend on the input glucose levels, $G_g = G_n = G^*$.

We define two submodels containing the glycolytic and oxidative pathways as represented in our model and Aubert and Costalat's system respectively. We refer to the former as the *Inner Retinal Energy Metabolism* (or *IR*) submodel, and the latter as the *Aubert-Costalat Energy Metabolism* (or *AC*) submodel. To ensure that the pyruvate/lactate and ATP concentrations can reach physically reasonable steady states, the submodels also account for lactate transport and a baseline ATP consumption in each cell type. These processes balance the net ATP production and enable lactate levels (and hence pyruvate levels) to equilibrate if the lactate/pyruvate production by glycolysis does not exactly balance the consumption via oxidative metabolism. We represent the rates of lactate transport and baseline ATP consumption in the same way in each submodel (using equations (5.10) and (5.19) respectively) for simplicity, since we do not focus on these rates.

The IR submodel is defined by equations (5.2b), (5.2e), (5.5b) and (5.5e), with all reactions involved in the glutamate-glutamine cycle set to zero (i.e. $v_{WN,g} = v_{N,sg} = v_{N,sn} = v_{NW,n} = v_{WA,n} = v_{W,ns} = v_{W,sg} = 0$). We fix the glucose levels to $G_x = G^*$, and the blood lactate levels to $L_b = L_b^*$ as in our full model (see §5.1), where G^* and L_b^* are positive constants. Furthermore, in order to allow the metabolic processes in the glial and neuronal cells to remain uncoupled, we clamp the lactate levels in the ECS at an estimated realistic value, $L_s = L_s^* > 0$. Then the lactate transport terms for each cell type depend only on its own intracellular lactate levels. All other definitions and reaction rates are unchanged from §5.1. In the neurons, we set the initial concentrations to their resting steady state values predicted by this submodel.

These values are calculated by setting the rates of change of the concentrations to zero under conditions where neurons are inactive. In the glial cells, since equations (5.2b) and (5.2e) remain unchanged between resting conditions and neuronal stimulation, the concentrations reach the same steady states under resting conditions and neuronal stimulation. Therefore, in order for the glial concentrations to exhibit some time evolution, we choose the initial values for the concentrations as moderate perturbations from the resting steady states. A summary of the IR submodel is shown in the middle column of Table 5.1.

The AC submodel is given by equations (4.10b)–(4.10d), (4.10f) and (4.10g) from Aubert and Costalat's model [1], with the rates $v_{L,\text{trans},yx}$ and $v_{\text{Pump},x} - v_{\text{CK},x} + v_{\text{ATPases},x}$ used in [1] (see §4.2) replaced by $v_{L,yx}$ and $v_{A0,x}$ respectively from our model (see equations (5.10) and (5.19) respectively), and $\phi(A_x)$ set to 0, which corresponds to assuming that AMP concentrations are low. We note that the lactate transport rates, $v_{L,\text{trans},yx}$, in [1] are identical to those in our model, but with different notation. The terms $v_{\text{Pump},x} - v_{\text{CK},x} + v_{\text{ATPases},x}$ denote net ATP consumption by Na^+/K^+ ATPase pumps, creatine kinase reactions and other ATPases in [1], whereas $v_{A0,x}$ in our model denotes a baseline ATP consumption rate that accounts for the same processes but using a different approach. We set $G_x = G^*$, $L_s = L_s^*$, $L_b = L_b^*$, (i.e. the same values as those in the IR submodel). We set the initial neuronal concentrations to the resting steady state values of this submodel (the concentrations for which the rates of change under resting conditions are zero). Using the same argument as for the IR submodel, the initial values for the glial concentrations are moderate perturbations from their resting steady states. All other definitions and reaction rates are as defined earlier (see §4.2.2). A summary of the AC submodel is shown in the right hand column of Table 5.1.

The reaction rates and concentrations included in this submodel are shown in red in Figure 5.3, while Figure 5.4 compares the AC and IR submodels.

5.3.2 *Asymptotic Approximation to the AC Submodel*

Nondimensionalising the AC submodel and substituting the parameter values from Tables 4.1–4.2 reveals that, on a typical timescale in our model, T_0 (see §5.2), the GAP, PEP and pyruvate concentrations are quasisteady, as discussed below. This leads to a simplified system that has a very similar form to the IR submodel.

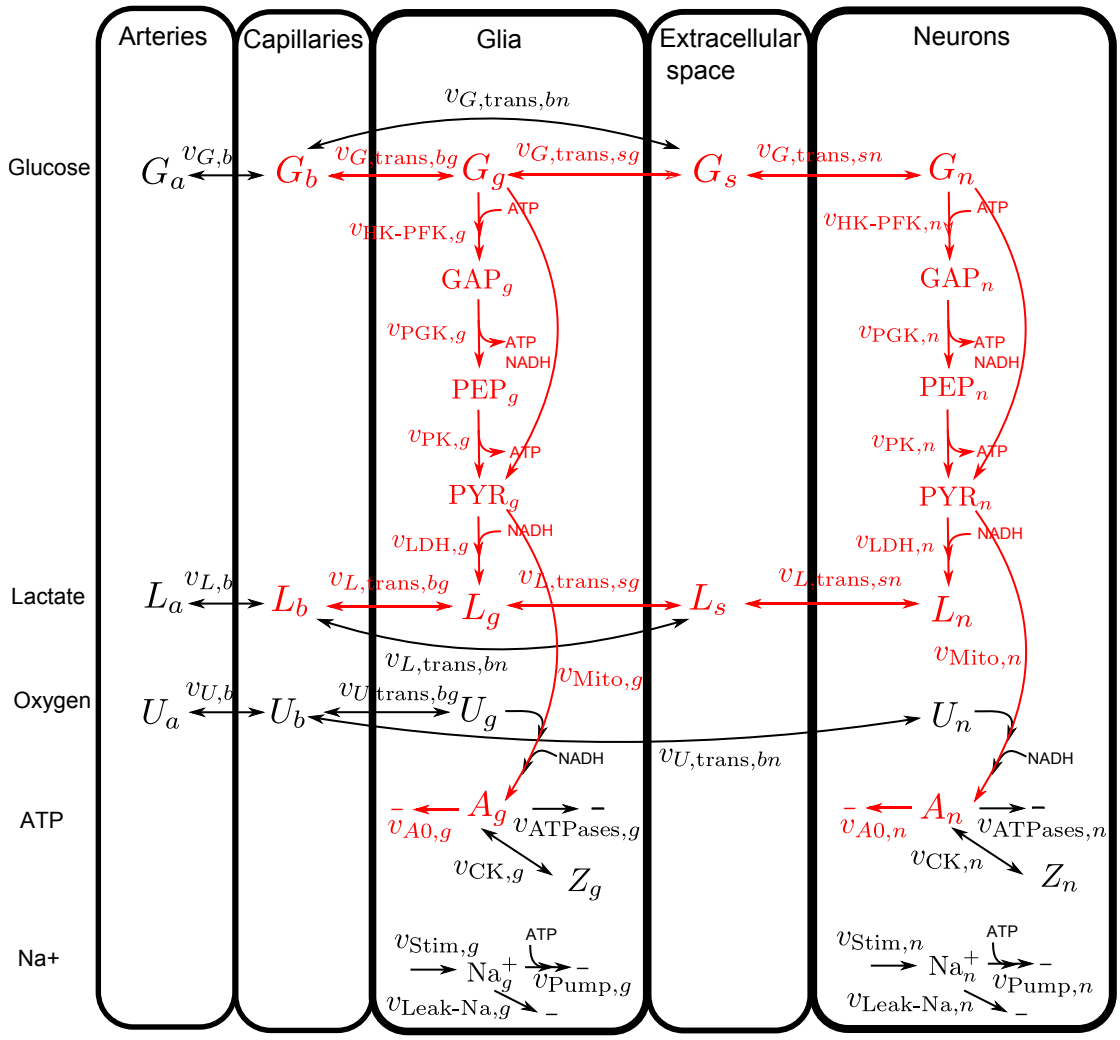


Figure 5.3.: Schematic diagram of Aubert and Costalat's model of cerebral metabolism [1] (see equations (4.10)–(4.19) in Chapter 4). The components shown in red are included in the AC submodel (see Table 5.1).

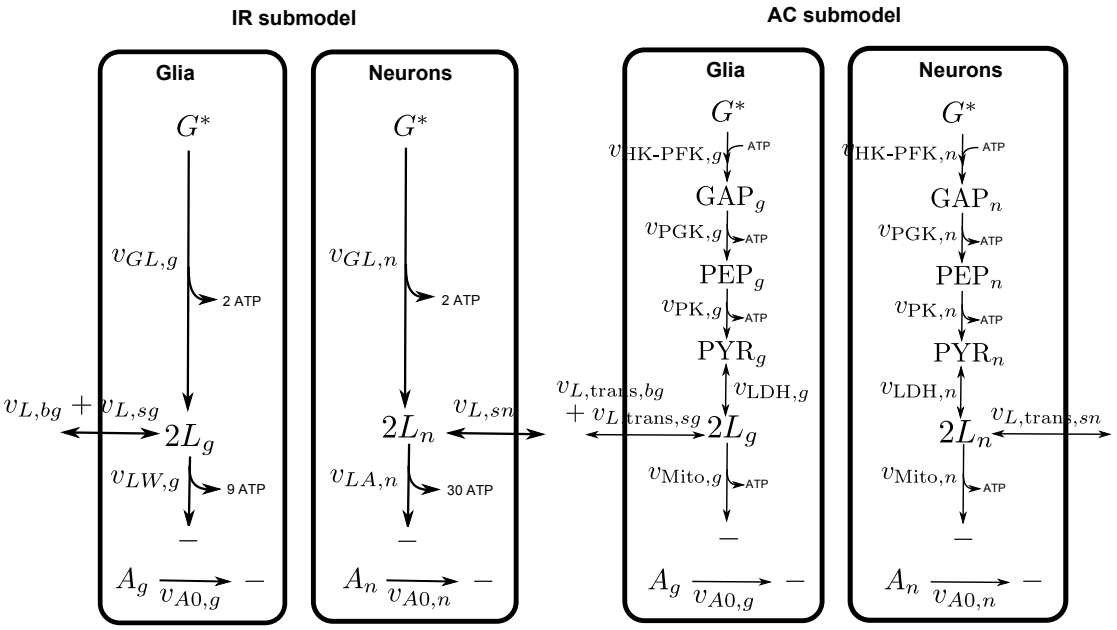


Figure 5.4.: Schematic diagram comparing the IR submodel and the AC submodel (See Table 5.1), in the glial cells and neuronal cells).

Submodel	**IR**	**AC**
Governing ODEs	(5.2b), (5.2e), (5.5b), (5.5e)	(4.10b)–(4.10d), (4.10f), (4.10g)
Initial conditions	Glia: moderate perturbation from resting steady state of IR submodel, neurons: resting steady state of IR submodel	Glia: moderate perturbation from resting steady state of AC submodel, neurons: resting steady state of AC submodel
Reaction rates	(5.10), (5.12), (5.19)	(5.10), (4.23), (4.24), (4.25), (4.27), (4.26), (5.19)
Assumptions	$v_{W,sg} = 0$, $v_{WN,g} = 0$, $v_{W,ns} = 0$, $v_{WA,n} = 0$, $G_x = G^*$, $L_b = L_b^*$, $L_s = L_s^*$	$G_x = G^*$, $L_s = L_s^*$, $L_b = L_b^*$, $\phi(A_x) = 0$, $v_{\text{ATPases},x} + v_{\text{Pump},x} - v_{\text{CK},x}$ replaced by (5.19)

Table 5.1.: Governing ODEs, initial conditions and reaction rates in the IR submodel and AC submodel.

We nondimensionalise the AC submodel by defining the following dimensionless variables,

$$l_x = \frac{L_x}{L_r}, \qquad \hat{\mathrm{GAP}}_x = \frac{\mathrm{GAP}_x}{[\mathrm{GAP}]_r}, \qquad \hat{\mathrm{PEP}}_x = \frac{\mathrm{PEP}_x}{[\mathrm{PEP}]_r}, \qquad \hat{\mathrm{PYR}}_x = \frac{\mathrm{PYR}_x}{[\mathrm{PYR}]_r},$$
$$a_x = \frac{A_x}{A_r}, \qquad b_x = \frac{B_x}{B_r}, \qquad \tau = \frac{t}{T_0}, \tag{5.30}$$

where concentrations have been rescaled by values that reflect their typical orders of magnitude, estimated using the simulation results (see Figures 4.8–4.13). The scalings for the model variables are as follows,

$$L_r = 1.0\mathrm{mM}, \qquad [\mathrm{GAP}]_r = 0.01\mathrm{mM}, \qquad [\mathrm{PEP}]_r = 0.05\mathrm{mM},$$
$$[\mathrm{PYR}]_r = 0.17\mathrm{mM}, \qquad A_r = 2.0\mathrm{mM}, \qquad B_r = 0.1\mathrm{mM},$$
$$T_0 = \frac{L_r}{v^{\max}_{L,bg}}. \tag{5.31}$$

Thus the scalings L_r, A_r, B_r and T_0 are the same as those in our model. We note that T_0 is a typical timescale in Aubert and Costalat's simulations as well as that in our model.

Using the following dimensionless parameter groupings,

$$\hat{v}^{\max}_{L,yx} = \frac{1}{2}\frac{T_0}{L_r} v^{\max}_{L,yx},$$
$$\hat{K}_{L,yx} = \frac{K_{L,yx}}{L_r},$$
$$\hat{k}_{\text{HK-PFK},x} = T_0 \mathrm{M}\left(g^*; k_{\text{HK-PFK},x}, \hat{K}_{\text{HK-PFK},G,x}\right)\left(\frac{K_{\text{HK-PFK},A,x}}{A_r}\right)^4,$$
$$\hat{K}_{\text{HK-PFK},G,x} = \frac{K_{\text{HK-PFK},G,x}}{G_r},$$
$$\hat{K}_{\text{HK-PFK},A,x} = \frac{K_{\text{HK-PFK},A,x}}{A_r},$$
$$\hat{k}_{\mathrm{PGK},x} = k_{\mathrm{PGK},x} T_0 \frac{B_r[\mathrm{GAP}]_r}{A_r}\frac{\mathrm{NAD}^{+*}}{\mathrm{NADH}^*},$$
$$\hat{k}_{\mathrm{PK},x} = k_{\mathrm{PK},x} T_0 \frac{B_r[\mathrm{PEP}]_r}{A_r},$$
$$\hat{k}^+_{\mathrm{LDH},x} = k^+_{\mathrm{LDH},x} T_0 \mathrm{NADH}^* \left(\frac{2v^{\max}_{L,bg}}{L_r}\right)^2,$$

$$
\begin{aligned}
\hat{k}^{-}_{\mathrm{LDH},x} &= k^{-}_{\mathrm{LDH},x} T_0 \mathrm{NAD}^{+*} \frac{L_r}{[\mathrm{PYR}]_r} \left(\frac{2 v^{\max}_{L,bg}}{L_r} \right)^2, \\
\hat{v}^{\max}_{\mathrm{Mito},x} &= \frac{1}{2} \frac{T_0}{A_r} \mathrm{M}\left(U^*; v^{\max}_{\mathrm{Mito},x}, K_{\mathrm{Mito},U,x} \right), \\
\hat{K}_{\mathrm{Mito,PYR},x} &= \frac{K_{\mathrm{Mito,PYR},x}}{[\mathrm{PYR}]_r}, \\
\hat{K}^{x}_{\mathrm{Mito},B,x} &= \frac{K^{x}_{\mathrm{Mito},B,x}}{B_r}, \\
\hat{v}^{\max}_{A0,x} &= v_{A0,x} \frac{T_0}{A_r}, \\
\hat{K}_{A0,x} &= \frac{K_{A0,x}}{A_r}, \\
r_1 &= 2 \frac{A_r}{L_r} \frac{v^{\max}_{L,bg}}{[\mathrm{GAP}]_r}, \\
r_2 &= 2 \frac{A_r}{L_r} \frac{v^{\max}_{L,bg}}{[\mathrm{PEP}]_r},
\end{aligned}
\tag{5.32}
$$

and defining the small parameter,

$$
\epsilon = \frac{2 v^{\max}_{L,bg}}{L_r} = 0.0058 \ll 1, \tag{5.33}
$$

the AC submodel becomes,

$$
\epsilon \frac{d \hat{\mathrm{GAP}}_x}{d\tau} = r_1 \left(2 \hat{v}_{\mathrm{HK\text{-}PFK},x} - \hat{v}_{\mathrm{PGK},x} \right), \tag{5.34a}
$$

$$
\epsilon \frac{d \hat{\mathrm{PEP}}_x}{d\tau} = r_2 \left(\hat{v}_{\mathrm{PGK},x} - \hat{v}_{\mathrm{PK},x} \right), \tag{5.34b}
$$

$$
\epsilon^2 \frac{d \hat{\mathrm{PYR}}_x}{d\tau} = \frac{A_r}{[\mathrm{PYR}]_r} \epsilon^2 \hat{v}_{\mathrm{PK},x} - \hat{v}_{\mathrm{LDH},x} - 2 \frac{A_r}{[\mathrm{PYR}]_r} \epsilon^2 \hat{v}_{\mathrm{Mito},x}, \tag{5.34c}
$$

$$
\epsilon^2 \frac{d l_x}{d\tau} = 2 \epsilon^2 \hat{v}_{L,yx} + \frac{[\mathrm{PYR}]_r}{[\mathrm{LAC}]_r} \hat{v}_{\mathrm{LDH},x}, \tag{5.34d}
$$

$$
\frac{d a_x}{d\tau} = -2 \hat{v}_{\mathrm{HK\text{-}PFK},x} + \hat{v}_{\mathrm{PGK},x} + \hat{v}_{\mathrm{PK},x} - \hat{v}_{A0,x} + 2 n_{\mathrm{OP}} \hat{v}_{\mathrm{Mito},x}, \tag{5.34e}
$$

$$
5\epsilon \frac{d b_x}{d\tau} = 2 \hat{v}_{\mathrm{HK\text{-}PFK},x} - \hat{v}_{\mathrm{PGK},x} - \hat{v}_{\mathrm{PK},x} + \hat{v}_{A0,x} - 2 n_{\mathrm{OP}} \hat{v}_{\mathrm{Mito},x}, \tag{5.34f}
$$

with initial conditions given by,

$$
u_x \left(\tau = 0 \right) = u_{x,0}, \tag{5.35}
$$

where $u \in \{\hat{\text{GAP}}, \hat{\text{PEP}}, \hat{\text{PYR}}, l, a, b\}$ and $u_{x,0} = U_{x,0}/[U]_r$. As the notation suggests, the parameter values $\hat{v}^{\max}_{L,yx}$, $\hat{K}_{L,yx}$, $\hat{v}^{\max}_{A0,x}$ and $\hat{K}_{A0,x}$ represent the same quantities as in the nondimensionalised IR model, since the reaction rates $\hat{v}_{L,yx}$ and $\hat{v}_{A0,x}$ have the same functional form here as in §5.2. We write,

$$\hat{v}_{L,yx} = \begin{cases} \hat{v}_{L,bg} + \hat{v}_{L,sg} & \text{for } x = g, \\ \hat{v}_{L,sn} & \text{for } x = n, \end{cases} \tag{5.36}$$

while the dimensionless reaction rates are,

$$\hat{v}_{L,yx} = \mathrm{M}\left(l_y; \hat{v}^{\max}_{L,yx}, \hat{K}_{L,yx}\right) - \mathrm{M}\left(l_x; \hat{v}^{\max}_{L,yx}, \hat{K}_{L,yx}\right), \tag{5.37a}$$

$$\hat{v}_{\text{HK-PFK},x} = \hat{k}_{\text{HK-PFK},x} \frac{a_x}{a_x^4 + \hat{K}^4_{\text{HK-PFK},A,x}}, \tag{5.37b}$$

$$\hat{v}_{\text{PGK},x} = \hat{k}_{\text{PGK},x} \hat{\text{GAP}}_x b_x, \tag{5.37c}$$

$$\hat{v}_{\text{PK},x} = \hat{k}_{\text{PK},x} \hat{\text{PEP}}_x b_x, \tag{5.37d}$$

$$\hat{v}_{\text{LDH},x} = \hat{k}^{+}_{\text{LDH},x} \hat{\text{PYR}}_x - \hat{k}^{-}_{\text{LDH},x} l_x, \tag{5.37e}$$

$$\hat{v}_{\text{Mito},x} = \mathrm{M}\left(\hat{\text{PYR}}_x; \hat{v}^{\max}_{\text{Mito},x}, \hat{K}_{\text{Mito,PYR},x}\right) \mathrm{M}\left(b_x; 1, \hat{K}_{\text{Mito},B,x}\right), \tag{5.37f}$$

where $yx \in \{bg, sg, sn\}$, $\hat{v}_{A0,x}$ is defined by equation (5.29d) and $g_x = g^*$, $l_s = l_s^*$, and $l_b = l_b^*$.

Figures 5.5 and 5.6 show the time evolution of the metabolite concentrations during 5 minutes of neuronal stimulation, for the AC submodel (—), and leading order asymptotic approximations on short (xxx), intermediate (xxx) and long (xxx) timescales, for which $\tau = \mathcal{O}(\epsilon^2)$, $\tau = \mathcal{O}(\epsilon)$ and $\tau = \mathcal{O}(1)$ respectively, with glial and neuronal glucose levels of 1.2mM. The figures reveal that each asymptotic approximation matches closely with the results of the AC submodel on the relevant timescale.

Details of the asymptotic analysis of equations (5.34) are given in Appendix B, where we follow a similar method to [267] for example. Here we discuss the key outcomes of this analysis. The conversion between pyruvate and lactate (at rate $\hat{v}_{\text{LDH},x}$) occurs within a few milliseconds (for which $\tau = \mathcal{O}(\epsilon^2)$). The dynamics of the GAP and PEP concentrations occur on a timescale of seconds (with $\tau = \mathcal{O}(\epsilon)$), however the pyruvate-lactate conversion has already reached a chemical equilibrium such that the evolution of the pyruvate concentration is determined by the dynamics of the lactate concentration. Within 2–3 minutes, the GAP and PEP concentrations reach quasisteady states and therefore are slave to the

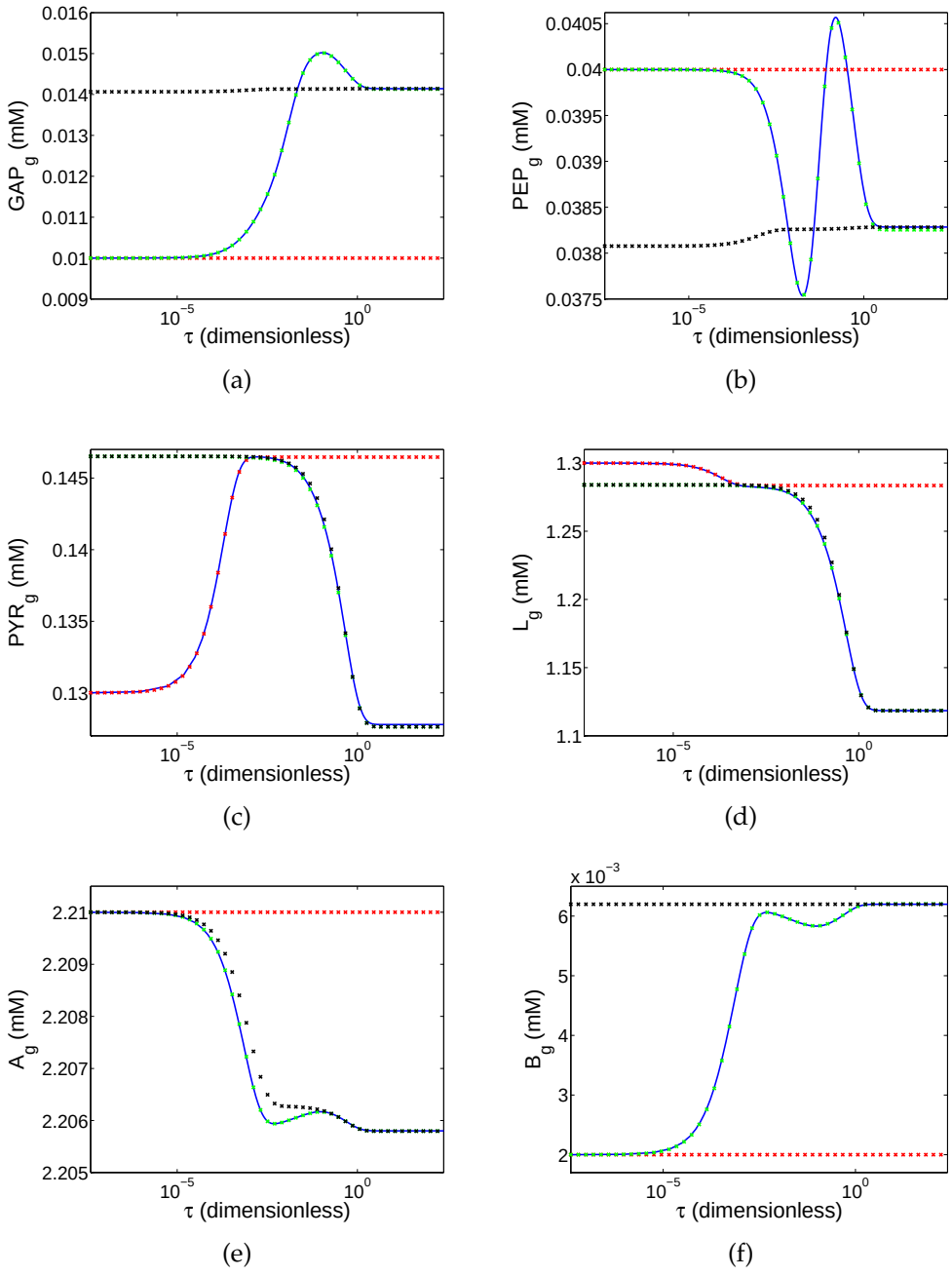


Figure 5.5.: Plots showing the time evolution of the glial GAP, PEP, pyruvate, lactate, ATP and ADP concentrations according to the asymptotic approximations on the short (xxx), intermediate (xxx) and long (xxx) timescales, and the AC submodel ((—); see Table 5.1), with glial and neuronal glucose levels of 1.2mM, during 5 minutes of neuronal stimulation. For details of the asymptotic approximations, see Appendix B. Since there is no change to glial metabolism in the AC submodel under resting conditions, the same results are obtained at rest.

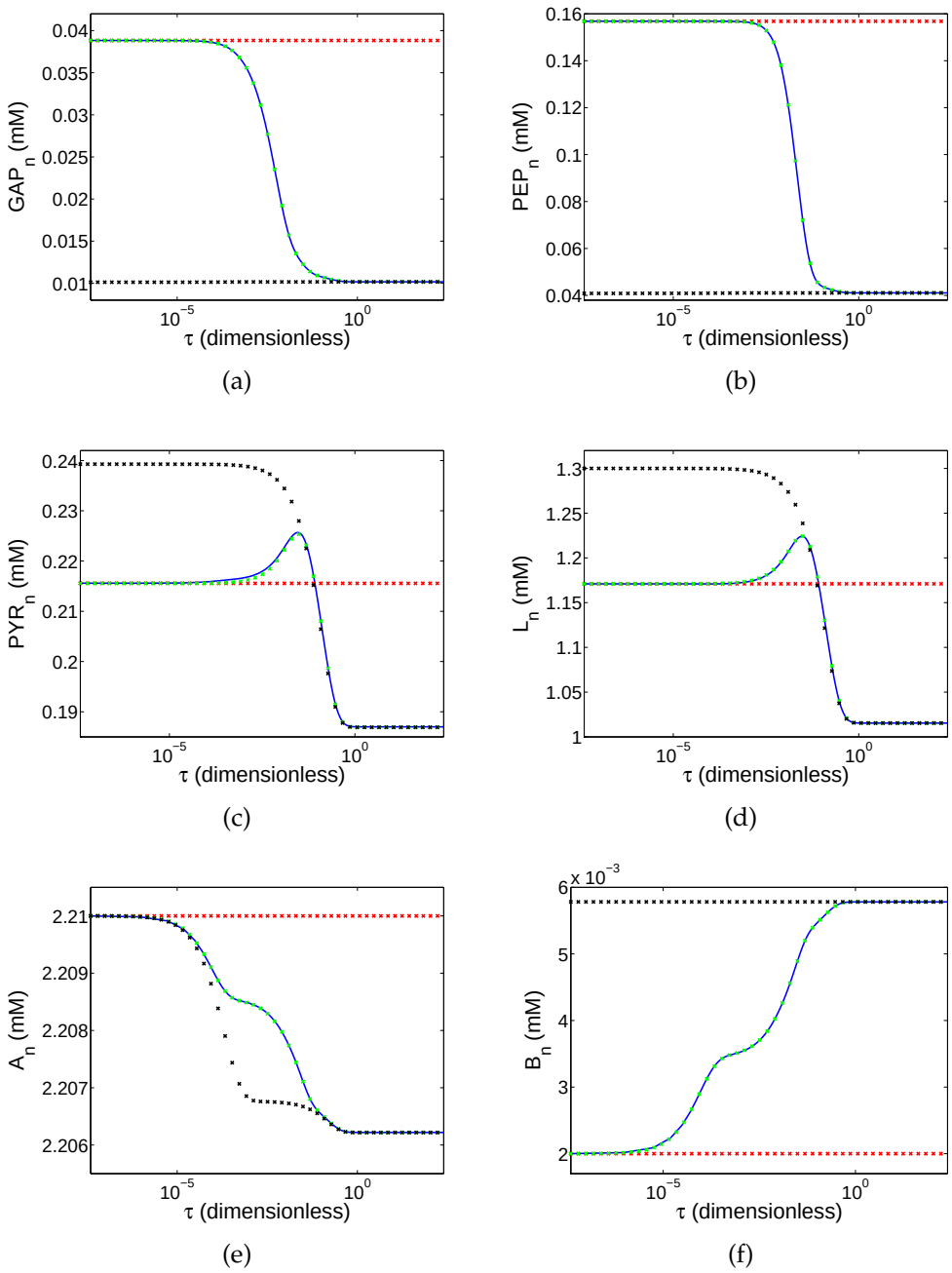


Figure 5.6.: Plots showing the time evolution of the neuronal GAP, PEP, pyruvate, lactate, ATP and ADP concentrations according to the asymptotic approximations on the short (xxx), intermediate (xxx) and long (xxx) timescales, and the AC submodel (—), with glial and neuronal glucose levels of 1.2mM, during 5 minutes of neuronal stimulation. The AC submodel is given in Table 5.1. For details of the asymptotic approximations, see Appendix B.

evolution of the lactate and ATP concentrations. In particular, the following algebraic equations determine the GAP, PEP and pyruvate concentrations,

$$\hat{\mathrm{GAP}}_x = 2\frac{\hat{k}_{\text{HK-PFK},x}}{\hat{k}_{\text{PGK},x}}\frac{a_x}{b_x}\frac{1}{a_x^4 + \hat{K}^4_{\text{HK-PFK},A,x}}, \tag{5.38a}$$

$$\hat{\mathrm{PEP}}_x = \frac{A_r}{[\mathrm{PYR}]_r}\frac{\hat{k}_{\text{PGK},x}}{\hat{k}_{\text{PK},x}}\hat{\mathrm{GAP}}_x, \tag{5.38b}$$

$$\hat{\mathrm{PYR}}_x = \frac{\hat{k}^-_{\text{LDH},x}}{\hat{k}^+_{\text{LDH},x}} l_x. \tag{5.38c}$$

Therefore, according to the asymptotic approximation to the AC submodel when $\tau = \mathcal{O}(1)$, the dynamics of the lactate and ATP concentrations are such that,

$$\begin{aligned}\frac{dl_x}{d\tau} = \left(\frac{\hat{k}^-_{\text{LDH},x}}{\hat{k}^+_{\text{LDH},x}} + \frac{L_r}{[\mathrm{PYR}]_r}\right)^{-1} \Bigg(2\frac{A_r}{[\mathrm{PYR}]_r}\hat{v}_{\text{HK-PFK},x} \\ -2\frac{A_r}{[\mathrm{PYR}]_r}\hat{v}_{\text{Mito},x} + 2\frac{L_r}{[\mathrm{PYR}]_r}\hat{v}_{L,yx}\Bigg),\end{aligned} \tag{5.39a}$$

$$\frac{da_x}{d\tau} = 2\hat{v}_{\text{HK-PFK},x} - \hat{v}_{A0,x} + 2n_{\text{OP}}\hat{v}_{\text{Mito},x}, \tag{5.39b}$$

with initial conditions (5.35), where the reaction rates $\hat{v}_{\text{HK-PFK},x}$, $\hat{v}_{L,yx}$ and $v_{A0,x}$ satisfy the appropriate equations in (5.37), and the reaction rate $\hat{v}_{\text{Mito},x}$ is now given by,

$$\hat{v}_{\text{Mito},x} = \mathrm{M}\left(l_x; \hat{v}^{\max}_{\text{Mito},x}, \frac{\hat{k}^+_{\text{LDH},x}}{\hat{k}^-_{\text{LDH},x}}\hat{K}_{\text{Mito,PYR},x}\right)\mathrm{M}\left(b_x; 1, \hat{K}_{\text{Mito},B,x}\right). \tag{5.40}$$

The concentrations of GAP, PEP and pyruvate are known via equations (5.38), with the ADP concentration governed by the ATP concentration via the conservation law in (5.21). The solutions are denoted by (xxx) in Figures 5.5 and 5.6. We note that the lactate concentration evolves on all three timescales, with the dynamics on the short timescale resulting from the rapid reaction rate $\hat{v}_{\text{LDH},x}$, and the dynamics on the intermediate and long timescales brought about by the reaction rate $\hat{v}_{\text{PK},x}$, lactate transport and oxidative metabolism.

We note that in the asymptotic approximation on the long timescale $\tau = \mathcal{O}(1)$ (given by equations (5.39)), all except four of the reaction rates and all but two of the metabolites have been eliminated. The remaining system is in a form that

Submodel	Nondimensionalised IR	Simplified AC
Governing ODEs	(5.23b), (5.23e), (5.25b) (5.25e)	(5.39)
Initial conditions	Glia: moderate perturbation from resting steady state of nondimensionalised IR submodel, neurons: resting steady state of nondimensionalised IR submodel	Glia: moderate perturbation from resting steady state of Simplified AC submodel, neurons: resting steady state of Simplified AC submodel
Reaction rates	(5.27), (5.29a), (5.29d)	(5.27), (5.37b), (5.40),(5.29d)
Assumptions	$\hat{v}_{W,sg} = 0$, $\hat{v}_{WN,g} = 0$, $\hat{v}_{W,ns} = 0$, $\hat{v}_{WA,n} = 0$, $g_x = g^*$, $l_s = l_s^*$, $l_b = l_b^*$	$l_s = l_s^*$, $l_b = l_b^*$, $\phi(a_x) = 0$, $\hat{v}_{\text{ATPases},x} + \hat{v}_{\text{Pump},x} - \hat{v}_{\text{CK},x}$ replaced by (5.19)

Table 5.2.: Governing ODEs, initial conditions and reaction rates in the nondimensionalised IR submodel and Simplified AC submodel.

closely resembles the IR submodel. We refer to the asymptotic approximation on the long timescale as the *Simplified AC* submodel.

The dimensionless IR submodel is given by equations (5.23b), (5.23e), (5.25b) and (5.25e), the conservation law (5.21), the relevant initial conditions from (5.26), reaction rates (5.27), (5.29a) and (5.29d), and with $g_x = g^*$, $l_s = l_s^*$ and $l_b = l_b^*$. The submodel equations are summarised in Table 5.2. Figure 5.7 shows the physical systems corresponding to the ODEs in the nondimensionalised IR submodel and Simplified AC submodel. The similarities between the two systems are evident from this figure and from their ODEs. The simplified reaction rate denoting glycolysis and pyruvate-lactate conversion is denoted by $\hat{v}_{GL,x}$ and $\hat{v}_{\text{HK-PFK},x}$ in the dimensionless IR and Simplified AC submodel respectively ($x \in \{g, n\}$). Likewise, the simplified rates denoting lactate-pyruvate conversion followed by oxidative metabolism are denoted by $\hat{v}_{LW,g}$ and $\hat{v}_{\text{Mito},g}$ in the glial cells, and $\hat{v}_{LA,n}$ and $\hat{v}_{\text{Mito},n}$ in the neurons.

5.3.3 *Comparison of the IR Submodel and the Simplified AC Submodel*

Our goal in the remainder of this chapter is to compare the qualitative behaviour of the Simplified AC submodel with that of the dimensionless IR submodel. First, however, we estimate parameter values in the IR submodel that are

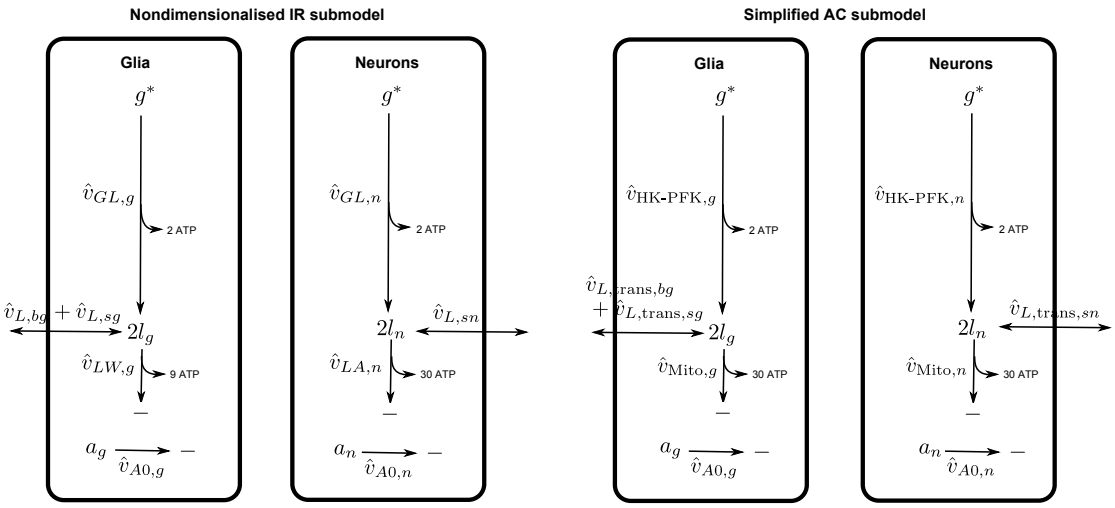


Figure 5.7.: Schematic diagram comparing the nondimensionalised IR submodel and the Simplified AC submodel (See Table 5.2), in the glial cells and neuronal cells).

equivalent to those in the AC (or Simplified AC) submodels, which we use in our simulations.

Firstly, we consider the ODEs and stoichiometries in the two systems, as shown in Figure 5.7. In both systems, glycolysis produces two lactate and two ATP molecules per glucose molecule consumed. For each pair of lactate molecules, neuronal oxidative metabolism produces 30 ATP molecules, but glial oxidative metabolism produces 9 ATP molecules in the dimensionless IR submodel compared to 30 in the Simplified AC submodel, due to the different modelling assumptions. The reaction rates are also scaled differently in the two systems. Table 5.3 shows the rates of lactate and ATP production/consumption due to each reaction rate.

We now compare the outputs of the dimensionless IR and Simplified AC submodels, using equivalent parameter values in both systems. Firstly, the clamped lactate levels in the bloodstream and ECS are chosen to be $L_b^* = 0.343$mM and $L_s^* = 0.950$mM, using typical values from simulations of Aubert and Costalat's model (see Figures 4.8 and 4.9). Then the values of the dimensionless parameter groupings in the Simplified AC submodel can be derived from Aubert and Costalat's parameter choices (given in Tables 4.1–4.2) and the scalings in (5.31) by using (5.22) and (5.32). From these values, the equivalent parameter groupings in the dimensionless IR submodel can be found as outlined below.

Rate	**Expression in IR submodel**	**Expression in Simplified AC submodel**
Lactate production by glycolysis	$2\hat{v}_{GL,x}$	$2q_x\hat{v}_{\text{HK-PFK},x}$
Lactate consumption by glial oxidative metabolism	$2\hat{v}_{LW,g}$	$2q_x\hat{v}_{\text{Mito},g}$
Lactate consumption by neuronal oxidative metabolism	$2\hat{v}_{LA,n}$	$2q_x\hat{v}_{\text{Mito},n}$
ATP production by glial oxidative metabolism	$9\hat{v}_{LW,g}$	$30q_x\hat{v}_{\text{Mito},g}$
ATP production by neuronal oxidative metabolism	$30\hat{v}_{LA,n}$	$30q_x\hat{v}_{\text{Mito},n}$
Increase/decrease in lactate through lactate transport	$2\hat{v}_{L,yx}$	$2\dfrac{L_r}{A_r}q_x\hat{v}_{L,yx}$
Baseline ATP consumption	$\hat{v}_{A0,x}$	$\hat{v}_{A0,x}$

Table 5.3.: Analogous reaction rates in the nondimensionalised IR submodel and the Simplified AC submodel (see Table 5.2).

As shown in Table 5.3, the lactate and ATP production/consumption rates in the dimensionless IR and Simplified AC submodels are scaled differently, with the exception of the rate $\hat{v}_{A0,x}$. We rescale each reaction rate apart from $\hat{v}_{A0,x}$ in the Simplified AC submodel by multiplying it by a factor of,

$$q_x = \frac{A_r}{[\text{PYR}]_r}\left(\frac{\hat{k}^-_{\text{LDH},x}}{\hat{k}^+_{\text{LDH},x}} + \frac{L_r}{[\text{PYR}]_r}\right)^{-1}. \tag{5.41}$$

The baseline ATP consumption rate in both submodels, $\hat{v}_{A0,x}$, given in equation (5.29d) with $\hat{K}_{A0,x} \ll A_r$, takes the constant value $\hat{v}^{\max}_{A0,x}$ for typical physiological ATP concentrations (see §5.1). As we established in §5.3.1, this reaction rate accounts for the combined effect of the ATP consumption rates $\hat{v}_{\text{ATPases},x}$, $\hat{v}_{\text{Pump},x}$ and $\hat{v}_{\text{CK},x}$ in Aubert and Costalat's model [1]. Therefore, we assume that the equivalent quantity in terms of Aubert and Costalat's parameter values is $\hat{v}_{\text{Pump},x} + \hat{v}_{\text{ATPases},x} - \hat{v}_{\text{CK},x}$. However, this quantity in Aubert and Costalat's model [1] depends on the variables Na^+_x, Z_x, C_x, which are clamped at typical physiological levels in the AC submodel. Denoting the clamped concentrations and corresponding reaction rates by the * symbol, we obtain,

$$\hat{v}^*_{A0,x} = \hat{v}^{\max}_{A0,x} = \hat{v}^*_{\text{Pump},x} + \hat{v}_{\text{ATPases},x} - \hat{v}^*_{\text{CK},x}, \tag{5.42}$$

where,

$$\hat{v}^*_{\text{Pump},x} = \frac{S_m}{V_x} T_0 k_{\text{Pump}} \text{Na}^{+*}_x \frac{a^*_x}{\left(1 + \frac{A_r a^*_x}{K_{m,\text{Pump}}}\right)},$$

$$\hat{v}^*_{\text{CK},x} = k^+_{\text{CK}} T_0 Z^*_x \left(a_{\text{Tot},x} - a^*_x\right) - k^-_{\text{CK}} T_0 C^*_x a^*_x.$$

The parameter $\hat{K}_{A0,x}$ can take any value that satisfies $\hat{K}_{A0,x} \ll 1$. We choose $\hat{K}_{A0,x} = 1 \times 10^{-3}$.

As stated earlier, we distinguish between resting conditions and neuronal stimulation in the submodels by increasing $\hat{v}^{\max}_{A0,n}$ during neuronal stimulation. In Aubert and Costalat's model [1], the rate $\hat{v}^*_{\text{Pump},n} + \hat{v}_{\text{ATPases},n} - \hat{v}^*_{\text{CK},n}$ increases during neuronal stimulation due to the rise in the neuronal Na^+ concentration and hence in the reaction rate $\hat{v}_{\text{Pump},n}$. To reflect this change in the typical Na^+ concentrations between resting conditions and neuronal stimulation, we define two distinct values, $\text{Na}^{+*}_{n,\text{Rest}}$ and $\text{Na}^{+*}_{n,\text{Stim}}$, denoting the neuronal Na^+ concentration during resting conditions and neuronal stimulation respectively. The corresponding values of $\hat{v}^*_{\text{Pump},n}$ are,

$$\hat{v}^*_{\text{Pump},n} = \begin{cases} \frac{S_m}{V_n} T_0 k_{\text{Pump}} \text{Na}^{+*}_{n,\text{Rest}} \dfrac{a^*_n}{\left(1 + \frac{A_r a^*_n}{K_{m,\text{Pump}}}\right)} & \text{under resting conditions,} \\ \frac{S_m}{V_n} T_0 k_{\text{Pump}} \text{Na}^{+*}_{n,\text{Stim}} \dfrac{a^*_n}{\left(1 + \frac{A_r a^*_n}{K_{m,\text{Pump}}}\right)} & \text{during neuronal stimulation.} \end{cases}$$

The change in value $\hat{v}^*_{\text{Pump},n}$ between resting conditions and neuronal stimulation causes an alteration in the value of $\hat{v}^{max}_{A0,n}$ according to equation (5.42).

The glycolytic rates in the two submodels, $\hat{v}_{GL,x}$ and $\hat{v}_{\text{HK-PFK},G,x}$, have the same glucose dependence but different ATP dependence. Matching the K_m values of the Michaelis-Menten glucose dependences yields $\hat{K}_{GL,x} = \hat{K}_{\text{HK-PFK},G,x}$. For the ATP dependences, we make a crude approximation, defining comparable parameter values in the submodels as those for which $\hat{v}_{GL,x} = \hat{v}_{\text{HK-PFK},G,x}$ at typical physiological ATP concentrations. Estimating typical ATP concentrations to be $\bar{a}_g = 0.9$ and $\bar{a}_n = 1$ using Figure A.2 in Appendix A, yields,

$$\hat{v}^{\max}_{GL,x} = q_x \hat{k}_{\text{HK-PFK},x} \frac{1}{\left(a_{\text{Tot},x} - \bar{a}_x\right)} \frac{\bar{a}_x}{\bar{a}^4_x + \hat{K}^4_{\text{HK-PFK},A,x}}.$$

We use a similar approach to find the equivalent parameter values in the rates of ATP production by oxidative metabolism, comparing the reaction rate $\hat{v}_{LW,g}$ with $(30/9)\hat{v}_{\text{Mito},g}$, and $\hat{v}_{LA,n}$ with $\hat{v}_{\text{Mito},n}$. Since these rates have the same lactate dependence, we equate the K_m values as before, giving $\hat{K}_{\text{Mito},L,g} = \hat{K}_{LW,g}$ in the glial cells and $\hat{K}_{\text{Mito},L,n} = \hat{K}_{LA,n}$ in the neurons. As the reaction rate expressions do not have the same ATP dependence, we proceed in a similar way as for the glycolytic rates, choosing the equivalent parameters as those for which the ATP production rates are equal for $a_x = \bar{a}_x$ for $x \in \{g, n\}$, which gives,

$$\hat{v}^{\max}_{\text{LW},g} = \frac{15}{9} q_x \hat{v}^{\max}_{\text{Mito},g} \frac{1}{\frac{A_r}{B_r}\left(a_{\text{Tot},g} - \bar{a}_g\right) + \hat{K}_{\text{Mito},B,g}}, \tag{5.43}$$

$$\hat{v}^{\max}_{\text{LA},n} = \frac{1}{2} q_x \hat{v}^{\max}_{\text{Mito},n} \frac{1}{\frac{A_r}{B_r}\left(a_{\text{Tot},n} - \bar{a}_n\right) + \hat{K}_{\text{Mito},B,n}}. \tag{5.44}$$

From §5.3.2, with the exception of the glial ATP concentration, the ODEs governing the time evolution of the lactate and ATP concentrations in the IR and Simplified AC submodels have the same form, with reaction rates $v_{GL,x}$ and $v_{\text{HK-PFK},x}$ denoting the glycolytic rates, $v_{LW,g}$ and $v_{\text{Mito},g}$ denoting the glial oxidative rates and $v_{LA,n}$ and $v_{\text{Mito},n}$ denoting the neuronal oxidative rates in the IR and Simplified AC submodels respectively. The two submodels use different expressions for these reaction rates, and assume a different stoichiometry for oxidative metabolism in the glial cells. However, the fact that the ODEs for these systems have the same form in all other respects justifies our chosen phenomenological rate for glycolysis, which neglects the intermediate reactions. The long timescale asymptotic approximation of the AC submodel shows that the intermediate reactions in the glycolytic pathway in [1] do not affect the dynamics of the metabolites in our model on the timescales of interest.

We now compare the expressions used for the glycolytic and oxidative rates in the IR submodel and Simplified AC submodel. The glycolytic rate in the IR submodel is linearly dependent on ADP levels to represent its increase with energy demand (see §5.1). The Simplified AC submodel predicts a more complicated dependence on ATP, of the form $A_x(A_x^4 + K^4_{\text{HK-PFK},A,x})^{-1}$. This expression was taken from Heinrich and Schuster [248], who found that this functional form provided a good fit with their empirical data when describing the ATP-dependence of the metabolic flux through steps 1–3 in the glycolytic pathway (see Chapter 4). For very small ATP concentrations, $v_{\text{HK-PFK},x} \to 0$

Parameter in IR sub-model	Analogous parameter in Simplified AC sub-model	Value
$\hat{v}^{\max}_{L,bg}$	$\frac{1}{2}\frac{L_r}{A_r}q_x v^{\max}_{L,bg}$	5.8×10^{-3}
$\hat{K}_{L,bg}$	$\hat{K}_{L,bg}$	0.5
$\hat{v}^{\max}_{L,sg}$	$\frac{1}{2}\frac{L_r}{A_r}q_x v^{\max}_{L,sg}$	0.076
$\hat{K}_{L,sg}$	$\hat{K}^{sg}_{t,LAC}$	0.5
$\hat{v}^{\max}_{L,sn}$	$\frac{1}{2}\frac{L_r}{A_r}q_x \hat{v}^{\max}_{L,sn}$	0.29
$\hat{K}_{L,sn}$	$\hat{K}^{sn}_{t,LAC}$	0.5
$\hat{v}^{\max}_{A0,g}$	$\hat{v}^{\max}_{A0,g}$	30
$\hat{K}_{A0,g}$	$\hat{K}_{A0,g}$	2
$\hat{v}^{\max}_{A0,n}$	$\hat{v}^{\max}_{A0,n}$	70
$\hat{K}_{A0,n}$	$\hat{K}_{A0,n}$	2
$\hat{v}^{\max}_{GL,g}$	$\frac{B_r}{A_r}q_x \hat{k}_{\text{HK-PFK},g}\frac{1}{\left(a_{\text{Tot},g}-\bar{a}_g\right)}\frac{\bar{a}_g}{\bar{a}_g^4+\hat{K}^4_{\text{HK-PFK},A,g}}$	0.12
$\hat{K}_{GL,g}$	$\hat{K}_{\text{HK-PFK},G,g}$	0.05
$\hat{v}^{\max}_{GL,n}$	$\frac{B_r}{A_r}q_x \hat{k}_{\text{HK-PFK},n}\frac{1}{\left(a_{\text{Tot},n}-\bar{a}_n\right)}\frac{\bar{a}_n}{\bar{a}_n^4+\hat{K}^4_{\text{HK-PFK},A,n}}$	0.047
$\hat{K}_{GL,n}$	$\hat{K}_{\text{HK-PFK},G,n}$	0.05
$\hat{v}^{\max}_{LA,n}$	$\frac{1}{2}\frac{B_r}{A_r}q_x \hat{v}^{\max}_{\text{Mito},n}\frac{1}{\left(a_{\text{Tot},n}-\bar{a}_n\right)+\hat{K}_{\text{Mito},B,n}}$	0.0402
$\hat{K}_{LA,n}$	$\hat{K}_{\text{Mito},L,n}$	20
$\hat{v}^{\max}_{LW,g}$	$\frac{9}{30}\frac{B_r}{A_r}q_x \hat{v}^{\max}_{\text{Mito},g}\frac{1}{\left(a_{\text{Tot},g}-\bar{a}_g\right)+\hat{K}_{\text{Mito},B,g}}$	5.82×10^{-3}
$\hat{K}_{LW,g}$	$\hat{K}_{\text{Mito},L,g}$	0.05
g_b	g_b	4.56
l_b	l_b	0.343
V_g	V_g	0.25
V_s	V_s	0.2
V_n	V_n	0.45

Table 5.4.: Analogous parameters in nondimensionalised IR submodel and the Simplified AC submodel (see Table 5.2).

(see Figure 5.9) whereas $v_{GL,x}$ is at its maximum. As glycolysis requires ATP molecules to take place (in steps 1 and 3), the glycolytic rate is very low in ATP-deprived conditions, so $v_{\text{HK-PFK},x}$ is more realistic than $v_{GL,x}$ in this scenario. However, very low ATP levels reflect a pathological situation (the most extreme case being cell death if $A_x \to 0$), in which case our model has already fulfilled its purpose by giving us insight into the system behaviour prior to the onset of pathology. The subsequent dynamics of other metabolites is a possible topic for future work. For ATP levels in the typical physiological range, $v_{GL,x}$ behaves in a similar way to $v_{\text{HK-PFK},x}$ in that it decreases with ATP levels.

The IR submodel assumes that the rate of oxidative metabolism has a linear dependence on ADP levels, whereas the Simplified AC submodel assumes a saturating dependence. Aubert and Costalat's choice of $K_{\text{Mito},A,x}$ is obtained from a large possible range of values based on empirical data (see [268]), and other equally valid choices could be made. If $K_{\text{Mito},A,x} \gg B_r$, the linear dependence in the IR submodel becomes a good approximation. As the typical ADP concentration is $B_r = 0.1\text{mM}$, this is not true for Aubert and Costalat's choices, $K_{\text{Mito},A,g} = K_{\text{Mito},A,n} = 0.005\text{mM}$.

Based on the above arguments, we expect the two submodels to be qualitatively but not quantitatively the same for typical physiological metabolite concentrations. Figure 5.8 shows the glucose dose response of the steady state concentrations during resting conditions and neuronal stimulation in the dimensionless IR submodel (denoted by (xxx) and $(\cdots)$ respectively) and the Simplified AC submodel (denoted by (—) and (- - -) respectively), using the parameter values in Table 5.4. The outputs of the two submodels have qualitatively the same glucose dose responses for typical metabolite concentrations. Since the glycolytic and oxidative metabolic rates in the IR and AC submodels are identical to those in the corresponding full models, this indicates that, where both our model in §5.1 and Aubert and Costalat's system [1] are valid, the glycolytic and oxidative pathways in these models exhibit similar glucose dose responses.

The ATP dose responses for the glycolytic and oxidative rates in the dimensionless IR submodel and the Simplified AC submodel are shown in Figure 5.9 (with parameter values taken from Table 5.4). This figure shows that the steady state ATP concentrations are quantitatively the same in both submodels when $A_x = \bar{A}_x$, due to our parameter choices. However, the steady state ATP concentrations shown in Figure 5.8 are generally not equal to $\bar{A}_g$ or $\bar{A}_n$.

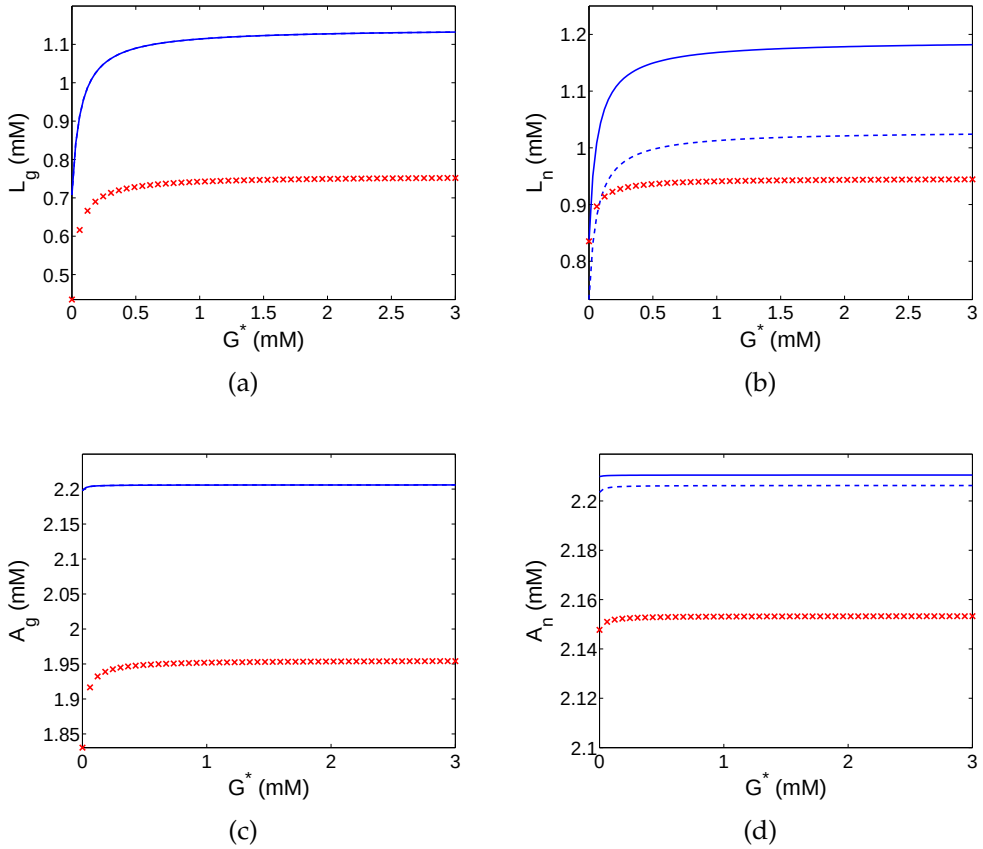


Figure 5.8.: Plots showing glucose dose response of the steady state lactate and ATP concentrations in the IR submodel ((xxx): rest; (· · ·): neuronal stimulation), and the Simplified AC submodel ((—): rest, (- - -): neuronal stimulation). Both submodels are summarised in Table 5.2 and the parameter values in Table 5.4. We note that, in the glial cells, the glucose dose response curves are coincident during resting conditions and neuronal stimulation, since, in both submodels, the equations in the glial cells are unchanged by neuronal stimulation (as the glial uptake of glutamate and Na^+ are not included).

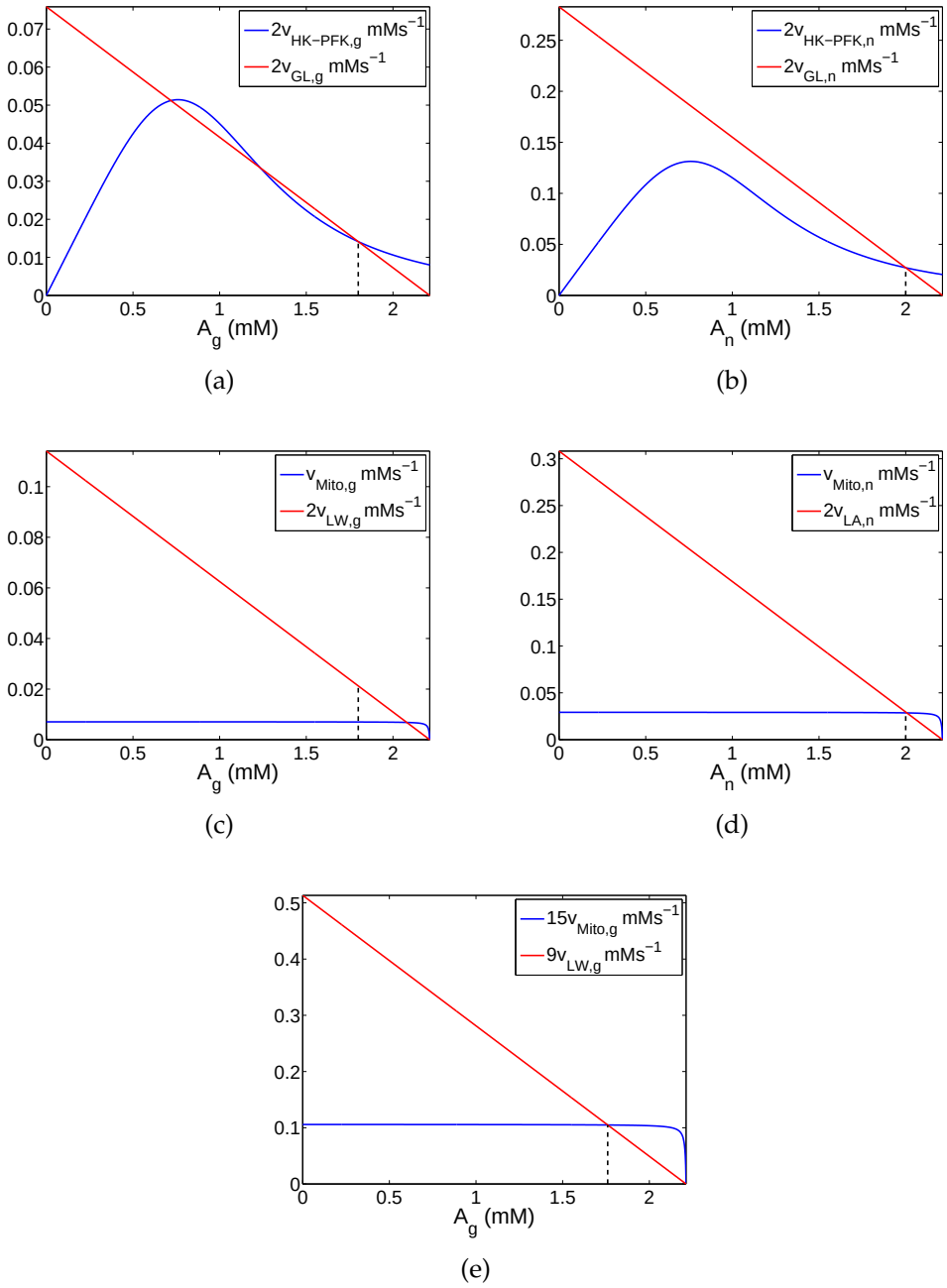


Figure 5.9.: Plots showing ATP dose response of the glycolytic and oxidative rates (—) in the IR submodel (see (5.12) with $(YZ, m) \in \{(GL, x), (LW, g), (LA, n)\}$) and (—) in the Simplified AC submodel (see (5.37b) and (5.40)). The parameter values used are given in Table 5.4. (a) $2v_{GL,g}$ and $2v_{\text{HK-PFK,g}}$, and (b) $2v_{GL,n}$ and $2v_{\text{HK-PFK,n}}$ show the rates of glycolytic lactate production; (c) $2v_{LW,g}$ and $v_{\text{Mito,g}}$, and (d) $2v_{LA,n}$ and $v_{\text{Mito,n}}$ show the rates of oxidative lactate consumption; (e) $9v_{LW,g}$ and $30v_{\text{Mito,g}}$ shows the rates of glial oxidative ATP production; the rates of neuronal ATP production, $30v_{LA,n}$ and $30v_{\text{Mito,n}}$, are the same as the results shown in (d), but multiplied by a factor of 15. The black dotted lines denote $A_x = \bar{A}_x$.

The above results suggest that it is possible to reverse engineer parameter values such that the results of the two submodels closely match quantitatively. Therefore, to test these conclusions, we perform simulations using these tuned parameter values. We note that making such changes means that the parameter values n_{OP}, $K_{\text{HK-PFK},A,x}$ and $K_{\text{Mito},A,x}$ no longer match the original values used in [1], so our objective here is to reveal the causes of the quantitative differences in the results of the submodels, not to use a fully realistic set of parameters. We make the following alterations to parameter values:

- The oxidative reaction denoted by rate $v_{LW,g}$ in the IR submodel produces ATP at a rate of 30 ATP molecules, rather than 9, for each pair of lactate molecules consumed;
- $K_{\text{HK-PFK},A,x}$ is changed such that $v_{\text{HK-PFK},x}$ has an approximately linear ADP dependence when $A = \bar{A}$, and the equivalent value $K_{GL,x}$, in the IR submodel is altered accordingly;
- $K_{\text{Mito},A,x}$ in the AC submodel is altered such that it fulfils the condition $K_{\text{Mito},A,x} \gg B_r$ (such that $v_{\text{Mito},x}$ is approximately linear), and the equivalent value, $K_{LW,g}$, in the IR submodel is altered accordingly;
- The values of $\bar{A}_x$ are altered such that the steady state lactate and ATP concentrations in the two submodels match as closely as possible for a given glucose input G^* (we choose $G^* = 3\,\text{mM}$). A close match can be obtained under either resting conditions or neuronal stimulation, but we choose an optimal match under both conditions.

The first of these changes matches the stoichiometries of the two submodels, while the second and third ensure both submodels have approximately the same (linear) ATP dependence around the ATP concentrations where they match closely, $\bar{A}_x$. If the values of $K_{\text{Mito},A,x}$ and $K_{\text{HK-PFK},A,x}$ are chosen to fulfil the above criteria, the overall rates $v_{\text{HK-PFK},x}$ and $v_{\text{Mito},x}$ are altered, which means the lactate and ATP concentrations no longer reach the same steady states. We therefore alter the remaining parameters in these reaction rates, $v^{\max}_{\text{Mito},x}$ and $k_{\text{HK-PFK},x}$, so the steady state lactate and ATP concentrations maintain the same order of magnitude. We also alter the baseline ATP consumption rates such that the steady state attained by the ATP concentrations is close to $\bar{A}_x$. This ensures that our linear approximations are valid. Since the steady state ATP concentrations depend on the model parameters, the values of $\bar{A}_x$ are then

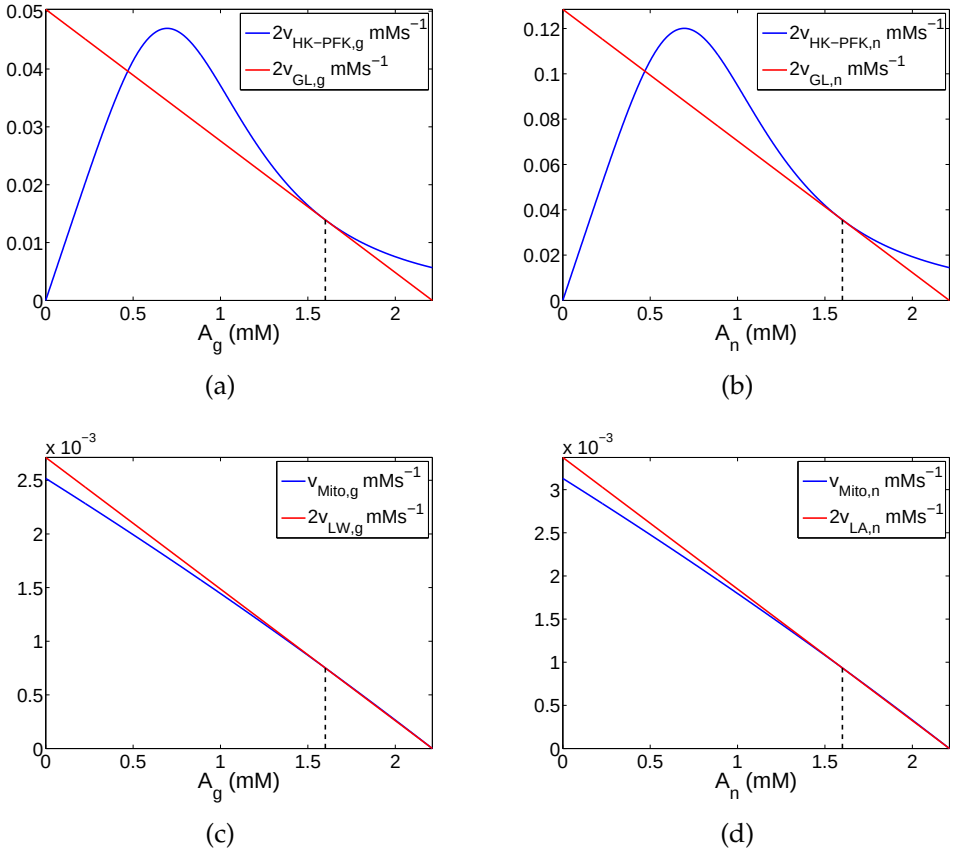


Figure 5.10.: Plots showing ATP dose response of the rates of glycolysis and oxidative metabolism in (—) the IR submodel (see (5.12) with $(YZ, m) \in \{(GL, x), (LW, g), (LA, n)\}$) and (—) the Simplified AC submodel (see (5.37b) and (5.40)). The parameter values used are given in Table 5.4. (a) $2v_{GL,g}$ and $2v_{\text{HK-PFK,g}}$, and (b) $2v_{GL,n}$ and $2v_{\text{HK-PFK,n}}$ show the rates of glycolytic lactate production; (c) $2v_{LW,g}$ and $v_{\text{Mito,g}}$, and (d) $2v_{LA,n}$ and $v_{\text{Mito,n}}$ show the rates of oxidative lactate consumption. The black dotted lines denote $A_x = \bar{A}_x$.

re-evaluated such that they match as closely as possible with the steady state ATP concentrations. The second, third and fourth steps are iterated until an optimum match is reached between the results of the two submodels. More details on the techniques used are given in Appendix C. The adapted parameter values are given in Table 5.4. Figure 5.10 shows the ATP dose responses of the glycolytic and oxidative rates using the adapted parameter values. The rates in the two submodels match where $A_x = \bar{A}_x$, and remain close together for ATP concentrations close to $\bar{A}_x$.

Figure 5.11 shows the glucose dose response of the steady state lactate and ATP concentrations in the IR and Simplified AC submodels using the adapted

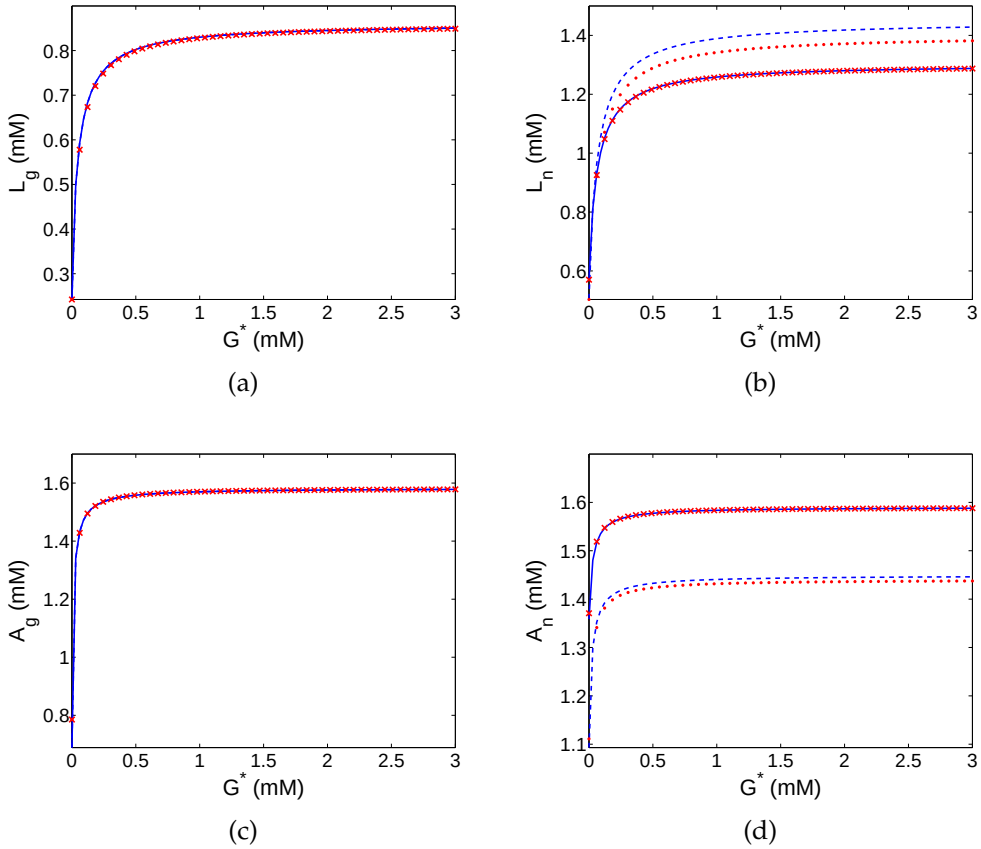


Figure 5.11.: Plots showing how steady state levels of lactate and ATP vary with glucose levels in the IR submodel ((xxx): rest; (· · ·): neuronal stimulation), and the Simplified AC submodel ((—): rest, (- - -): neuronal stimulation). For details of the submodels and associated parameter values see Tables 5.2 and Appendix C. We note that, in the glial cells, the glucose dose response curves are coincident during resting conditions and neuronal stimulation, since, in both submodels, the equations in the glial cells are unchanged by neuronal stimulation (as the glial uptake of glutamate and Na^+ are not included).

parameter values. We note that the reason for investigating whether a good quantitative match between the submodels can be achieved is not to justify our choice of expressions for the glycolytic and oxidative rates, but rather to check how quantitative differences arise. The good match between the steady states in Figure 5.11 suggests that the quantitative differences between the results of the submodels are due to the choices of reaction rate expressions for the glycolytic and oxidative rates, and also the different stoichiometries used for glial oxidative metabolism. Although the original dose response curves in Figure 5.8 for the two submodels do not quantitatively match, the results are within the same order of magnitude, and the qualitative behaviour is the same. The quantitative differences between the results are not large compared to the range of measurements for these reaction rates found in current literature. The large range of possible values is due to the lack of availability of empirical evidence in human cells and *in vivo*.

In conclusion, our phenomenological approach to representing the glycolytic and oxidative rates in §5.1 can produce qualitatively the same model outputs as Aubert and Costalat's more detailed multi-step approach [1] and the outputs are quantitatively similar. Since the reaction rate expressions in both models are equally justified based on the current available information, this indicates that our model includes sufficient detail to make reasonable predictions, as it exhibits the relevant behaviour. Furthermore, the fact that the asymptotic approximation to the AC submodel and the original AC submodel very closely match on long timescales provides greater justification for our decision to neglect the intermediate reaction rates in glycolysis.

5.4 DISCUSSION

We have developed a compartmental ODE model that describes the time-evolution of key metabolites in the inner retina, which can be used to investigate how the mechanisms regulating metabolite levels may break down in pathological conditions. Our model monitors the levels of glucose, lactate, glutamate, glutamine, ATP and ADP, and accounts for glycolysis, oxidative metabolism, intercellular transport and the glutamate-glutamine cycle.

Since many key processes in inner retinal metabolism are similar to those in cerebral metabolism, our model has aspects in common with existing models,

e.g. [1, 238–240], in terms of the compartments included and of the expressions used to model the rates of intracellular reactions and intercellular transport.

However, to our knowledge, our model is the first compartmental ODE model to explore inner retinal metabolic regulation, and that links energy metabolism, intercellular nutrient transport and the glutamate-glutamine cycle. Many distinguishing features of our model mean that it can be used to investigate how fluctuating blood glucose levels affect metabolite levels in the inner retinal tissue, and whether such fluctuations may trigger glutamate accumulation in the ECS, leading to excitotoxic damage to the neurons.

We use combined reaction rates to model the glycolytic pathway and the processes involved in oxidative metabolism. To investigate whether these reaction rates can capture the key aspects of the more detailed rates in Aubert and Costalat's model [1], we compared the outputs of reactions in both models. Two submodels were defined, the AC and IR submodel, each incorporating glycolysis and oxidative metabolism, with additional terms included to ensure steady states are reached. We used multiple timescale analysis to show that, on a typical timescale in Aubert and Costalat's simulations in [1], the metabolic intermediates GAP, PEP and pyruvate in [1] can be eliminated, yielding a system that represents glycolysis, oxidative metabolism and pyruvate-lactate conversion via three metabolites and two reaction rates in each cell type, analogous to ours.

The AC and IR submodels exhibit qualitatively similar behaviour. The simplicity of our model renders it more amenable to analysis (see Chapter 6), ultimately making it easier to understand the behaviour of the system under normal and pathological conditions.

6

MODEL PREDICTIONS ON DIABETIC RETINOPATHY

Questions relating to the causes of and treatments for diabetic retinopathy are addressed in this chapter, using the mathematical model developed in Chapter 5. We perform numerical simulations of the model to determine how glial cells regulate inner retinal metabolite levels, and to investigate the impact of large fluctuations in blood glucose levels in diabetic patients. We also consider how the malfunction of other regulatory mechanisms such as glutamate uptake from the ECS by the glia may affect the metabolite levels in the inner retinal tissue. In particular, we test for the accumulation of glucose, lactate and extracellular glutamate, since abnormally high concentrations may be harmful to the cells, via osmotic effects, alterations in the pH and excitotoxicity respectively.

To facilitate parameter estimation and analysis, the model is decomposed, in §6.1, into two submodels: one incorporating energy metabolism and the other involving the glutamate-glutamine cycle. Each submodel can be analysed separately, and the glutamate-glutamine submodel is found to have at most one unique steady state. In §6.2, we describe how we estimate parameter values from existing data. Numerical results for our model are presented in §6.3. These results provide a possible explanation of how inner retinal metabolite concentrations in healthy individuals vary in time according to the energy demand of the neurons. We then use the experimentally measured diurnally varying blood glucose levels in [125], in groups of healthy and diabetic individuals, as the input to our model. The results suggest that fluctuations in the blood glucose concentrations of diabetes sufferers may lead to glucose accumulation in the inner retina, which may be damaging, e.g. via osmotic swelling. However, in our model, hyperglycaemia alone did not lead to elevated glutamate concentrations. We investigate possible disruptions to inner retinal metabolism that may cause pathology in §6.4, by varying specific

parameters that may be linked to retinal diseases. The sensitivity of our model to perturbations in the rate of glial glutamate uptake from the ECS suggests that a reduction in this parameter may lead to excitotoxic concentrations of glutamate in the ECS. Furthermore, alterations in this parameter have been detected experimentally following the onset of diabetes [220, 222]. These findings, and the results of our model, suggest that reduced glutamate uptake by the glial cells (possibly due to glial cell damage by abnormally high glucose concentrations) is a plausible cause of excitotoxic damage to neurons, a characteristic feature of diabetic retinopathy. The chapter ends in §6.5 where we discuss our findings and give ideas for future work.

6.1 Decomposition of our model into glucose-lactate and glutamate-glutamine submodels

We proceed by examining two simplified versions of our model (see equations (5.23)–(5.26) and Figure 5.1): the *glucose-lactate* and *glutamate-glutamine* submodels. These submodels are more analytically tractable than the full model; in particular we find that the glutamate-glutamine submodel has at most one unique steady state.

Inspection of equations (5.23)–(5.25) reveals that the glutamate-glutamine cycle affects the glucose and lactate concentrations via ATP levels, this coupling being effected via reaction rates $\hat{v}_{GL,g}$, $\hat{v}_{GL,n}$, $\hat{v}_{LW,g}$ and $\hat{v}_{LA,n}$. Further, the impact of the glucose and lactate concentrations on the glutamate-glutamine cycle is via the production of glutamate from lactate in the glial cells (at rate $\hat{v}_{LW,g}$) and the dependence of reaction rates $\hat{v}_{WN,g}$, $\hat{v}_{W,ns}$, $\hat{v}_{W,sg}$ and $\hat{v}_{WA,n}$ on ATP.

6.1.1 *Glucose-Lactate Submodel*

If we fix the dimensionless glial and neuronal ATP concentrations so that $a_g = \tilde{a}_g$ and $a_n = \tilde{a}_n$ respectively, then equations (5.23a), (5.23b), (5.24a), (5.24b), (5.25a) and (5.25b), and the relevant initial conditions in (5.26), decouple from the full model, forming the *glucose-lactate submodel*. The reactions rates are identical to those defined in Chapter 5, except that in equations (5.29a), $a_x = \tilde{a}_x$.

We note further that equations (5.23a), (5.24a) and (5.25a) are independent of the lactate concentrations. Therefore, the three ODEs for the glucose concentrations also decouple.

Although it is nontrivial to find analytical steady state solutions of the glucose-lactate submodel, extensive simulations in many parameter regimes indicate that there is at most one physically realistic steady state (i.e. one for which the glucose and lactate concentrations are real and non-negative).

6.1.2 *Glutamate-Glutamine Submodel*

Holding the concentrations of lactate in the glial cells and ATP in the glial and neuronal cells fixed so that $l_g = \tilde{l}_g$, $a_g = \tilde{a}_g$ and $a_n = \tilde{a}_n$ equations (5.23c), (5.23d), (5.24c), (5.24d), (5.25c) and (5.25d), and the appropriate initial conditions from (5.26), decouple from the full model, defining the *glutamate-glutamine submodel*. The reaction rates are identical to those defined in Chapter 5, except that in equation (5.29a), $l_g = \tilde{l}_g$, and in equations (5.29), $a_x = \tilde{a}_x$.

The glutamate-glutamine submodel has at most one steady state which can be determined analytically. Setting the rates of change in equations (5.23c), (5.23d), (5.24c), (5.24d), (5.25c) and (5.25d) to zero, we find that, at the steady state, the rates of the reactions in the glutamate-glutamine cycle balance in the following way,

$$\hat{v}_{LW,g} = \hat{v}_{WN,g} - \hat{v}_{W,sg}, \tag{6.1a}$$

$$\hat{v}_{N,gs} = \hat{v}_{WN,g}, \tag{6.1b}$$

$$\hat{v}_{W,sg} = \frac{V_n}{V_g}\hat{v}_{W,ns}, \tag{6.1c}$$

$$\hat{v}_{N,gs} = \frac{V_n}{V_g}\hat{v}_{N,sn}, \tag{6.1d}$$

$$\hat{v}_{W,ns} = \hat{v}_{WN,n} - \hat{v}_{WA,n}, \tag{6.1e}$$

$$\hat{v}_{N,ns} = \hat{v}_{WN,n}. \tag{6.1f}$$

In particular, during dark conditions, $\hat{v}_{W,ns}^{\max} = 0 = \hat{v}_{W,gs}$ (see §5.1), and equations (6.1) supply,

$$\hat{v}_{LW,g} = \hat{v}_{WN,g} = \hat{v}_{N,gs} = \frac{V_n}{V_g}\hat{v}_{N,sn} = \frac{V_n}{V_g}\hat{v}_{WN,n} = \frac{V_n}{V_g}\hat{v}_{WA,n}. \tag{6.2}$$

Equations (5.28), (5.29) and (6.1) can be used to determine the following analytical expressions for the steady state glutamate and glutamine concentrations in terms of $\tilde{l}_g$, $\tilde{a}_g$, $\tilde{a}_n$ and parameter values,

$$\text{Glutamate:} \begin{cases} w_{n,\text{SS}} = \hat{K}_{WA,n} \dfrac{\alpha}{1-\alpha}, & \text{(6.3a)} \\ w_{s,\text{SS}} = \hat{K}_{W,gs,W} \dfrac{\beta}{1-\beta}, & \text{(6.3b)} \\ w_{g,\text{SS}} = \hat{K}_{WN,g,W} \dfrac{\gamma}{1-\gamma}, & \text{(6.3c)} \end{cases}$$

$$\text{Glutamine:} \begin{cases} n_{n,\text{SS}} = \left(4w_{n,\text{SS}} + \hat{K}_{WN,n}\right) \dfrac{\lambda}{1-\lambda}, & \text{(6.4a)} \\ n_{s,\text{SS}} = \hat{K}_{N,sn} \dfrac{\kappa}{1-\kappa}, & \text{(6.4b)} \\ n_{g,\text{SS}} = \hat{K}_{N,gs} \dfrac{\mu}{1-\mu}, & \text{(6.4c)} \end{cases}$$

where,

$$\alpha = \frac{V_g}{V_n} \frac{\text{M}\left(l_g; \hat{v}^{\max}_{LW,g}, \hat{K}_{LW,g}\right)}{\hat{v}^{\max}_{WA,n}} \frac{\left(a_{\text{Tot}} - \tilde{a}_g\right)}{\left(a_{\text{Tot}} - \tilde{a}_n\right)}, \tag{6.5a}$$

$$\beta = \frac{\dfrac{V_n}{V_g} \dfrac{\text{M}\left(\tilde{a}_n; \hat{v}^{\max}_{W,ns}, \hat{K}_{W,ns,A}\right)}{\text{M}\left(\tilde{a}_g; \hat{v}^{\max}_{W,sg}, \hat{K}_{W,sg,A}\right)} \dfrac{\hat{K}_{WA,n}}{\hat{K}_{W,ns,W}} \alpha}{1 - \left[\left(\dfrac{V_n}{V_g} \dfrac{\text{M}\left(\tilde{a}_n; \hat{v}^{\max}_{W,ns}, \hat{K}_{W,ns,A}\right)}{\text{M}\left(\tilde{a}_g; \hat{v}^{\max}_{W,sg}, \hat{K}_{W,sg,A}\right)} - 1\right) \dfrac{\hat{K}_{WA,n}}{\hat{K}_{W,ns,W}} + 1\right] \alpha}, \tag{6.5b}$$

$$\gamma = \frac{\text{M}\left(l_g; \hat{v}^{\max}_{LW,g}, \hat{K}_{LW,g}\right)\left(a_{\text{Tot}} - \tilde{a}_g\right)}{\text{M}\left(\tilde{a}_g; \hat{v}^{\max}_{WN,g}, \hat{K}_{WN,g,A}\right)} + \frac{\text{M}\left(\tilde{a}_g; \hat{v}^{\max}_{W,sg}, \hat{K}_{W,sg,A}\right)}{\text{M}\left(\tilde{a}_g; \hat{v}^{\max}_{WN,g}, \hat{K}_{WN,g,A}\right)} \beta, \tag{6.5c}$$

$$\lambda = \frac{V_g}{V_n} \frac{\text{M}\left(\tilde{a}_g; \hat{v}^{\max}_{WN,g}, \hat{K}_{WN,g,A}\right)}{\hat{v}^{\max}_{WN,n}} \gamma, \tag{6.5d}$$

$$\kappa = \frac{\hat{v}^{\max}_{WN,n}}{\hat{v}^{\max}_{N,sn}} \lambda, \tag{6.5e}$$

$$\mu = \frac{V_n}{V_g} \frac{\hat{v}^{\max}_{N,sn}}{\hat{v}^{\max}_{N,gs}} \kappa + \frac{\dfrac{\hat{K}_{N,sn}}{\hat{K}_{N,gs}} \kappa}{\left(\dfrac{\hat{K}_{N,sn}}{\hat{K}_{N,gs}} - 1\right) \kappa + 1}. \tag{6.5f}$$

Before continuing, we note that, for the steady state glutamate and glutamine concentrations to be physically realistic (real, finite and non-negative), the values of α, β, γ, λ, κ and μ are subject to the constraints described below. Further, we note that equations (6.5) are hierarchical in that β is given in terms of α, γ is written in terms of β, and so on. Referring to equation (6.3a) and noting that $\hat{K}_{WA,n} > 0$ by definition, we have that $0 \leq w_{n,\mathrm{SS}} < \infty$ if,

$$0 \leq \alpha < 1. \tag{6.6a}$$

Likewise, given that $\hat{K}_{W,gs,W}$, $\hat{K}_{WN,g,W}$, $\hat{K}_{WN,n}$, $\hat{K}_{N,sn}$ and $\hat{K}_{N,gs}$ are positive by definition, the following constraints also apply,

$$0 \leq \beta < 1, \tag{6.6b}$$
$$0 \leq \gamma < 1, \tag{6.6c}$$
$$0 \leq \lambda < 1, \tag{6.6d}$$
$$0 \leq \kappa < 1, \tag{6.6e}$$
$$0 \leq \mu < 1. \tag{6.6f}$$

Due to the hierarchical nature of equations (6.5), the parameter groupings β, γ, λ, κ and μ depend on the parameter grouping α. Therefore, each of the above constraints can be written in terms of α (as described in Appendix D), giving the following stricter bounds on α,

$$0 < \alpha < \alpha^*, \tag{6.7}$$

where,

$$\alpha^* = \min\left(1\,,\, F_\alpha(1)\,,\, F_\alpha\left(\hat{v}^{\max}_{WN,n}\right)\,,\, F_\alpha\left(\frac{\hat{v}^{\max}_{N,sn}\mathrm{M}\left(\tilde{a}_g;\hat{v}^{\max}_{WN,g},\hat{K}_{WN,g,A}\right)}{\mathrm{M}\left(\tilde{a}_g;\hat{v}^{\max}_{W,sg},\hat{K}_{W,sg,A}\right)}\kappa^*\right)\right), \tag{6.8}$$

where F_α and κ^* are defined as follows,

$$F_\alpha(\hat{v}) = \frac{\hat{v}-\omega}{\chi\left(\hat{v}-\omega\right) + \dfrac{V_g}{V_n}\dfrac{\hat{K}_{WA,n}}{\hat{K}_{W,ns,W}}\mathrm{M}\left(\tilde{a}_n;\hat{v}^{\max}_{W,ns},\hat{K}_{W,ns,A}\right)}, \tag{6.9a}$$

$$\omega = \frac{V_g}{V_n} \mathrm{M}\left(\tilde{l}_g; \hat{v}^{\max}_{LW,g}, \hat{K}_{LW,g}\right)\left(a_{\mathrm{Tot}} - \tilde{a}_g\right), \tag{6.9b}$$

$$\chi = \left(\frac{V_n}{V_g}\frac{\mathrm{M}\left(\tilde{a}_n; \hat{v}^{\max}_{W,ns}, \hat{K}_{W,ns,A}\right)}{\mathrm{M}\left(\tilde{a}_g; \hat{v}^{\max}_{W,sg}, \hat{K}_{W,sg,A}\right)} - 1\right)\frac{\hat{K}_{WA,n}}{\hat{K}_{W,ns,W}} + 1; \tag{6.9c}$$

$$\kappa^* = \begin{cases} \kappa_+ & \text{if } \dfrac{\hat{K}_{N,sn}}{\hat{K}_{N,gs}} > 1, \\ \left(\dfrac{V_n}{V_g}\dfrac{\hat{v}^{\max}_{N,sn}}{\hat{v}^{\max}_{N,gs}} + 1\right)^{-1} & \text{if } \dfrac{\hat{K}_{N,sn}}{\hat{K}_{N,gs}} = 1, \\ \kappa_- & \text{if } \dfrac{\hat{K}_{N,sn}}{\hat{K}_{N,gs}} < 1, \end{cases} \tag{6.9d}$$

$$\kappa_\pm = \frac{-\left(\dfrac{V_n}{V_g}\dfrac{\hat{v}^{\max}_{N,sn}}{\hat{v}^{\max}_{N,gs}} + 1\right) \pm \sqrt{\left(\dfrac{V_n}{V_g}\dfrac{\hat{v}^{\max}_{N,sn}}{\hat{v}^{\max}_{N,gs}} + 1\right)^2 + 4\dfrac{V_n}{V_g}\dfrac{\hat{v}^{\max}_{N,sn}}{\hat{v}^{\max}_{N,gs}}\left(\dfrac{\hat{K}_{N,sn}}{\hat{K}_{N,gs}} - 1\right)}}{2\dfrac{V_n}{V_g}\dfrac{\hat{v}^{\max}_{N,sn}}{\hat{v}^{\max}_{N,gs}}\left(\dfrac{\hat{K}_{N,sn}}{\hat{K}_{N,gs}} - 1\right)}. \tag{6.9e}$$

In particular, during dark conditions, when $\beta = 0$ and $\hat{v}_{W,ns} = 0$, the definitions of $F_\alpha(\hat{v})$ in (6.9) simplifies to,

$$F_\alpha(\hat{v}) = \chi^{-1}, \tag{6.10}$$

reducing the constraint on α in (6.7) to,

$$0 < \alpha < \min\left(1\,,\, \chi^{-1}\right). \tag{6.11}$$

Replacing $\tilde{l}_g$, $\tilde{a}_g$ and $\tilde{a}_n$ in equations (6.3)–(6.4) by the time-dependent variables l_g, a_g and a_n respectively, and comparing the resulting system with equations (6.3)–(6.4) reveals the impact of the ATP and lactate concentrations on the steady state glutamate and glutamine concentrations.

We note that, since the ATP concentrations are time-dependent, the dependence of the steady state glutamate and glutamine concentrations on ATP levels means an indirect dependence on the parameters that affect the ATP concentrations, i.e. $\hat{v}^{\max}_{W,sg}$, $\hat{K}_{W,sg,W}$, $\hat{K}_{W,sg,A}$, $\hat{v}^{\max}_{WN,g}$, $\hat{K}_{WN,g,W}$, $\hat{K}_{WN,g,A}$, $\hat{v}^{\max}_{A0,g}$ and $\hat{K}_{A0,g}$ in the glial cells, and $\hat{v}^{\max}_{W,ns}$, $\hat{K}_{W,ns,W}$, $\hat{K}_{W,ns,A}$, $\hat{v}^{\max}_{WA,n}$, $\hat{K}_{WA,n,W}$, $\hat{v}^{\max}_{A0,n}$ and $\hat{K}_{A0,n}$ in the neurons.

The constraints derived above also indicate which parameter values yield physically reasonable solutions (i.e. those for which the concentrations reach a steady state at long times), which limits the ranges for realistic model parameters in the following section.

6.2 PARAMETER ESTIMATION

The parameter values used to describe normal physiological behaviour in our model are summarised in Tables 6.1–6.3. These values are estimated from measurements of the associated parameters, metabolite concentrations and reaction rates, using the following procedure (described in more detail in Appendix E):

1. Find ranges of measurements of parameters (see Tables 6.1–6.3);
2. Determine parameter values (within the measured ranges if possible) for which steady state concentrations in the glucose-lactate and glutamate-glutamine submodels (see §6.1) match physiological values (given in Table 6.4) under dark conditions;
3. Adjust parameters such that the solutions to the glutamate-glutamine submodel approach realistic steady states under light conditions, using the constraints in (6.7);
4. Refine parameter estimates such that the steady state reaction rates $v_{W,ns}$, $v_{LW,g}$ and $v_{WN,g}$ in the glutamate-glutamine submodel match the rates in [233];
5. Repeat step 2–4 for numerical solutions to the full model.

We note that the $V_{\max}$ values for reaction rates $v_{W,ns}$ and $v_{A0,n}$ alter between light and dark conditions (see equations (5.8) and (5.9)), which correspond to neuronal stimulation and resting conditions respectively. Therefore we estimate different values for these parameters under light and dark conditions. The right hand columns of Tables 6.1–6.3 show the parameter values used in our model. These yield a good match with the typical measured concentrations (in Table 6.4), while keeping as many parameters as possible within the measured ranges (in the third columns of Tables 6.1–6.3).

The steady state concentrations predicted by our model using our final parameter estimates (see Tables 6.1–6.3), and the corresponding concentrations

Symbol	Parameter	Initial estimates	Refs	Final estimates
$v^{max}_{G,bg}$	$V_{\max}$ for blood-glial glucose transport	9–25 μM s^{-1}	[1, 269, 270]	20 μM s^{-1}
$K_{G,bg}$	K_m for blood-glial glucose transport	1–10 mM	[1, 269–271]	10 mM
$v^{max}_{G,sg}$	$V_{\max}$ for glia-ECS glucose transport	5–10^6 μM s^{-1}	[1, 239]	50 μM s^{-1}
$K_{G,sg}$	K_m for glia-ECS glucose transport	1–10 mM	[1, 269–271]	1.0 mM
$v^{max}_{G,sn}$	$V_{\max}$ for ECS-neuron glucose transport	5–35 μM s^{-1}	[197, 239, 272]	35 μM s^{-1}
$K_{G,sn}$	K_m for ECS-neuron glucose transport	2–10 mM	[1, 271]	2.0 mM
$v^{max}_{L,bg}$	$V_{\max}$ for blood-glial lactate transport	2–6 μM s^{-1}	[1, 269]	3.0 μM s^{-1}
$K_{L,bg}$	K_m for blood-glial lactate transport	0.5–5 mM	[1, 212, 269]	1.0 mM
$v^{max}_{L,sg}$	$V_{\max}$ for glia-ECS lactate transport	40–400 μM s^{-1}	[1, 199, 239]	100 μM s^{-1}
$K_{L,sg}$	K_m for glia-ECS lactate transport	0.4–8 mM	[1, 194, 198, 199]	4.0 mM
$v^{max}_{L,sn}$	$V_{\max}$ for ECS-neuron lactate transport	8–300 μM s^{-1}	[1, 239]	80 μM s^{-1}
$K_{L,sn}$	K_m for ECS-neuron lactate transport	0.5–0.7 mM	[1, 194, 198, 273]	600 μM
G_b	Blood glucose concentration	4–6 mM	[274, 275]	5.0 mM
L_b	Blood lactate concentration	0.4–1 mM	[1, 276]	0.70 mM
$v^{max}_{N,gs}$	$V_{\max}$ for glia-ECS glutamine transport	3–80 μM s^{-1}	[177, 215]	80 μM s^{-1}
$K_{N,gs}$	K_m for glia-ECS glutamine transport	0.2–3 mM	[177, 213–215]	0.2 mM
$v^{max}_{N,sn}$	$V_{\max}$ for ECS-neuron glutamine transport	2–50 μM s^{-1}	[177, 215]	6.2 μM s^{-1}
$K_{N,sn}$	K_m for ECS-neuron glutamine transport	0.1–2 mM	[177, 185, 214, 215]	1.0 mM

Table 6.1.: Estimated parameter values associated with intercellular transport rates in our model.

Symbol	Parameter	Initial estimates	Refs	Final estimates
$v^{max}_{W,sn,\text{Light}}$	$V_{\max}$ for neuronal glutamate release during neuronal activity	40 μM s^{-1} *	[215]	2.2 μM s^{-1}
$K_{W,sn,W}$	K_m for neuronal glutamate release with respect to glutamate	0.3–2 mM	[179, 203, 205, 215, 277]	1.0 mM
$K_{W,sn,A}$	K_m for neuronal glutamate release with respect to ATP	0.2 mM *	[215]	0.2 mM
$v^{max}_{W,sg}$	$V_{\max}$ for glial glutamate uptake	1–100 μM s^{-1}	[215, 278]	30 μM s^{-1}
$K_{W,sg,W}$	K_m for glial glutamate uptake with respect to glutamate	2–220 μM	[175–177, 186, 215, 278–281]	20 μM
$K_{W,sg,A}$	K_m for glial glutamate uptake with respect to ATP			0.2 mM
$v^{max}_{WN,g}$	$V_{\max}$ for glial glutamine production	1 μM s^{-1} *	[282]	60 μM s^{-1}
$K_{WN,g,W}$	K_m for glial glutamine production with respect to glutamate	2–15 mM	[215, 282, 283]	30 mM
$K_{WN,g,A}$	K_m for glial glutamine production with respect to ATP	2–3 mM	[175, 215, 280, 282]	10 mM
$v^{max}_{WN,n}$	$V_{\max}$ for neuronal glutamate production	0.2 mM s^{-1} *	[284]	6.0 μM s^{-1}
$K_{WN,n}$	K_m for neuronal glutamate production	0.6–10 mM	[280, 284]	3.0 mM
$v^{max}_{WA,n}$	$V_{\max}$ for neuronal glutamate oxidation via TCA cycle	5 mM s^{-1} *	[285, 286]	5.0 mM s^{-1}

Table 6.2.: Estimated parameter values associated with the glutamate-glutamine cycle in our model [* denotes the parameters for which only one measurement was found in the literature.]

Symbol	Parameter	Initial estimates	Refs	Final estimates
$v^{max}_{GL,g}$, $v^{max}_{GL,n}$	$V_{\max}$ for glycolytic lactate production (glial or neuronal)	$30\,\mathrm{mM\,s^{-1}}$ *	[286–288]	$30\,\mathrm{mM\,s^{-1}}$
$K_{GL,g}$, $K_{GL,n}$	K_m for glycolytic lactate production (glial or neuronal), with respect to glucose	20 mM	[286–288]	6.0 mM
$v^{max}_{LA,n}$	$V_{\max}$ for neuronal lactate oxidation via TCA cycle	$5\,\mathrm{mM\,s^{-1}}$ *	[285, 286]	$65\,\mathrm{mM\,s^{-1}}$
$K_{LA,n}$	K_m for neuronal lactate oxidation via TCA cycle, with respect to lactate	0.3–20 mM	[285, 286]	5.0 mM
$K_{WA,n}$	K_m for neuronal glutamate oxidation via TCA cycle, with respect to lactate	0.2 M *	[285, 286]	44 mM
$v^{max}_{A0,g}$	$V_{\max}$ for background glial ATP consumption	$30\,\mu\mathrm{M\,s^{-1}}$ *	[209]	$8.3\,\mu\mathrm{M\,s^{-1}}$
$K_{A0,g}$	K_m for background glial ATP consumption			$0.2\,\mu$M
$v^{max}_{A0,n,\mathrm{Light}}$	$V_{\max}$ for background neuronal ATP consumption when neurons are active	$70\,\mu\mathrm{M\,s^{-1}}$ *	[209]	$180\,\mu\mathrm{M\,s^{-1}}$
$v^{max}_{A0,n,\mathrm{Dark}}$	$V_{\max}$ for background neuronal ATP consumption when neurons are inactive	$70\,\mu\mathrm{M\,s^{-1}}$ *	[209]	$90\,\mu\mathrm{M\,s^{-1}}$
$K_{A0,n}$	K_m for background neuronal ATP consumption			$2.0\,\mu$M
$v^{max}_{LW,g}$	$V_{\max}$ for glial glutamate production via TCA cycle	$30\,\mathrm{mM\,s^{-1}}$ *	[286, 289–291]	$30\,\mathrm{mM\,s^{-1}}$
$K_{LW,g}$	K_m for glial glutamate production via TCA cycle, with respect to lactate	20 mM *	[286, 289–291]	3.0 mM
V_b	Fractional volume of vasculature	0.05	[216, 292–297]	0.05
V_g	Fractional volume of glia	0.25	[216, 292–297]	0.25
V_s	Fractional volume of ECS	0.2	[216, 292–297]	0.2
V_n	Fractional volume of neurons	0.5	[216, 292–297]	0.5

Table 6.3.: Estimated parameter values associated with other aspects of our model [* denotes the parameters for which only one measurement was found in the literature.]

Metabolite	**Species**	**Region**	**Rest / activity**	**Typical value**	**Refs**
Glucose	Human	Whole tissue	Rest	0.5–2 mM	[298]
Lactate	Human	Whole tissue	Rest	0.5–2.1 mM	[1, 273, 275, 286, 298]
Glutamate	Human	Whole tissue	Rest	7–11 mM	[215]
Glutamate	Human	ECS	Activity	2 μM	[158, 215, 286]
Glutamate	Human	Blood plasma	N/A	30–50 μM	[299]
Glutamine	Human	Whole tissue	Rest	3–5 mM	[215]
Glutamine	Human	ECS	Rest	0.1–0.3 mM	[215]
Glutamine	Human	Blood plasma	N/A	490 μM	[299]
ATP	Human	Whole tissue	Rest	2.1–3.0 mM	[300–302]
ATP	Human	ECS	Rest	3.0 nM	[302]
ATP+ADP	Rat	Whole tissue	Rest	3.1 mM	[286]

Table 6.4.: Estimates of realistic concentrations compared with the corresponding steady state values from simulations of our model.

Variable	Metabolite	Compartment	Steady state value	
			Dark	**Light**
G_g	Glucose	Glia	1.6 mM	0.5 mM
G_s	Glucose	ECS	1.3 mM	0.4 mM
G_n	Glucose	Neurons	1.1 mM	0.2 mM
G_T	Glucose	Whole tissue	1.5 mM	0.6 mM
L_g	Lactate	Glia	0.5 mM	0.2 mM
L_s	Lactate	ECS	0.5 mM	0.1 mM
L_n	Lactate	Neurons	0.5 mM	0.1 mM
L_T	Lactate	Whole tissue	0.5 mM	0.2 mM
W_g	Glutamate	Glia	2.3 mM	26.7 mM
W_s	Glutamate	ECS	0	2.7 μM
W_n	Glutamate	Neurons	21.3 mM	5.3 mM
W_T	Glutamate	Whole tissue	11.0 mM	9.3 mM
N_g	Glutamine	Glia	0.09 mM	1.0 mM
N_s	Glutamine	ECS	0.08 mM	0.7 mM
N_n	Glutamine	Neurons	7.7 mM	17.4 mM
N_T	Glutamine	Whole tissue	3.8 mM	8.9 mM
A_g	ATP	Glia	2.9 mM	2.1 mM
A_n	ATP	Neurons	2.8 mM	1.5 mM
A_T	ATP	Whole tissue	2.1 mM	1.3 mM

Table 6.5.: Steady state concentrations predicted by our model.

in the whole tissue, are shown in Table 6.5. The concentrations in the whole tissue are derived from equation (E.1), the fractional volumes $V_b = 0.05$, $V_g = 0.25$, $V_s = 0.2$ and $V_n = 0.5$ and the concentrations of glutamate and glutamine in the capillaries and the extracellular ATP concentration as given in Table 6.4. According to Hargreaves and Pardridge [303], the capillary ATP concentration in the brain is approximately 5–10% of the intracellular ATP content. Since the fractional volume of the capillaries is 0.05, the contribution of the capillary ATP concentration to the total ATP levels in brain tissue are very small. We therefore neglect this. We note that, for each metabolite, the predicted steady state concentration in the whole tissue under dark conditions in our model is within the range of values measured under resting conditions.

6.3 RESULTS

In this section we use numerical results of our model to explore the changes in inner retinal metabolism between light and dark conditions, and with varying blood glucose levels.

6.3.1 *Simulated Dark-Light Cycle with Constant Blood Glucose*

We consider diurnal changes in energy metabolism and the glutamate-glutamine cycle in the inner retina to investigate which aspects of metabolic regulation become most important under dark conditions, in which neuronal activity and energy demand are low, and light conditions when they are high. This gives us information on the time at which pathological accumulations of metabolites are most likely to occur if regulatory mechanisms are disrupted. Simulation results showing the time evolution of concentrations in healthy inner retinal tissue during 12 hours of dark conditions followed by 12 hours of light are presented in Figure 6.2, using the parameter values stated in Tables 6.1–6.3. We explain these variations using the schematic diagram of our model in Figure 6.1.

During dark conditions, the neurons do not release glutamate into the ECS (shown at point 1 in Figure 6.1), so $v_{W,ns} = 0$, and $v_{A0,n}$, which incorporates the energy demand by the neuronal Na^+/K^+ pumps during stimulation, decreases (see Figure 6.4(e) and point 2 in Figure 6.1). The neuronal ATP concentration (see Figure 6.2(e)), increases as a result of the decreased energy consumption. This, in turn, causes a reduction in the glycolytic (point 3) and lactate oxidation (4) rates (see Figures 6.4(a), (b)), and a concomitant rise in the neuronal glucose and lactate concentrations (see Figures 6.2(a), (b)). The rate of oxidative glutamate metabolism in the neurons also decreases (5) due to the decline in energy demand (see Figure 6.4(c)).

Since neuronal glutamate release ceases at the onset of dark conditions (6), W_s falls to zero (Figure 6.2(c)) as does the rate of glial glutamate uptake (point 7, see Figure 6.3(c)), and thus the glial glutamate concentration decreases (Figure 6.2(c)), slowing the rate of glial glutamine production (8) at reaction rate $v_{WN,g}$ (Figure 6.3(d)). Thus the glutamine concentration in the glial cells is lowered (see Figure 6.2(d)). As a result, less glutamine is transported into the ECS (9) and neurons (point 10, see Figure 6.4(d)), and the rate of neuronal glutamate production from glutamine (11) is reduced (Figure 6.4(c)). Despite the reduced

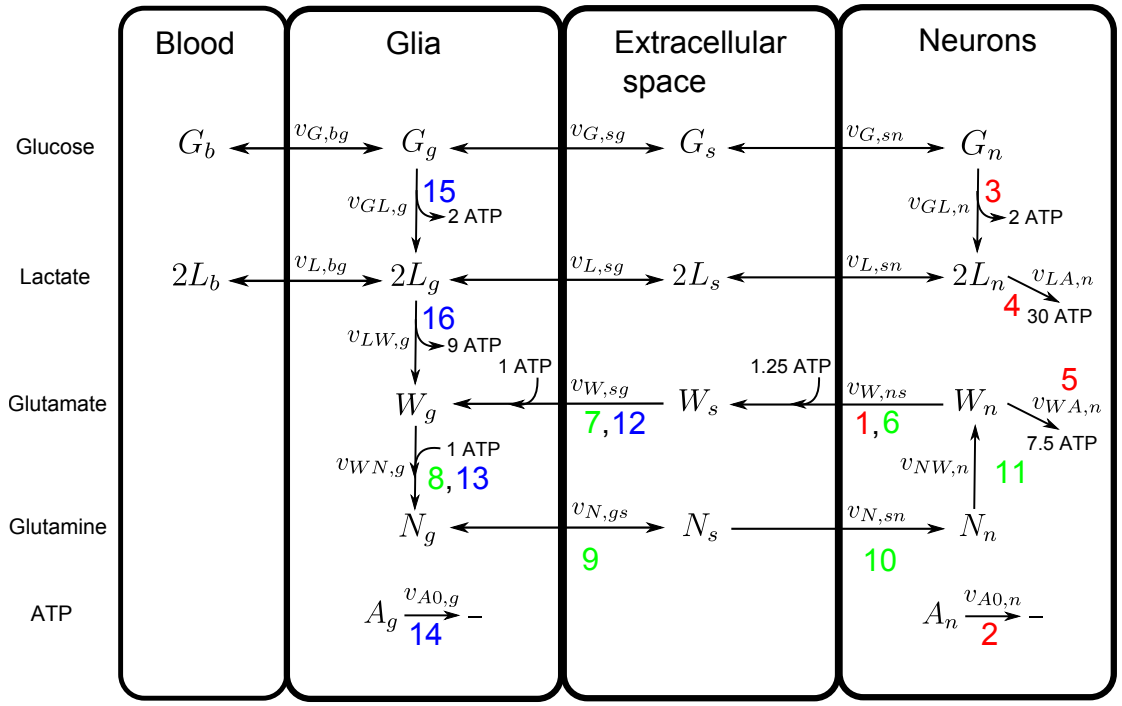


Figure 6.1.: Schematic diagram of our model of inner retinal metabolic regulation, showing how energy metabolism and the glutamate-glutamine cycle are linked (see text for more details).

production rate, there is still an overall increase in the neuronal glutamate concentration, since the effects of the decreased rate of oxidative metabolism, $v_{WA,n}$ and lack of glutamate release, $v_{W,ns}$, dominate (Figure 6.4(c)).

The reduced rates of glial glutamate uptake (12), $v_{W,sg}$, and glutamine production (13), $v_{WN,g}$ (see above) mean that these reactions consume ATP less rapidly. Since the baseline energy consumption rate (14), $v_{A0,g}$, is unchanged between light and dark conditions, this lowers the overall ATP demand in the glial cells (see Figure 6.3(e)). Thus, in the glial cells, the ATP concentration increases (Figure 6.2(e)). The concomitant reduction in the glial glycolytic (15) and lactate oxidation (16) rates (see Figures 6.3(a), (b)) leads to a rise in the glial glucose and lactate concentrations (see Figures 6.2(a), (b)). Under light conditions, the inner retinal neurons are activated and the effects described above are reversed.

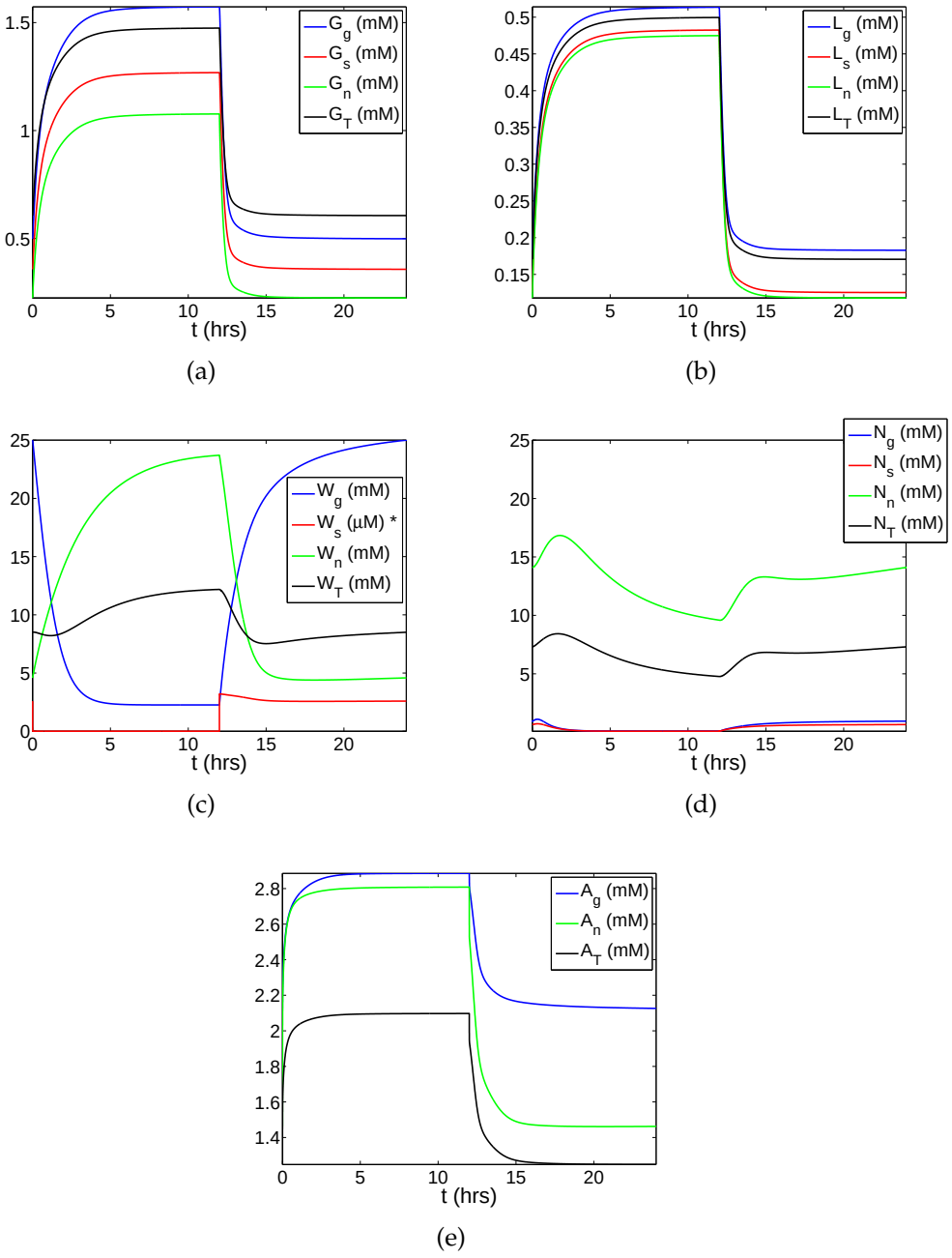


Figure 6.2.: Time evolution of the (a) glucose, (b) lactate, (c) glutamate, (d) glutamine and (e) ATP concentrations in the (—) glial cells, (—) ECS and (—) neuronal cells, and (—) averaged over the inner retinal tissue in a healthy individual, assuming a constant blood glucose concentration of 5 mM, according to our model of inner retinal metabolism given by equations (5.2)–(5.6), using the parameter values in Tables 6.1–6.3. *We note that W_s is plotted in units of μM rather than mM.

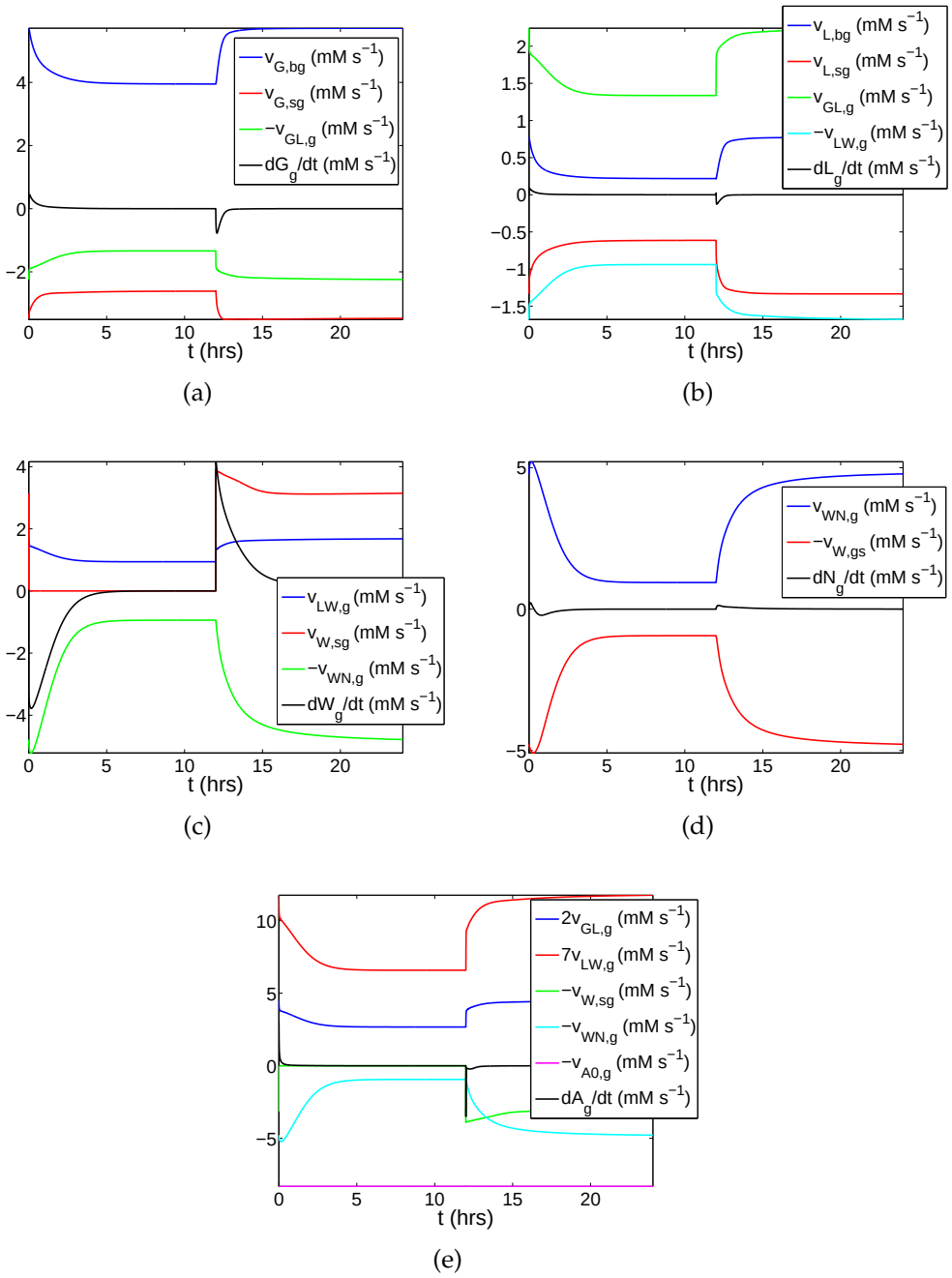


Figure 6.3.: Time evolution of the rates of change of the glial (a) glucose, (b) lactate, (c) glutamate, (d) glutamine and (e) ATP concentrations, and the contributions from each reaction rate in a healthy individual, assuming a constant blood glucose concentration of 5 mM, according to our model of inner retinal metabolism given by equations (5.2)–(5.6), using the parameter values in Tables 6.1–6.3.

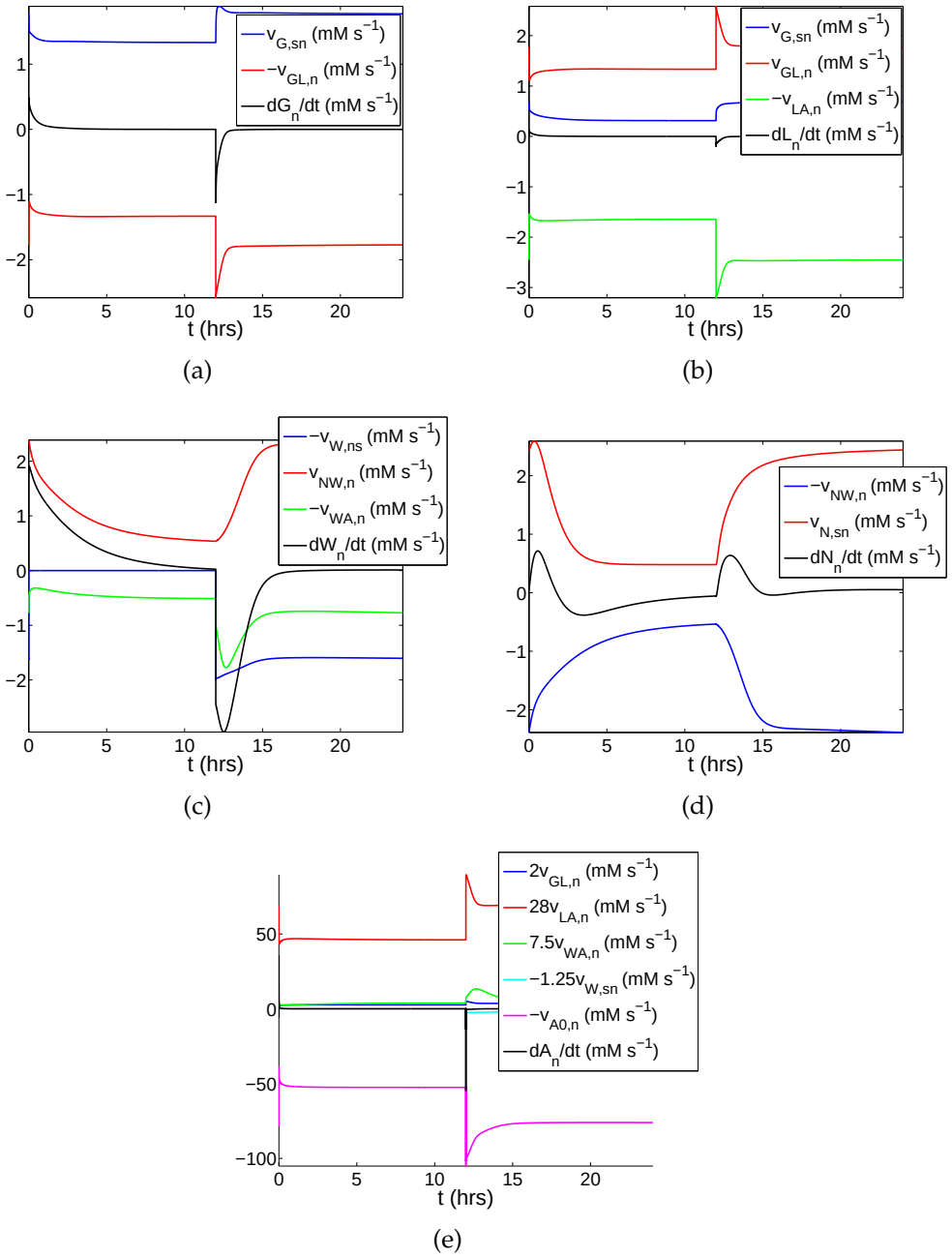


Figure 6.4.: Time evolution of the rates of change of the neuronal (a) glucose, (b) lactate, (c) glutamate, (d) glutamine and (e) ATP concentrations, and the contributions from each reaction rate in a healthy individual, assuming a constant blood glucose concentration of 5 mM, according to our model of inner retinal metabolism given by equations (5.2)–(5.6), using the parameter values in Tables 6.1–6.3.

As revealed by Figure 6.4(e), during both light and dark conditions, the time evolution of the neuronal ATP concentration is dominated by reaction rates $v_{LA,n}$ and $v_{A0,n}$. Thus, we have at leading order at the steady state,

$$\begin{aligned} & v_{LA,n}^{\max} \frac{L_n}{L_n + K_{LA,n}} \left(A_{\text{Tot}} - A_n\right) = v_{A0,n}^{\max} \frac{A_n}{A_n + K_{A0,n}}, \\ \implies & \frac{L_n}{L_n + K_{LA,n}} \left(A_{\text{Tot}} - A_n\right) \approx \frac{v_{A0,n}^{\max}}{v_{LA,n}^{\max}}, \end{aligned}$$

since $K_{A0,n} \ll A_n$. Thus, the dominating producer of neuronal ATP is lactate oxidation while the main consumer is the baseline ATP consumption rate (e.g. consumption by neuronal Na^+/K^+ pumps that are active during neuronal stimulation under light conditions, and other processes). Thus, our results suggest that, in a healthy retina, the ATP concentration in the neurons is most sensitive to changes in the neuronal lactate levels rather than the activity of the glutamate-glutamine cycle. This demonstrates the need for stringent control of neuronal lactate levels via the glia-neuron lactate shuttle (in which glial cells deliver lactate to the neurons in periods of high energy demand, described in §4.1), since it is the main energy substrate for the neurons.

From the above results we conclude that the increased energy demand under light conditions depletes the inner retinal glucose, lactate and ATP levels. Therefore, accumulations of glucose or lactate may be more likely to occur under dark conditions, even though the highest energy demand is during light. The glutamate-glutamine cycle is most active under light conditions, and leads to increased glial and extracellular glutamate concentrations and elevated glutamine levels in all compartments compared to dark conditions. In contrast, the neuronal glutamate levels are highest under dark conditions.

The results in Figures 6.2–6.4 correspond to the solutions of our model when the blood glucose concentration is held fixed at 5 mM. In practice blood glucose levels vary throughout the day. In the next section we perform simulations using time-varying blood glucose levels in healthy and diabetic individuals as model inputs, enabling us to compare inner retinal metabolic regulation in each case.

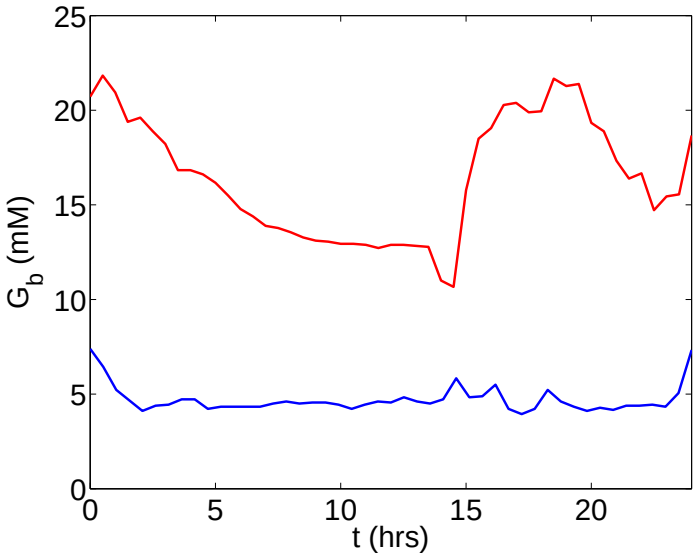


Figure 6.5.: Diurnal time evolution in the blood glucose concentrations over a 24-hour period starting and ending at 7:00 pm, taken from measurements by Hansen and Johansen [125] in (—) a group of healthy individuals and (—) a group of newly diagnosed, untreated diabetes sufferers (assuming that blood glucose levels at the same times on consecutive days are identical).

6.3.2 *Simulated Responses to Variation in Blood Glucose*

Hansen and Johansen [125] measured the blood glucose levels in a group of newly diagnosed, untreated diabetes sufferers, and a control group of non-diabetics. Figure 6.5 shows the data from their study, in which blood glucose levels were measured at regular intervals of a 24 hour period. To plot the data we assume that blood glucose levels at the same times on consecutive days are identical (since the data in [125] start and finish at 8:30 am whereas our simulations assume 12 hours of dark followed by 12 hours of light conditions). The average blood glucose levels in the healthy and diabetic groups ranged between 3.9 mM–7.4 mM and 10.7 mM–21.8 mM respectively, with time-averaged values of approximately 5 mM and 16 mM respectively. These results are consistent with the view that diabetes sufferers have higher average blood glucose concentrations, and that their blood glucose levels undergo significant fluctuations (see §4.1).

Using the time-varying blood glucose concentrations from [125] as model input, while all other conditions are kept the same as in Figures 6.2–6.4, we plot the time evolution of the inner retinal metabolite concentrations predicted

by our model for the healthy and diabetic groups in Figures 6.6–6.7. Increased blood glucose levels in the diabetic group increases the glucose, lactate and ATP levels in the inner retinal tissue.

During dark conditions, there is no neuronal glutamate release, and according to equations (6.3) and (6.4), the glial glutamate concentration at the steady state depends only on the reaction rates $v_{LW,g}$ and $v_{WN,g}$. The steady state glial glutamate concentration for which these reaction rates balance is approximately the same regardless of the blood glucose concentration (see Figures 6.6(e), (f)). Applying the same argument to balance $v_{WN,g}$ with $v_{N,gs}$, $V_g v_{N,gs}$ with $V_n v_{N,sn}$ and $v_{N,sn}$ with $v_{NW,n}$ means that the glial and extracellular glutamine concentrations are approximately unchanged between the control and diabetic groups (see Figures 6.7(a), (b)). In the neurons the steady state glutamate concentration is such that reaction rates $v_{NW,n}$ and $v_{WA,n}$ balance. Since $v_{NW,n}$ is approximately unchanged between the two groups, neither is $v_{WA,n}$, and in the neurons the glutamate concentration increases to compensate for the effect of the increased ATP levels on $v_{WA,n}$ (see Figures 6.6(e), (f)). Additionally, because $v_{NW,n}$ is approximately unchanged between groups, the neuronal glutamine concentration increases to balance the effects of the increased neuronal glutamate levels on $v_{N,sn}$ (see Figures 6.7(a), (b)).

Under light conditions, the neurons release glutamate, and glial glutamate uptake ensues. The rate of glutamate release in the neurons increases with the ATP concentration there, with a resultant increase in the extracellular glutamate levels and the rate of glial glutamate uptake. Since the neuronal ATP levels are highest in the diabetic group (this is more easily seen by comparing the ADP concentration, $B_x = A_{\text{Tot}} - A_x$, in Figures 6.7(e),(f)), the rate of glial glutamate uptake is elevated in this group. $v_{LW,g}$ is decreased in the diabetic group as before, and the overall effect of the decreased glial glutamate synthesis and increased uptake is a depletion in the glial glutamate levels. However, overall there is an increased rate of conversion of glutamate to glutamine in the glial cells in the diabetic group, which is brought about solely by the increased ATP concentration and leads to an increase in glutamine levels within the glia. Consequently, more glutamine is transported into the ECS and neurons, increasing the glutamine concentration there. The increased neuronal glutamine concentration induces more glutamate production, resulting in increased neuronal glutamate levels in the diabetic group (see Figures 6.6(e), (f)).

There is very little difference in the glutamate concentrations in all compartments between the control and diabetic groups. However, there is an accumulation of neuronal glutamine in the diabetic group under light conditions. Thus our results suggest that the glutamate-glutamine cycle is very resilient to fluctuating blood glucose concentrations, favouring the accumulation of glutamine rather than glutamate if the input to the glutamate-glutamine cycle (i.e. reaction rate $v_{LW,g}$) exceeds the output (reaction rate $v_{WA,n}$). This is a possible mechanism whereby the tissue may be protected from glutamate toxicity. According to these results, hyperglycaemia alone is insufficient to produce excitotoxic damage to neurons.

In both groups in [125], glucose concentrations are highest in the bloodstream, lower in the glial cells and in the ECS, and lowest in the neurons. This illustrates the regulated transport of glucose through the cell membranes, particularly in the glial cells since there is a large difference between the glucose levels in the blood and glial cells. Our model suggests that the glial cells enveloping the capillaries act as a barrier to prevent fluctuations in blood glucose levels from propagating to the neuronal cells.

The concentrations of glucose and lactate in all compartments are much higher in the diabetic group than in the control group (see Figures 6.6(a)–(d)). Although the glial cells continue to protect themselves and the neurons from large fluctuations in blood glucose levels, our results suggest that, when the blood glucose becomes very high, this protective mechanism is unable to prevent intracellular glucose and lactate levels from becoming abnormally high. The elevated intracellular glucose concentrations may have a damaging effect on the glial and/or neuronal cells: if the intracellular glucose concentration rises too high, osmotic effects draw water into the cell to balance the build-up of glucose, causing cell swelling. Osmotic swelling has been detected in diabetic retinae [304]. Also, since lactate is acidic, if present in high concentrations in a cell, it changes the intracellular pH, denaturing the enzymes that catalyse vital reactions, causing cell damage.

6.4 PARAMETER SENSITIVITY ANALYSIS

In the previous section we found that elevated blood glucose concentrations may cause accumulation of glucose in the inner retinal tissue. This could lead to osmotic swelling of the cells as found in [304], and provides a possible

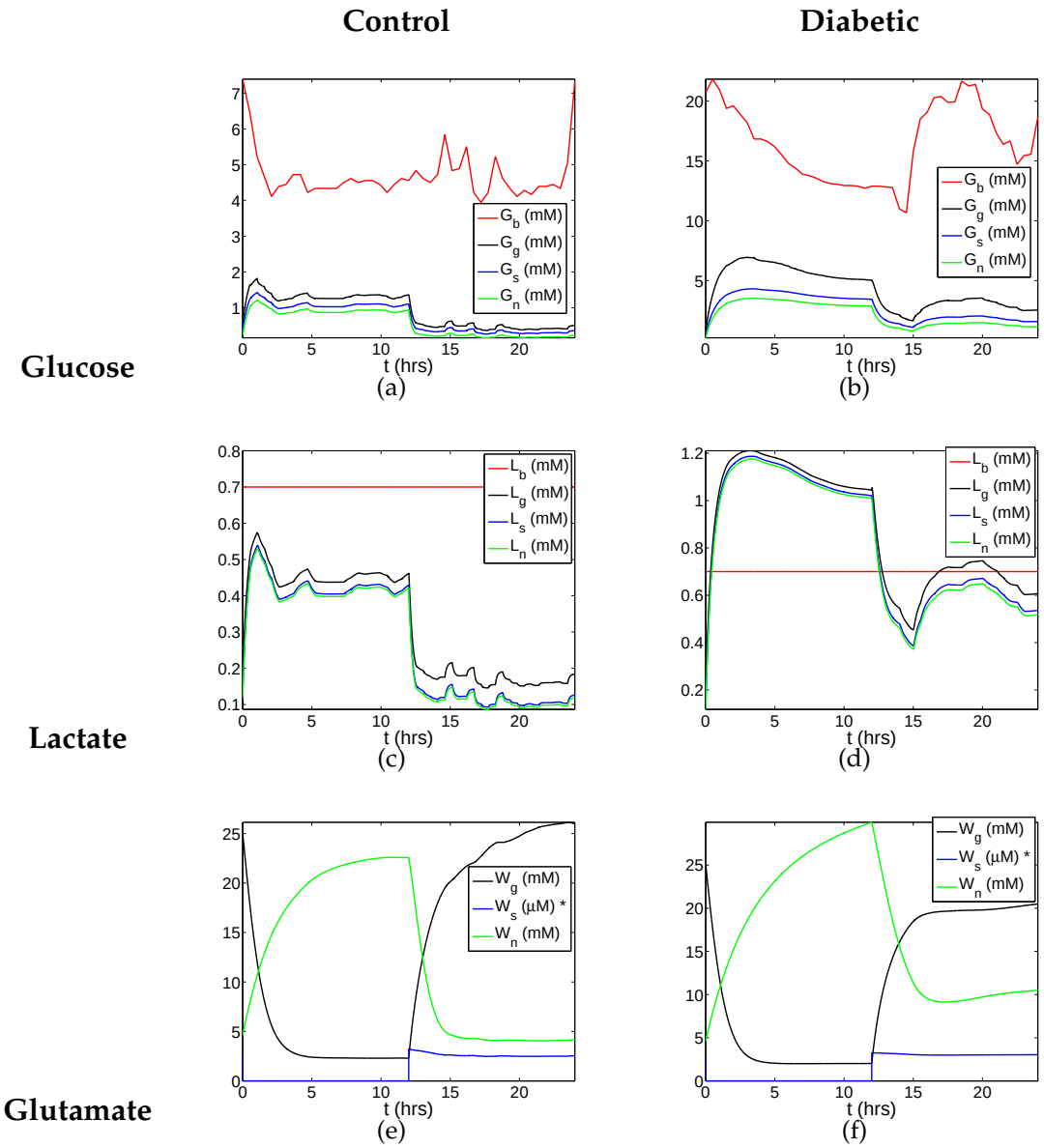


Figure 6.6.: Time evolution of the glucose, lactate and glutamate concentrations in the bloodstream (glucose and lactate only), glia, ECS and neurons in the control group and diabetic group in Hansen and Johansen's study [125], according to our model of inner retinal metabolism given by equations (5.2)–(5.6), using the parameter values in Tables 6.1–6.3. Simulations are performed over a 24-hour period starting and ending at 7:00 pm, comprising 12 hours of dark conditions followed by 12 hours of light. Due to regulated nutrient transport through cell membranes, only a limited amount of glucose and lactate enters the glial cells from the bloodstream, less enters the ECS, and still less enters the neurons. *We note that W_s is plotted in units of μM rather than mM.

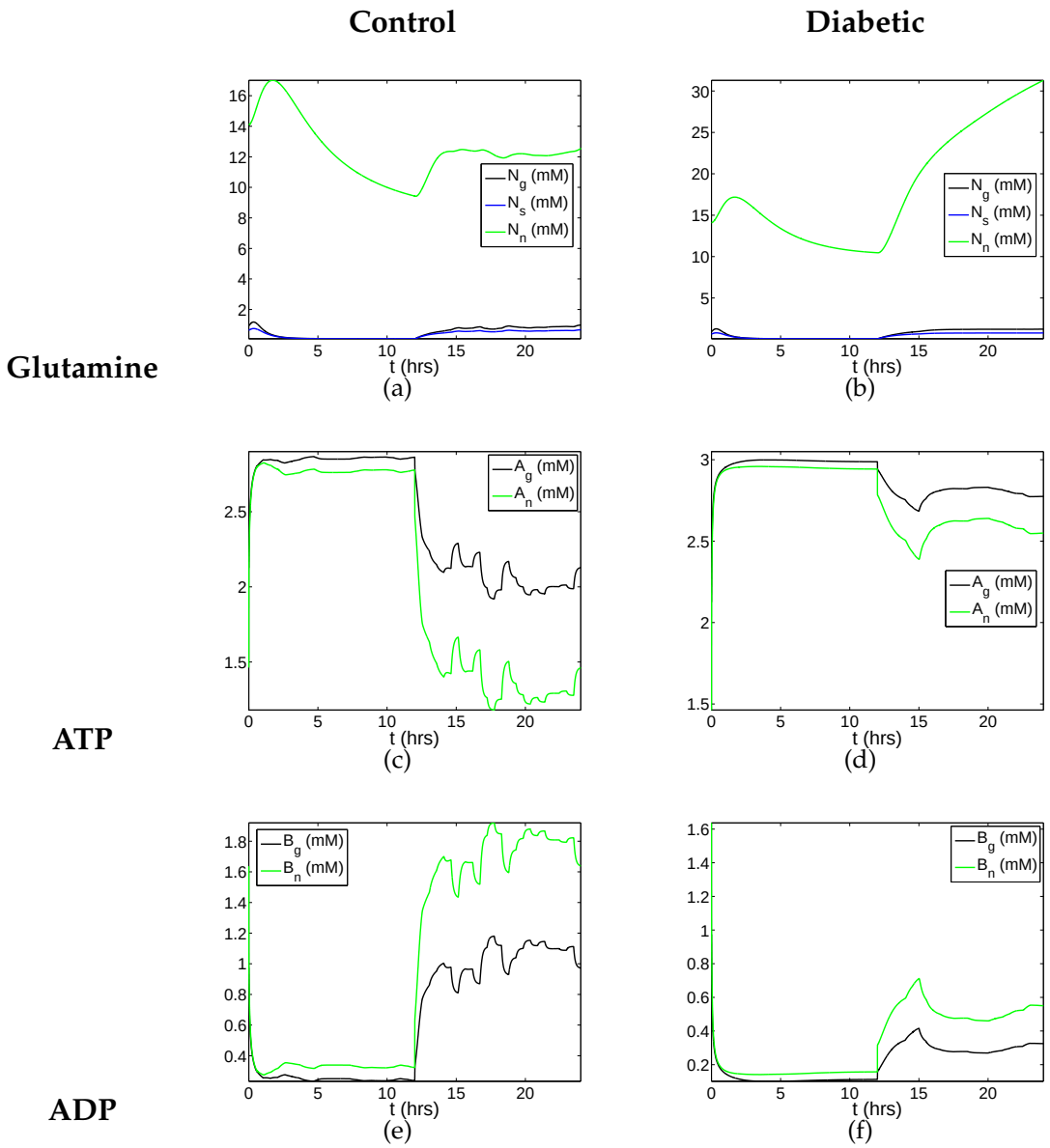


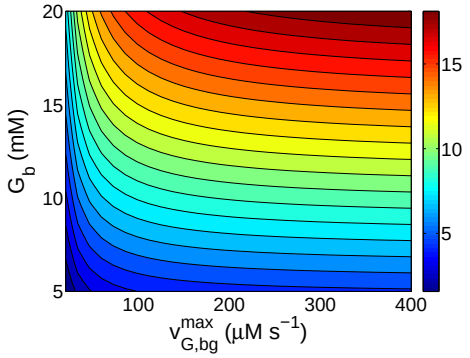
Figure 6.7.: Time evolution of the glutamine, ATP and ADP concentrations in the glia, ECS and neurons in the control group and diabetic group in Hansen and Johansen's study [125], according to our model of inner retinal metabolism given by equations (5.2)–(5.6), using the parameter values in Tables 6.1–6.3. Simulations are performed over a 24-hour period starting and ending at 7:00 pm, comprising 12 hours of dark conditions followed by 12 hours of light.

explanation for the decreased rate of glutamate oxidation observed in [221]. However, as discussed in §4.1, several studies have shown that the neuronal cell death that characterises early diabetic retinopathy may be caused by excitotoxicity [220], which, according to our model, cannot be accounted for by hyperglycaemia alone. To identify other metabolic changes that may lead to or contribute to pathology, in the following sections we vary blood glucose levels in combination with other model parameters denoting proposed causes of diabetic retinopathy. Such parameter alterations represent observed defects in the retinae of diabetes sufferers (as outlined in §4.1). We examine the effects of varying parameters on the glucose, lactate and glutamate concentrations following 12 hours of light and dark conditions, in particular, monitoring for accumulations in the inner retinal tissue.

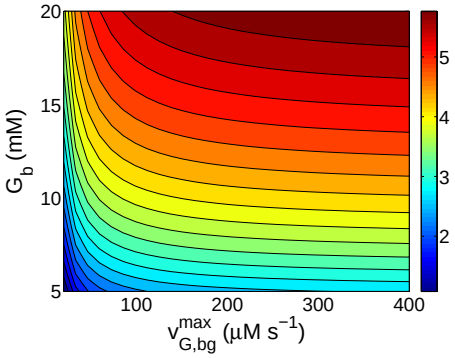
6.4.1 *Degeneration of Retinal Capillary Walls*

The most widely documented clinical indicator of diabetic retinopathy is the degeneration of the retinal capillary walls, which increases their permeability to glucose [218, 219]. We account for this effect by increasing the maximum rate of blood-glial glucose transport ($v_{G,bg}^{\max}$). The effects of varying $v_{G,bg}^{\max}$, in combination with varying blood glucose levels, on the glial and neuronal glucose and lactate concentrations under dark conditions are shown in Figures 6.8(a)–(d). The results for light conditions are qualitatively the same, but with lower glucose and lactate concentrations in each compartment. Increasing the rate of blood-glial glucose transport has the same qualitative effect on inner retinal metabolite levels as increasing the blood glucose concentration, exacerbating any damage caused by hyperglycemia.

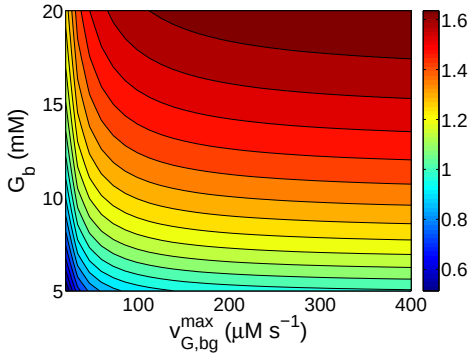
As shown in Figure 6.8(a), when $v_{G,bg}^{\max}$ is increased by an order of magnitude, for $G_b = 5\,\text{mM}$, the extracellular glutamate concentration, W_s, following 12 hours of light conditions rises with $v_{G,bg}^{\max}$ but saturates at $3.1\,\mu\text{M}$. Extracellular glutamate concentrations exceeding $30\,\mu\text{M}$ are thought to be toxic to neurons [305, 306], and concentrations above $60\,\mu\text{M}$ are classed as well within the excitotoxic range [307]. Hence, $3.1\,\mu\text{M}$ is far below excitotoxic levels. During darkness $W_{s,\text{SS}} = 0$ since the neurons do not release glutamate (not shown). Thus, according to our model, increased permeability of the capillary walls does not explain excitotoxicity in diabetic retinae.



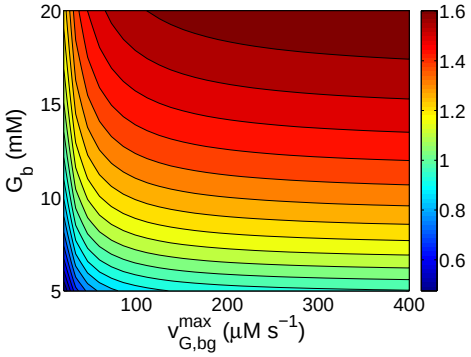
(a) $G_g(t = 12\,\text{hrs})$, dark, (mM)



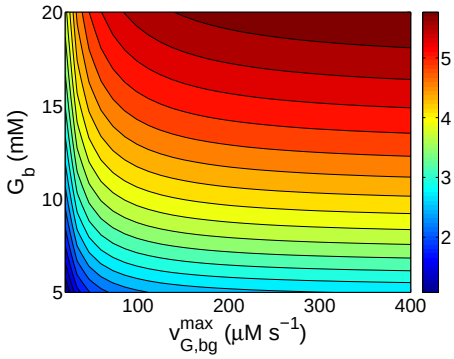
(b) $G_n(t = 12\,\text{hrs})$, dark, (mM)



(c) $L_g(t = 12\,\text{hrs})$, dark, (mM)



(d) $L_n(t = 12\,\text{hrs})$, dark, (mM)



(e) $W_s(t = 12\,\text{hrs})$, light, (μM)

Figure 6.8.: Variation in the (a) glial glucose, (b) neuronal glucose, (c) glial lactate, and (d) neuronal lactate concentration at $t = 12$ hours under dark conditions, and (e) extracellular glutamate concentration at $t = 12$ hours of light conditions, with blood glucose concentration and the rate of blood-glial glucose transport, according to our model of inner retinal metabolism given by equations (5.2)–(5.6). All other parameter values as shown in Tables 6.1–6.3.

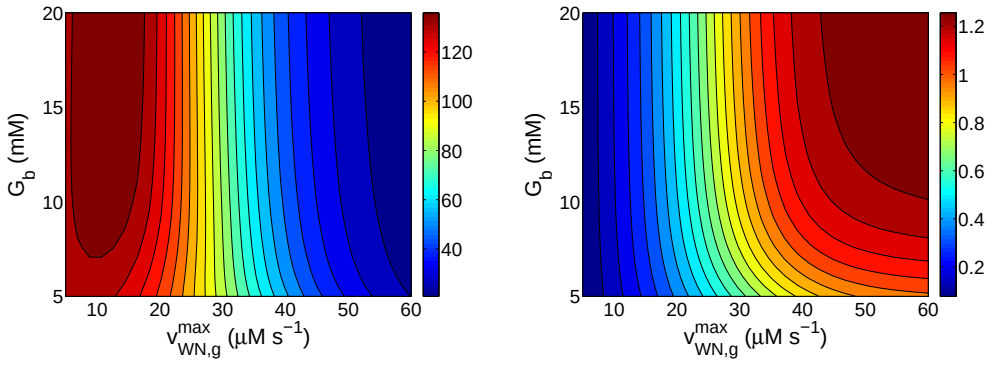
6.4.2 *Reduced Activity of Glutamine Synthetase*

Lieth et al. [221] proposed that the insulin shortage in diabetes sufferers leads to down-regulation of glutamine synthetase, the enzyme catalysing the conversion of glutamate to glutamine. We test the effects of this alteration by decreasing $v^{\max}_{WN,g}$ in our model, focusing on the impact on the glutamate-glutamine cycle under its maximal metabolic stress, i.e. during light conditions. The effects of varying $v^{\max}_{WN,g}$ and the blood glucose concentration on the glial, extracellular and neuronal glutamate and glutamine concentrations are shown in Figure 6.9. These results suggest that, as glial conversion of glutamate to glutamine is slowed, this reaction acts as a bottle-neck in the glutamate-glutamine cycle, leading to a rise in glial glutamate levels and a fall in the extracellular and neuronal glutamate and all glutamine concentrations. Since the glutamate levels in the ECS are lowered, this does not lead to excitotoxicity. Glial cells are able to withstand accumulations in intracellular glutamate concentrations, although extremely high glutamate levels over a long period may cause damage. We conclude that, although down-regulation of glutamine synthetase in the glial cells does not directly lead to excitotoxicity according to our model, it may, along with the elevated glucose concentrations, damage the glial cells, impairing their regulatory functions.

6.4.3 *Decreased Glial Glutamate Uptake from the ECS*

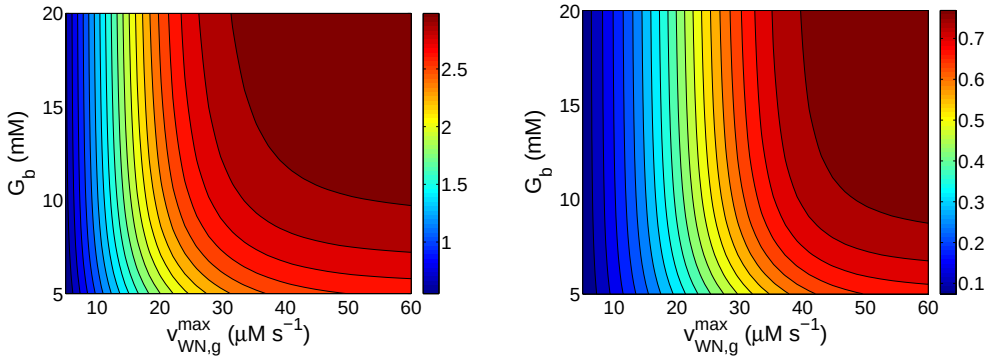
Lau et al. [220] and Li and Puro [222] found the rate of glial glutamate uptake was reduced in diabetes sufferers due to decreased expression of glutamate transporter proteins. Figure 6.10 shows the effects of varying the rate of glial glutamate uptake and blood glucose levels on the steady state glial and extracellular glutamate concentrations, under light conditions ($W_{s,SS} = 0$ during darkness).

If the rate of glial glutamate uptake decreases, the extracellular glutamate concentration rises until a steady state is reached with $V_g v_{W,sg} = V_n v_{W,ns}$. If the uptake rate becomes too low, the extracellular glutamate levels accumulate. Thus, if the maximal rate of glial glutamate uptake decreases beyond approximately $5\,\mu\mathrm{M\,s^{-1}}$, the extracellular glutamate concentration rises to excitotoxic levels, using the concentrations in [305–307] as a guide (see Figure 6.10(b)). All



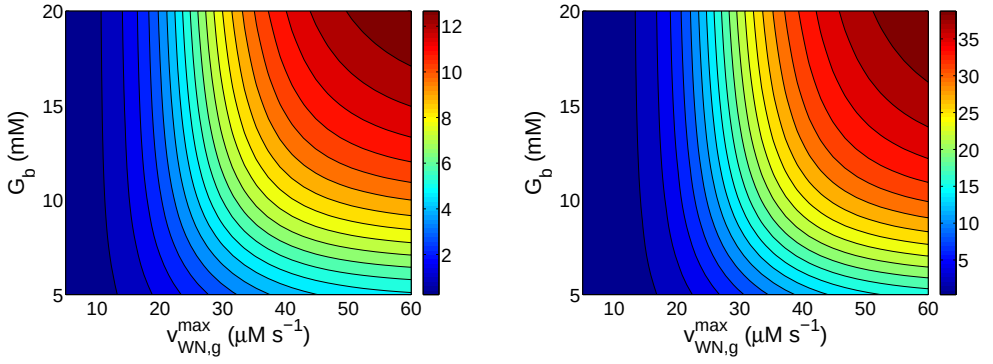
(a) $W_g(t = 12\,\text{hrs})$, light, (mM)

(b) $N_g(t = 12\,\text{hrs})$, light, (mM)



(c) $W_s(t = 12\,\text{hrs})$, light, (μM)

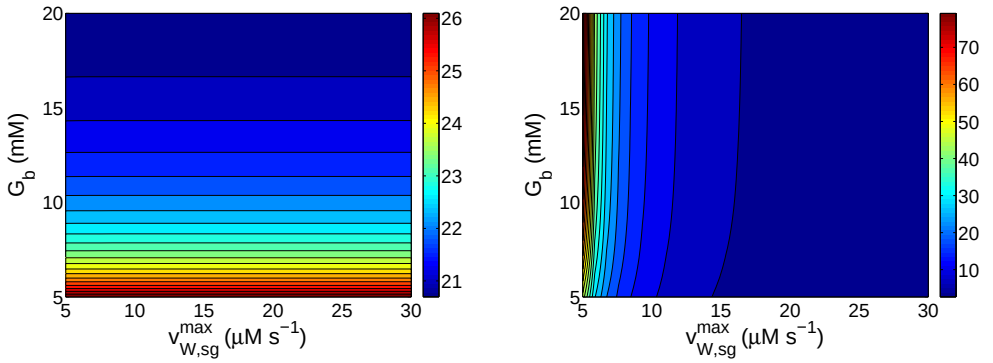
(d) $N_s(t = 12\,\text{hrs})$, light, (mM)



(e) $W_n(t = 12\,\text{hrs})$, light, (mM)

(f) $N_n(t = 12\,\text{hrs})$, light, (mM)

Figure 6.9.: Variation in the (a,c,e) glutamate and (b,d,f) glutamine concentration in the (a,b) glial cells, (c,d) ECS, and (e,f) neuronal cells at $t = 12$ hours under light conditions with blood glucose concentration and the rate of conversion of glutamate to glutamine by the glial cells, according to our model of inner retinal metabolism given by equations (5.2)–(5.6). All other parameter values as shown in Tables 6.1–6.3.



(a) $W_g(t = 12\,\text{hrs})$, light, (mM) (b) $W_s(t = 12\,\text{hrs})$, light, (μM)

Figure 6.10.: Variation in the glutamate concentration in the (a) glial cells and (b) ECS at $t = 12$ hours under light conditions with blood glucose concentration and the rate of glutamate uptake by the glial cells, according to our model of inner retinal metabolism given by equations (5.2)–(5.6). All other parameter values as shown in Tables 6.1–6.3. Extracellular glutamate increases to excitotoxic levels as glial glutamate uptake falls.

other glutamate and glutamine concentrations are unchanged (including the glial glutamate concentration shown in Figure 6.10(a)).

Our findings suggest that the decreased glial glutamate uptake from the ECS may be responsible for the accumulation of extracellular glutamate in the retinae of diabetes sufferers, leading to damage and death of the neuronal cells. From our results we are able to predict a multi-faceted, cumulative process by which inner retinal cells are damaged by diabetes (see Figure 6.11). According to our results, two mechanisms may lead to glial cell damage: firstly, hyperglycaemia increases glucose levels throughout the inner retina (see Figure 6.6(b)). If intracellular glucose levels become too high, this may damage the glial cells (and possibly the neurons) via osmotic swelling, as reported in [304]. Secondly, the lack of insulin in diabetes sufferers may lead to a slower conversion from glutamate to glutamine in the glial cells [221], allowing glutamate to accumulate to toxic levels (see Figure 6.9(a)). One of the ways in which glial cell damage presents itself is via the down-regulation of the transport proteins involved in glial glutamate uptake from the ECS [220, 222]. As a result, glutamate uptake is reduced, allowing glutamate levels to build up in the ECS (see Figure 6.10(b)). This damages and kills the neuronal cells via excitotoxicity [220], causing vision loss. Degradation of the inner retinal capillary walls increases their permeability [218, 219], which causes further increases to the intracellular glucose concentrations (see Figure 6.8), increasing the resulting damage.

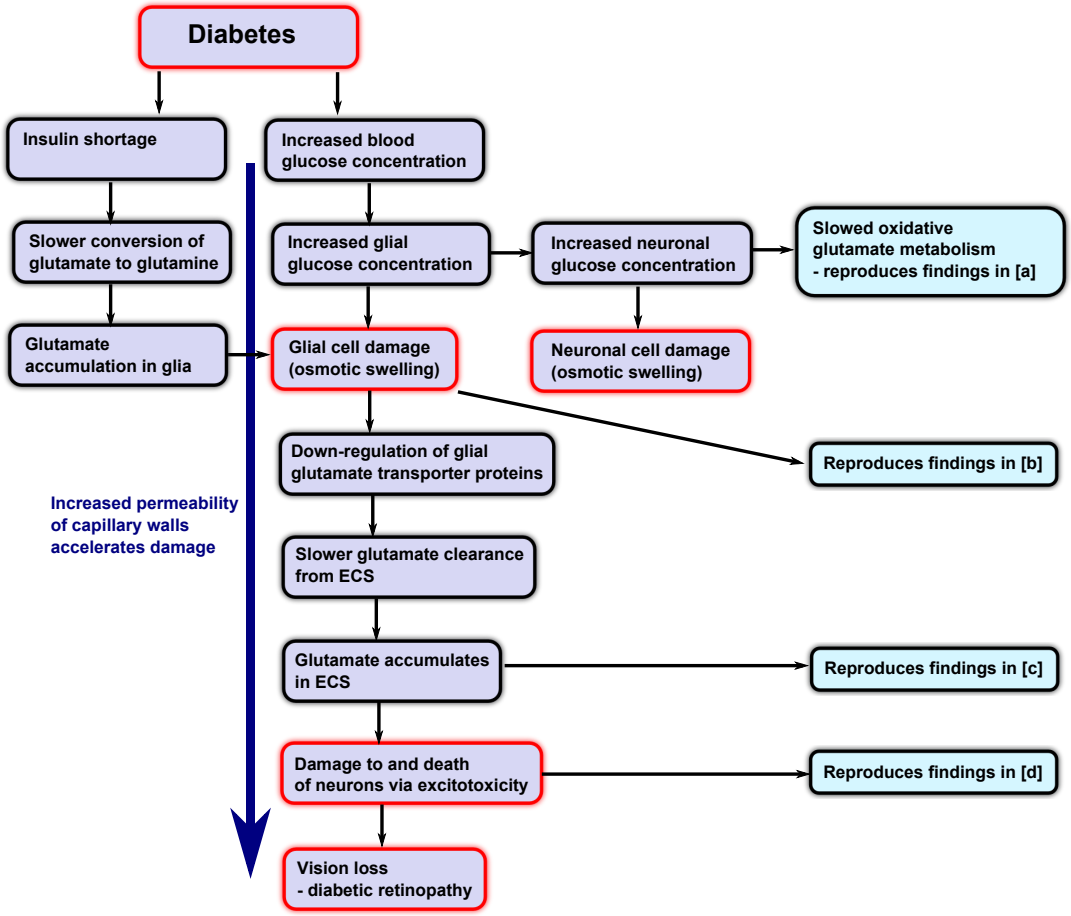


Figure 6.11.: Diagram summarising our predictions of the initiating events in diabetic retinopathy, based on the results of our model of inner retinal metabolism. In the situations outlined in the diagram, the solutions to our model reproduce the qualitative findings in (a) [221], (b) [304], (c) [220, 222], and (d) [218, 220].

6.5 DISCUSSION OF OUR MODEL OF INNER RETINAL METABOLIC REGULATION

The final three chapters of this thesis present our examination of metabolic regulation in the inner retinal tissue. We focused on how glial cells regulate nutrient levels in the environment surrounding the neurons e.g. via limited glucose transport through their cell membranes, controlling the input to the glutamate-glutamine cycle and clearing glutamate from the ECS. In Chapter 4 we introduced the key processes associated with inner retinal energy metabolism, intercellular transport and the glutamate-glutamine cycle, and reviewed relevant existing models. Mathematical models that fulfil several of our objectives are those continuum compartmental ODE models of cerebral metabolism proposed in [1, 238–240].

We formulated a compartmental ODE model of inner retinal metabolism in Chapter 5, incorporating the concentrations of glucose, lactate, glutamate, glutamine and ATP in the glial and neuronal cells and ECS within the inner retina. The rates of glycolysis, oxidative metabolism, nutrient transport and the glutamate-glutamine cycle were included. In particular, our model incorporates the production and breakdown of glutamate in glia and neurons respectively, via oxidative metabolism, and the coupling between blood glucose levels, energy metabolism and the glutamate-glutamine cycle via the ATP concentrations. To the best of our knowledge, ours is the only existing model that considers such links and that distinguishes between each step within the glutamate-glutamine cycle. It is also the only model to use a compartmental approach to model metabolite concentrations within the inner retinal glial and neuronal cells. These features of our model enable us to predict the consequences of large amplitude fluctuations in blood glucose levels on the inner retinal glutamate and glutamine concentrations. Since glutamate is neuroactive while glutamine is not, it is important to include each step of the glutamate-glutamine cycle, in order to distinguish carefully between the accumulation of glutamate and glutamine, since the former may lead to excitotoxicity while the latter will not. Through the above features our model is specialised to identify those mechanisms that may cause metabolites to accumulate to cytotoxic levels in the inner retinal tissue.

We justified some of our simplifying assumptions by comparing reaction rate expressions in our model with those used by Aubert and Costalat [1] for

their model of energy metabolism. In particular, we used multiple-timescale analysis to test our assumption that some intermediate steps in the glycolytic pathway are rapid compared to others. We found that a single-step reaction rate derived using these rapid kinetics assumptions is a good approximation to the full multi-step glycolytic rate in Aubert and Costalat's model. We also showed that our simple, phenomenological reaction rate expressions yield the same qualitative model dynamics as Aubert and Costalat's detailed expressions under typical physiological conditions.

At the beginning of Chapter 6 we explained how holding the ATP concentrations fixed in the glial and neuronal cells means that the glucose and lactate concentrations (in all compartments) decouple from the full model, as do the glutamate and glutamine concentrations when the glial lactate concentration and the glial and neuronal ATP concentrations are fixed. The glutamate-glutamine submodel has at most one steady state which we found analytically, revealing how the glutamate and glutamine concentrations depend on the metabolite levels and reaction rates within the glutamate-glutamine cycle, the ATP concentrations and the glial glutamate production rate, $v_{LW,g}$ (the input to the glutamate-glutamine cycle). Further, ensuring physically realistic steady states for the glutamate and glutamine concentrations led to constraints on parameters, aiding parameter estimation.

Using the average measured time-varying blood glucose concentrations in healthy and diabetic participants by Hansen and Johansen [125] as model input, we used our model to predict the diurnal variation in inner retinal metabolite levels in both cases. The differences between predicted metabolite concentrations in the healthy and diabetic groups suggest that in diabetes sufferers, glucose may accumulate within the inner retinal tissue, damaging glial cells (and perhaps also the neurons) via osmotic swelling, as observed in [304]. Since hyperglycemia lowers the energy demand of the glia and neurons at the steady state, this slows the rate of oxidative glutamate metabolism, as measured in [221].

In the later stages of diabetic retinopathy, retinal capillary walls may become damaged, increasing their permeability to glucose [218, 219]. We investigated the effects of this in our model by increasing the $V_{\max}$ value for blood-glial glucose transport. According to our model solutions, this further increases the inner retinal glucose and lactate concentrations, magnifying the effect of an elevated blood glucose concentration.

Another mechanism that is potentially damaging to the glial cells, detected in [221], is a reduction in the rate of glutamine synthesis from glutamate in the glial cells, thought to be due to lowered insulin levels. This results in abnormally high intracellular glutamate concentrations in the glia. Although the glial cells have the ability to withstand accumulations in glutamate levels, if the glutamate concentration becomes extremely high this may lead to cell damage.

Neither of the above defects explain the excitotoxic damage to the neurons found in [218, 220], suggesting that they are contributors to rather than sole causes of the neuronal damage characterising diabetic retinopathy. Lau et al. [220] and Li and Puro [222] found that the transporter proteins mediating glial glutamate uptake were down-regulated in diabetes sufferers, and hypothesised that this was the result of earlier damage to glial cells. Reducing the rate of glial glutamate uptake in our model greatly increases the predicted steady state glutamate concentration in the ECS until it reaches excitotoxic levels. This indicates that the down-regulation of glial glutamate transporter proteins in diabetes sufferers may produce extracellular glutamate concentrations high enough to damage and kill the neuronal cells via excitotoxicity. It thus explains the increased rate of neuronal cell death detected in [218, 220].

Our findings suggest that the large amplitude fluctuations in the blood glucose levels of diabetes sufferers are not directly linked with damage to the neuronal cells, but may harm the glial cells via osmotic swelling, initiating a chain of events resulting in impaired glial glutamate uptake, causing neuronal cell death via excitotoxicity. The degradation of the retinal capillary walls may accelerate pathogenesis by causing further accumulation of glucose and lactate concentrations within the inner retina, further fuelling the chain. Alternatively, glial cell damage may be independent of blood glucose levels. For instance, according to our results, slowed conversion of glutamate to glutamine in the glial cells leads to glutamate accumulation in the glia. If this is severe, it may be the cause of glial damage or contribute to the existing damage via hyperglycemia.

Although we ensured that our parameter estimates were as realistic as possible, basing them on experimental measurements in mammalian cells *in vivo* where possible, *in vivo* measurements in human retinae may become increasingly available in the future, e.g. due to enhancements in imaging techniques, allowing much more accurate parameter estimates to be obtained.

Our model is designed to be simple and tractable and, as such, focuses solely on the key mechanisms in inner retinal metabolism. Similar models of cerebral metabolism account for other species such as oxygen, carbon dioxide, NAD^+ and NADH [238, 240], other models decompose the tissue into more compartments, providing information at a subcellular level [252, 253]. Having gained an understanding of core components of inner retinal metabolism, incorporating such additional detail in future models may generate insight into the subcellular events associated with the development of diabetic retinopathy, and lead to the identification of new treatment targets. Based on the insight gained from our model, an aim for future work is to identify whether connections exist between diabetic damage to glial cells and the down-regulation of glial glutamate uptake from the ECS. For instance, an agent-based model including the signalling pathways by which the glial cells regulate the expression of glutamate transporter proteins may reveal such links.

Clinical observations are also needed in order to support or refute our predictions, and also to deduce whether the down-regulation of glutamate transporter proteins may be caused by osmotic swelling, the accumulation of glutamate in the glial cells following the down-regulation of glutamine synthetase enzyme, both or neither.

Analysis and simulations of our model have revealed new insights into the way glial cells regulate the inner retinal metabolite levels, how this changes between light and dark conditions and the effects of altered metabolism and blood glucose levels. We can use these results to predict defects that may be responsible for problems associated with diabetic retinopathy [218, 220–222, 304]. Current therapeutic strategies target diabetic retinopathy at a late stage, often when vision is already significantly impaired. It is likely that better results will be achieved by targeting the disease at an earlier stage, improving the quality of life for many diabetes patients.

A

REPRODUCTION OF SIMULATION RESULTS IN AUBERT AND COSTALAT'S MODEL

In order to reproduce the simulation results in [1], which are useful in Chapters 4 and 5, we used *ode15s* to integrate equations (4.10)–(4.19), taking parameter values from [1].

Figures A.1–A.2 show our simulations of equations (4.10a)–(4.12b) under resting conditions, using the parameter values and initial conditions recorded in [1] (see Tables 4.1–4.2 and equations (4.19)). Since in [1] the initial conditions are defined as the resting steady state concentrations, and the model is simulated under resting conditions, we expect all concentrations to remain in a steady state. However, this is not the case in our simulations: as shown in Figures A.1–A.2, the concentrations evolve in time and reach steady states that differ from those recorded in [1]. Furthermore, the simulated concentrations of neuronal GAP, NADH and lactate become negative at long times.

To check that this is not due to an error in our simulations, we analytically substitute the parameter choices and resting steady state concentrations recorded in [1] (see Tables 4.1–4.2 and equations (4.18)) into equations (4.10a)–(4.12b) under resting conditions (with $v_{\text{Stim},x} = 0$). Taking the initial value of $X^{-1}dX/dt$ for each concentration X in the glia and neurons, we obtain the results in the second column of Table A.1, some of which are not close to zero. (The initial rates of change of concentrations in the bloodstream and ECS, are all close to zero and thus not shown.) As Table A.1 and Figures A.1–A.2 suggest, it was not possible for us to reproduce the resting steady state concentrations given in [1] by using the parameter choices stated in [1].

Using the following alternative parameter values:

- $v^{\max}_{\text{Mito},g} = 9.7 \times 10^{-3}\,\text{mM}\,\text{s}^{-1}$;
- $v^{\max}_{\text{Mito},n} = 0.0403\,\text{mM}\,\text{s}^{-1}$;

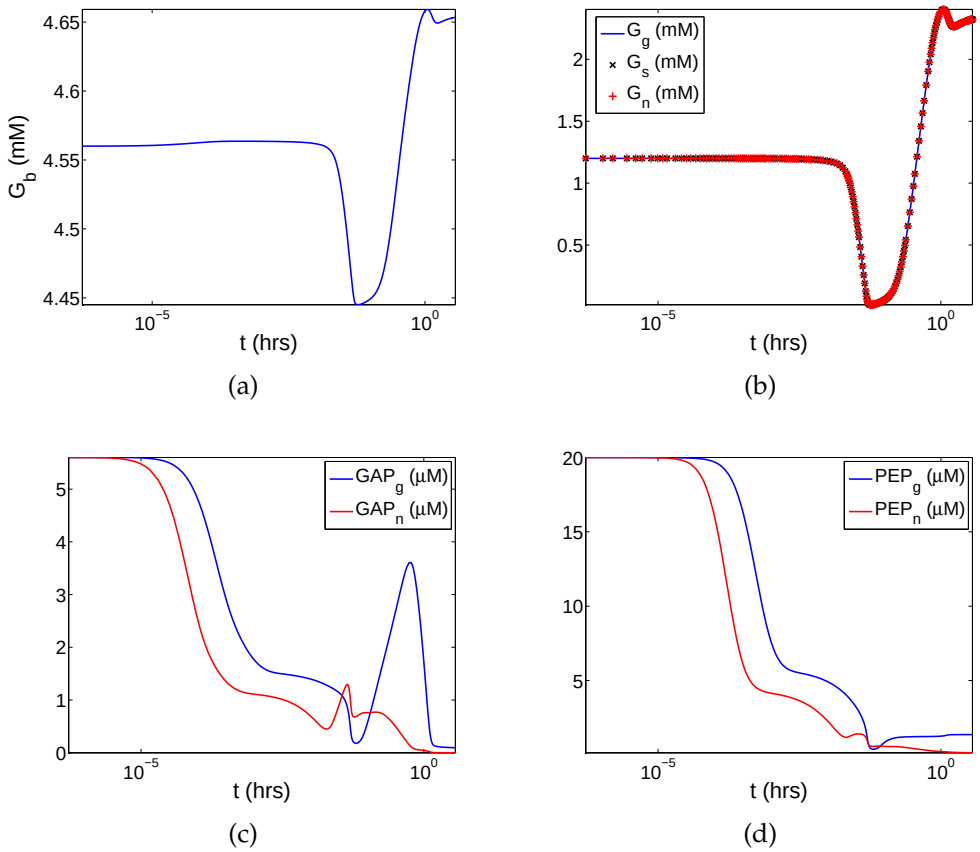


Figure A.1.: Our simulations of time evolution of cerebral metabolite concentrations, using the governing equations, parameter values and initial conditions specified in [1].

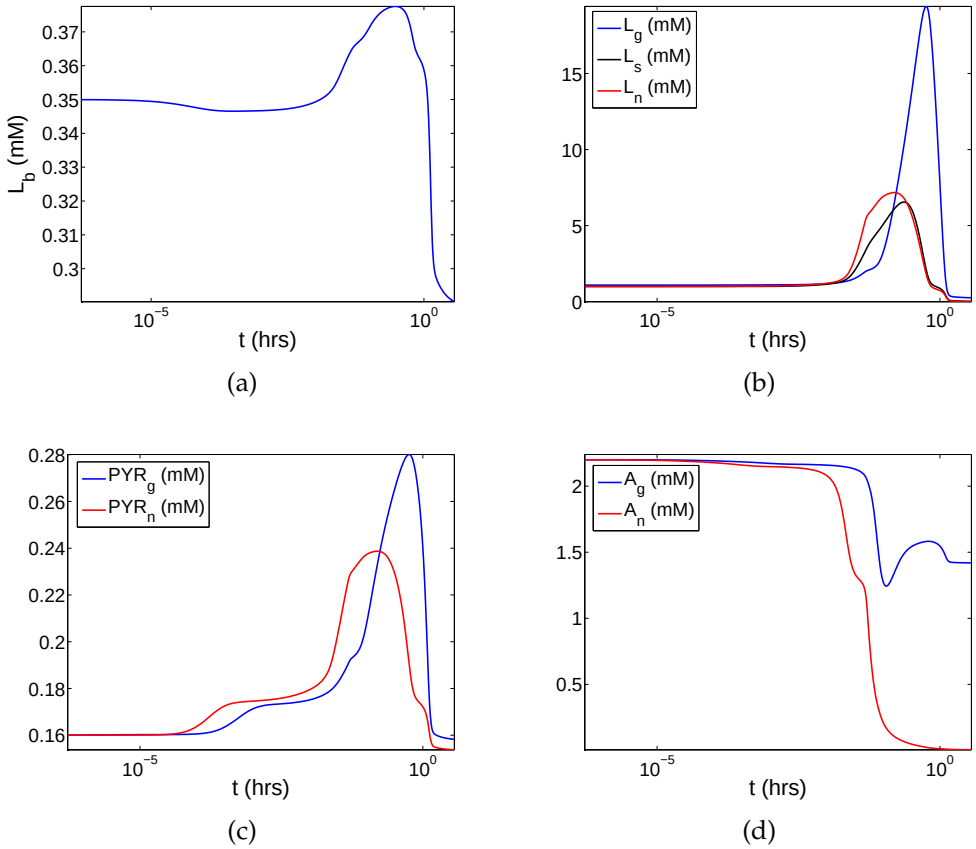


Figure A.2.: Our simulations of time evolution of cerebral metabolite concentrations, using the governing equations, parameter values and initial conditions specified in [1].

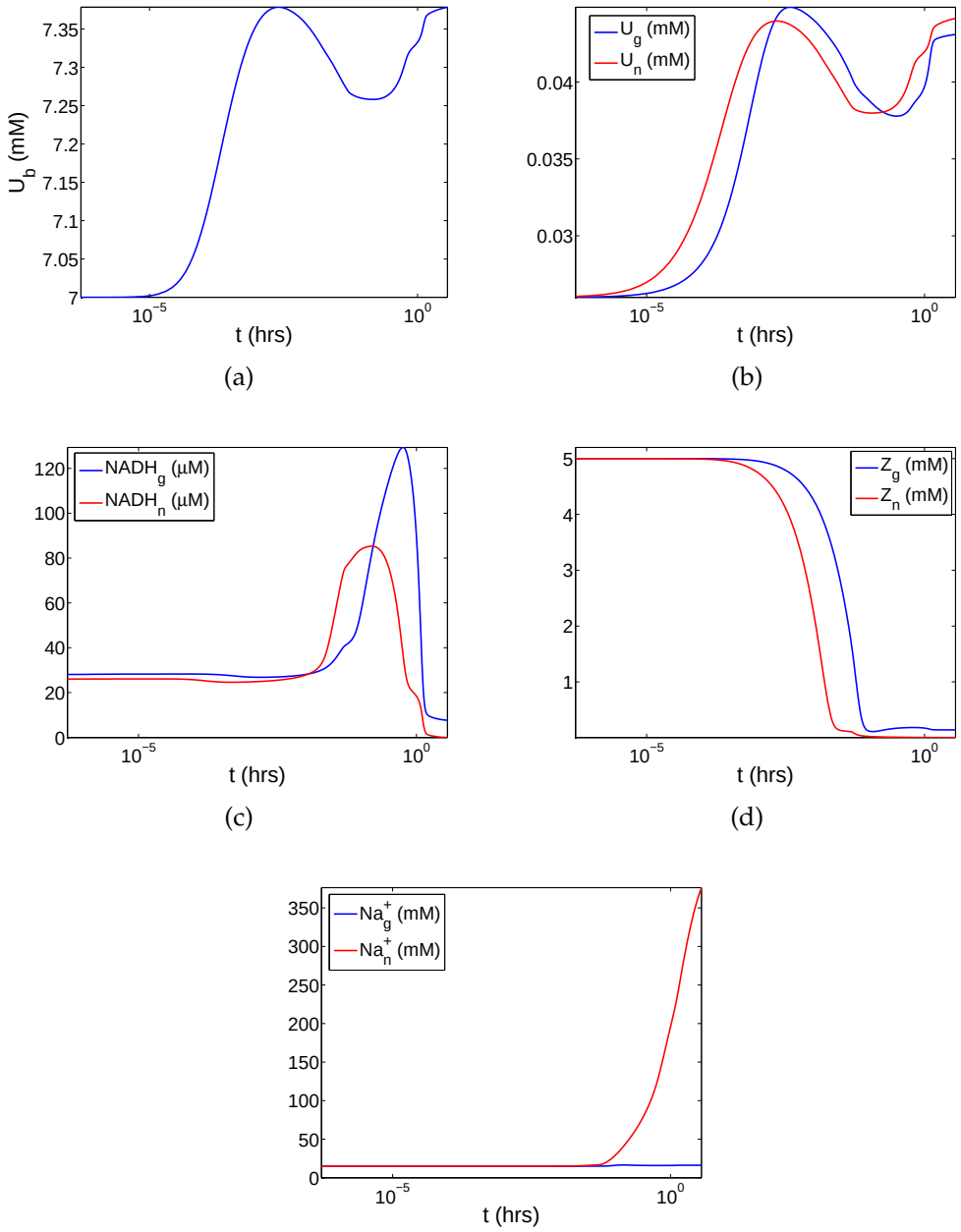


Figure A.3.: Our simulations of time evolution of cerebral metabolite concentrations, using the governing equations, parameter values and initial conditions specified in [1].

Variable	$\frac{1}{X}\frac{dX}{dt}\Big\vert_{t=0}$	Contributing reaction rates at $t = 0$ (mM s^{-1})
G_g	-1.67×10^{-3}	$v_{G,\text{trans},bg} = 0.0020$, $v_{G,\text{trans},sg} = 0$, $-v_{\text{HK-PFK},g} = -0.0041$
GAP_g	0.0246	$2v_{\text{HK-PFK},g} = 0.0081$, $-v_{\text{PGK},g} = -0.0080$
PEP_g	-6.11×10^{-3}	$v_{\text{PGK},g} = 0.0080$, $-v_{\text{PK},g} = -0.0081$
PYR_g	0.256	$v_{\text{PK},g} = 0.0081$, $-v_{\text{LDH},g} = 0.0355$, $-v_{\text{Mito},g} = -0.0026$
L_g	-0.0353	$v_{\text{LDH},g} = -0.0355$, $-v_{\text{LAC,trans},gs} = -0.0014$, $-v_{\text{LAC,trans},gb} = -0.0016$
A_g	-0.0160	$-2v_{\text{HK-PFK},g} = -0.0081$, $v_{\text{PGK},g} = 0.0080$, $v_{\text{PK},g} = 0.0081$, $-v_{\text{ATPases},g} = -0.020$, $-v_{\text{Pump},g} = -0.0620$, $n_{\text{OP}}v_{\text{Mito},g} = 0.0388$, $v_{\text{CK},g} = -2.2922 \times 10^{-4}$
U_g	0.273	$v_{U,bg} = 0.0149$, $-n_{\text{Aero}}v_{\text{Mito},g} = -0.0078$
NADH_g	1.46	$v_{\text{PGK},g} = 0.0080$, $-v_{\text{LDH},g} = 0.0355$, $-v_{\text{Mito},g} = -0.0026$
Z_g	5.84×10^{-5}	$-v_{\text{CK},g} = 2.2922 \times 10^{-4}$
Na^+_g	-5.02×10^{-7}	$v_{\text{Leak-Na},g} = 0.1861$, $-3v_{\text{Pump},g} = -0.1861$
Variable	$\frac{1}{X}\frac{dX}{dt}\Big\vert_{t=0}$	**Contributing reaction rates at $t = 0$ (mMs^{-1})**
G_n	-8.67×10^{-3}	$v_{G,\text{trans},sn} = 0$, $-v_{\text{HK-PFK},n} = -0.0104$
GAP_n	0.0701	$2v_{\text{HK-PFK},n} = 0.0208$, $-v_{\text{PGK},n} = -0.0204$
PEP_n	-0.0163	$v_{\text{PGK},n} = 0.0204$, $-v_{\text{PK},n} = -0.0207$
PYR_n	0.141	$v_{\text{PK},n} = 0.0207$, $-v_{\text{LDH},n} = 0.0128$, $-v_{\text{Mito},n} = -0.0109$
L_n	-0.0128	$v_{\text{LDH},n} = -0.0128$, $-v_{L,\text{trans},ns} = 0$
A_n	-0.066	$-2v_{\text{HK-PFK},n} = -0.0208$, $v_{\text{PGK},n} = 0.0204$, $v_{\text{PK},n} = 0.0207$, $-v_{\text{ATPases},n} = -0.17$, $-v_{\text{Pump},n} = -0.1595$, $n_{\text{OP}}v_{\text{Mito},n} = 0.1629$, $v_{\text{CK},n} = -5.2657 \times 10^{-4}$
U_n	1.14	$v_{U_m,bn} = 0.0623$, $-n_{\text{Aero}}v_{\text{Mito},n} = -0.0326$
NADH_n	0.858	$v_{\text{PGK},n} = 0.0204$, $-v_{\text{LDH},n} = 0.0128$, $-v_{\text{Mito},n} = -0.0109$
Z_n	1.05×10^{-4}	$-v_{\text{CK},n} = 5.2657 \times 10^{-4}$
Na^+_n	-1.29×10^{-6}	$v_{\text{Leak-Na},n} = 0.4785$, $-3v_{\text{Pump},n} = -0.4785$

Table A.1.: Initial rates of change of concentrations when the parameter choices and initial conditions were substituted (analytically) into the governing equations in [1].

- $v_{\text{ATPases},g} = 0.0212\,\text{mM}\,\text{s}^{-1}$;
- $v_{\text{ATPases},n} = 0.1716\,\text{mM}\,\text{s}^{-1}$;

we obtain all resting steady state concentrations to within 2% of the values recorded in [1], and replicate the results in Figures 2–4 of [1], as shown in Figures 4.8–4.13 in Chapter 4.

B

ASYMPTOTIC ANALYSIS OF THE AC SUBMODEL

The asymptotic analysis described in this appendix enables us to simplify the dimensionless AC submodel on the timescale over which the nutrient concentrations included in our model (i.e. the lactate and ATP concentrations) evolve, eliminating the glycolytic intermediates GAP, PEP and pyruvate. We follow a similar method to [267] for example.

The dimensionless AC submodel is given in equations (5.34) and (5.35), where the small parameter ϵ is defined in equation (5.33). We use series expansions of the form $u_x(\tau) = u_{x,0}(\tau) + \epsilon u_{x,1}(\tau) + \epsilon^2 u_{x,2}(\tau) + \cdots$ for each dependent variable $u_x(\tau) \in \{\hat{\text{GAP}}_x(\tau), \hat{\text{PEP}}_x(\tau), \hat{\text{PYR}}_x(\tau), l_x(\tau), a_x(\tau), b_x(\tau)\}$, which yields the following dimensionless reaction rate expressions,

$$\hat{v}_{L,yx}(l_x) = \hat{v}_{L,yx,0} + \epsilon\hat{v}_{L,yx,1} + \hat{v}^{yx}_{L,yx,2}\epsilon^2 + \cdots, \tag{B.1a}$$

$$\hat{v}_{\text{HK-PFK},x}(a_x) = \hat{v}_{\text{HK-PFK},x,0} + \hat{v}_{\text{HK-PFK},x,1}\epsilon + \hat{v}_{\text{HK-PFK},x,2}\epsilon^2 + \cdots, \tag{B.1b}$$

$$\hat{v}_{\text{PGK},x}(\hat{\text{GAP}}_x, b_x) = \hat{v}_{\text{PGK},x,0} + \hat{v}_{\text{PGK},x,1}\epsilon + \hat{v}_{\text{PGK},x,2}\epsilon^2 + \cdots, \tag{B.1c}$$

$$\hat{v}_{\text{PK},x}(\hat{\text{PEP}}_x, b_x) = \hat{v}_{\text{PK},x,0} + \hat{v}_{\text{PK},x,1}\epsilon + \hat{v}_{\text{PK},x,2}\epsilon^2 + \cdots, \tag{B.1d}$$

$$\hat{v}_{\text{LDH},x}(\hat{\text{PYR}}_x, l_x) = \hat{v}_{\text{LDH},x,0} + \hat{v}_{\text{LDH},x,1}\epsilon + \hat{v}_{\text{LDH},x,2}\epsilon^2 + \cdots, \tag{B.1e}$$

$$\hat{v}_{\text{Mito},x}(\hat{\text{PYR}}_x, b_x) = \hat{v}_{\text{Mito},x,0} + \hat{v}_{\text{Mito},x,1}\epsilon + \hat{v}_{\text{Mito},x,2}\epsilon^2 + \cdots, \tag{B.1f}$$

with,

$$\hat{v}_{L,yx,0}(l_{x,0}) = \text{M}\left(l^*_y; \hat{v}^{\max}_{L,yx}, \hat{K}_{L,yx}\right) - \text{M}\left(l_{x,0}; \hat{v}^{\max}_{L,yx}, \hat{K}_{L,yx}\right), \tag{B.2a}$$

$$\hat{v}_{L,yx,1}(l_{x,1}, l_{x,0}) = -\hat{v}^{\max}_{L,yx}\left(1 - \text{M}\left(l_{x,0}; 1, \hat{K}_{L,yx}\right)\right) \frac{l_{x,1}}{l_{x,0} + \hat{K}_{L,yx}}, \tag{B.2b}$$

$$\hat{v}_{\text{HK-PFK},x,0}(a_{x,0}) = \hat{k}_{\text{HK-PFK},x}\frac{a_{x,0}}{a_{x,0}^4 + \hat{K}_{\text{HK-PFK},A,x}^4}, \tag{B.3a}$$

$$\hat{v}_{\text{HK-PFK},x,1}(a_{x,1}, a_{x,0}) = \hat{k}_{\text{HK-PFK},x}\left(1 - \frac{4a_{x,0}^4}{a_{x,0}^4 + \hat{K}_{\text{HK-PFK},A,x}^4}\right) \frac{a_{x,1}}{a_{x,0}^4 + \hat{K}_{\text{HK-PFK},A,x}^4}, \tag{B.3b}$$

$$\hat{v}_{\text{PGK},x,0}(\hat{\text{GAP}}_{x,0}, b_{x,0}) = \hat{k}_{\text{PGK},x}\hat{\text{GAP}}_{x,0}b_{x,0}, \tag{B.4a}$$

$$\hat{v}_{\text{PGK},x,1}(\hat{\text{GAP}}_{x,0}, b_{x,0}, \hat{\text{GAP}}_{x,1}, b_{x,1}) = \hat{k}_{\text{PGK},x}\left(\hat{\text{GAP}}_{x,0}b_{x,1} + \hat{\text{GAP}}_{x,1}b_{x,0}\right), \tag{B.4b}$$

$$\hat{v}_{\text{PK},x,0}(\hat{\text{PEP}}_{x,0}, b_{x,0}) = \hat{k}_{\text{PK},x}\hat{\text{PEP}}_{x,0}b_{x,0}, \tag{B.5a}$$

$$\hat{v}_{\text{PK},x,1}(\hat{\text{PEP}}_{x,0}, b_{x,0}, \hat{\text{PEP}}_{x,1}, b_{x,1}) = \hat{k}_{\text{PK},x}\left(\hat{\text{PEP}}_{x,0}b_{x,1} + \hat{\text{PEP}}_{x,1}b_{x,0}\right), \tag{B.5b}$$

$$\hat{v}_{\text{LDH},x,0}(\hat{\text{PYR}}_{x,0}, l_{x,0}) = \hat{k}^+_{\text{LDH},x}\hat{\text{PYR}}_{x,0} - \hat{k}^-_{\text{LDH},x}l_{x,0}, \tag{B.6a}$$

$$\hat{v}_{\text{LDH},x,1}(\hat{\text{PYR}}_{x,1}, l_{x,1}) = \hat{k}^+_{\text{LDH},x}\hat{\text{PYR}}_{x,1} - \hat{k}^-_{\text{LDH},x}l_{x,1}, \tag{B.6b}$$

$$\hat{v}_{\text{Mito},x,0}(\hat{\text{PYR}}_{x,0}, b_{x,0}) = \text{M}\left(\hat{\text{PYR}}_{x,0}; \hat{v}^{\max}_{\text{Mito},x}, \hat{K}_{\text{Mito,PYR},x}\right) \text{M}\left(b_{x,0}; 1, \hat{K}_{\text{Mito},B,x}\right), \tag{B.7a}$$

$$\hat{v}_{\text{Mito},x,1}(\hat{\text{PYR}}_{x,0}, b_{x,0}, \hat{\text{PYR}}_{x,1}, b_{x,1}) = \text{M}\left(\hat{\text{PYR}}_{x,0}; \hat{v}^{\max}_{\text{Mito},x}, \hat{K}_{\text{Mito,PYR},x}\right) \frac{b_{x,1}}{b_{x,0} + \hat{K}_{\text{Mito},B,x}}\left(1 - \text{M}\left(b_{x,0}; \hat{K}_{\text{Mito},B,x}\right)\right) + \text{M}\left(b_{x,0}; \hat{v}^{\max}_{\text{Mito},x}, \hat{K}_{\text{Mito},B,x}\right) \frac{\hat{\text{PYR}}_{x,1}}{\hat{\text{PYR}}_{x,0} + \hat{K}_{\text{Mito,PYR},x}}\left(1 - \text{M}\left(\hat{\text{PYR}}_{x,0}; \hat{K}_{\text{Mito,PYR},x}\right)\right). \tag{B.7b}$$

In order to explicitly show the relative orders of magnitude of each term in equations (5.34), concentration scalings and dimensionless parameter groupings are chosen such that the reaction rates are $\mathcal{O}(1)$ as are parameter groupings r_1

and r_2. The other parameter groupings containing the typical concentrations in system (5.34) are,

$$\frac{A_r}{[\mathrm{PYR}]_r} \approx 12,$$

which is between $\mathcal{O}(1)$ and $\mathcal{O}(\epsilon^{-1})$, and,

$$\frac{[\mathrm{PYR}]_r}{L_r} \approx 0.17,$$

which is between $\mathcal{O}(1)$ and $\mathcal{O}(\epsilon)$. We do not associate these quantities with a specific order of ϵ at this stage since this may lead to errors.

For the ATP and ADP concentrations, the conservation law in equation (5.21) gives,

$$a_{x,0} + \epsilon a_{x,1} + \cdots + \frac{B_r}{A_r}\left(b_{x,0} + \epsilon b_{x,1} + \cdots\right) = a_{\mathrm{Tot},x}. \tag{B.8}$$

The ratio B_r/A_r is equal to 5ϵ. Thus the leading order approximation to equation (B.8) is,

$$a_{x,0} = a_{\mathrm{Tot},x}. \tag{B.9}$$

Since reaction rates $v_{\mathrm{PGK},x}$, $v_{\mathrm{PK},x}$ and $v_{\mathrm{Mito},x}$ depend on the ADP concentration, the first order correction term is also needed, which is,

$$b_{x,0} = -\frac{a_{x,1}}{5}.$$

Although the ATP concentration is approximately constant at all times in the submodels, it is affected by other processes in our full model that are not included in the submodels, e.g. consumption by the glutamate-glutamine cycle. We therefore incorporate the ODE for ATP in this analysis to show that our asymptotic approximation at long timescales is not reliant on the assumption in equation (B.9).

Next, we note that in equations (5.34c) and (5.34d), the terms including the reaction rate $\hat{v}_{\mathrm{LDH},x}$ are large compared to the other terms. On a timescale with $\tau = \mathcal{O}(1)$, equations (5.34c) and (5.34d) both give $\hat{v}_{\mathrm{LDH},x} = 0$ to leading order, and the system is underdetermined. To prevent the large terms from dominating both equations (5.34c) and (5.34d), we take a linear combination

of the two equations in which the leading order terms are eliminated, and use this to replace equation (5.34d) (or (5.34c), with the same result). Inspection of equations (5.34c) and (5.34d) elucidates that the leading order terms can be eliminated by taking the linear combination,

$$\frac{d\hat{\mathrm{PYR}}_x}{d\tau} + \frac{L_r}{[\mathrm{PYR}]_r}\frac{dl_x}{d\tau} = \frac{A_r}{[\mathrm{PYR}]_r}\hat{v}_{\mathrm{PK},x}(\hat{\mathrm{PEP}}_x, b_x) - 2\frac{A_r}{[\mathrm{PYR}]_r}\hat{v}_{\mathrm{Mito},x}(\hat{\mathrm{PYR}}_x, b_x) + 2\frac{L_r}{[\mathrm{PYR}]_r}\hat{v}_{L,yx}(l_x). \quad \text{(B.10)}$$

To summarise, in the system (5.34), equation (5.34d) is replaced with equation (B.10) while (5.34c) is unchanged. From the left hand sides of the ODEs in (5.34) it is evident that the corresponding variables evolve on three separate timescales, for which $\tau = \mathcal{O}\left(\epsilon^2\right)$, $\tau = \mathcal{O}\left(\epsilon\right)$ and $\tau = \mathcal{O}\left(1\right)$. Exploiting this fact we make an asymptotic approximation to the system (5.34) on each timescale, whose solutions closely match those of the original system (and become identical to them as $\epsilon \to 0$).

To examine the *short* timescale, for which $\tau = \mathcal{O}\left(\epsilon^2\right)$, we define $\tau_2 = \epsilon^{-2}\tau$, which is $\mathcal{O}(1)$ over this timescale, and the equations in (5.34) with the adaptations described above become,

$$\frac{d\hat{\mathrm{GAP}}_x}{d\tau_2} = \epsilon r_1\left(2\hat{v}_{\text{HK-PFK},x} - \hat{v}_{\mathrm{PGK},x}\right), \quad \text{(B.11a)}$$

$$\frac{d\hat{\mathrm{PEP}}_x}{d\tau_2} = \epsilon r_2\left(\hat{v}_{\mathrm{PGK},x} - \hat{v}_{\mathrm{PK},x}\right), \quad \text{(B.11b)}$$

$$\frac{d}{d\tau_2}\left(\hat{\mathrm{PYR}}_x + \frac{l_r}{[\mathrm{PYR}]_r}l_x\right) = \epsilon^2\left\{\frac{A_r}{[\mathrm{PYR}]_r}\hat{v}_{\mathrm{PK},x} - 2\frac{A_r}{[\mathrm{PYR}]_r}\hat{v}_{\mathrm{Mito},x} + 2\frac{l_r}{[\mathrm{PYR}]_r}\hat{v}_{L,xy}\right\}, \quad \text{(B.11c)}$$

$$\frac{d\hat{\mathrm{PYR}}_x}{d\tau_2} = -\hat{v}_{\mathrm{LDH},x} + \epsilon^2\frac{A_r}{[\mathrm{PYR}]_r}\left\{\hat{v}_{\mathrm{PK},x} - 2\hat{v}_{\mathrm{Mito},x}\right\}, \quad \text{(B.11d)}$$

$$\frac{da_x}{d\tau_2} = \epsilon^2\left(-2\hat{v}_{\text{HK-PFK},x} + \hat{v}_{\mathrm{PGK},x} + \hat{v}_{\mathrm{PK},x} - \hat{v}_{A0,x} + 2n_{\mathrm{OP}}\hat{v}_{\mathrm{Mito},x}\right), \quad \text{(B.11e)}$$

$$5\frac{db_x}{d\tau_2} = \epsilon\left(2\hat{v}_{\text{HK-PFK},x} - \hat{v}_{\mathrm{PGK},x} - \hat{v}_{\mathrm{PK},x} + \hat{v}_{A0,x} - 2n_{\mathrm{OP}}\hat{v}_{\mathrm{Mito},x}\right). \quad \text{(B.11f)}$$

Regardless of whether the ratios $A_r/[\mathrm{PYR}]_r$ and $L_r/[\mathrm{PYR}]_r$ are taken to be $\mathcal{O}(1)$ or $\mathcal{O}(\epsilon^{-1})$, the left hand side of equations (B.11c) and (B.11d) remain $\mathcal{O}(1)$ while the parameter groupings $\epsilon^2 A_r/[\mathrm{PYR}]_r$ and $\epsilon^2 L_r/[\mathrm{PYR}]_r$ are $\mathcal{O}(\epsilon^{-1})$ or $\mathcal{O}(\epsilon^{-2})$.

We represent the solutions as power series in ϵ as described above, which gives the following leading order asymptotic approximation to the system (B.11) as $\epsilon \to 0$,

$$\frac{d\hat{\mathrm{GAP}}_{x,0}}{d\tau_2} = 0, \tag{B.12a}$$

$$\frac{d\hat{\mathrm{PEP}}_{x,0}}{d\tau_2} = 0, \tag{B.12b}$$

$$\frac{d}{d\tau_2}\left(\hat{\mathrm{PYR}}_{x,0} + \frac{L_r}{[\mathrm{PYR}]_r} l_{x,0}\right) = 0, \tag{B.12c}$$

$$\frac{d\hat{\mathrm{PYR}}_{x,0}}{d\tau_2} = -\hat{v}_{\mathrm{LDH},x,0}(\hat{\mathrm{PYR}}_{x,0}, l_{x,0}), \tag{B.12d}$$

$$\frac{da_{x,0}}{d\tau_2} = 0, \tag{B.12e}$$

$$\frac{db_{x,0}}{d\tau_2} = 0. \tag{B.12f}$$

The concentrations $\hat{\mathrm{PYR}}_{x,0}$ and $l_{x,0}$ reach a steady state before the quantity $\hat{v}_{\mathrm{LDH},x,0}(\hat{\mathrm{PYR}}_{x,0}, l_{x,0})$ can change sign (since equations (B.12c) and (B.12d) reveal that the rates of change $d\hat{\mathrm{PYR}}_{x,0}/d\tau_2$ and $dl_{x,0}/d\tau_2$ are $-\hat{v}_{\mathrm{LDH},x,0}$ and $([\mathrm{PYR}]_r/L_r)\hat{v}_{\mathrm{LDH},x,0}$ respectively). Therefore, $\hat{v}_{\mathrm{LDH},x,0}$, remains either positive or negative for all τ_2, giving the following solutions to (B.12) with the initial conditions as outlined above,

$$\hat{\mathrm{GAP}}_{x,0}(\tau_2) = \hat{\mathrm{GAP}}_{x,0}(0), \tag{B.13a}$$

$$\hat{\mathrm{PEP}}_{x,0}(\tau_2) = \hat{\mathrm{PEP}}_{x,0}(0), \tag{B.13b}$$

$$\hat{\mathrm{PYR}}_{x,0}(\tau_2) = \hat{\mathrm{PYR}}_{x,0}(0) + \frac{L_r}{[\mathrm{PYR}]_r}\left(l_{x,0}(0) - l_{x,0}(\tau_2)\right), \tag{B.13c}$$

$$l_{x,0}(\tau_2) = \frac{\beta_{\mathrm{LDH},x}}{\alpha_{\mathrm{LDH},x}} - \left(\frac{\beta_{\mathrm{LDH},x}}{\alpha_{\mathrm{LDH},x}} - l_{x,0}(0)\right)\exp\left(-\alpha_{\mathrm{LDH},x}\tau_2\right), \tag{B.13d}$$

$$a_{x,0}(\tau_2) = a_{x,0}(0), \tag{B.13e}$$

$$b_{x,0}(\tau_2) = b_{x,0}(0), \tag{B.13f}$$

where,

$$\alpha_{\mathrm{LDH},x} = \hat{k}^+_{\mathrm{LDH},x} + \hat{k}^-_{\mathrm{LDH},x}, \tag{B.14a}$$

$$\beta_{\mathrm{LDH},x} = \left(\frac{[\mathrm{PYR}]_r}{L_r}\hat{\mathrm{PYR}}_{x,0}(0) + l_{x,0}(0)\right)\hat{k}^+_{\mathrm{LDH},x}. \tag{B.14b}$$

According to the leading order approximation, the GAP, PEP, ATP and ADP concentrations evolve very slowly on this timescale and, as such, remain close to their initial values. In contrast, the pyruvate and lactate concentrations exhibit significant time evolution on this timescale due to the rapid reaction rate $\hat{v}_{\text{LDH},x}(\text{P}\hat{\text{Y}}\text{R}_x, l_x)$. We now consider the first order correction terms (i.e. the terms $\mathcal{O}(\epsilon)$) in the asymptotic approximation to the system (5.34) on the short timescale, which are,

$$\frac{d\text{G}\hat{\text{A}}\text{P}_{x,1}}{d\tau_2} = r_1\left(2\hat{v}_{\text{HK-PFK},x,0}(a_{x,0}) - \hat{v}_{\text{PGK},x,0}(\text{G}\hat{\text{A}}\text{P}_{x,0}, b_{x,0})\right), \tag{B.15a}$$

$$\frac{d\text{P}\hat{\text{E}}\text{P}_{x,1}}{d\tau_2} = r_2\left(\hat{v}_{\text{PGK},x,0}(\text{G}\hat{\text{A}}\text{P}_{x,0}, b_{x,0}) - \hat{v}_{\text{PK},x,0}(\text{P}\hat{\text{E}}\text{P}_{x,0}, b_{x,0})\right), \tag{B.15b}$$

$$\begin{aligned}\frac{d}{d\tau_2}\left(\text{P}\hat{\text{Y}}\text{R}_{x,1} + \frac{L_r}{[\text{PYR}]_r}l_{x,1}\right) = \epsilon\Bigg\{&\frac{A_r}{[\text{PYR}]_r}\hat{v}_{\text{PK},x,0}(\text{P}\hat{\text{E}}\text{P}_{x,0}, b_{x,0})\\ &-2\frac{A_r}{[\text{PYR}]_r}\hat{v}_{\text{Mito},x,0}(\text{P}\hat{\text{Y}}\text{R}_{x,0}, b_{x,0}) + 2\frac{L_r}{[\text{PYR}]_r}\hat{v}_{L,yx,0}(l_{x,0})\Bigg\},\end{aligned} \tag{B.15c}$$

$$\frac{d\text{P}\hat{\text{Y}}\text{R}_{x,1}}{d\tau_2} = -\hat{v}_{\text{LDH},x,1}(\text{P}\hat{\text{Y}}\text{R}_{x,1}, l_{x,1}) + \epsilon\frac{A_r}{[\text{PYR}]_r}\left(\hat{v}_{\text{PK},x,0} - 2\hat{v}_{\text{Mito},x,0}\right), \tag{B.15d}$$

$$\frac{da_{x,1}}{d\tau_2} = 0, \tag{B.15e}$$

$$\begin{aligned}5\frac{db_{x,1}}{d\tau_2} = 2\hat{v}_{\text{HK-PFK},x,0}(a_{x,0}) - \hat{v}_{\text{PGK},x,0}(\text{G}\hat{\text{A}}\text{P}_{x,0}, b_{x,0}) - \hat{v}_{\text{PK},x,0}(\text{P}\hat{\text{E}}\text{P}_{x,0}, b_{x,0})\\ +\hat{v}_{A0,x,0}(a_{x,0}) - 2n_{\text{OP}}\hat{v}_{\text{Mito},x,0}(\text{P}\hat{\text{Y}}\text{R}_{x,0}, b_{x,0}).\end{aligned} \tag{B.15f}$$

Although terms on the right hand sides of equations (B.15c) and (B.15d) are linear in ϵ, they are included because many of them are comparable to the terms $\mathcal{O}(1)$. The values of $\epsilon A_r/[\text{PYR}]_r\hat{v}_{\text{PK},x,0}$ and $2\epsilon A_r/[\text{PYR}]_r\hat{v}_{\text{Mito},x,0}$ are both approximately 0.1 in the glia, and in the neurons they are approximately 0.3 and 0.4 respectively. The terms $2\epsilon L_r/[\text{PYR}]_r\hat{v}^{\max}_{L,bg}$, $2\epsilon L_r/[\text{PYR}]_r\hat{v}^{\max}_{L,sg}$ and $2\epsilon L_r/[\text{PYR}]_r\hat{v}^{\max}_{L,sn}$ are approximately 0.03, 0.4 and 1.7 respectively.

Substituting the solutions from (B.13) into the reaction rates in equations (B.2)–(B.6) reveals that $\hat{v}_{\text{HK-PFK},x,0}$, $\hat{v}_{\text{PGK},x,0}$ and $\hat{v}_{\text{PK},x,0}$ are constant in time, whilst $\hat{v}_{\text{LDH},x,1}$ is linearly dependent on $\text{P}\hat{\text{Y}}\text{R}_{x,1}(\tau_2)$ and $l_{x,1}(\tau_2)$, and $\hat{v}_{\text{Mito},x,0}$ and $\hat{v}_{L,yx,0}$ have a Michaelis-Menten dependence on the time-varying quantities

$\hat{\text{PYR}}_{x,0}(\tau_2)$ and $l_{x,0}(\tau_2)$ respectively. The solutions to equations (B.15) subject to the initial conditions,

$$\hat{\text{GAP}}_{x,1}(0),\ \hat{\text{PEP}}_{x,1}(0),\ \hat{\text{PYR}}_{x,1}(0),\ l_{x,1}(0),\ a_{x,1}(0) = 0,$$

(i.e. with the correction terms initially equal to zero), are,

$$\hat{\text{GAP}}_{x,1}(\tau_2) = r_1\left(2\hat{v}_{\text{HK-PFK},x,0} - \hat{v}_{\text{PGK},x,0}\right)\tau_2, \tag{B.16a}$$

$$\hat{\text{PEP}}_{x,1}(\tau_2) = r_2\left(\hat{v}_{\text{PGK},x,0} - \hat{v}_{\text{PK},x,0}\right)\tau_2, \tag{B.16b}$$

$$\begin{aligned}\hat{\text{PYR}}_{x,1}(\tau_2) + \frac{L_r}{[\text{PYR}]_r}l_{x,1}(\tau_2) &= \epsilon\frac{A_r}{[\text{PYR}]_r}\hat{v}_{\text{PK},x,0}\tau_2 \\ &\quad -2\epsilon\frac{A_r}{[\text{PYR}]_r}\int\left(\hat{v}_{\text{Mito},x,0}(\hat{\text{PYR}}_{x,0}(\tau_2), b_{x,0})\right)\,d\tau_2 \\ &\quad +2\epsilon\frac{L_r}{[\text{PYR}]_r}\int\hat{v}_{L,yx,0}(l_{x,0}(\tau_2))\,d\tau_2,\end{aligned} \tag{B.16c}$$

$$\begin{aligned}\int\frac{d}{d\tau_2}\left[\left(\hat{v}_{\text{LDH},x}(\hat{\text{PYR}}_{x,1}l_{x,1}(\tau_2))\right) + \hat{v}_{\text{LDH},x}(\hat{\text{PYR}}_{x,1}l_{x,1}(\tau_2))\right]\,d\tau_2 \\ = \epsilon\hat{k}^+_{\text{LDH},x}\frac{A_r}{[\text{PYR}]_r}\int\hat{v}_{\text{PK},x,0}\,d\tau_2 \\ -2\epsilon\hat{k}^+_{\text{LDH},x}\frac{A_r}{[\text{PYR}]_r}\int\left(\hat{v}_{\text{Mito},x,0}(\hat{\text{PYR}}_{x,0}(\tau_2), b_{x,0})\right)\,d\tau_2 \\ +2\epsilon\hat{k}^-_{\text{LDH},x}\frac{L_r}{[\text{PYR}]_r}\int\hat{v}_{L,yx,0}(l_{x,0}(\tau_2))\,d\tau_2,\end{aligned} \tag{B.16d}$$

$$a_{x,1}(\tau_2) = 0, \tag{B.16e}$$

$$\begin{aligned}5b_{x,1}(\tau_2) &= \left(2\hat{v}_{\text{HK-PFK},x,0} - \hat{v}_{\text{PGK},x,0} - \hat{v}_{\text{PK},x,0} + \hat{v}_{A0,x,0}\right)\tau_2 \\ &\quad -2n_{\text{OP}}\int\hat{v}_{\text{Mito},x,0}(\hat{\text{PYR}}_{x,0}(\tau_2), b_{x,0})\,d\tau_2.\end{aligned} \tag{B.16f}$$

To deduce the orders of magnitude of integrals $\int\hat{v}_{\text{Mito},x,0}(\hat{\text{PYR}}_{x,0}(\tau_2), b_{x,0})\,d\tau_2$ and $\int\hat{v}_{L,yx,0}(l_{x,0}(\tau_2))\,d\tau_2$, without calculating them in full, we use the principle that, for general functions f and g of an independent variable s, if $\text{f}(s) \leq \text{g}(s) \forall s \in [a,b]$, where $a, b \in \mathbb{R}$, then $\int_a^b \text{f}(s)\,ds \leq \int_a^b \text{g}(s)\,ds$. The functions $\hat{v}_{\text{Mito},x,0}$ and $\hat{v}_{L,yx,0}$, are bounded above and below by constants as follows,

$$0 \leq \hat{v}_{\text{Mito},x,0} \leq \hat{v}^{\max}_{\text{Mito},x}, \qquad -\hat{v}^{\max}_{L,yx} \leq \hat{v}_{L,yx,0} \leq \hat{v}^{\max}_{L,yx},$$

since $\hat{v}^{\max}_{\text{Mito},x}$ has a saturating dependence on the pyruvate and ADP concentrations, and $\hat{v}_{L,yx,0}$ in both the forward and reverse directions has a saturating

dependence on the extracellular and intracellular lactate concentrations respectively. Hence,

$$0 \leq \int_0^{\tau_2} \hat{v}_{\text{Mito},x,0}\, ds \leq \hat{v}^{\max}_{\text{Mito},x}\tau_2,$$
$$-\hat{v}^{\max}_{L,yx}\tau_2 \leq \int_0^{\tau_2} \hat{v}_{L,yx,0}\, ds \leq \hat{v}^{\max}_{L,yx}\tau_2.$$

Since the leading order solutions for the GAP, PEP, ATP and ADP concentrations are approximately constant on this timescale, so are the reaction rates $\hat{v}_{\text{HK-PFK},x}$, $\hat{v}_{\text{PGK},x}$, $\hat{v}_{\text{PK},x}$ and $\hat{v}_{A0,x}$. Imposing the above constraints on the right hand side of equation (B.16d) gives,

$$\begin{aligned}
&\left| \int \left[\frac{d}{d\tau_2} \left(\hat{v}_{\text{LDH},x}(\hat{\text{PYR}}_{x,1} l_{x,1}(\tau_2)) \right) + \hat{v}_{\text{LDH},x}(\hat{\text{PYR}}_{x,1} l_{x,1}(\tau_2)) \right] d\tau_2 \right| \\
&\leq \epsilon \int \left(\hat{k}^{+}_{\text{LDH},x} \frac{A_r}{[\text{PYR}]_r} \hat{v}_{\text{PK},x,0} - 2\hat{k}^{+}_{\text{LDH},x} \frac{A_r}{[\text{PYR}]_r} \hat{v}^{\max}_{\text{Mito},x,0} \right. \\
&\qquad \left. + 2\epsilon \hat{k}^{-}_{\text{LDH},x} \frac{L_r}{[\text{PYR}]_r} \hat{v}^{\max}_{L,yx,0} \right) \tau_2 \, d\tau_2.
\end{aligned}$$

Using an integrating factor of $\exp(-\tau_2)$, we obtain,

$$\begin{aligned}
&\left| v_{\text{LDH},x}(\hat{\text{PYR}}_{x,1} l_{x,1}(\tau_2)) \right| \leq \epsilon \left(\hat{k}^{+}_{\text{LDH},x} \frac{A_r}{[\text{PYR}]_r} \hat{v}_{\text{PK},x,0} \right. \\
&\qquad \left. - 2\hat{k}^{+}_{\text{LDH},x} \frac{A_r}{[\text{PYR}]_r} \hat{v}^{\max}_{\text{Mito},x,0} + 2\epsilon \hat{k}^{-}_{\text{LDH},x} \frac{L_r}{[\text{PYR}]_r} \hat{v}^{\max}_{L,yx,0} \right) (\tau_2 - 1).
\end{aligned}$$

Combining the constraints derived above, the correction terms $\epsilon\hat{\text{GAP}}_{x,1}(\tau_2)$ and $\epsilon\hat{\text{PEP}}_{x,1}(\tau_2)$ increase linearly with τ_2, while the maximum possible rate of increase of $\epsilon\hat{\text{PYR}}_{x,1}(\tau_2)$, $\epsilon l_{x,1}(\tau_2)$, $\epsilon a_{x,1}(\tau_2)$ is linearly with τ_2, and $\epsilon b_{x,1}(\tau_2)$ remains at zero for all time. Thus all correction terms remain at $\mathcal{O}(\epsilon)$ until $\tau_2 = \mathcal{O}(\epsilon^{-1})$ (and some remain $\mathcal{O}(\epsilon)$ for longer times), meaning that the leading order approximation is accurate for $\tau_2 = \mathcal{O}(1)$, or $\tau = \mathcal{O}(\epsilon^2)$.

When τ_2 becomes $\mathcal{O}\left(\epsilon^{-1}\right)$ or greater, the short timescale approximation given above becomes inaccurate, and a new approximation to the system is derived on the *intermediate* timescale, for which $\tau_1 = \epsilon^{-1}\tau = \epsilon\tau_2$. Denoting the solutions using power series in ϵ as before, the leading order asymptotic

approximation to the system in (5.34) as $\epsilon \to 0$ on the intermediate timescale is,

$$\frac{d\hat{\text{GAP}}_{x,0}}{d\tau_1} = r_1 \left(2\hat{v}_{\text{HK-PFK},x,0}(a_{x,0}) - \hat{v}_{\text{PGK},x,0}(\hat{\text{GAP}}_{x,0}, b_{x,0})\right), \tag{B.17a}$$

$$\frac{d\hat{\text{PEP}}_{x,0}}{d\tau_1} = r_2 \left(\hat{v}_{\text{PGK},x,0}(\hat{\text{GAP}}_{x,0}, b_{x,0}) - \hat{v}_{\text{PK},x,0}(\hat{\text{PEP}}_{x,0}, b_{x,0})\right), \tag{B.17b}$$

$$\begin{aligned}\frac{d}{d\tau_1}\left(\hat{\text{PYR}}_{x,0} + \frac{L_r}{[\text{PYR}]_r} l_{x,0}\right) = \epsilon \Bigg(&\frac{A_r}{[\text{PYR}]_r}\hat{v}_{\text{PK},x,0}(\hat{\text{PEP}}_{x,0}, b_{x,0}) \\ &-2\frac{A_r}{[\text{PYR}]_r}\hat{v}_{\text{Mito},x,0}(\hat{\text{PYR}}_{x,0}, b_{x,0}) + 2\frac{L_r}{[\text{PYR}]_r}\hat{v}_{L,yx,0}(l_{x,0})\Bigg),\end{aligned} \tag{B.17c}$$

$$\hat{v}_{\text{LDH},x,0}(\hat{\text{PYR}}_{x,0}, l_{x,0}) = 0, \tag{B.17d}$$

$$\frac{da_{x,0}}{d\tau_1} = 0, \tag{B.17e}$$

$$\begin{aligned}5\frac{db_{x,0}}{d\tau_1} = 2\hat{v}_{\text{HK-PFK},x,0}(a_{x,0}) - \hat{v}_{\text{PGK},x,0}(\hat{\text{GAP}}_{x,0}, b_{x,0}) - \hat{v}_{\text{PK},x,0}(\hat{\text{PEP}}_{x,0}, b_{x,0}) \\ +\hat{v}_{A0,x,0}(a_{x,0}) - 2n_{\text{OP}}\hat{v}_{\text{Mito},x,0}(\hat{\text{PYR}}_{x,0}, b_{x,0})\end{aligned}. \tag{B.17f}$$

As discussed earlier, the terms on the right hand sides of equation (B.17c) are included since they are not negligible compared to the $\mathcal{O}(1)$ terms.

For an accurate asymptotic approximation, the leading order solutions on the short and intermediate timescales are matched at the time at which they overlap. To this end, we set the initial conditions for the leading order solutions on the intermediate timescale to the values of the leading order solutions at the short timescale as $\tau_2 \to \infty$. As $\tau_2 \to \infty$ the solutions $\hat{\text{GAP}}_{x,0}$, $\hat{\text{PEP}}_{x,0}$, $a_{x,0}$, $b_{x,0}$, $l_{x,0}$ and $\hat{\text{PYR}}_{x,0}$ in equations (B.13) tend to $\hat{\text{GAP}}_{x,0}(0)$, $\hat{\text{PEP}}_{x,0}(0)$, $a_{x,0}(0)$, $b_{x,0}(0)$, $\beta_{\text{LDH},x}/\alpha_{\text{LDH},x}$ and $\hat{\text{PYR}}_{x,0}(0) + (L_r/[\text{PYR}]_r)(l_{x,0}(0) - \beta_{\text{LDH},x}/\alpha_{\text{LDH},x})$ respectively. Therefore, we set these as the initial conditions for the system (B.12). The solutions to equations (B.17d) and (B.17e) are,

$$\hat{\text{PYR}}_{x,0}(\tau_1) = \frac{\hat{k}^-_{\text{LDH},x}}{\hat{k}^+_{\text{LDH},x}} l_{x,0}(\tau_1), \tag{B.18a}$$

$$a_{x,0} = a_{x,0}(0), \tag{B.18b}$$

which reduces the system to,

$$\frac{d\hat{\text{GAP}}_{x,0}}{d\tau_1} = r_1 \left(2\hat{v}_{\text{HK-PFK},x,0}(a_{x,0}) - \hat{v}_{\text{PGK},x,0}(\hat{\text{GAP}}_{x,0}, b_{x,0})\right), \tag{B.19a}$$

$$\frac{d\hat{\mathrm{PEP}}_{x,0}}{d\tau_1} = r_2\left(\hat{v}_{\mathrm{PGK},x,0}(\hat{\mathrm{GAP}}_{x,0}, b_{x,0}) - \hat{v}_{\mathrm{PK},x,0}(\hat{\mathrm{PEP}}_{x,0}, b_{x,0})\right), \tag{B.19b}$$

$$\frac{dl_{x,0}}{d\tau_1} = \epsilon\left(\frac{[\mathrm{PYR}]_r}{L_r}\frac{\hat{k}^-_{\mathrm{LDH},x}}{\hat{k}^+_{\mathrm{LDH},x}} + 1\right)^{-1}\left(\frac{A_r}{[\mathrm{PYR}]_r}\hat{v}_{\mathrm{PK},x,0}(\hat{\mathrm{PEP}}_{x,0}, b_{x,0})\right. \tag{B.19c}$$
$$\left. -2\frac{A_r}{[\mathrm{PYR}]_r}\hat{v}_{\mathrm{Mito},x,0}(\hat{\mathrm{PYR}}_{x,0}, b_{x,0}) + 2\frac{L_r}{[\mathrm{PYR}]_r}\hat{v}_{L,yx,0}(\hat{\mathrm{PYR}}_{x,0}, l_{x,0})\right),$$

$$5\frac{db_{x,0}}{d\tau_1} = 2\hat{v}_{\text{HK-PFK},x,0}(a_{x,0}) - \hat{v}_{\mathrm{PGK},x,0}(\hat{\mathrm{GAP}}_{x,0}, b_{x,0}) - \hat{v}_{\mathrm{PK},x,0}(\hat{\mathrm{PEP}}_{x,0}, b_{x,0})$$
$$+\hat{v}_{A0,x,0}(a_{x,0}) - 2n_{\mathrm{OP}}\hat{v}_{\mathrm{Mito},x,0}(\hat{\mathrm{PYR}}_{x,0}, b_{x,0}), \tag{B.19d}$$

All reaction rates in these equations are nonlinear with the exception of $\hat{v}_{\text{HK-PFK},x,0}(a_{x,0})$ and $\hat{v}_{A0,x,0}(a_{x,0})$ since the ATP concentration is constant (see (B.18)). The pyruvate concentration is determined by the time evolution of the lactate concentration since it remains proportional to it. The numerical solutions of equations (B.19) subject to the initial conditions outlined above, and (B.18) are shown in Figure 5.5. The correction terms are as follows,

$$\frac{d\hat{\mathrm{GAP}}_{x,1}}{d\tau_1} = r_1\left(2\hat{v}_{\text{HK-PFK},x,1}(a_{x,1}, a_{x,0})\right. \tag{B.20a}$$
$$\left. -\hat{v}_{\mathrm{PGK},x,1}(\hat{\mathrm{GAP}}_{x,1}, b_{x,1}, \hat{\mathrm{GAP}}_{x,0}, b_{x,0})\right),$$

$$\frac{d\hat{\mathrm{PEP}}_{x,1}}{d\tau_1} = r_2\left(\hat{v}_{\mathrm{PGK},x,1}(\hat{\mathrm{GAP}}_{x,1}, b_{x,1}, \hat{\mathrm{GAP}}_{x,0}, b_{x,0})\right. \tag{B.20b}$$
$$\left. -\hat{v}_{\mathrm{PK},x,1}(\hat{\mathrm{PEP}}_{x,1}, b_{x,1}, \hat{\mathrm{PEP}}_{x,0}, b_{x,0})\right),$$

$$\frac{d}{d\tau_1}\left(\hat{\mathrm{PYR}}_{x,1} + \frac{L_r}{[\mathrm{PYR}]_r}l_{x,1}\right) = \frac{A_r}{[\mathrm{PYR}]_r}\epsilon\left(\hat{v}_{\mathrm{PK},x,1}(\hat{\mathrm{PEP}}_{x,1}, b_{x,1}, \hat{\mathrm{PEP}}_{x,0}, b_{x,0})\right.$$
$$\left. -2\hat{v}_{\mathrm{Mito},x,1}(\hat{\mathrm{PYR}}_{x,1}, b_{x,1}, \hat{\mathrm{PYR}}_{x,0}, b_{x,0})\right) + 2\frac{L_r}{[\mathrm{PYR}]_r}\hat{v}_{L,yx,1}(l_{x,1}, l_{x,0}), \tag{B.20c}$$

$$\frac{d\hat{\mathrm{PYR}}_{x,0}}{d\tau_1} = -2\hat{v}_{\mathrm{LDH},x,1}(\hat{\mathrm{PYR}}_{x,1}, l_{x,1})$$
$$+\epsilon\frac{A_r}{[\mathrm{PYR}]_r}\left(\hat{v}_{\mathrm{PK},x,0}(\hat{\mathrm{PEP}}_{x,1}, b_{x,1}, \hat{\mathrm{PEP}}_{x,0}, b_{x,0})\right. \tag{B.20d}$$
$$\left. -2\hat{v}_{\mathrm{Mito},x,0}(\hat{\mathrm{PYR}}_{x,1}, b_{x,1}, \hat{\mathrm{PYR}}_{x,0}, b_{x,0})\right),$$

$$\frac{da_{x,1}}{d\tau_1} = -2\hat{v}_{\text{HK-PFK},x,0}(a_{x,0}) + \hat{v}_{\mathrm{PGK},x,0}(\hat{\mathrm{GAP}}_{x,0}, b_{x,0}) + \hat{v}_{\mathrm{PK},x,0}(\hat{\mathrm{PEP}}_{x,0}, b_{x,0})$$
$$-\hat{v}_{A0,x,0}(a_{x,0}) + 2n_{\mathrm{OP}}\hat{v}_{\mathrm{Mito},x,0}(\hat{\mathrm{PYR}}_{x,0}, b_{x,0}), \tag{B.20e}$$

$$5\frac{db_{x,1}}{d\tau_1} = 2\hat{v}_{\text{HK-PFK},x,1}(a_{x,0}, a_{x,1}) - \hat{v}_{\text{PGK},x,1}(\hat{\text{GAP}}_{x,1}, b_{x,1}, \hat{\text{GAP}}_{x,0}, b_{x,0}) - \hat{v}_{\text{PK},x,1}(\hat{\text{PEP}}_{x,1}, b_{x,1}, \hat{\text{PEP}}_{x,0}, b_{x,0}) + \hat{v}_{A0,x,1}(a_{x,0}) - 2n_{\text{OP}}\hat{v}_{\text{Mito},x,1}(\hat{\text{PYR}}_{x,1}, b_{x,1}, \hat{\text{PYR}}_{x,0}, b_{x,0}). \tag{B.20f}$$

Comparing the system above with the leading order equations in (B.17), we find that $da_{x,1}/d\tau_1 = -5db_{x,0}/d\tau_1$, to which the solution, subject to the initial condition $a_{x,1}(0) = 0$, is,

$$a_{x,1}(\tau_1) = -5(b_{x,0}(\tau_1) - b_{x,0}(0)),$$

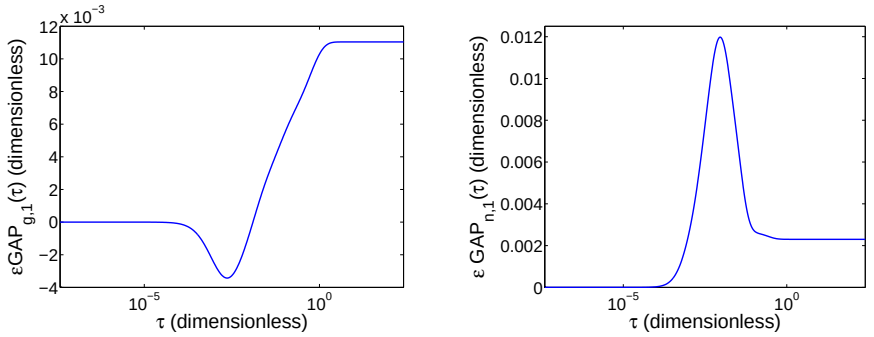
revealing that, since $b_{x,0}(\tau_1) = \mathcal{O}(1)$ on this timescale, $a_{x,1}(\tau_1)$ is also $\mathcal{O}(1)$. Substituting $\hat{\text{PYR}}_{x,0}(\tau_1)$ from equation (B.18) into equation (B.20d), and substituting the ODE for the lactate concentration at leading order (see equation (B.19c)) gives,

$$\hat{v}_{\text{LDH},x,1}(\hat{\text{PYR}}_{x,1}, l_{x,1}) = \epsilon \left(\frac{[\text{PYR}]_r}{L_r} \frac{\hat{k}^-_{\text{LDH},x}}{\hat{k}^+_{\text{LDH},x}} + 1 \right)^{-1} \left(\frac{A_r}{[\text{PYR}]_r} \hat{v}_{\text{PK},x,0}(\hat{\text{PEP}}_{x,0}, b_{x,0}) - 2\frac{A_r}{[\text{PYR}]_r} \hat{v}_{\text{Mito},x,0}(\hat{\text{PYR}}_{x,0}, b_{x,0}) - 2\frac{\hat{k}^-_{\text{LDH},x}}{\hat{k}^+_{\text{LDH},x}} \hat{v}_{L,yx,0}(l_{x,0}) \right),$$

giving $\hat{\text{PYR}}_{x,1}(\tau_1)$ in terms of $l_{x,1}(\tau_1)$. Since the terms on the right hand side of this equation are $\mathcal{O}(1)$, $\hat{\text{PYR}}_{x,1}(\tau_1) = \mathcal{O}(1)$ provided that $l_{x,1}(\tau_1) = \mathcal{O}(1)$. Solving the remaining ODEs, (B.20a)–(B.20c) and (B.20f) numerically gives the results in Figure B.1. Figure B.1 shows that the correction terms $\epsilon\hat{\text{GAP}}_{x,1}(\tau_1)$, $\epsilon\hat{\text{PEP}}_{x,1}(\tau_1)$ and $\epsilon l_{x,1}(\tau_1)$ for $x \in \{g, n\}$ are $\mathcal{O}(\epsilon)$ for all time, while the correction terms $\epsilon b_{x,1}(\tau_1)$ are $\mathcal{O}(\epsilon^2)$ for all time. Hence, all correction terms remain $\mathcal{O}(\epsilon)$ on the timescale $\tau_1 = \mathcal{O}(1)$.

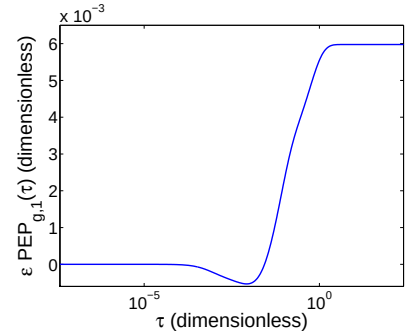
These correction terms grow to $\mathcal{O}(1)$ and must be accounted for when $\tau_1 = \mathcal{O}(\epsilon^{-1})$, meaning that a different asymptotic approximation is required on the *long* timescale for which $\tau = \mathcal{O}(1)$. On this timescale, the leading order asymptotic approximation to the system in (5.34) as $\epsilon \to 0$ is,

$$r_1 \left(2\hat{v}_{\text{HK-PFK},x,0}(a_{x,0}) - \hat{v}_{\text{PGK},x,0}(\hat{\text{GAP}}_{x,0}, b_{x,0}) \right) = 0, \tag{B.21a}$$

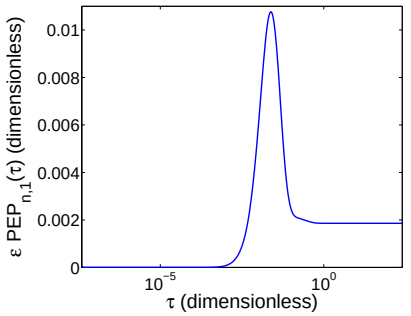


(a) $\epsilon \hat{\text{GAP}}_{g,1}(\tau)$

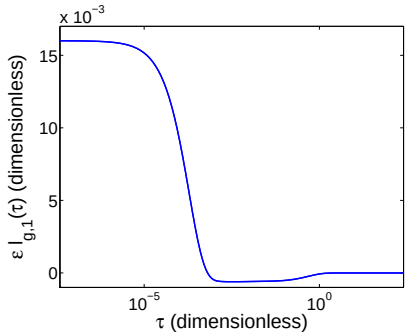
(b) $\epsilon \hat{\text{GAP}}_{n,1}(\tau)$



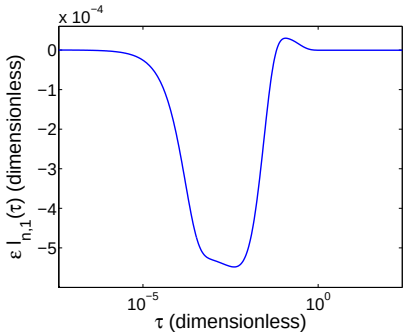
(c) $\epsilon \hat{\text{PEP}}_{g,1}(\tau)$



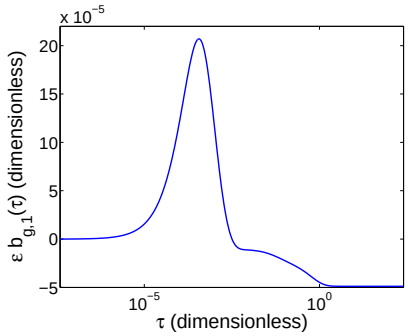
(d) $\epsilon \hat{\text{PEP}}_{n,1}(\tau)$



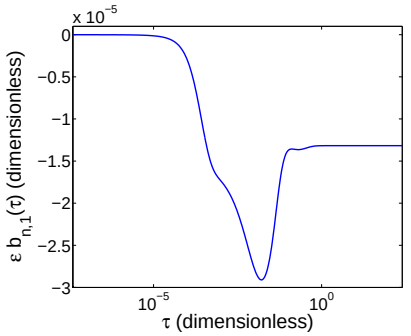
(e) $\epsilon l_{g,1}(\tau)$



(f) $\epsilon l_{n,1}(\tau)$



(g) $\epsilon b_{g,1}(\tau)$



(h) $\epsilon b_{n,1}(\tau)$

Figure B.1.: Time evolution of the correction terms in the asymptotic approximation to the AC submodel (see Table 5.2) on the intermediate timescale $\tau = \mathcal{O}(\epsilon)$. For parameter values see Tables 4.1–4.2.

$$r_2\left(\hat{v}_{\mathrm{PGK},x,0}(\hat{\mathrm{GAP}}_{x,0},b_{x,0})-\hat{v}_{\mathrm{PK},x,0}(\hat{\mathrm{PEP}}_{x,0},b_{x,0})\right)=0, \tag{B.21b}$$

$$\begin{aligned}\frac{d}{d\tau}\left(\hat{\mathrm{PYR}}_{x,0}+\frac{L_r}{[\mathrm{PYR}]_r}l_{x,0}\right)&=\frac{A_r}{[\mathrm{PYR}]_r}\hat{v}_{\mathrm{PK},x,0}(\hat{\mathrm{PEP}}_{x,0},b_{x,0})\\&\quad-2\frac{A_r}{[\mathrm{PYR}]_r}\hat{v}_{\mathrm{Mito},x,0}(\hat{\mathrm{PYR}}_{x,0},b_{x,0})+2\frac{L_r}{[\mathrm{PYR}]_r}\hat{v}_{L,yx,0}(l_{x,0}),\end{aligned} \tag{B.21c}$$

$$\hat{v}_{\mathrm{LDH},x,0}(\hat{\mathrm{PYR}}_{x,0},l_{x,0})=0, \tag{B.21d}$$

$$\begin{aligned}\frac{da_{x,0}}{d\tau}=-2\hat{v}_{\text{HK-PFK},x,0}(a_{x,0})+\hat{v}_{\mathrm{PGK},x,0}(\hat{\mathrm{GAP}}_{x,0},b_{x,0})+\hat{v}_{\mathrm{PK},x,0}(\hat{\mathrm{PEP}}_{x,0},b_{x,0})\\-\hat{v}_{A0,x,0}(a_{x,0}),+2n_{\mathrm{OP}}\hat{v}_{\mathrm{Mito},x,0}(\hat{\mathrm{PYR}}_{x,0},b_{x,0}),\end{aligned} \tag{B.21e}$$

$$\begin{aligned}2\hat{v}_{\text{HK-PFK},x,0}(a_{x,0})-\hat{v}_{\mathrm{PGK},x,0}(\hat{\mathrm{GAP}}_{x,0},b_{x,0})-\hat{v}_{\mathrm{PK},x,0}(\hat{\mathrm{PEP}}_{x,0},b_{x,0})\\+\hat{v}_{A0,x,0}(a_{x,0}),-2n_{\mathrm{OP}}\hat{v}_{\mathrm{Mito},x,0}(\hat{\mathrm{PYR}}_{x,0},b_{x,0})=0.\end{aligned} \tag{B.21f}$$

We note that equation (B.21f) determines the ADP concentration, not the ATP concentration, as the two evolve on different timescales. The solutions to equations (B.21a)–(B.21c) and (B.21f) are,

$$\hat{\mathrm{GAP}}_x=2\frac{\hat{k}_{\text{HK-PFK},x}}{\hat{k}_{\mathrm{PGK},x}}\frac{a_x}{b_x}\frac{1}{a_x^4+\hat{K}^4_{\text{HK-PFK},A,x}}, \tag{B.22a}$$

$$\hat{\mathrm{PEP}}_x=\frac{A_r}{[\mathrm{PYR}]_r}\frac{\hat{k}_{\mathrm{PGK},x}}{\hat{k}_{\mathrm{PK},x}}\hat{\mathrm{GAP}}_x, \tag{B.22b}$$

$$\hat{\mathrm{PYR}}_x=\frac{\hat{k}^-_{\mathrm{LDH},x}}{\hat{k}^+_{\mathrm{LDH},x}}l_x, \tag{B.22c}$$

$$b_{x,0}(\tau)=\frac{\hat{K}_{\mathrm{Mito},B,x}}{\frac{\hat{v}^{\max}_{\mathrm{Mito},x}}{2n_{\mathrm{OP}}}\left(-2\hat{v}_{\text{HK-PFK},x}+\hat{v}_{A0,x}\right)\left(\frac{\hat{k}^+_{\mathrm{LDH},x}\hat{K}_{\mathrm{Mito,PYR},x}}{\hat{k}^-_{\mathrm{LDH},x}l_{x,0}(\tau)}+1\right)^{-1}-1}. \tag{B.22d}$$

and incorporating the above results into equations (5.34) yields the following governing ODEs for $\tau=\mathcal{O}(1)$,

$$\begin{aligned}\frac{dl_{x,0}}{d\tau}&=\left(\frac{\hat{k}^-_{\mathrm{LDH},x}}{\hat{k}^+_{\mathrm{LDH},x}}+\frac{L_r}{[\mathrm{PYR}]_r}\right)^{-1}\left(2\frac{A_r}{[\mathrm{PYR}]_r}\hat{v}_{\text{HK-PFK},x,0}(a_{x,0})\right.\\&\quad\left.-2\frac{A_r}{[\mathrm{PYR}]_r}\hat{v}_{\mathrm{Mito},x,0}(l_{x,0},b_{x,0})+2\frac{L_r}{[\mathrm{PYR}]_r}\hat{v}_{L,yx,0}(l_{x,0})\right),\\\frac{da_{x,0}}{d\tau}&=2\hat{v}_{\text{HK-PFK},x,0}(a_{x,0})-\hat{v}_{A0,x,0}(a_{x,0})+2n_{\mathrm{OP}}\hat{v}_{\mathrm{Mito},x,0}(l_{x,0},b_{x,0}),\end{aligned}$$

where,

$$\hat{v}_{\text{Mito},x,0}(l_{x,0}, b_{x,0}) = \text{M}\left(l_{x,0}; \hat{v}^{\max}_{\text{Mito},x}, \frac{\hat{k}^{+}_{\text{LDH},x}}{\hat{k}^{-}_{\text{LDH},x}}\hat{K}_{\text{Mito,PYR},x}\right)\text{M}\left(b_{x,0}; 1, \hat{K}_{\text{Mito},B,x}\right),$$

obtained by substituting the expression in (B.22c) for the pyruvate concentration into equation (B.7). We match the asymptotic approximation on the long timescale with that on the intermediate timescale in a similar way to before, by setting the initial conditions (i.e. the solutions as $\tau \to 0$) for the system (5.39) equal to the solutions to the ODEs in (B.21) as $\tau_1 \to \infty$. Reaction rates $\hat{v}_{\text{HK-PFK},x,0}$, $\hat{v}_{LAC,yx,0}$ and $v_{A0,x,0}$ are given by the equations in (B.1).

To leading order, the concentrations of GAP, PEP, pyruvate and ADP are quasisteady: following a change in the lactate and ATP concentrations, the remaining metabolites equilibrate very rapidly. Therefore, all concentrations in the system are determined by the time evolution of the lactate and ATP levels. The numerical solutions to the leading order equations are shown in Figure 5.5. We note that the lactate concentration evolves on all three timescales, with the dynamics on the short timescale resulting from the rapid reaction rate $\hat{v}_{\text{LDH},x}(\text{P}\hat{\text{Y}}\text{R}_x, l_x)$, and the dynamics on the intermediate and long timescales brought about by the reaction rate $\hat{v}_{\text{PK},x}(\text{P}\hat{\text{E}}\text{P}_x, b_x)$, lactate transport and oxidative metabolism. The correction terms on the $\tau = \mathcal{O}(1)$ timescale are,

$$\frac{d\text{G}\hat{\text{A}}\text{P}_{x,0}}{d\tau} = r_1\left(2\hat{v}_{\text{HK-PFK},x,1}(a_{x,1}, a_{x,0}) - \hat{v}_{\text{PGK},x,1}(\text{G}\hat{\text{A}}\text{P}_{x,1}, b_{x,1}, \text{G}\hat{\text{A}}\text{P}_{x,0}, b_{x,0})\right), \tag{B.23a}$$

$$\begin{aligned}\frac{d\text{P}\hat{\text{E}}\text{P}_{x,0}}{d\tau} = r_2\big(&\hat{v}_{\text{PGK},x,1}(\text{G}\hat{\text{A}}\text{P}_{x,1}, b_{x,1}, \text{G}\hat{\text{A}}\text{P}_{x,0}, b_{x,0}) \\ &-\hat{v}_{\text{PK},x,1}(\text{P}\hat{\text{E}}\text{P}_{x,1}, b_{x,1}, \text{P}\hat{\text{E}}\text{P}_{x,0}, b_{x,0})\big),\end{aligned} \tag{B.23b}$$

$$\begin{aligned}\frac{d}{d\tau}\left(\text{P}\hat{\text{Y}}\text{R}_{x,1} + \frac{L_r}{[\text{PYR}]_r}l_{x,1}\right) = \frac{A_r}{[\text{PYR}]_r}\big(&\hat{v}_{\text{PK},x,1}(\text{P}\hat{\text{E}}\text{P}_{x,1}, b_{x,1}, \text{P}\hat{\text{E}}\text{P}_{x,0}, b_{x,0}) \\ &-2\hat{v}_{\text{Mito},x,1}(\text{P}\hat{\text{Y}}\text{R}_{x,1}, b_{x,1}, \text{P}\hat{\text{Y}}\text{R}_{x,0}, b_{x,0})\big) + 2\frac{L_r}{[\text{PYR}]_r}\hat{v}_{L,yx,1}(l_{x,1}, l_{x,0}),\end{aligned} \tag{B.23c}$$

$$\begin{aligned}&-2\hat{v}_{\text{LDH},x,1}(\text{P}\hat{\text{Y}}\text{R}_{x,1}, l_{x,1}, \text{P}\hat{\text{Y}}\text{R}_{x,0}, l_{x,0}) + \epsilon\left\{\frac{A_r}{[\text{PYR}]_r}\hat{v}_{\text{PK},x,0}(\text{P}\hat{\text{E}}\text{P}_{x,0}, b_{x,0})\right. \\ &\left.-2\frac{A_r}{[\text{PYR}]_r}\hat{v}_{\text{Mito},x,0}(\text{P}\hat{\text{Y}}\text{R}_{x,0}, b_{x,0}) - 2\frac{L_r}{[\text{PYR}]_r}\hat{v}_{L,yx,0}(l_{x,1}, l_{x,0})\right\} = 0,\end{aligned} \tag{B.23d}$$

$$\frac{da_{x,1}}{d\tau} = -2\epsilon\hat{v}_{\text{HK-PFK},x,1}(a_{x,1}, a_{x,0}) + \hat{v}_{\text{PGK},x,1}(\text{G}\hat{\text{A}}\text{P}_{x,1}, b_{x,1}, \text{G}\hat{\text{A}}\text{P}_{x,0}, b_{x,0}) + \hat{v}_{\text{PK},x,1}(\text{P}\hat{\text{E}}\text{P}_{x,1}, b_{x,1}, \text{P}\hat{\text{E}}\text{P}_{x,0}, b_{x,0}) - \hat{v}_{A0,x,1}(a_{x,1}, a_{x,0}) + 2n_{\text{OP}}\epsilon\hat{v}_{\text{Mito},x,1}(\text{P}\hat{\text{Y}}\text{R}_{x,1}, b_{x,1}, \text{P}\hat{\text{Y}}\text{R}_{x,0}, b_{x,0}), \tag{B.23e}$$

$$5\frac{db_{x,0}}{d\tau} = 2\epsilon\hat{v}_{\text{HK-PFK},x,1}(a_{x,1}, a_{x,0}) - \hat{v}_{\text{PGK},x,1}(\text{G}\hat{\text{A}}\text{P}_{x,1}, b_{x,1}, \text{G}\hat{\text{A}}\text{P}_{x,0}, b_{x,0}) - \hat{v}_{\text{PK},x,1}(\text{P}\hat{\text{E}}\text{P}_{x,1}, b_{x,1}, \text{P}\hat{\text{E}}\text{P}_{x,0}, b_{x,0}) + \hat{v}_{A0,x,1}(a_{x,1}, a_{x,0}) - 2n_{\text{OP}}\hat{v}_{\text{Mito},x,1}(\text{P}\hat{\text{Y}}\text{R}_{x,1}, b_{x,1}, \text{P}\hat{\text{Y}}\text{R}_{x,0}, b_{x,0}). \tag{B.23f}$$

Since the terms on the left hand sides of equations are $d\text{G}\hat{\text{A}}\text{P}_{x,0}/d\tau$, $d\text{P}\hat{\text{E}}\text{P}_{x,0}/d\tau$, $db_{x,0}/d\tau$ which are $\mathcal{O}(1)$, we have that, if $2\hat{v}_{\text{HK-PFK},x,1} = \mathcal{O}(1)$, then so is $\hat{v}_{\text{PGK},x,1}$, and therefore $\hat{v}_{\text{PK},x,1} = \mathcal{O}(1)$ also. From earlier, $\hat{v}_{A0,x,1} = 0$, meaning that, provided that $2\hat{v}_{\text{HK-PFK},x,1}$, $\hat{v}_{\text{PGK},x,1}$, $\hat{v}_{\text{PK},x,1} = \mathcal{O}(1)$, then so is $2n_{\text{OP}}\hat{v}_{\text{Mito},x,1}$. Furthermore, as stated earlier, the quantities $\epsilon A_r/[\text{PYR}]_r$ and $\epsilon L_r/[\text{PYR}]_r$ are $\mathcal{O}(1)$, as are reaction rates $\hat{v}_{\text{PK},x,0}$, $2\hat{v}_{\text{Mito},x,0}$ and $\hat{v}_{L,yx,0}$. Hence, $2\hat{v}_{\text{LDH},x,1} = \mathcal{O}(1)$, meaning that, if $l_{x,1}(\tau) = \mathcal{O}(1)$, then so is $\text{P}\hat{\text{Y}}\text{R}_{x,1}(\tau)$, and vice-versa.

From equations (B.23e) and (B.23f), $da_{x,1}/d\tau = -5db_{x,0}/d\tau$. Integrating this result subject to the initial condition $a_{x,1}(0) = 0$ gives,

$$a_{x,1}(\tau) = -5(b_{x,0}(\tau) - b_{x,0}(0)) = \mathcal{O}(1).$$

Having found that $a_{x,1}(\tau) = \mathcal{O}(1)$, it becomes obvious that $2\hat{v}_{\text{HK-PFK},x,1}$, and therefore $\hat{v}_{\text{PGK},x,1}$, $\hat{v}_{\text{PK},x,1}$ and $2n_{\text{OP}}\hat{v}_{\text{Mito},x,1}$, are $\mathcal{O}(1)$. From this we deduce that $\text{G}\hat{\text{A}}\text{P}_{x,1}(\tau)$, $\text{P}\hat{\text{E}}\text{P}_{x,1}(\tau)$, $\text{P}\hat{\text{Y}}\text{R}_{x,1}(\tau)$, $b_{x,1}(\tau) = \mathcal{O}(1)$, and then from our argument above, $l_{x,1}(\tau) = \mathcal{O}(1)$ also. The correction terms are therefore negligible compared to the leading order terms and this asymptotic approximation is accurate on the timescale for which $\tau = \mathcal{O}(1)$.

C

CONDITIONS FOR AN OPTIMUM MATCH BETWEEN THE AC AND IR SUBMODEL RESULTS

We discuss, in §5.3.3, how the parameter values in the IR and Simplified AC submodels can be tuned to find the best possible quantitative match between the submodel results. This can be achieved using the method in this appendix.

In the neurons, it is possible to find a value of $\bar{A}_n$ such that the steady state lactate and ATP concentrations in the two submodels match closely for a given glucose input G^*, during either resting conditions or neuronal stimulation. Using the same technique in the glial cells results in matching steady state ATP levels or lactate levels at the steady state, but not both, due to the different stoichiometries in the submodels. Choosing values of $\bar{A}_g$ and $\bar{A}_n$, to be the steady state ATP concentrations during neuronal stimulation for $G^* = 3\,\text{mM}$, in the glial and neuronal cells, respectively we obtain the results in Figure C.1.

Redefining the stoichiometry in the IR submodel such that glial oxidative metabolism produces 30 ATP molecules from each pair of lactate molecules, the glial lactate concentrations at the steady state also match more closely, as shown in Figure C.2. Now the value of $\bar{A}_n$ is set between the steady state neuronal ATP concentrations of the Simplified AC submodel during resting conditions and neuronal stimulation for $G^* = 3\,\text{mM}$, which provides the optimum match between the submodel results.

We further improve the quantitative agreement between the submodel results by using different parameter values from those originally chosen by Aubert and Costalat [1], such that the reaction rates for glycolysis and oxidative metabolism in both submodels exhibit approximately the same linear dependence on ADP levels for concentrations around specific values. In what follows, we explain how the alternative parameter values are derived.

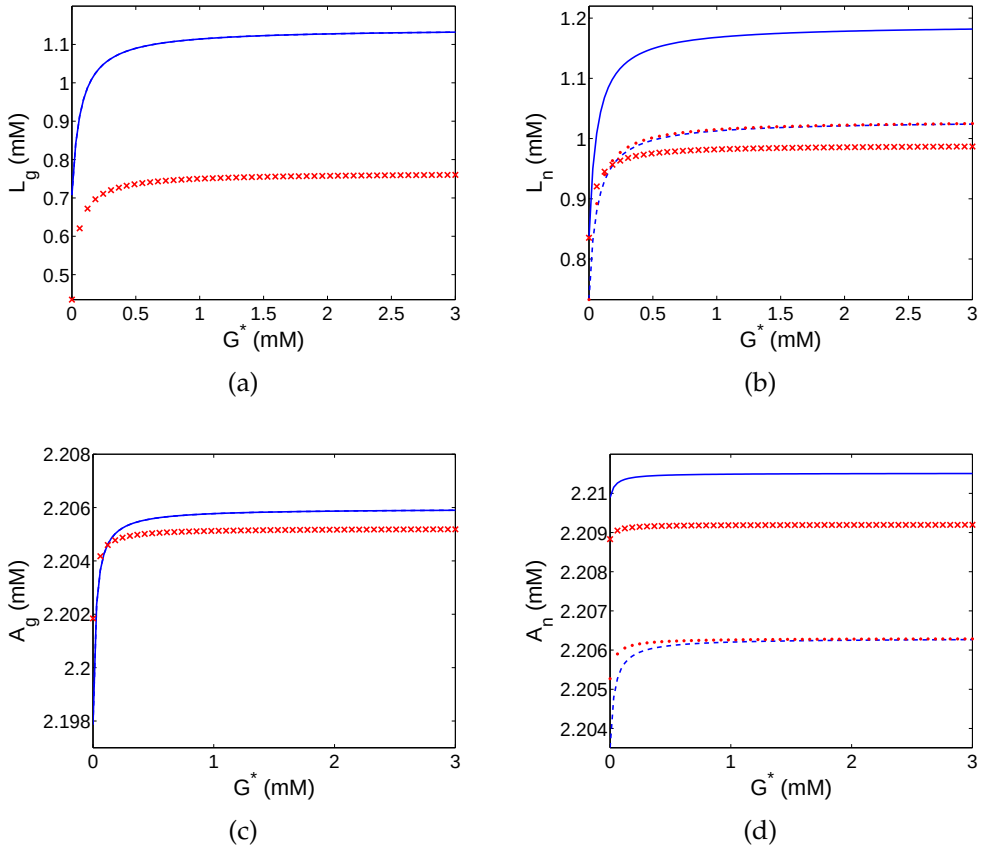


Figure C.1.: Plots showing glucose dose response of the steady state lactate and ATP concentrations in the IR submodel ((xxx): rest, ($\cdots$): neuronal stimulation) and the Simplified AC submodel ((—): rest, (- - -): neuronal stimulation) (see Table 5.2). The values of $\bar{A}_g$ and $\bar{A}_n$ have been set equal to the steady state ATP concentrations of the Simplified AC submodel during neuronal stimulation for $G^* = 3\,\text{mM}$, in the glial and neuronal cells respectively. The parameter values used are given in Table 5.4.

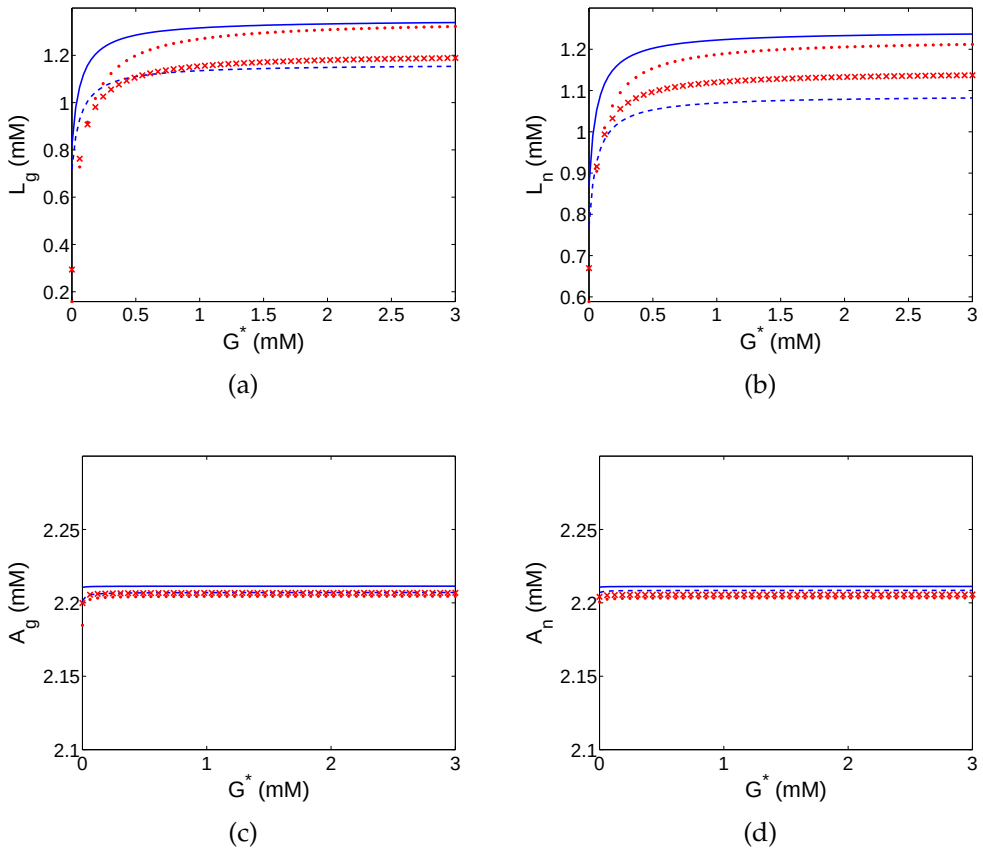


Figure C.2.: Plots showing glucose dose response of the steady state lactate and ATP concentrations in the IR submodel ((xxx): rest, (· · ·): neuronal stimulation) and the Simplified AC submodel ((—): rest, (- - -): neuronal stimulation). The stoichiometry of the IR submodel has been altered such that glial oxidative lactate metabolism to produce glutamate (denoted by the rate $v_{LW,g}$) produces 30 ATP molecules rather than 9 for each pair of lactate molecules consumed. Otherwise, both submodels are as summarised in Table 5.2 and the parameter values in Table 5.4.

Due to our parameter choices in the IR submodel, the reaction rates $v_{GL,x}$ match the corresponding rates in the Simplified AC submodel, $v_{\text{HK-PFK},x}$, for the ATP concentrations $A_x = \bar{A}_x$, and have the same glucose dependence. We now determine the parameter values $k_{\text{HK-PFK},x}$ and $K_{\text{HK-PFK},A,x}$ in the Simplified AC submodel to ensure the ADP dependences of the glycolytic rates are approximately the same in both submodels for chosen ATP concentrations $A_x = \bar{A}_x$.

The required parameter values are those for which, if the ATP concentration is perturbed from $\bar{A}_x$ by small amount δ (i.e. $A_x = \bar{A}_x + \delta$), we have,

$$\underbrace{\frac{\bar{A}_x + \delta}{\left(\bar{A}_x + \delta\right)^4 + K^4_{\text{HK-PFK},A,x}}}_{\text{AC submodel}} \approx \alpha \underbrace{\left(A_{\text{Tot}} - \bar{A}_x - \delta\right)}_{\text{IR submodel}}, \tag{C.1}$$

where α is a constant to be determined. For $\delta \ll \bar{A}_x$, we neglect terms $\mathcal{O}\left(\delta^2\right)$ and higher, and $\left(\bar{A}_x + \delta\right)^4$ expands to $\bar{A}_x^4 + 4\bar{A}_x^3\delta$. Substituting this into equation (C.1) and rearranging, we obtain,

$$\frac{\bar{A}_x + \delta}{\bar{A}_x^4 + K^4_{\text{HK-PFK},A,x}} \left(1 + \frac{4\bar{A}_x^3\delta}{\bar{A}_x^4 + K^4_{\text{HK-PFK},A,x}}\right)^{-1} \approx \alpha \left(A_{\text{Tot}} - \bar{A}_x - \delta\right).$$

Assuming that $\delta \ll \bar{A}_x/4 + K^4_{\text{HK-PFK},A,x}/\left(4\bar{A}_x^3\right)$ and using a binomial expansion we obtain,

$$\frac{\bar{A}_x + \delta}{\bar{A}_x^4 + K^4_{\text{HK-PFK},A,x}} \left(1 - \frac{4\bar{A}_x^3\delta}{\bar{A}_x^4 + K^4_{\text{HK-PFK},A,x}}\right) \approx \alpha \left(A_{\text{Tot}} - \bar{A}_x - \delta\right).$$

Equating coefficients of δ and neglecting terms $\mathcal{O}\left(\delta^2\right)$, we find that,

$$\frac{\bar{A}_x}{\bar{A}_x^4 + K^4_{\text{HK-PFK},A,x}} \approx \alpha \left(A_{\text{Tot}} - \bar{A}_x\right), \tag{C.2}$$

$$\frac{1}{\bar{A}_x^4 + K^4_{\text{HK-PFK},A,x}} \left(\frac{4\bar{A}_x^4}{\bar{A}_x^4 + K^4_{\text{HK-PFK},A,x}} - 1\right) \approx \alpha. \tag{C.3}$$

We note that equation (C.2) is already fulfilled by the value of $v_{GL,x}^{max}$ in Table 5.4. Substituting α from equation (C.2) into equation (C.3) and rearranging, we obtain,

$$K_{\text{HK-PFK},A,x} \approx \bar{A}_x \left(\frac{3A_{Tot} - 4\bar{A}_x}{A_{Tot}} \right)^{1/4}. \tag{C.4}$$

Choosing this value of $K_{\text{HK-PFK},A,x}$ means that reaction rates $v_{GL,x}$ and $v_{\text{HK-PFK},x}$ have the same ADP dependence when $A_x = \bar{A}_x$. For the value of $K_{\text{HK-PFK},A,x}$ to be real and positive, we must have that $0 < \bar{A}_x \leq 3A_{Tot}/4$. This approximation applies for sufficiently small changes in ATP levels, fulfilling the condition $\delta < \min\left[\bar{A}_x,\ \bar{A}_x/4 + K_{\text{HK-PFK},A,x}^4 / \left(4\bar{A}_x^3\right)\right]$.

Using parameter values that fulfil these conditions in the Simplified AC submodel, and the equivalent values in the IR submodel, derived using the expressions in Table 5.4, the two submodels closely match quantitatively, as shown in Figure 5.11.

D

CONSTRAINTS ON PARAMETERS IN GLUTAMATE-GLUTAMINE SUBMODEL

THE GLUTAMATE-GLUTAMINE SUBMODEL, defined by equations (5.23c), (5.24c), (5.25c), (5.23d), (5.24d) and (5.25d), and the corresponding initial conditions from (5.26) with L_g, A_g and A_n fixed, possesses at most one steady state.

Equations (6.6) specify constraints on the parameter groupings α, β, γ, λ, κ and μ (which are defined in equations (6.5)) for which the steady state glutamate and glutamine concentrations in the submodel are real, finite and non-negative. Since the parameter groupings β, γ, λ, κ and μ each depend on the parameter grouping α, it is clearer to rewrite each of the above constraints in terms of α using the technique described in this appendix.

Before continuing, we note that by definition, the $V_{\max}$ values ($\hat{v}^{\max}_{LW,g}$, $\hat{v}^{\max}_{WN,g}$, $\hat{v}^{\max}_{N,gs}$, $\hat{v}^{\max}_{N,sn}$, $\hat{v}^{\max}_{NW,n}$, $\hat{v}^{\max}_{WA,n}$, $\hat{v}^{\max}_{W,ns}$ and $\hat{v}^{\max}_{W,sg}$), K_m values ($\hat{K}_{LW,g}$, $\hat{K}_{WN,g,W}$, $\hat{K}_{WN,g,A}$, $\hat{K}_{N,gs}$, $\hat{K}_{N,sn}$, $\hat{K}_{WN,n}$, $\hat{K}_{WA,n}$, $\hat{K}_{W,ns,W}$, $\hat{K}_{W,ns,A}$, $\hat{K}_{W,sg,W}$ and $\hat{K}_{W,sg,A}$), fractional volumes (V_g and V_n) and dimensionless ATP concentrations ($\tilde{a}_g$, $\tilde{a}_n$ and a_{Tot}) are non-negative. It follows that all of the Michaelis-Menten expressions that appear in equations (6.5) are non-negative. Further, $\tilde{a}_g \leq a_{\text{Tot}}$, and likewise for $\tilde{a}_n$.

Noting the hierarchical nature of equations (6.5), since, in equation (6.5f), parameter grouping μ is written in terms of κ, the constraint (6.6f) on μ can be written as a constraint on κ. Since κ depends on λ, which in turn depends on γ, and so on, all of the constraints can be written as constraints on α.

We begin by rewriting constraint on μ in terms of κ and combining it with the existing bounds on κ given in (6.6e). Using the definition of μ in equation

(6.5f), if κ fulfils condition (6.6e) then $\mu > 0$ automatically. For $\mu < 1$ we require that,

$$\mu = \frac{V_n}{V_g}\frac{\hat{v}^{\max}_{N,sn}}{\hat{v}^{\max}_{N,gs}}\kappa + \frac{\dfrac{K_{N,sn}}{K_{N,gs}}\kappa}{\left(\dfrac{K_{N,sn}}{K_{N,gs}} - 1\right)\kappa + 1} < 1. \tag{D.1}$$

For the inequality in (D.1) to be satisfied, subject to constraint (6.6e), we have that,

$$0 < \kappa < \kappa^*, \tag{D.2}$$

where the upper bound κ^* is less than 1 and is given by equation (6.9d), in which $\kappa_\pm$ are given by equation (6.9e). Next we rewrite constraint (D.2) in terms of λ using equation (6.5e), and combine it with (6.6d), giving,

$$0 < \lambda < \lambda^*, \tag{D.3}$$

where,

$$\lambda^* = \min\left(1\,,\, \frac{\hat{v}^{\max}_{N,sn}}{\hat{v}^{\max}_{WN,n}}\kappa^*\right).$$

Similarly we can use condition (D.3) to derive upper and lower bounds on γ, β and hence α, each time adding in the relevant condition from (6.6), giving,

$$\begin{aligned}
&0 < \gamma < \gamma^*,\\
&0 < \beta < \beta^*,\\
&0 < \alpha < \alpha^*,
\end{aligned}$$

where,

$$\begin{aligned}
\gamma^* &= \min\left(1\,,\, F_\gamma\left(\hat{v}^{\max}_{WN,n}\right)\,,\, F_\gamma\left(\hat{v}^{\max}_{N,sn}\kappa^*\right)\right),\\
\beta^* &= \min\left(1\,,\, F_\beta\left(\hat{v}^{\max}_{WN,n}\right)\,,\, F_\beta\left(\frac{\hat{v}^{\max}_{N,sn}\mathrm{M}\left(\tilde{a}_g; \hat{v}^{\max}_{WN,g}, \hat{K}_{WN,g,A}\right)}{\mathrm{M}\left(\tilde{a}_g; \hat{v}^{\max}_{W,sg}, \hat{K}_{W,sg,A}\right)}\kappa^*\right)\right),
\end{aligned}$$

α^* is given by equation (6.8), and

$$F_\gamma(\hat{v}) = \frac{V_n}{V_g} \frac{\hat{v}}{\mathrm{M}\left(\tilde{a}_g; \hat{v}^{\max}_{WN,g}, \hat{K}_{WN,g,A}\right)},$$

$$F_\beta(\hat{v}) = \frac{V_n}{V_g} \frac{\hat{v}}{\mathrm{M}\left(\tilde{a}_g; \hat{v}^{\max}_{W,sg}, \hat{K}_{W,sg,A}\right)} - \frac{\mathrm{M}\left(l_g; \hat{v}^{\max}_{LW,g}, \hat{K}_{LW,g}\right)\left(a_{\mathrm{Tot}} - \tilde{a}_g\right)}{\mathrm{M}\left(\tilde{a}_g; \hat{v}^{\max}_{W,sg}, \hat{K}_{W,sg,A}\right)},$$

$$F_\alpha(\hat{v}) = \frac{\hat{v} - \omega}{\chi\left(\hat{v} - \omega\right) + \frac{V_g}{V_n} \frac{\hat{K}_{WA,n}}{\hat{K}_{W,ns,W}} \mathrm{M}\left(\tilde{a}_n; \hat{v}^{\max}_{W,ns}, \hat{K}_{W,ns,A}\right)},$$

and $F_\alpha(\hat{v})$ is given in equation (6.9a), with ω and χ defined in equations (6.9b) and (6.9c).

E

ESTIMATION OF PARAMETERS IN INNER RETINAL METABOLISM

We give more details in this appendix on how the steps outlined in §6.2 were carried out.

E.1 EXPERIMENTAL MEASUREMENTS OF PARAMETERS

Tables 6.1–6.3 show the ranges of values of the model parameters documented in the literature. Measurements of typical metabolite concentrations are stated in Table 6.4. Some values in the table are derived from direct measurements using some simplifying assumptions, for example, to convert between the units of measurement and standard units. Such assumptions are detailed below.

Where possible we use parameter values that best describe inner retinal metabolism in humans. Some data are available for the human brain, for example using MRI imaging. However, many measurements are taken from other mammals, often rat brain tissue. When no human data are available, we consider data from several different mammalian tissues, we apply the data in Tables 6.1–6.3 to our model by assuming that the properties of retinal blood vessels, glia and neurons are similar to those of other brain regions, and ignore differences between the parameters in human retinae and those of other mammals.

Reaction rates are often measured in units of mol min^{-1} (g wet weight)$^{-1}$, mol min^{-1} (mg protein)$^{-1}$, molecules s^{-1} (glial cell)$^{-1}$ or molecules s^{-1} (neuronal cell)$^{-1}$. The values shown in Tables 6.1–6.3 have been converted to mM or $\text{mM}\,\text{s}^{-1}$ in the following way.

A concentration of 1 mole (g wet weight)$^{-1}$ is equivalent to 10^6 mM (taking the density of human tissue to be 1 g (mL)$^{-1}$), and thus 1 mole min^{-1} (g wet weight)$^{-1}$ is equivalent to approximately $2 \times 10^4\,\text{mM}\,\text{s}^{-1}$. Note that 100 mg

of cell protein is equivalent to approximately 1 g of wet weight [286]. Taking the cell density to be $1\,\mathrm{g\,(mL)^{-1}}$, 100 mg cell protein is approximately 1 mL of tissue. Thus the density of extracted cell protein is 10^5 mg protein L^{-1} and 1 mole min^{-1} (mg protein)$^{-1}$ is equivalent to $1 \times 10^8\,\mathrm{mM\,min^{-1}}$ or $2 \times 10^6\,\mathrm{mM\,s^{-1}}$.

We convert from ATP molecules (glial cell)$^{-1}\,\mathrm{s}^{-1}$ to $\mathrm{mM\,s^{-1}}$ by noting a human brain of volume $1400\,\mathrm{cm}^3$ [293] contains approximately 85×10^9 glial cells [308]. In particular we deduce that 1 ATP molecule (glial cell)$^{-1}\,\mathrm{s}^{-1}$ is equivalent to 6×10^9 ATP molecules $\mathrm{L}^{-1}\,\mathrm{s}^{-1}$, or $10^{-11}\,\mathrm{mM\,s^{-1}}$. Following Azevedo et al. [309] who claim that there are similar numbers of glia and neurons in the human brain parameter estimates with the units molecules (neuronal cell)$^{-1}\,\mathrm{s}^{-1}$ can be converted to $\mathrm{mM\,s^{-1}}$ in the same way.

Finally, before discussing our estimates of specific parameters, we explain how we converted mg/dL to standard units (mM). Taking the mass of 1 mole of glucose to be 180 g [310], a concentration of $1\,\mathrm{mg\,dL^{-1}}$ is equivalent to 0.06 mM.

Parameter Values Associated with Glycolysis and the TCA Cycle

The reaction rates $v_{GL,g}$, $v_{GL,n}$, $v_{LW,g}$, $v_{LA,n}$ and $v_{WA,n}$ represent the rates of the glycolytic or oxidative pathways via a single reaction (we justified the use of such phenomenological expressions in Chapter 5). To estimate parameter values associated with these reaction rates, we account only for the dose dependence of the reaction rates on the concentration of the key substrates included in our model.

We first consider the rate of partial oxidative lactate metabolism in the glial cells, $v_{LW,g}$, which, according to our model, consumes lactate and ADP and produces glutamate and ATP. Referring to our discussion in §4.1, in particular, Figure 4.5(a), the rate limiting step of this pathway is the formation of acetyl CoA, for which the net reaction is,

$$2\ \text{Pyruvate} + 2\mathrm{NAD}^+ + 2\mathrm{CoA} \rightarrow 2\mathrm{NADH} + 2\mathrm{H}^+ + 2\ \text{Acetyl CoA} + 2\mathrm{CO}_2.$$

As specified in §5.1, we assume that the substrates in the steps of the glycolytic and oxidative pathways are abundant, except for those included in our model and pyruvate, which is rapidly converted to lactate and vice versa. NAD^+ and CoA are not incorporated in our model, and hence assumed to be plentiful. From §5.1, to derive the rate $v_{LW,g}$, we assume that the rate of pyruvate oxidation

is given by equation (5.12), where $(YZ, m) = (\mathrm{PYR}\,W, g)$. We take typical values of $v_{\mathrm{PYR}\,W,g}B$, $K_{\mathrm{PYR}\,W,g}$ and [PYR] to be 18.3 μMs^{-1} [286], 1.5 mM[291] and 0.09 mM [286] respectively, and take a typical ADP concentration, B, to be the measured value given in Table 6.4. Assuming that the maximum value of $v_{LW,g}$ is the maximum rate of its rate-limiting step yields $v^{\max}_{LW,g} \approx 30$ mMs^{-1}. Equating $v_{LW,g}$ and $v_{\mathrm{PYR}\,W,g}$ at typical cellular lactate and pyruvate concentrations,and substituting the estimated values of $v^{\max}_{LW,g}$, $v^{\max}_{\mathrm{PYR}\,W,g}$, $K_{\mathrm{PYR}\,W,g}$, and typical lactate, pyruvate and ADP concentrations gives $K_{LW,g} \approx 20$ mM.

Partial oxidative glutamate metabolism (denoted by rate $v_{WA,n}$ in our model) passes through the TCA cycle but not Acetyl CoA formation (see Figure 4.5(b)), so we approximate the net reaction using the following equation,

$$\alpha\mathrm{KG} + \mathrm{NAD}^+ + \mathrm{CoA} \rightarrow \text{Succinyl-CoA} + \mathrm{NADH} + \mathrm{H}^+ + \mathrm{CO}_2.$$

We estimate the kinetic parameters for $v_{WA,n}$ using similar arguments to those used for $v_{LW,g}$, taking $v^{\max}_{WA,n}B$ to be 3.33 μMs^{-1} [286], and the K_m with respect to αKG to be 4 mM [285], we obtain $v^{\max}_{WA,n} \approx 5\,\mathrm{mM\,s^{-1}}$, and $K_{WA,n} \approx 0.2$ M.

According to Figure 4.4, full oxidative lactate metabolism (rate $v_{LA,n}$) passes through both major regulatory steps. As αKGDH is the rate-limiting enzyme, we assume that it regulates the reaction rate through the pathway. We use similar arguments as before to estimate the kinetic parameters associated with $v_{LA,n}$, giving $v^{max}_{LA,n} = 5\,\mathrm{mM\,s^{-1}}$, and $K_{LA,n} = 20$ mM.

The substrate for glycolysis, (rates $v_{GL,g}$ and $v_{GL,n}$ in the glial and neuronal cells respectively) is glucose, and the regulatory step is the following reaction,

$$\text{Fructose 6-P} + \mathrm{ATP} \rightarrow \mathrm{ADP} + \text{Fructose 1,6-bisphosphate}.$$

Assuming a typical F 6-P concentration of 0.2 mM [286], a $V_{\max}$ of 16.7 $\mu\mathrm{M\,s^{-1}}$ [286], a K_m with respect to F 6-P of 4 mM [311] and that glial and neuronal cells have similar kinetic parameters associated with glycolysis, we obtain the initial estimates for parameter values $v^{\max}_{GL,g}$, $v^{\max}_{GL,n}$, $K_{GL,g}$ and $K_{GL,n}$ given in Table 6.2.

E.1.0.1 *Assumptions to Derive Other Parameters*

For each nutrient and cell type, most transport is via a single type of transmembrane protein, (see Table E.1). We therefore assume that, in our model, the $V_{\max}$ and K_m values for metabolite exchange between compartments in our model

Reaction rate	Main transporter molecule involved
$v_{G,bg}$	GLUT1 (55 kDa)
$v_{G,sg}$	GLUT1 (45 kDa)
$v_{G,sn}$	GLUT3
$v_{L,bg}$	MCT3
$v_{L,sg}$	MCT1
$v_{L,sn}$	MCT2
$v_{W,sg}$	EAAT1 − 2
$v_{W,ns}$	Synaptic vesicles
$v_{N,gs}$	SN1
$v_{N,sn}$	SAT, ATA

Table E.1.: Table listing dominant transporter molecules for each transport reaction.

are identical to those measured in the corresponding transporter molecule in Table E.1.

We assume that the reaction rates $v_{A0,g}$ and $v_{A0,n}$ are approximately constant except when A_g or $A_n \to 0$ (see §5.1). Thus, when estimating $K_{A0,g}$ and $K_{A0,n}$, we require only that inequalities (5.19) hold. Given the typical ATP concentrations recorded in Table 6.4, we set $K_{A0,x} = 2\,\mu$M for $x \in \{g, n\}$.

The proportion of the brain volume occupied by each compartment is known. The glia, neurons, ECS and blood vessels occupy 50%, 25%, 20% and 5% of the brain volume respectively [216, 292–297].

E.2 USING GLUCOSE-LACTATE AND GLUTAMATE-GLUTAMINE SUBMODELS TO REFINE PARAMETER ESTIMATES

Some parameter estimates (see Tables 6.1–6.3) vary widely, due to the different methods and conditions under which they were collected. We note the discussion in §4.2 on the controversy over the glucose and lactate transport rate parameters used in previous mathematical models of cerebral metabolism. Furthermore, only one measurement was available for some parameters. We narrow down our search for parameter values which closely match those in physiological conditions by taking them from the measured metabolite concentrations in brain tissue under resting conditions, shown in Table 6.4. In doing this we assume that these are equivalent to the concentrations in inner retinal

tissue when the neurons are inactive, under dark conditions. We proceed as follows.

Assuming the fractional volumes of the compartments in the inner retinal tissue are the same as those in brain tissue, the metabolite concentrations in each compartment are related to the concentrations in the whole brain given in Table 6.4 by the following condition,

$$C_T = V_b C_b + V_g C_g + V_s C_s + V_n C_n, \tag{E.1}$$

where C_T, C_b, C_g, C_s and C_n are the concentrations of a given nutrient in the whole tissue (or whole brain), blood vessels, glia, ECS and neurons respectively, and V_b, V_g, V_s and V_n are the fractional volumes of blood vessels, glia, ECS and neurons respectively, which sum to 1.

Equations (6.3a)–(6.4c) constrain the parameter values in the glutamate-glutamine cycle against the steady state concentrations under dark conditions, which can be estimated from the resting concentrations in Table 6.4. Additionally, by fixing the ATP concentrations at their steady state values, we can use the constraints in equations (6.8) on the parameter values in the glutamate-glutamine cycle such that the glutamate and glutamine concentrations reach steady states during light conditions. We note that changes to the parameter values that ensure constraints (6.8) are satisfied under light conditions alter the steady states predicted by our model. However, the above techniques allow us to derive parameter values that give results close to the typical physiological values.

Information about typical nutrient concentrations enables us to check some of the parameter estimates associated with the greatest uncertainty. Gruetter et al. [233] used MRI scans during neuronal activity to estimate the reaction rates $v_{WN,g}$, $v_{LW,g}$ and $v_{W,ns}$ to be $4.3\,\mu\text{Ms}^{-1}$, $1.5\,\mu\text{Ms}^{-1}$ and $2.8\,\mu\text{Ms}^{-1}$ respectively. We assume that these data are more accurate than some of the data in Tables 6.2–6.3 since they relate to *in vivo* studies of the human brain. We use the values stated in Table 6.4 as typical nutrient concentrations (although in practice the concentrations are different under light conditions (i.e. during neuronal activity) when Gruetter et al.'s measurements were taken). Equating the measurements in [233] with the corresponding reaction rates in our model we have,

$$v_{WN,g}^{\max} \frac{W_g}{W_g + K_{WN,g,W}} \frac{A_g}{A_g + K_{WN,g,A}} \approx 4.3\,\mu\text{Ms}^{-1},$$

$$v_{LW,g}^{\max} \frac{L_g}{L_g + K_{LW,g}} \left(A_{\text{Tot}} - \tilde{A}_g\right) \approx 1.5\,\mu\text{Ms}^{-1},$$
$$v_{W,ns} = v_{W,ns}^{\max} \frac{W_n}{W_n + K_{W,ns,W}} \frac{A_n}{A_n + K_{W,ns,A}} \approx 2.8\,\mu\text{Ms}^{-1}.$$

Using the ranges of concentrations stated in Table 6.4 gives three further constraints on the model parameters.

In the case of the rate of neuronal glutamate release, taking typical neuronal glutamate and ATP concentrations to be 10 mM and 2.5 mM respectively, and $v_{W,ns}^{\max} = 40\,\mu\text{Ms}^{-1}$, $K_{W,ns,A} = 0.2\,\text{mM}$ and $K_{W,ns,W}$ between 0.3–2 mM, as given in Table 6.2 we find that the maximum and minimum values of $v_{W,ns}$ are 36 and 31 μMs^{-1} respectively, much higher than the value reported in [233]. The values of $v_{W,ns}^{\max}$ and $K_{W,ns,A}$ given in Table 6.2 are based on individual measurements and thus are associated with significant uncertainty, particularly based on the wide ranges over which measurements of other parameters vary. Even if the value of $K_{W,ns,A}$ is varied by an order of magnitude from the value given in Table 6.2, the rate of $v_{W,ns}$ is still too high. We therefore conclude that the value of $v_{W,ns}^{\max}$ is significantly lower than given in Table 6.2. Similar analysis can be used to derive more accurate estimates for the parameters corresponding to reaction rates $v_{WN,g}$ and $v_{LW,g}$.

Finally, we allow the ATP concentrations to vary in time and perform further refinements to our parameter estimates, iterating parameter changes using a bisection method until the steady state concentrations predicted by our model are within the ranges given in Table 6.4. We adjust the parameters based on their qualitative effects on the steady state concentrations (see equations (6.3a)–(6.4c)) and the ODEs in the glucose-lactate submodel.

BIBLIOGRAPHY

[1] A. Aubert and R. Costalat. Interaction between astrocytes and neurons studied using a mathematical model of compartmentalized energy metabolism. Journal of Cerebral Blood Flow and Metabolism, 25:1476–1490, 2005.

[2] L. Alexander. Sight loss UK 2013: The latest evidence. Technical report, RNIB, 2013.

[3] J. R. Evans, M. Michelessi, and G. Virgili. Laser photocoagulation for proliferative diabetic retinopathy. The Cochrane Library, 11:1–53, 2014.

[4] S. D. Schwartz, C. D. Regillo, B. L. Lam, D. Eliott, P. J. Rosenfeld, N. Z. Gregori, J. Hubschman, J. L. Davis, G. Heilwell, and M. Spirn et al. Human embryonic stem cell-derived retinal pigment epithelium in patients with age-related macular degeneration and Stargardt's macular dystrophy: follow-up of two open-label phase 1/2 studies. The Lancet, 385:509–516, 2014.

[5] M. Suter, C. Remé, C. Grimm, A. Wenzel, M. Jäättela, P. Esser, N. Kociok, M. Leist, and C. Richter. Age-related macular degeneration the lipofuscin componentn-retinyl-N-retinylidene ethanolamine detaches proapoptotic proteins from mitochondria and induces apoptosis in mammalian retinal pigment epithelial cells. Journal of Biological Chemistry, 275(50):39625–39630, 2000.

[6] M. A. Zarbin. Age-related macular degeneration: review of pathogenesis. European journal of ophthalmology, 8(4):199–206, 1997.

[7] C. Owsley, G. R. Jackson, M. White, R. Feist, and D. Edwards. Delays in rod-mediated dark adaptation in early age-related maculopathy. Ophthalmology, 108(7):1196–1202, 2001.

[8] S. B. Laughlin, R. R. de Ruyter van Steveninck, and J. C. Anderson. The metabolic cost of neural information. Nature Neuroscience, 1:36 – 41, 1998.

[9] H. Lee and Y. Wei. Mitochondria and aging. In Advances in Mitochondrial Medicine, pages 311–327. Springer, 2012.

[10] L. Walter and S. S. Lee. Mitochondria as a key determinant of aging. In The Encyclopedia of Life Sciences. John Wiley & Sons, Ltd, 2001.

[11] S. Gartner and P. Henkind. Aging and degeneration of the human macula. 1. outer nuclear layer and photoreceptors. British Journal of Ophthalmology, 65(1):23–28, 1981.

[12] S. H. Sarks. Ageing and degeneration in the macular region: a clinico-pathological study. British Journal of Ophthalmology, 60(5):324–341, 1976.

[13] H. G. Garg, M. K. Cowman, and C. A. Hales. Carbohydrate Chemistry, Biology and Medical Applications. Elsevier Science, 2011. ISBN 9780080558141.

[14] H. Kolb. Gross anatomy of the eye, . URL `http://webvision.med.utah.edu/`. Accessed: 11 April 2015.

[15] E. N. Pugh Jr and T. D. Lamb. Handbook of Biological Physics, volume 3: Molecular Mechanisms of Visual Transduction, chapter Phototransduction in Vertebrate Rods and Cones: Molecular Mechanisms of Amplification, Recovery and Light Adaptation, pages 183–255. Elsevier Science B. V., 2000.

[16] Y. Koutalos and K. Yau. Regulation of sensitivity in vertebrate rod photoreceptors by calcium. Trends in Neurosciences, 19:73–81, 1996.

[17] H. Kolb. Simple anatomy of the retina, . URL `http://webvision.med.utah.edu/book/part-i-foundations/simple-anatomy-of-the-retina/`. Accessed: 11 April 2015.

[18] R. W. Young. The renewal of photoreceptor cell outer segments. The Journal of Cell Biology, 33:61–72, 1967.

[19] G. A. Limb and H. Jayaram. Experimental Approaches to Diabetic Retinopathy, volume 20, chapter Regulatory and Pathogenic Roles of Müller Glial Cells in Retinal Neovascular Processes and Their Potential for Retinal Regeneration, pages 98–108. Karger, 2010.

[20] G. S. Hageman, P. J. Luthert, N. H. V. Chong, L. V. Johnson, D. H. Anderson, and R. E. Mullins. An integrated hypothesis that considers drusen as biomarkers of immune-mediated processes at the RPE-Bruch's membrane interface in aging and age-related macular degeneration. Progress in Retinal and Eye Research, 20:706–732, 2001.

[21] S. S. Miller, B. A. Hughes, and T. E. Machen. Fluid transport across retinal pigment epithelium is inhibited by cyclic AMP. Proceedings of the National Academy of Science, USA, 79:2111–2115, 1982.

[22] N. D. Wangsa-Wirawan and R. A. Linsenmeier. Retinal oxygen: Fundamental and clinical aspects. Archives of Ophthalmology, 121:547–557, 2003.

[23] R. A. Linsenmeier and R. D. Braun. Oxygen distribution and consumption in the cat retina during normoxia and hypoxemia. The Journal of General Physiology, 99:177–197, 1992.

[24] J. L. Haines, M. A. Hauser, S. Schmidt, W. K. Scott, L. M. Olson, P. Gallins, K. L. Spencer, S. Y. Kwan, M. Noureddine, J. R. Gilbert, N. Schnetz-Boutaud, E. A. Postel A. Agarwal, and M. A. Pericak-Vance. Complement factor H variant increases the risk of age-related macular degeneration. Science, 308:419–421, 2005.

[25] B. Anderson Jr and H. A. Saltzman. Retinal oxygen utilization measured by hyperbaric blackout. Archives of Ophthalmology, 72(6):792–795, 1964.

[26] R. Zuckerman and J. J. Weiter. Oxygen transport in the bullfrog retina. Experimental Eye Research, 30:117–127, 1980.

[27] B. Hille et al. Ion channels of excitable membranes, volume 507. Sinauer Sunderland, MA, 2001.

[28] T. Ikezu and H. E. Gendelman. Neuroimmune pharmacology. Springer Science & Business Media, 2008.

[29] S. C. Hsu and R. S. Molday. Glyceraldehyde-3-phosphate dehydrogenase is a major protein associated with the plasma membrane of retinal photoreceptor outer segments. Journal of Biological Chemistry, 265(22): 13308–13313, 1990.

[30] S. Hsu and R. S. Molday. Glycolytic enzymes and a GLUT–1 glucose transporter in the outer segments of rod and cone photoreceptor cells. The Journal of Biological Chemistry, 266:21745–21752, 1991.

[31] J. C. Besharse, J. G. Hollyfield, and M. E. Rayborn. Turnover of rod photoreceptor outer segments. II. Membrane addition and loss in relationship to light. The Journal of Cell Biology, 75:507–527, 1977.

[32] R. S. Molday. Photoreceptor membrane proteins, phototransduction, and retinal degenerative diseases: The Freidenwald lecture. Investigative Ophthalmology and Visual Science, 39:2493–2513, 1998.

[33] M. Pavelka and J. Roth. Functional Ultrastructure: An Atlas of Tissue Biology and Pathology. Springer, New York, 2005.

[34] M. H. Chaitin, B. G. Schneider, M. O. Hall, and D. S. Papermaster. Actin in the photoreceptor connecting cilium: immunocytochemical localization to the site of outer segment disk formation. The Journal of Cell Biology, 99:239–247, 1984.

[35] C. J. Bassi and M. K. Powers. Shedding of rod outer segments is light-driven in goldfish. Investigative Ophthalmology and Visual Science, 31: 2314–2319, 1990.

[36] M. M. LaVail. Rod outer segment disk shedding in rat retina: relationship to cyclic lighting. Science, 194:1071–1074, 1976.

[37] M. P. White, P. A. Hock, and M. F. Marmor. Electrophysiological correlates of rod outer segment disc shedding in rabbit retina. Vision Research, 27: 357–361, 1987.

[38] R. W. Young. The renewal of the rod and cone outer segments in the rhesus monkey. The Journal of Cell Biology, 49:303–318, 1967.

[39] J. W. Crabb, W. Miyagi, X. Gu, K. Shadrach, K. A. West, H. Sakaguchi, M. Kamei, A. Hasan, L. Yan, M. E. Rayborn, R. G. Salomon, and J. G. Hollyfield. Drusen proteome analysis: An approach to the etiology of age-related macular degeneration. Proceedings of the National Academy of Sciences of the United States of America, 99:14682–14687, 2002.

[40] L. M. Shulman and D. A. Fox. Dopamine inhibits mammalian photoreceptor Na^+, K^+–ATPase activity via a selective effect on the $\alpha 3$ isozyme. Proceedings of the National Academy of Sciences, 93(15):8034–8039, 1996.

[41] A. Ames III, L. Ying-Ying, E. C. Heher, and C. Rising Kimble. Energy metabolism of rabbit retina as related to function: High cost of Na^+ transport. The Journal of Neuroscience, 12:840–853, 1992.

[42] K. Yau. Phototransduction mechanism in retinal rods and cones: The Friedenwald lecture. Investigative Ophthalmology and Visual Science, 35:9–32, 1994.

[43] R. D. Braun, R. A. Linsenmeier, and T. K. Goldstick. Oxygen consumption in the inner and outer retina of the cat. Investigative Ophthalmology and Visual Science, 36:542–554, 1995.

[44] L. M. Haugh-Scheidt, R. A. Linsenmeier, and E. R. Griff. Oxygen consumption in the isolated toad retina. Experimental Eye Research, 61: 63–72, 1995.

[45] B. K. K. Fung, J. B. Hurley, and L. Stryer. Flow of information in the light-triggered cyclic nucleotide cascade of vision. Proceedings of the National Academy of Sciences of the United States of America, 78:152–156, 1981.

[46] E. E. Fesenko, S. S. Kolesnikov, and A. L. Lyubarsky. Induction by cyclic GMP of cationic conductance in plasma membrane of retinal rod outer segment. Nature, 313:310–313, 1985.

[47] A. Ames III, T. F. Walseths, R. A. Heymansq, M. Barad, R. M. Graeffs, and N. D. Goldberg. Light-induced increases in cGMP metabolic flux correspond with electrical responses of photoreceptors. The Journal of Biological Chemistry, 261:13034–13042, 1986.

[48] K. Yau and K. Nakatani. Light-induced reduction of cytoplasmic free calcium in retinal rod outer segment. Nature, 313:579–582, 1985.

[49] S. C. Hsu and R. S. Molday. Glucose metabolism in photoreceptor outer segments: Its role in phototransduction and in NADPH-requiring reactions. Journal of Biological Chemistry, 269(27):17954–17959, 1994.

[50] W. Hemmer, I. Riesinger, T. Wallimann, H. M. Eppenberger, and A. F. G. Quest. Brain-type creatine kinase in photoreceptor cell outer segments: role of a phosphocreatine circuit in outer segment energy metabolism and phototransduction. Journal of Cell Science, 106:671–684, 1993.

[51] R. A. McFarland and W. H. Forbes. The effects of variations in the concentration of oxygen and glucose on dark adaptation. The Journal of Cell Physiology, 24(1):69–98, 1940.

[52] V. A. Saks and R. Ventura-Clapier. Cellular bioenergetics: role of coupled creatine kinases, volume 13. Springer Science & Business Media, 2012.

[53] A. Ames III. CNS energy metabolism as related to function. Brain Research Reviews, 34:42–68, 2000.

[54] T. Wallimann. Dissecting the role of creatine kinase. Current Biology, 4 (1):42–46, 1994.

[55] S. Gudbjarnason, P. Mathesc, and K. G. Ravensc. Functional compartmentation of ATP and creatine phosphate in heart muscle. Journal of Molecular and Cellular Cardiology, 1(3):325–339, 1970.

[56] T. Wallimann, G. Wegmann, H. Moser, R. Huber, and H. M. Eppenberger. High content of creatine kinase in chicken retina: Compartmentalized localization of creatine kinase isoenzymes in photoreceptor cells. Proceedings of the National Academy of Science of the United States of America, 83:3816–3819, 1986.

[57] J. D. Linton, L. C. Holzhausen, N. Babai, H. Song, K. J. Miyagishima, G. W. Stearns, K. Lindsay, J. Wei, A. O. Chertov, T. A. Peters, et al. Flow of energy in the outer retina in darkness and in light. Proceedings of the National Academy of Sciences, 107(19):8599–8604, 2010.

[58] C. Owsley, G. R. Jackson, A. V. Cideciyan, Y. Huang, S. L. Fine, A. C. Ho, M. G. Maguire, V. Lolley, and S. G. Jacobson. Psychophysical evidence for rod vulnerability in age-related macular degeneration. Investigative Ophthalmology and Visual Science, 41:267–273, 2000.

[59] C. A. Curcio, N. E. Medeiros, and C. L. Millican. Photoreceptor loss in age-related macular degeneration. Investigative Ophthalmology and Visual Science, 37:1236–1249, 1996.

[60] N. M. Bressler and J. P. Gills. Age related macular degeneration: New hope for a common problem comes from photodynamic therapy. British Medical Journal, 321:1425–1427, 2000.

[61] W. R. Green, P. J. McDonnell, and J. H. Yeo. Pathologic features of senile macular degeneration. Ophthalmology, 92:615–627, 1985.

[62] S. H. Sarks and J. P. Sarks. Age-related macular degeneration: atrophic form. In S. J. Ryan, A. P. Schachat, and R. M. Murphy, editors, Retina, volume 2: Medical retina, pages 1071–1102. Mosby Incorporated, St Louis, USA, 1994.

[63] J. Ambati, B. K. Ambati, S. H. Yoo, S. Ianchulev, and A. P. Adamis. Age-related macular degeneration: Etiology, pathogenesis, and therapeutic strategies. Survey of Ophthalmology, 48:257–293, 2003.

[64] D. M. Snodderly. Evidence for protection against age-related macular degeneration by carotenoids and antioxidant vitamins. The American Journal of Clinical Nutrition, 62:1448S–1461S, 1995.

[65] W. R. Green and C. Enger. Age-related macular degeneration histopathologic studies. Ophthalmology, 100:1519–1535, 1993.

[66] R. J. Klein, C. Zeiss, E. Y. Chew, J. Y. Tsai, R. S. Sackler, C. Haynes, A. K. Henning, J. P. San Giovanni, S. M. Mane, S. T. Mayne, M. B. Bracken, F. L. Ferris, J. Ott, C. Barnstable, and J. Hoh. Complement factor H polymorphism in age-related macular degeneration. Science, 308:385–389, 2005.

[67] M. W. Stewart, S. Grippon, and P. Kirkpatrick. Aflibercept. Nature reviews Drug discovery, 11(4):269–270, 2012.

[68] T. H. Tezel, N. S. Bora, and H. J. Kaplan. Pathogenesis of age-related macular degeneration. Trends in Molecular Medicine, 10:417–420, 2004.

[69] T. A. Ciulla, R. P. Danis, and A. Harris. Age-related macular degeneration: A review of experimental treatments. Survey of Ophthalmology, 43:134–146, 1998.

[70] J. M. Seddon, U. A. Ajani, R. D. Sperduto, R. Hiller, N. Blair, T. C. Burton, M. D. Farber, E. S. Gragoudas, J. Haller, and D. T. Miller. Dietary

carotenoids, vitamins A, C, and E, and advanced age-related macular degeneration. Eye disease case-control study group. Journal of the American Medical Association, 272:1413–1420, 1994.

[71] J. Goldberg, G. Flowerdew, E. Smith, J. A. Brody, and M. O. M. Tso. Factors associated with age-related macular degeneration. American Journal of Epidemiology, 128:700–710, 1988.

[72] S. West, S. Vitale, J. Hallfrisch, B. Mu noz, D. Muller, S. Bressler, and N. M. Bressler. Are antioxidants or supplements protective for age-related macular degeneration? Archives of Ophthalmology, 112:222–227, 1994.

[73] L. Feeney-Burns, E. S. Hilderbrand, and S. Eldridge. Aging human RPE: Morphometric analysis of macular, equatorial and peripheral cells. Investigative Opthalmology and Visual Science, 25:195–200, 1984.

[74] N. I. Krinsky. Carotenoid protection against oxidation. Pure and Applied Chemistry, 51:649–660, 1979.

[75] N. I. Krinsky. Photobiology of carotenoid protection. In Regan J. D. and Parrish J. A., editors, The science of photomedicine, pages 397–403. Plenum Press, New York, 1982.

[76] S. M. Meyers and A. A. Zachary. Monozygotic twins with age-related macular degeneration. Archives of Ophthalmology, 106:651–653, 1988.

[77] D. H. Gurne, M. O. Tso, D. P. Edward, and H. Ripps. Antiretinal antibodies in serum of patients with age-related macular degeneration. Ophthalmology, 98:602–607, 1991.

[78] J. Esparza-Gordillo, J. M. Soria, A. Buil, L. Almasy, J. Blangero, J. Fontcuberta, and S. R. de Còrdoba. Genetic and environmental factors influencing the human factor H plasma levels. Immunogenetics, 56:77, 2004.

[79] F. G. Holz, C. Bellman, S. Staudt, F. Schütt, and H. E. Völcker. Fundus autofluorescence and development of geographic atrophy in age-related macular degeneration. Investigative Ophthalmology and Visual Science, 42:1051–1056, 2001.

[80] G. E. Eldred and M. R. Lasky. Retinal age pigments generated by self-assembling lysosomotropic detergents. Nature, 361:724–726, 1993.

[81] J. C. Javitt, L. P. Aiello, Y. Chiang, F. L. Ferris, J. K. Canner, and S. Greenfield. Preventive eye care in people with diabetes is cost-saving to the federal government: implications for health-care reform. Diabetes care, 17(8):909–917, 1994.

[82] V. J. Fraser. Diseases and Disorders. Marshall Cavendish Corporation, 2008.

[83] R. A. Kowluru and P. Chan. Oxidative stress and diabetic retinopathy. Experimental, 2007:Article ID: 43603 (online), 2007.

[84] R. Rabinowitz, R. Yagev, A. Shoham, and T. Lifshitz. Comparison between clinical and ultrasound findings in patients with vitreous hemorrhage. Eye, 18:253–256, 2004.

[85] A. J. Barber. A new view of diabetic retinopathy: a neurodegenerative disease of the eye. Progress in Neuro-Psychopharmacology and Biological Psychiatry, 27(2):283–290, 2003.

[86] E. Rungger–Brändle, A. A. Dosso, and P. M. Leuenberger. Glial reactivity, an early feature of diabetic retinopathy. Investigative ophthalmology & visual science, 41(7):1971–1980, 2000.

[87] H. Asi and I. Perlman. Relationships between the electroretinogram a-wave, b-wave and oscillatory potentials and their application to clinical diagnosis. Documenta ophthalmologica, 79(2):125–139, 1992.

[88] R. W. Rodieck. The vertebrate retina: principles of structure and function. WH Freeman, 1973.

[89] D. C. Hood and M. A. Finkelstein. Sensitivity to light. John Wiley and Sons, New York, 1986.

[90] E. Dodt. Cone electroretinography by flicker. Nature Publishing Group, 1951.

[91] J. C. Armington, E. P. Johnson, and L. A. Riggs. The scotopic a-wave in the electrical response of the human retina. The Journal of physiology, 118(3):289–298, 1952.

[92] R. D. Penn and W. A. Hagins. Signal transmission along retinal rods and the origin of the electroretinographic a-wave. Nature Publishing Group, 1969.

[93] R. F. Miller and J. E. Dowling. Intracellular responses of the Müller (glial) cells of mudpuppy retina: their relation to b-wave of the electroretinogram. Journal of neurophysiology, 33(3):323–341, 1970.

[94] P. A. Sieving, K. Murayama, and F. Naarendorp. Push–pull model of the primate photopic electroretinogram: a role for hyperpolarizing neurons in shaping the b-wave. Visual neuroscience, 11(03):519–532, 1994.

[95] J. Ding, L. V. Johnson, R. Herrmann, S. Farsiu, S. G. Smith, M. Groelle, B. E. Mace, P. Sullivan, J. A. Jamison, U. Kelly, et al. Anti-amyloid therapy protects against retinal pigmented epithelium damage and vision loss in a model of age-related macular degeneration. Proceedings of the National Academy of Sciences, 108(28):E279–E287, 2011.

[96] P. Walter, R. A. Widder, C. Lüke, P. Königsfeld, and R. Brunner. Electrophysiological abnormalities in age-related macular degeneration. Graefe's archive for clinical and experimental ophthalmology, 237(12):962–968, 1999.

[97] H. Sakai, Y. Tani, E. Shirasawa, Y. Shirao, and K. Kawasaki. Development of electroretinographic alterations in streptozotocin-induced diabetes in rats. Ophthalmic research, 27(1):57–63, 1995.

[98] S. Juen and G. F. Kieselbach. Electrophysiological changes in juvenile diabetics without retinopathy. Archives of ophthalmology, 108(3):372–375, 1990.

[99] S. E. Simonsen. The value of the oscillatory potential in selecting juvenile diabetics at risk of developing proliferative retinopathy. Acta ophthalmologica, 58(6):865–878, 1980.

[100] M. Segawa, Y. Hirata, S. Fujimori, and K. Okada. The development of electroretinogram abnormalities and the possible role of polyol pathway activity in diabetic hyperglycemia and galactosemia. Metabolism, 37(5): 454–460, 1988.

[101] E. J. Crampin, A. A. Gaffney, and P. K. Maini. Reaction and diffusion on growing domains: Scenarios for robust pattern formation. Bulletin of Mathematical Biology, 61(6):1093–1120, 1999.

[102] T. L. Jackson and H. M. Byrne. A mathematical model to study the effects of drug resistance ratio and vasculature on the response of solid tumors to chemotherapy. Mathematical Biosciences, 164(1):17–38, 2000.

[103] H. P. Greenspan. Models for the growth of a solid tumour by diffusion. Studies in Applied Mathematics, 52:317–340, 1972.

[104] C. T. Dollery, C. J. Bulpitt, and E. M. Kohner. Oxygen supply to the retina from the retinal and choroidal circulations at normal and increased arterial oxygen tensions. Investigative Ophthalmology and Visual Science, 8 (6):588–594, 1969.

[105] R. A. Linsenmeier. Effects of light and darkness on oxygen distribution and consumption in the cat retina. The Journal of General Physiology, 88:521–542, 1986.

[106] L. M. Haugh, R. A. Linsenmeier, and T. K. Goldstick. Mathematical models of the spatial distribution of retinal oxygen tension and consumption, including changes upon illumination. Annals of Biomedical Engineering, 18(1):19–36, 1990.

[107] M. Tsacopoulos and S. Poitry. Kinetics of oxygen consumption after a single flash of light in photoreceptors of the drone (apis mellifera). Journal of General Physiology, 80(1):19–55, 1982.

[108] S. Poitry, M. Tsacopoulos, A. Fein, and C. Cornwall. Kinetics of oxygen consumption and light-induced changes of nucleotides in solitary rod photoreceptors. Journal of General Physiology, 108(2):75–87, 1996.

[109] W. Hemmer, E. Zanolla, E. M. Furter-Graves, H. M. Eppenberger, and T. Wallimann. Creatine kinase lsoenzymes in chicken cerebellum: Specific localization of brain-type creatine kinase in Bergmann glial cells and muscle-type creatine kinase in purkinje neurons. European Journal of Neuroscience, 6(4):538–549, 1994.

[110] B. Alberts. Molecular Biology of the Cell. Garland Science, New York, 4 edition, 2002.

[111] M. Novotová, M. Pavlovicová, V. I. Veksler, R. Ventura-Clapier, and I. Zahradník. Ultrastructural remodeling of fast skeletal muscle fibers induced by invalidation of creatine kinase. Americal Journal of Physiology: Cell Physiology, 291(6):C1279–C1285, 2006.

[112] R. J. M. Lane, editor. Handbook of muscle disease. Marcel Dekker Inc., New York, 1996.

[113] R. A. Meyer, H. L. Sweeney, and M. J. Kushmerick. A simple analysis of the "phosphocreatine shuttle". American Journal of Physiology, 246(Cell Physiology 15):C365–C377, 1984.

[114] V. A. Saks, O. Kongas, M. Vendel, and L. Kay. Role of the creatine/phosphocreatine system in the regulation of mitochondrial respiration. Acta Physiologica Scandinavica, 168(4):635–641, 2000.

[115] A. P. Minton. The influence of macromolecular crowding and macromolecular confinement on biochemical reactions in physiological media. The Journal of Biophysical Chemistry, 276(14):10577–10580, 2001.

[116] S. Erickson-Viitanen, P. Viitaneng, P. J. Geiger, W. C. T. Yang, and S. P. Bessman. Compartmentation of mitochondrial creatine phosphokinase. The Journal of Biological Chemistry, 257(23):14395–14404, 1982.

[117] V. A. Selivanov, S. Krause, J. Roca, and M. Cascante. Modeling of spatial metabolite distributions in the cardiac sarcomere. Biophysical Journal, 92 (10):3492–3500, 2007.

[118] V. Saks, A. Kuznetsov, T. Andrienko, Y. Usson, F. Appaix, K. Guerrero, T. Kaambre, P. Sikk, M. Lemba, and M. Vendelin. Heterogeneity of ADP diffusion and regulation of respiration in cardiac cells. Biophysical Journal, 84(5):8436–8456, 2003.

[119] V. Saks, N. Beraud, and T. Wallimann. Metabolic compartmentation a system level property of muscle cells. International Journal of Molecular Sciences, 9:751–767, 2008.

[120] M. K. Aliev and V. A. Saks. Compartmentalized energy transfer in cardiomyocytes: Use of mathematical modeling for analysis of *In Vivo* regulation of respiration. Biophysical Journal, 73(1):428–445, 1997.

[121] B. Korzeniewski. Regulation of ATP supply during muscle contraction : theoretical studies. Biochemical Journal, 330(3):1189–1195, 1998.

[122] B. Korzeniewski and J. A. Zoladz. A model of oxidative phosphorylation in mammalian skeletal muscle. Biophysical Chemistry, 92(1–2):17–34, 2001.

[123] F. Wu, F. Yang, K. C. Vinnakota, and D. A. Beard. Computer modeling of mitochondrial tricarboxylic acid cycle, oxidative phosphorylation, metabolite transport, and electrophysiology. The Journal of Biological Chemistry, 282:24525–24537, 2007.

[124] M. Vendelin, O. Kongas, and V. Saks. Regulation of mitochondrial repiration in heart cells analyzed by reaction-diffusion model of energy transfer. American Journal of Physiology - Cell Physiology, 278:C747–C764, 2000.

[125] A. P. Hansen and K. Johansen. Diurnal patterns of blood glucose, serum free fatty acids, insulin, glucagon and growth hormone in normals and juvenile diabetics. Diabetologia, 6(1):27–33, 1970.

[126] G. G. Haddad and S. P. Yu. Brain Hypoxia and Ischemia: With Special Emphasis on Development. Contemporary Clinical Neuroscience. Humana Press, 2009. ISBN 9781603275798.

[127] G. P. Talwar and L. M. Srivastava. Textbook of biochemistry and human biology. PHI Learning, 2002. ISBN 9788120319653.

[128] R. D. Braun and R. A. Linsenmeier. Retinal oxygen tension and the electroretinogram during arterial occlusion in the cat. Investigative Ophthalmology and Visual Science, 36(3):523–541, 1995.

[129] D. Yu and S. J. Cringle. Oxygen distribution and consumption within the retina in vascularised and avascular retinas and in animal models of retinal disease. Progress in Retinal and Eye Research, 20:175–208, 2001.

[130] S. Duke-Elder and K. C. Wybar. System of Ophthalmology, volume II. The anatomy of the visual system. C. V. Mosby Co, St. Louis, first edition, 1961.

[131] J. R. Levick. An Introduction to Cardiovascular physiology. Arnold, London, third edition, 2000.

[132] S. J. Cringle., D. Yu, and E. Su. Intraretinal oxygen consumption in the rat *In Vivo*. Investigative Ophthalmology and Visual Science, 43:1922–1927, 2002.

[133] T. A. Bailey, R. A. Alexander, S. R. Dubovy, P. J. Luthert, and N. H. V. Chong. Measurement of TIMP–3 expression and Bruch's membrane thickness in human macula. Experimental Eye Research, 73:851–858, 2001.

[134] J. J. Nordlund, R. E. Boissy, V. J. Hearing, W. Oetting, R. King, and J. Ortonne. The Pigmentary System: Physiology and Pathophysiology. Blackwell Publishing, Oxford, 2006.

[135] B. B. Benson and D. Krause Jr. The concentration and isotopic fractionation of oxygen dissolved in freshwater and seawater in equilibrium with the atmosphere. Limnology and Oceanography, 29:620–632, 1984.

[136] P. T. V. M. De Jong. Age-related macular degeneration. New England Journal of Medicine, 355(14):1474–1485, 2006.

[137] W. H. Press. Numerical Recipes 3rd Edition: The Art of Scientific Computing. Cambridge University Press, 2007.

[138] M. N. O. Sadiku and C. N. Obiozor. A simple introduction to the method of lines. International Journal of Electrical Engineering Education, 37(3): 282–296, 2000.

[139] E. Zauderer. Patial Differential Equations of Applied Mathematics. John Wiley and Sons, New Jersey, third edition, 2006.

[140] W. E. Schiesser. The Numerical Method of Lines. Academic Press, San Diego, California, 1991.

[141] L. F. Shampine and M. W. Reichelt. The Matlab ODE suite. SIAM Journal on Scientific Computing, 18(1):1–22, 1997.

[142] M. Schmidt, A. Giessl, T. Laufs, T. Hankeln, U. Wolfrum, and T. Burmester. How does the eye breathe? Evidence for neuroglobin-mediated oxygen supply in the mammalian retina. Journal of Biological Chemistry, 278(3): 1932–1935, 2003.

[143] T. Burmester and T. Hankeln. Neuroglobin: a respiratory protein of the nervous system. Physiology, 19(3):110–113, 2004.

[144] P. Tosqui and M. F. Colombo. Neuroglobin and cytoglobin: two new members of globin family. Revista brasileira de hematologia e hemoterapia, 33(4):307–311, 2011.

[145] J. G. Reich and E. E. Selkov. Energy metabolism of the cell. Academic Press, London, 1981.

[146] J. L. Treichel, M. M. Henry, C. M. B. Skumatz, J. T. Eells, and J. M. Burke. Formate, the toxic metabolite of methanol, in cultured ocular cells. NeuroToxicology, 24:825–834, 2003.

[147] H. Sun, R. S. Molday, and J. Nathans. Retinal stimulates ATP hydrolysis by purified and reconstituted ABCR, the photoreceptor-specific ATP-binding cassette transporter responsible for Stargardt disease. The Journal of Biological Chemistry, 274(12):8269–8281, 1999.

[148] T. Wallimann, M. Wyss, D. Brdiczka, K. Nicolay, and H. M. Eppenberger. Intracellular compartmentation, structure and function of creatine kinase isoenzymes in tissues with high and fluctuating energy demands: the 'phosphocreatine circuit' for cellular energy homeostasis. Biochemical Journal, 281(1):21–40, 1992.

[149] H. J. Green, R. L. Hughson, G. W. Orr, and D. A. Ranney. Anaerobic threshold, blood lactate, and muscle metabolites in progressive exercise. Journal of Applied Physiology, 54:1032–1038, 1983.

[150] K. Yoshizaki, Y. Seo, H. Nishikawa, and T. Morimoto. Application of pulsed-gradient ^{31}P NMR on frog muscle to measure the diffusion rates of phosphorus compounds in cells. Biophysical Journal, 38:209–211, 1982.

[151] J. Mendez and A. Keys. Density and composition of mammalian muscle. Metabolism, 9:184–188, 1960.

[152] S. A. Smith, S. J. Montain, R. P. Matott, G. P. Zientara, F. A. Jolesz, and R. A. Fielding. Effects of creatine supplementation on the energy cost of muscle contraction: a ^{31} P-MRS study. Journal of Applied Physiology, 87: 116–123, 1999.

[153] J. R. Williamson, C. Ford, J. Illingworth, and B. Safer. Coordination of citric acid cycle activity with electron transport flux. Circulation research, 38(5 Suppl 1):I39–51, 1976.

[154] L. Notari, I. M. Pepe, C. Cugnoli, and A. Morellia. Adenylate kinase activity in rod outer segments of bovine retina. Biochimica et Biophysica Acta – Bioenergetics, 1504(2–3):438–443, 2001.

[155] J. A. Bittl and J. S. Ingwall. Reaction rates of creatine kinase and ATP synthesis in the isolated rat heart. Journal of Biological, 260:3512–3517, 1985.

[156] R. Simó, J. M. Sundstrom, and D. A. Antonetti. Ocular anti-VEGF therapy for diabetic retinopathy: the role of VEGF in the pathogenesis of diabetic retinopathy. Diabetes care, 37(4):893–899, 2014.

[157] Y. Liu, M. Wang, A. D. Morris, A. S. F. Doney, G. P. Leese, E. R. Pearson, and C. N. A. Palmer. Glycemic exposure and blood pressure influencing progression and remission of diabetic retinopathy a longitudinal cohort study in GoDARTS. Diabetes care, 36(12):3979–3984, 2013.

[158] B. S. Meldrum. Glutamate as a neurotransmitter in the brain: Review of physiology and pathology. The Journal of Nutrition, 130:107S–1015S, 2000.

[159] X. Yang. Characterization of receptors for glutamate and GABA in retinal neurons. Progress in neurobiology, 73(2):127–150, 2004.

[160] O. A. C. Petroff. Book review: GABA and glutamate in the human brain. The Neuroscientist, 8(6):562–573, 2002.

[161] K. L. Davis. Neuropsychopharmacology: The Fifth Generation of Progress: an Official Publication of the American College of Neuropsychopharmacology. M - Medicine Series. Lippincott Williams & Wilkins, 2002.

[162] S. Brady, G. Siegel, R. W. Albers, and D. Price. Basic Neurochemistry: Molecular, Cellular and Medical Aspects. Elsevier Science, 2005.

[163] M. Simard, G. Arcuino, T. Takano, Q. S. Liu, and M. Nedergaard. Signaling at the gliovascular interface. The Journal of neuroscience, 23(27): 9254–9262, 2003.

[164] K. Kacem, P. Lacombe, J. Seylaz, and G. Bonvento. Structural organization of the perivascular astrocyte endfeet and their relationship with the endothelial glucose transporter: a confocal microscopy study. Glia, 23(1): 1–10, 1998.

[165] P. J. Magistretti, L. Pellerin, D. L. Rothman, and R. G. Shulman. Energy on demand. Science, 283:496–497, 1999.

[166] L. Demetrius, P. J. Magistretti, and L. Pellerin. Alzheimer's disease: the Amyloid hypothesis and the Inverse Warburg effect. Frontiers in Physiology, 5(522):522, 2015.

[167] C. Iadecola and M. Nedergaard. Glial regulation of the cerebral microvasculature. Nature neuroscience, 10(11):1369–1376, 2007.

[168] A. B. Patel, J. C. K. Lai, G. M. I. Chowdhury, F. Hyder, D. L. Rothman, R. G. Shulman, and K. L. Behar. Direct evidence for activity-dependent glucose phosphorylation in neurons with implications for the astrocyte-to-neuron lactate shuttle. Proceedings of the National Academy of Sciences, 111 (14):5385–5390, 2014.

[169] M. A. Tarczyluk, D. A. Nagel, J. D. O'Neil, H. R. Parri, E. H. Y. Tse, M. D. Coleman, and E. J. Hill. Functional astrocyte–neuron lactate shuttle in a human stem cell-derived neuronal network. Journal of Cerebral Blood Flow & Metabolism, 33(9):1386–1393, 2013.

[170] L. Pellerin and P. J. Magistretti. Sweet sixteen for ANLS. Journal of Cerebral Blood Flow & Metabolism, 32(7):1152–1166, 2012.

[171] A. Bouzier-Sore and L. Pellerin. Unraveling the complex metabolic nature of astrocytes. Frontiers in cellular neuroscience, 7(179):1–13, 2013.

[172] M. Bélanger, I. Allaman, and P. J. Magistretti. Brain energy metabolism: focus on astrocyte-neuron metabolic cooperation. Cell metabolism, 14(6): 724–738, 2011.

[173] A. Reichenbach and A. Bringmann. Müller Cells in the Healthy and Diseased Retina. Springer, 2010.

[174] A. Gjedde and S. Marrett. Glycolysis in neurons, not astrocytes, delays oxidative metabolism of human visual cortex during sustained checkerboard stimulation *in vivo*. Journal of Cerebral Blood Flow & Metabolism, 21(12):1384–1392, 2001.

[175] S. Poitry, C. Poitry-Yamate, J. Ueberfeld, P. R. MacLeish, and M. Tsacopoulos. Mechanisms of glutamate metabolic signaling in retinal glial (Müller) cells. The Journal of Neuroscience, 20:1809–1821, 2000.

[176] C. M. Anderson and R. A. Swanson. Astrocyte glutamate transport. Glia, 32:1–14, 2000.

[177] L. Hertz. Functional interactions between neurons and astrocytes I. Turnover and metabolism of putative amino acid transmitters. Progress in Neurobiology, 13:277–323, 1979.

[178] Y. Daikhin and M. Yudkoff. Compartmentation of brain glutamate metabolism in neurons and glia. The Journal of Nutrition, 130:1026S–1031S, 2000.

[179] Y. I. Shigeri, R. P. Seal, and K. Shimamoto. Molecular pharmacology of glutamate transporters, EAATs and VGLUTs. Brain Research Reviews, 45:250–265, 2004.

[180] V. Lebon, K. F. Petersen, G. W. Cline, J. Shen, G. F. Mason, S. Dufour, K. L. Behar, G. I. Shulman, and D. L. Rothman. Astroglial contribution to brain energy metabolism in humans revealed by ^{13}C nuclear magnetic resonance spectroscopy: Elucidation of the dominant pathway for neurotransmitter glutamate repletion and measurement of astrocytic oxidative metabolism. The Journal of Neuroscience, 22:1523–1531, 2002.

[181] B. V. Bui, M. Kalloniatis, and A. J. Vingrys. Retinal function loss after monocarboxylate transport inhibition. Investigative Ophthalmology and Visual Science, 45:584–593, 2004.

[182] E. Lieth, K. F. LaNoue, D. A. Antonetti, M. Ratza, and The Penn State Retina Research Group. Diabetes reduces glutamate oxidation and glutamine synthesis in the retina. Experimental Eye Research, 70(6):723–730, 2000.

[183] M. A. García-Espinosa, T. B. Rodrigues, A. Sierra, M. Benito, C. Fonseca, H. L. Gray, B. L. Bartnik, M. L. García-Martín, P. Ballesteros, and S. Cerdán. Cerebral glucose metabolism and the glutamine cycle as detected by *in vivo* and *in vitro* ^{13}C NMR spectroscopy. Neurochemistry International, 45:297–303, 2004.

[184] J. Engel Jr, T. A. Pedley, J. Aicardi, and M. A. Dichter. Epilepsy: A Comprehensive Textbook, volume 1. Lippincott Williams and Wilkins, second edition, 2008.

[185] A. Blot, D. Billups, M. Bjørkmo, A. Z. Quazi, N. M. Uwechue, F. A. Chaudhry, and B. Billups. Functional expression of two system A glutamine transporter isoforms in rat auditory brainstem neurons. Neuroscience, 164:998–1008., 2009.

[186] R. A. Hawkins. The blood-brain barrier and glutamate. The American Journal of Clinical Nutrition, 90:867S–874S, 2009.

[187] J. M. Berg, J. L. Tymoczko, and L. Stryer. Biochemistry. W. H. Freeman, sixth edition, 2008.

[188] S. Jitrapakdee and J. C. Wallace. Structure, function and regulation of pyruvate carboxylase. Biochemical Journal, 340:1–16, 1999.

[189] V. Mastorodemos, I. Zaganas, C. Spanaki, M. Bessa, and A. Plaitakis. Molecular basis of human glutamate dehydrogenase under changing energy demands. Journal of Neuroscience Research, 79:65–73, 2005.

[190] W. C. Gamberino, D. A. Berkich, C. J. Lynch, B. Xu, and K. F. LaNoue. Role of pyruvate carboxylase in facilitation of synthesis of glutamate and glutamine in cultured astrocytes. Journal of Neurochemistry, 69: 2312–2325, 1997.

[191] M. C. McKenna, J. H. Stevenson, X. Huang, and I. B. Hopkins. Differential distribution of the enzymes glutamate dehydrogenase and aspartate aminotransferase in cortical synaptic mitochondria contributes to metabolic compartmentation in cortical synaptic terminals. Neurochemistry International, 37:229–241, 2000.

[192] N. R. Sibson, A. Dhankhar, G. F. Mason, D. L. Rothman, K. L. Behar, and R. G. Shulman. Stoichiometric coupling of brain glucose metabolism and

glutamatergic neuronal activity. Proceedings of the National Acacemy of Sciences of the United States of America, 95:316–321, 1998.

[193] S. J. Vannucci, F. Maher, and I. A. Simpson. Glucose transporter proteins in brain: Delivery of glucose to neurons and glia. Glia, 21:2–21, 1997.

[194] L. Hertz and G. A. Dienel. Lactate transport and transporters: General principles and functional roles in brain cells. Journal of Neuroscience Research, 79:11–18, 2004.

[195] A. Loaiza, O. H. Porras, and L. F. Barros. Glutamate triggers rapid glucose transport stimulation in astrocytes as evidenced by real–time confocal microscopy. The Journal of Neuroscience, 23:7337–7342, 2003.

[196] S. Nagamatsu, H. Sawa, K. Kamada, Y. Nakamichi, K. Yoshimoto, and T. Hoshino. Neuron–specific glucose transporter (NSGT): CNS distribution of GLUT3 rat glucose transporter (RGT3) in rat central neurons. Federation of European Biochemical Societies Letters, 3:289–295, 1993.

[197] F. Maher, T. M. Davies-Hill, P. G. Lysoko, R. C. Henneberry, and I. A. Simpson. Expression of two glucose transporters, GLUT1 and GLUT3, in cultured cerebellar neurons: Evidence for neuron–specific expression of GLUT3. Molecular and Cellular Neurosciences, 2:351–360, 1991.

[198] A. P. Halestrap and N. T. Price. The proton–linked monocarboxylate transporter (MCT) family: structure, function and regulation. Biochemical Journal, 343:281–299, 1999.

[199] S. Bröer, B. Rahman, G. Pellegri, L. Pellerin, J. Martin, S. Verleysdonk, B. Hamprecht, and P. J. Magistretti. Comparison of lactate transport in astroglial cells and monocarboxylate transporter 1 (MCT 1) expressing xenopus laevis oocytes. The Journal of Biological Chemistry, 272:30096–30102, 1997.

[200] S. Kahlert and G. Reiser. Glial perspectives of metabolic states during cerebral hypoxia–calcium regulation and metabolic energy. Cell Calcium, 36:295–302, 2004.

[201] Q. Tong, C. Ye, R. J. McCrimmon, H. Dhillon, B. Choi, M. D. Kramer, J. Yu, Z. Yang, L. M. Christiansen, C. E. Lee, C. S. Choi, J. M. Zigman, G. I. Shulman, R. S. Sherwin, J. K. Elmquist, and B. B. Lowell. Synaptic

glutamate release by ventromedial hypothalamic neurons is part of the neurocircuitry that prevents hypoglycemia. Cell Metabolism, 5:383–393, 2007.

[202] P. M. Burger, E. MehI, P. Cameron, P. R. Maycox, M. Baumert, F. Lottspeich, P. De Camilli, and R. Jahn. Synaptic vesicles immunoisolated from rat cerebral cortex contain high levels of glutamate. Neuron, 3:715–720, 1989.

[203] T. Li, F. K. Ghishan, and L. Bai. Molecular physiology of vesicular glutamate transporters in the digestive system. World Journal of Gastroenterology, 11:1731–1736, 2005.

[204] T. Mukherjee, D. Mandal, and A. Bhaduri. Leishmania plasma membrane Mg^{2+}–ATPase is a H^+/K^+–antiporter involved in glucose symport. The Journal of Biological Chemistry, 276:5563–5569, 2001.

[205] S. Naito and T. Ueda. Characterization of glutamate uptake into synaptic vesicles. Journal of Neurochemistry, 44:99–109, 1985.

[206] J. T. Russell. δpH, H^+ diffusion potentials, and Mg^{2+} ATPase in neurosecretory vesicles isolated from bovine neurohypophyses. The Journal, 259: 9496–9507, 1984.

[207] L. Toll and B. D. Howard. Role of Mg^{2+}–ATPase and a pH gradient in the storage of catecholamines in synaptic vesicles. Catecholamines in Synaptic Vesicles, 17:2517–2523, 1978.

[208] O. P. Ottersen and J. Storm-Mathisen. Glutamate. Elsevier, 2000.

[209] M. S. Gazzaniga. The cognitive neurosciences. MIT Press, 2004.

[210] N. Zerangue and M. P. Kavanaugh. Flux coupling in a neuronal glutamate transporter. Nature, 383:634–637, 1996.

[211] Y. Chen and R. A. Swanson. Astrocytes and brain injury. Journal of Cerebral Blood Flow & Metabolism, 23(2):137–149, 2003.

[212] R. G. Shulman, F. Hyder, and D. L. Rothman. Cerebral energetics and the glycogen shunt: Neurochemical basis of functional imaging. Proceedings of the National Academy of Sciences of the United States of America, 98: 6417–6422, 2001.

[213] S. Bröer and N. Brookes. Transfer of glutamine between astrocytes and neurons. 77, 77:705–719, 2001.

[214] B. P. Bode. Recent molecular advances in mammalian glutamine transport. The Journal of Nutrition, 131:2475S–2485S, 2001.

[215] M. Erecińska and I. A. Silver. Metabolism and role of glutamate in mammalian brain. Progress in Neurobiology, 35:245–296, 1990.

[216] J. H. Byrne and J. L. Roberts, editors. From molecules to networks: an introduction to cellular and molecular neuroscience. Academic Press, 2009.

[217] H. A. Krebs. Metabolism of amino-acids: The synthesis of glutamine from glutamic acid and ammonia, and the enzymic hydrolysis of glutamine in animal tissues. Biochemical Journal, 29:1951–1969, 1935.

[218] A. J. Barber, E. Lieth, K. Lieth, A. Sonny, D. A. Antonetti, A. G. Buchanan, and T. W. Gardner. Neural apoptosis in the retina during experimental and human diabetes. early onset and effect of insulin. Journal of Clinical Investigation, 102(4):783, 1998.

[219] B. T. Hawkins, T. F. Lundeen, K. M. Norwood, H. L. Brooks, and R. D. Egleton. Increased blood–brain barrier permeability and altered tight junctions in experimental diabetes in the rat: contribution of hyperglycaemia and matrix metalloproteinases. Diabetologia, 50(1):202–211, 2007.

[220] J. C. M. Lau, R. A. Kroes, J. R. Moskal, R. Joseph, and R. A. Linsenmeier. Diabetes changes expression of genes related to glutamate neurotransmission and transport in the Long-Evans rat retina. Molecular vision, 19: 1538, 2013.

[221] E. Lieth, A. J. Barber, B. Xu, C. Dice, M. J. Ratz, D. Tanase, and J. M. Strother. Glial reactivity and impaired glutamate metabolism in short-term experimental diabetic retinopathy. Penn State Retina Research Group. Diabetes, 47(5):815–820, 1998.

[222] Q. Li and D. G. Puro. Diabetes-induced dysfunction of the glutamate transporter in retinal Müller cells. Investigative ophthalmology & visual science, 43(9):3109–3116, 2002.

[223] T. Höfer, L. Venance, and C. Giaume. Control and plasticity of intercellular calcium waves in astrocytes: a modeling approach. The Journal of neuroscience, 22(12):4850–4859, 2002.

[224] A. Reichenbach, J. U. Stolzenburg, W. Eberhardt, T. I. Chao, D. Dettmer, and L. Hertz. What do retinal Müller (glial) cells do for their neuronal small siblings? Journal of chemical neuroanatomy, 6(4):201–213, 1993.

[225] P. Marcaggi, D. T. Thwaites, J. W. Deitmer, and J. A. Coles. Chloride-dependent transport of NH^{4+} into bee retinal glial cells. European Journal of Neuroscience, 11(1):167–177, 1999.

[226] A. M. Bailey, B. C. Thorne, and S. M. Peirce. Multi-cell agent-based simulation of the microvasculature to study the dynamics of circulating inflammatory cell trafficking. Annals of biomedical engineering, 35(6): 916–936, 2007.

[227] N. Cannata, F. Corradini, and E. Merelli. Multiagent modelling and simulation of carbohydrate oxidation in cell. International Journal of Modelling, Identification and Control, 3(1):17–28, 2008.

[228] G. Broderick, M. Ru'aini, E. Chan, and M. J. Ellison. A life-like virtual cell membrane using discrete automata. *In silico* biology, 5(2):163–178, 2005.

[229] J. Kleinle, K. Vogt, H. R. Lüscher, L. Müller, W. Senn, K. Wyler, and J. Streit. Transmitter concentration profiles in the synaptic cleft: an analytical model of release and diffusion. Biophysical journal, 71(5): 2413–2426, 1996.

[230] H. C. Tuckwell and R. M. Miura. A mathematical model for spreading cortical depression. Biophysical journal, 23(2):257–276, 1978.

[231] E. Somersalo, Y. Cheng, and D. Calvetti. The metabolism of neurons and astrocytes through mathematical models. Annals of biomedical engineering, 40(11):2328–2344, 2012.

[232] A. K. Gombert and J. Nielsen. Mathematical modelling of metabolism. Current Opinion in Biotechnology, 11(2):180–186, 2000.

[233] R. Gruetter, E. R. Seaquist, and K. Ugurbil. A mathematical model of compartmentalized neurotransmitter metabolism in the human brain.

American Journal of Physiology-Endocrinology And Metabolism, 281(1): E100–E112, 2001.

[234] G. F. Mason, D. L. Martin, S. B. Martin, D. Manor, N. R. Sibson, A. Patel, D. L. Rothman, and K. L. Behar. Decrease in GABA synthesis rate in rat cortex following GABA-transaminase inhibition correlates with the decrease in GAD 67 protein. Brain research, 914(1):81–91, 2001.

[235] N. R. Sibson, G. F. Mason, J. Shen, G. W. Cline, A. Z. Herskovits, J. E. M. Wall, K. L. Behar, D. L. Rothman, and R. G. Shulman. In vivo ^{13}C NMR measurement of neurotransmitter glutamate cycling, anaplerosis and TCA cycle flux in rat brain during [2-^{13}C] glucose infusion. Journal of neurochemistry, 76(4):975–989, 2001.

[236] J. M. N. Duarte, B. Lanz, and R. Gruetter. Compartmentalized cerebral metabolism of [1, 6–^{13}C] glucose determined by *in vivo* ^{13}C NMR spectroscopy at 14.1 T. Frontiers in neuroenergetics, 3:1–15, 2011.

[237] F. A. Massucci, M. Di Nuzzo, F. Giove, B. Maraviglia, I. P. Castillo, E. Marinari, and A. De Martino. Energy metabolism and glutamate-glutamine cycle in the brain: a stoichiometric modeling perspective. BMC systems biology, 7(1):103, 2013.

[238] M. Cloutier, F. B. Bolger, J. P. Lowry, and P. Wellstead. An integrative dynamic model of brain energy metabolism using in vivo neurochemical measurements. Journal of computational neuroscience, 27(3):391–414, 2009.

[239] I. A. Simpson, A. Carruthers, and S. J. Vannucci. Supply and demand in cerebral energy metabolism: the role of nutrient transporters. Journal of Cerebral Blood Flow & Metabolism, 27(11):1766–1791, 2007.

[240] D. Calvetti and E. Somersalo. Dynamic activation model for a glutamatergic neurovascular unit. Journal of theoretical biology, 274(1):12–29, 2011.

[241] A. Aubert and R. Costalat. A model of the coupling between brain electrical activity, metabolism, and hemodynamics: application to the interpretation of functional neuroimaging. Neuroimage, 17(3):1162–1181, 2002.

[242] A. Aubert, R. Costalat, P. J. Magistretti, and L. Pellerin. Brain lactate kinetics: modeling evidence for neuronal lactate uptake upon activation. Proceedings of the National Academy of Sciences of the United States of America, 102(45):16448–16453, 2005.

[243] L. F. Barros, O. H. Porras, and C. X. Bittner. Why glucose transport in the brain matters for PET. Trends in neurosciences, 28(3):117–119, 2005.

[244] R. B. Buxton, E. C. Wong, and L. R. Frank. Dynamics of blood flow and oxygenation changes during brain activation: the balloon model. Magnetic resonance in medicine, 39(6):855–864, 1998.

[245] A. Gjedde. Cerebrovascular disease, chapter The relation between brain function and cerebral blood flow and metabolism, pages 23–40. Lippincott-Raven, Philadelphia, 1997.

[246] M. S. Vafaee and A. Gjedde. Model of blood-brain transfer of oxygen explains nonlinear flow-metabolism coupling during stimulation of visual cortex. Journal of Cerebral Blood Flow & Metabolism, 20(4):747–754, 2000.

[247] R. Heinrich and S. Schuster. The Regulation of Cellular Systems. Springer US, 2012.

[248] R. Heinrich and S. Schuster. The regulation of cellular systems. 1996. New York: Chapman & Hall, 1996.

[249] J. Duarte and R. Gruetter. Characterization of cerebral glucose dynamics *in vivo* with a four–state conformational model of transport at the blood–brain barrier. Journal of neurochemistry, 121(3):396–406, 2012.

[250] M. Di Nuzzo, F. Giove, and B. Maraviglia. A biochemical framework for modeling the functional metabolism of the human brain. Biophysics and Bioengineering Letters, 1–26(2):2, 2010.

[251] M. DiNuzzo, S. Mangia, B. Maraviglia, and F. Giove. Changes in glucose uptake rather than lactate shuttle take center stage in subserving neuroenergetics: evidence from mathematical modeling. Journal of Cerebral Blood Flow & Metabolism, 30(3):586–602, 2009.

[252] A. Aubert, L. Pellerin, P. J. Magistretti, and R. Costalat. A coherent neurobiological framework for functional neuroimaging provided by a model integrating compartmentalized energy metabolism. Proceedings of the National Academy of Sciences, 104(10):4188–4193, 2007.

[253] M. Rizzi, M. Baltes, U. Theobald, and M. Reuss. *In vivo* analysis of metabolic dynamics in saccharomyces cerevisiae: II. Mathematical model. Biotechnology and bioengineering, 55(4):592–608, 1997.

[254] R. Jolivet, P. J. Magistretti, and B. Weber. Deciphering neuron-glia compartmentalization in cortical energy metabolism. Frontiers in neuroenergetics, 1:4, 2009.

[255] S. Mangia, I. A. Simpson, S. J. Vannucci, and A. Carruthers. The *in vivo* neuron-to-astrocyte lactate shuttle in human brain: Evidence from modeling of measured lactate levels during visual stimulation. Journal of neurochemistry, 109(s1):55–62, 2009.

[256] M. DiNuzzo, S. Mangia, B. Maraviglia, and F. Giove. Glycogenolysis in astrocytes supports blood-borne glucose channeling not glycogen-derived lactate shuttling to neurons: evidence from mathematical modeling. Journal of Cerebral Blood Flow & Metabolism, 30(12):1895–1904, 2010.

[257] S. Mangia, I. Tkáč, R. Gruetter, P. Van de Moortele, B. Maraviglia, and K. Uğurbil. Sustained neuronal activation raises oxidative metabolism to a new steady-state level: evidence from ^{1}H NMR spectroscopy in the human visual cortex. Journal of Cerebral Blood Flow & Metabolism, 27 (5):1055–1063, 2007.

[258] R. Jolivet, I. Allaman, L. Pellerin, P. J. Magistretti, and B. Weber. Comment on recent modeling studies of astrocyte–neuron metabolic interactions. Journal of Cerebral Blood Flow & Metabolism, 30(12):1982–1986, 2010.

[259] R. Guillevin, C. Menuel, J. Vallée, J. Françoise, L. Capelle, C. Habas, G. De Marco, J. Chiras, and R. Costalat. Mathematical modeling of energy metabolism and hemodynamics of WHO grade II gliomas using *in vivo* MR data. Comptes rendus biologies, 334(1):31–38, 2011.

[260] R. Costalat, J. Francoise, C. Menuel, M. Lahutte, J. Vallée, G. De Marco, J. Chiras, and R. Guillevin. Mathematical modeling of metabolism and hemodynamics. Acta biotheoretica, 60(1-2):99–107, 2012.

[261] M. Lahutte-Auboin, R. Guillevin, J. Françoise, J. Vallée, and R. Costalat. On a minimal model for hemodynamics and metabolism of lactate: application to low grade glioma and therapeutic strategies. Acta biotheoretica, 61(1):79–89, 2013.

[262] P. Orlowski, M. Chappell, C. S. Park, V. Grau, and S. Payne. Modelling of pH dynamics in brain cells after stroke. Interface focus, 1(3):408–416, 2011.

[263] P. Orlowski, D. O'Neill, V. Grau, Y. Ventikos, and S. Payne. Modelling of the physiological response of the brain to ischaemic stroke. Interface focus, 3(2):20120079, 2013.

[264] M. Cloutier and P. Wellstead. Dynamic modelling of protein and oxidative metabolisms simulates the pathogenesis of Parkinson's disease. Systems Biology, IET, 6(3):65–72, 2012.

[265] S. Genc, I. A. Kurnaz, and M. Ozilgen. Astrocyte–neuron lactate shuttle may boost more ATP supply to the neuron under hypoxic conditions–*in silico* study supported by *in vitro* expression data. BMC systems biology, 5(1):162, 2011.

[266] S. Genc, E. Sorguven, M. Ozilgen, and K. I. Aksan. Unsteady exergy destruction of the neuron under dynamic stress conditions. Energy, 59: 422–431, 2013.

[267] G. R. Mirams, H. M. Byrne, and J. R. King. A multiple timescale analysis of a mathematical model of the Wnt/β-catenin signalling pathway. Journal of mathematical biology, 60(1):131–160, 2010.

[268] A. Aubert, R. Costalat, and R. Valabrègue. Modelling of the coupling between brain electrical activity and metabolism. Acta Biotheoretica, 49: 301–326, 2001.

[269] W. M. Pardridge. Brain metabolism: A perspective from the blood–brain barrier. Physiological Reviews, 63(4):1481–1535, 1983.

[270] L. Leybaert. Neurobarrier coupling in the brain: A partner of neurovascular and neurometabolic coupling? Journal of Cerebral Blood Flow and Metabolism, 25:2–16, 2005.

[271] J. Y. Khan, R. A. Rajakumar, R. A. McKnight, U. P. Devaskar, and S. U. Devaskar. Developmental regulation of genes mediating murine brain glucose uptake. American Journal of Physiology, 276:R892–R900, 1999.

[272] M. Holbein, M. Béchir, S. Ludwig, J. Sommerfield, S. R. Cottini, M. Keel, R. Stocker, and J. F. Stover. Differential influence of arterial blood glucose on cerebral metabolism following severe traumatic brain injury. Critical Care, 13(1):R13, 2009.

[273] A. Bouzier-Sore, P. Voisin, V. Bouchaud, E. Bezancon, J. Franconi, and L. Pellerin. Competition between glucose and lactate as oxidative energy substrates in both neurons and astrocytes: A comparitive NMR study. European Journal of Neuroscience, 24:1687–1694, 2006.

[274] J. V. Passonneau, R. A. Hawkins, W. D. Last, and F. A. Welsh, editors. Cerebral Metabolism and Neural Function. Williams and Wilkins, 1980.

[275] W. M. Abi-Saab, D. G. Maggs, T. Jones, R. Jacob, V. Srihari, J. Thompson, D. Kerr, P. Leone, J. H. Krystal, D. D. Spencer, M. J. During, and R. S. Sherwin. Striking differences in glucose and lactate levels between brain extracellular fluid and plasma in conscious human subjects: Effects of hyperglycemia and hypoglycemia. Journal of Cerebral Blood Flow and Metabolism, 22:271–279, 2002.

[276] D. Lafrance, L. C. Lands, and D. H. Burns. Measurement of lactate in whole human blood with near–infrared transmission spectroscopy. Talanta, 60(4):635–641, 2003.

[277] S. S. L. Anderson. Expression and purification of recominant vesicular glutamate transporter VGLUT1 using PC12 cells and High Five insect cells. Biological Procedures Online, 6(1):105–112, 2004.

[278] S. Duan, C. M. Anderson, B. A. Stein, and R. A. Swanson. Glutamate induces rapid upregulation of astrocyte glutamate transport and cell-surface expression of GLAST. The Journal of Neuroscience, 9(23):10193–10200, 1999.

[279] T. L. Smith and A. Zsigo. Increased Na^+–dependent uptake in astrocytes chronically exposed to ethanol. Neuroscience Letters, 218:142–144, 1996.

[280] M. Palmada and J. J. Centelles. Excitatory amino acid neurotransmission. pathways for metabolism, storage and reuptake of glutamate in brain. Frontiers in Bioscience, 3:701–718, 1998.

[281] H. A. H. D'haenen, J. A. den Boer, and P. Willner. Biological Psychiatry, volume 1. John Wiley and Sons, 2002.

[282] F. Rosier, D. Lambert, and M. Mertens-Strijthagen. Effect of glucose deprivation on rat glutamine synthetase in cultured astrocytes. Biochemical Journal, 315:607–612, 1996.

[283] V. Pamiljans, P. R. Krishnaswamy, G. Dumville, and A. Meister. Studies on the mechanism of glutamine synthesis; isolation and properties of the enzyme from sheep brain. Biochemistry, 1(1):153–158, 1962.

[284] A. M. Benjamin. Control of glutaminase activity in rat brain cortex *In Vitro*: Influence of glutamate, phosphate, ammonium, calcium and hydrogen ions. Brain Research, 208:363–377, 1981.

[285] K. R. Sheu and J. P. Blass. The α–ketoglutarate dehydrogenase complex. Annals of the New York Academy of Sciences, 893:61–78, 1999.

[286] L. Hertz and G. A. Dienel. Energy metabolism in the brain. International Review of Neurobiology, 51:1–102, 2002.

[287] A. Gualberto, P. Molinero, and F. Sobrino. The effect of experimental hypothyroidism on phosphofructokinase activity and fructose 2, 6–biphosphate concentrations in rat heart. Biochemical Journal, 244:137–142, 1987.

[288] J. R. Williamson. Glycolytic control mechanisms I: Inhibitions of glycolysis by acetate and pyruvate in the isolated, perfused rat heart. Journal of Biological Chemistry, 240:2308–2321, 1965.

[289] C. T. Putman, M. P. Matsos, E. Hultman, N. L. Jones, and G. J. F. Heigenhauser. Pyruvate dehydrogenase activation in inactive muscle during and after maximal exercise in men. American Journal of Physiology, 276(3): E483–E488, 1999.

[290] C. T. Putman, N. L. Jones, L. C. Lands, T. M. Bragg, M. G. Hollidge-Horvat, and G. J. F. Heigenhauser. Skeletal muscle pyruvate dehydrogenase activity during maximal exercise in humans. American Journal of Physiology, 269:E458–E468, 1995.

[291] E. Pineda, R. Encalada, J. S. Rodríguez-Zavala, A. Olivos-García, R. Moreno-Sánchez, and E. Saavedra. Pyruvate: Ferredoxin oxidoreductase and bifunctional aldehyde–alcohol dehydrogenase are essential for energy metabolism under oxidative stress in entamoeba histolytica. The Federation of European Biochemical Societies Journal, 277:3382–3395, 2010.

[292] G. E. Cold and B. L. Dahl. Topics in neuroanaesthesia and neurointensive care: experimental and clinical studies upon cerebral circulation metabolism and intercranial pressure. Springer, 2002.

[293] R. Milner. The Encyclopedia of Evolution: Humanity's Search For Its Origins. Holt, 1993.

[294] R. D. Fields. Chair's introduction. In Purinergic signalling in neuron-glia interactions, volume 276. John Wiley and Sons, 2006.

[295] H. C. Hemmings and P. M. Hopkins. Foundations of anesthesia: basic sciences for clinical practice. Elsevier Health Sciences, 2006.

[296] L. Sherwood. Human physiology: from cells to systems. Cengage Learning, 2008.

[297] G. I. Hatton and V. Parpura. Glial neuronal signaling, volume 1. Springer, 2004.

[298] R. Gruetter, E. J. Novotny, S. D. Boulware, D. L. Rothman, G. F. Mason, G. I. Shulman, R. G. Shulman, and W. V. Tamborlane. Direct measurement of brain glucose concentrations in humans by ^{13}C NMR spectroscopy. Proceedings of the National Academy of Sciences, 89(3):1109–1112, 1992.

[299] Q. R. Smith. Transport of glutamate and other amino acids at the blood-brain barrier. The Journal of nutrition, 130(4):1016S–1022S, 2000.

[300] C. Chih and E. L. Roberts. Energy substrates for neurons during neural activity: A critical review of the astrocyte-neuron lactate shuttle hypothesis. Journal of Cerebral Blood Flow & Metabolism, 23(11):1263–1281, 2003.

[301] K. Roth and M. W. Weiner. Determination of cytosolic ADP and AMP concentrations and the free energy of ATP hydrolysis in human muscle and brain tissues with ^{31}P NMR spectroscopy. Magnetic resonance in medicine, 22(2):505–511, 1991.

[302] A. Melani, D. Turchi, M. G. Vannucchi, S. Cipriani, M. Gianfriddo, and F. Pedata. ATP extracellular concentrations are increased in the rat striatum during *in vivo* ischemia. Neurochemistry international, 47(6): 442–448, 2005.

[303] K. M. Hargreaves and W. M. Pardridge. Neutral amino acid transport at the human blood-brain barrier. Journal of Biological Chemistry, 263(36): 19392–19397, 1988.

[304] A. Bringmann, T. Pannicke, J. Grosche, M. Francke, P. Wiedemann, S. N. Skatchkov, N. N. Osborne, and A. Reichenbach. Müller cells in the healthy and diseased retina. Progress in retinal and eye research, 25(4):397–424, 2006.

[305] M. Ankarcrona, D. Ankarcrona, M. Jeannette, E. Bonfoco, B. Zhivotovsky, S. Orrenius, S. A. Lipton, and P. Nicotera. Glutamate-induced neuronal death: a succession of necrosis or apoptosis depending on mitochondrial function. Neuron, 15(4):961–973, 1995.

[306] E. Morishita, S. Masuda, M. Nagao, Y. Yasuda, and R. Sasaki. Erythropoietin receptor is expressed in rat hippocampal and cerebral cortical neurons, and erythropoietin prevents *in vitro* glutamate-induced neuronal death. Neuroscience, 76(1):105–116, 1996.

[307] D. Attwell. Brain uptake of glutamate: food for thought. The Journal of nutrition, 130(4):1023S–1025S, 2000.

[308] R. W. Williams and K. Herrup. The control of neuron number. Annual Review of Neuroscience, 11:423–453, 1988.

[309] F. A. C. Azevedo, L. R. B. Carvalho, L. T. Grinberg, J. M. Farfel, R. E. L. Ferretti, R. E. P. Leite, W. J. Filho, R. Lent, and S. Herculano-Houzel. Equal numbers of neuronal and nonneuronal cells make the human brain an isometrically scaled–up primate brain. The Journal of Comparative Neurology, 513(5):532–541, 2009.

[310] D. A. Ucko. Basics for Chemistry. Elsevier Science, 2013.

[311] K. B. Storey. Functional metabolism: regulation and adaptation. Wiley-IEEE, 2004.